

Study of Oil/Pressboard Progressive Creeping Discharge
under Highly Divergent Electric Field

Von der Fakultät für Elektrotechnik und Informatik
der Gottfried Wilhelm Leibniz Universität Hannover

zur Erlangung des akademischen Grades

Doktor-Ingenieur (Dr.-Ing.)

genehmigte Dissertation

von

M.Sc. Xin Zhou

geboren am 09. September 1988

in Chongqing, China

2022

1. Referent: Prof. Dr.-Ing. Ernst Gockenbach

2. Referent: Prof. Dr.techn. Stefan Kornhuber

Vorsitzender: Prof. Dr.-Ing. Peter Werle

Tag der Promotion: 16. März. 2022

CONTENT

Content	I
List of Acronyms and Abbreviations	III
Acknowledgement	V
Abstract	VI
Kurzfassung	VIII
1 Introduction	1
1.1 Problem Statement	1
1.2 Research Objective.....	2
1.3 Thesis Structure	2
2 Theoretical Background and Literature Review	4
2.1 Transformer Failure and Insulation System	4
2.2 Interface Phenomena	12
2.3 Creeping Discharges at Liquid/Solid Interfaces.....	23
3 Test Facilities and Measurement Techniques	32
3.1 Electrode Geometry and Electrode Configuration	32
3.2 Construction of Test Cells	35
3.3 Sample Information and Sample Processing.....	37
3.4 Measurement and Analytic Techniques	40
3.5 Test Set-up.....	49
4 Influences of Ageing and Field Intensity on AC Creeping Discharges	53
4.1 Introduction	53
4.2 Sample Preparation and Experimental Setup	53
4.3 Results of Preliminary Tests.....	55
4.4 Results of Long-term Constant-Stress Creeping Discharge Tests	63
4.5 Conclusions	80
5 Tracking Phenomena of AC Creeping Discharges	82
5.1 Introduction	82
5.2 The Internal Treeing Phenomenon	82
5.3 Revisiting White Marks, Carbonization and Bubbling of Internal Treeing	95
5.4 The Surface Tracking Phenomenon	101
5.5 Discussion	104
5.6 Conclusions	105
6 Influences of Temperature and Stress Type on AC Creeping Discharges	107
6.1 Introduction	107
6.2 Experimental Setup and Measurement Techniques	108
6.3 Test Results	110
6.4 Discussion	127

6.5 Conclusions	129
7 Influences of Temperature and Oil Flowing on DC Creeping Discharges	130
7.1 Introduction	130
7.2 Theoretical Background	130
7.3 Sample Preparation and Test Setup.....	137
7.4 Results of Preliminary Tests.....	138
7.5 Results of DC Creeping Discharge Tests	146
7.6 Discussion	157
7.7 Conclusions	161
8 Conclusions	163
References	166

LIST OF ACRONYMS AND ABBREVIATIONS

AC	Alternating Current
ASTM	American Society for Testing Materials
BTA	1,2,3- Benzotriazol
CAPD	Chaotic Analysis of Partial Discharge
CDF	Cumulative Distribution Function
CIGRE	International Council on Large Electric Systems
DC	Direct Current
DGA	Dissolved Gas Analysis
DWT	Discrete Wavelet Transform
DP	Degree of Polymerization
ECT	Electrostatic Charging Tendency
EDL	Electric Double Layer
EHD	Electro-Hydrodynamic
EHV	Extra-High Voltage
FEM	Finite-Element Method
FFT	Fast Fourier Transform
FID	Flame Ionization Detector
GaAs	Gallium Arsenide
HV	High Voltage
HVAC	High Voltage Alternating Current
HVDC	High Voltage Direct Current
IEC	International Electrotechnical Commission
IEEE	Institute of Electrical and Electronics Engineers
ISO	International Organization for Standardization
KFT	Karl Fischer Titration

LCC	Line-Commutated Converter
MSD	Multi-Scale Signal Decomposition
OD	Oil Directed
OF	Oil Forced
ON	Oil Natural
PD	Partial Discharge
PDC	Polarization and Depolarization Current
PDF	Probability Density Function
PDIV	Partial Discharge Inception Voltage
PE	Polyethylene
ppm	parts per million
PRPD	Phase-Resolved Partial Discharge
PSA	Pulse Sequence Analysis
RMS	Root Mean Square
SEM	Scanning Electron Microscope
SPMD	Swarming Pulsive Micro-Discharges
TCD	Thermal Conductivity Detector
TDCG	Total Dissolved Combustible Gases
UHV	Ultra-High Voltage
XLPE	Cross-Linked Polyethylene

ACKNOWLEDGEMENT

Foremost, I would like to extend my sincere thanks to Prof. Ernst Gockenbach for his invaluable guidance during the research program and warmhearted help in preparing the defending presentation. Besides, I am grateful to Prof. Stefan Kornhuber for his thoughtful comments that improve the thesis quality a lot. Also, I owe a debt of gratitude to Prof. Peter Werle, the committee chair, for his support and motivation during my stay at Schering-Institut.

I would also like to acknowledge my colleagues at Schering-Institut: Dr. Hassan Saadati, Dr. Mahdi Rahimbakhsh, Dr. Hongda Guo, Mr. Mohammad Imani, Mr. Christian Eichler, Mr. Moritz Kuhnke, and the Werkstatt, for their dedicated support to the research activities and for the fruitful discussions that inspired me a lot. In particular, I am grateful to Dr. Xiang Zhang and Prof. Zhongdong Wang for their motivation when I faced detours and setbacks in my academic career.

I would like to thank my students: Mr. Alexy Rybakov, Mr. Huibin Shi, Ms. Ting Zhu-Humboldt, and Ms. Ying Li, for their enthusiasm for the high voltage engineering, excellent implementation of the laborious tests, and also for the trust and friendship. This work cannot be accomplished without their contributions.

Special thanks are given to my friends: Dr. Tianyan Jiang, Mr. Wentong Liao, and Mr. Yiqun Liu, for their enduring motivation and help in both academic and personal aspects.

Last but not least, I would like to express my deepest gratitude to my parents and my fiancée for their unwavering love, understanding, encouragement, and sacrifice.

ABSTRACT

As one of the most dangerous failure modes of transformers, the oil/pressboard progressive creeping discharge, as well as the corresponding insulation failure mechanisms, have thus far not been fully understood. The present thesis aims to gain a sound fundamental knowledge of the progressive creeping discharge, their influential factors, and the relevant failure mechanisms, as well as to contribute to an effective monitoring and diagnostic methodology.

This study explored the progressive creeping discharges under highly divergent AC and DC voltages, respectively. The tests conditions were configured to investigate the impacts of critical influential factors, including ageing, voltage level, temperature, stress waveform, and oil flowing, on creeping discharges. The discharge processes were systematically evaluated using tools such as partial discharge, gas analysis, temperature monitoring, and finite-element simulation. Comparative analyses and theoretical examinations were made to the insulation faults as well as their correlated physicochemical phenomena. A conventional techniques-based monitoring framework was proposed for the dangerous creeping discharges, and the applicability of a new detection technique based on synchronous PD and dielectric measurements was tested as well.

The characteristics of damage-free AC progressive creeping discharge, as well as the influences of pressboard ageing and field intensity, were investigated. It was found the progressive creeping discharge is a compound discharge that comprises mainly oil corona discharge and surface discharge. Pressboard ageing affected the discharge inception but had no influence on the interface breakdown strength. The damage-free discharge exhibited a constant PRPD pattern but had a diminishing PD intensity, where the pressboard ageing and voltage level jointly determine whether the discharges can be sustained or not. The damage-free discharge generated hydrogen principally and was located between D1/ D2 fault zones in the classical Duval's Triangle.

The insulation failures due to dangerous creeping discharges were comparatively studied. It was found the AC progressive creeping discharge could generate two faults to the pressboard, i.e., internal treeing (internal treeing) and surface tracking (surface tracking). The faults exhibited distinct electrical as well as physicochemical characteristics, and their occurrences were subject to pressboard ageing, voltage level, and pressboard density. A four-staged model was proposed to illustrate the development of internal treeing. The model highlighted the central role of the filament-like carbonization tracks in the pressboard interior, of which the onset and growth were theoretically expounded as well. A detection methodology was proposed for internal treeing, which was mainly based on continuous PD measurement, online temperature monitoring, and gas analysis. However, it was found still hard to detect a severe surface tracking fault due to the PD disappearance.

The influences of temperature and voltage waveforms on AC progressive creeping discharge were studied. Temperature affected the short-time electric strength of either interface or oil gap and could form a synergistic effect with a strong field in exacerbating the dissipation factor of pressboard. Moreover, it was found temperature can determine the fault types and discharge severity under either constant or step-wise stress, whereas the stress waveform had an obvious effect on the fault type only at high temperatures. Depending on the test temperature and stress waveforms, the test specimens failed due to tracking-free interface flashover, surface tracking, and internal treeing, respectively. Their PD quantities were comparatively evaluated. Moreover, it was found the synchronous PD and dielectric measurement is highly indicative of the internal treeing process, and it exhibited both high

detection sensitivity and discharge identification capability.

The DC progressive creeping discharge was evaluated against temperatures and forced oil flows. Temperature affected the DC conductivity of both oil and pressboard, the resistivity ratio of pressboard to oil, and the oil/pressboard interface charge relaxation time. Accordingly, the interface field distributions were evaluated against temperatures using the finite-element method. Moreover, both oil flow speed and temperatures affected the short-time DC interface electric strength as well as the progressive creeping discharge. Two types of discharges were found under static oil condition. They exhibited distinct PD characteristics and showed different responses to temperature changes. They were presumably associated with discharges in oil and pressboard, respectively. Furthermore, it was found that forced oil flows can alter the behaviors of DC creeping discharges drastically and generated a peculiar PD type (Pulse Train). The occurrence of the pulse train was subject to applied voltage level, temperature, and oil flowing velocity. A theoretical model was proposed to elucidate the pulse train, in which the interactions between space charges from different sources were discussed against voltage levels, oil flows, and temperatures.

The present thesis extends the knowledge of the oil/pressboard progressive creeping discharges. The research results are expected to serve as a base for future scientific studies and a piece of reference information for practical applications pertinent to progressive creeping discharges.

Keywords: power transformer, oil/pressboard, creeping discharge, partial discharge, interface phenomenon

KURZFASSUNG

Eine der gefährlichsten Fehlerarten in Transformatoren, die fortschreitende Kriechentladung in Öl/Feststoff Anordnungen sowie der dazugehörige Mechanismus des Isolationsfehlers sind noch nicht völlig geklärt. Die vorliegende Arbeit zielt auf die Erreichung einer soliden fundamentalen Kenntnis der fortschreitenden Kriechentladung, ihrer Einflussfaktoren und der entsprechenden Fehlermechanismen ab. Weiterhin soll sie einen Beitrag zur effektiven Überwachung und diagnostischen Methoden liefern.

Die Untersuchungen beinhalten die fortschreitenden Kriechentladungen bei stark inhomogenen elektrischen Feldern unter Wechsel- und Gleichspannung. Die Versuchsbedingungen wurden so konfiguriert, dass die Wirkung der kritischen Einflussfaktoren auf die Kriechentladungen wie Alterung, Höhe der Spannung, Temperatur, Beanspruchungsform und Ölfluss, untersucht werden konnte. Die Entladungsvorgänge wurden systematisch ausgewertet unter Verwendung von Methoden wie Teilentladung, Gasanalyse, Temperaturerfassung und Simulation mit Finiten Elementen. Vergleichende Analysen und theoretische Prüfungen wurden im Hinblick auf Isolierungsfehler und der dazugehörigen physio-chemischen Erscheinungen durchgeführt. Ein auf konventioneller Technik basierendes Monitoring Konzept wurde für die gefährlichen Kriechentladungen vorgeschlagen und die Anwendung neuer Detektionstechniken basierend auf synchroner Teilentladungserfassung und dielektrischen Messungen geprüft.

Die Eigenschaften von beschädigungsfreien fortschreitenden Kriechentladungen bei Wechselspannung und der Einfluss der Alterung des Pressspan sowie der Feldstärke wurden untersucht. Es wurde herausgefunden, dass die fortschreitende Kriechentladung eine zusammengesetzte Entladung ist, bestehend aus Korona-Entladungen in Öl und Oberflächenentladungen. Die Alterung von Pressspan beeinflusst den Einsatz der Entladung aber hat keinen Einfluss auf die Durchschlagsfestigkeit der Grenzfläche. Die beschädigungsfreie Entladung zeigt ein konstantes PRPD Muster aber mit abnehmender Teilentladungs-Aktivität, wobei die Alterung des Pressspans und die Spannungshöhe gemeinsam bestimmen, ob die die Entladungen unterbrochen werden oder nicht. Die beschädigungsfreie Entladung erzeugt grundsätzlich Wasserstoff und ist den Fehlerzonen D1/D2 des klassischen Duval Dreiecks zugeordnet.

Die Fehler der Isolierung infolge der gefährlichen Kriechentladungen wurden vergleichend untersucht. Es wurde herausgefunden, dass die fortschreitende Kriechentladung bei Wechselspannung zwei Fehlerarten im Pressspan erzeugen kann, die schnelle Kriechwegbildung (internes Treeing) und die langsame Kriechwegbildung (Oberflächen Kriechweg). Die Fehler weisen deutlich elektrische als auch physio-chemische Eigenschaften auf und ihr Erscheinen war abhängig vom Alterungszustand des Pressspans, Spannungshöhe und Dichte des Pressspans. Ein vierstufiges Modell wurde vorgeschlagen um die Entwicklung der schnellen Kriechwegbildung darzustellen. Das Modell betont die zentrale Rolle der faserähnlichen karbonisierten Kriechwege im Inneren des Pressspans, wobei Einsatz und Wachstum theoretisch erklärt werden. Eine Erkennungsmethode für die Schnelle Kriechwegbildung wurde vorgeschlagen, die im Wesentlichen auf Teilentladungsmessungen, online Temperaturerfassung und Gas Analyse basiert. Es war dennoch schwierig eine langsame Kriechwegbildung zu erfassen, da Teilentladungen verschwanden.

Die Einflüsse von Temperatur und Spannungsform auf fortschreitende Kriechwegentladungen wurden untersucht. Die Temperatur beeinflusste die kurzzeitige elektrische Feldstärke der

Grenzschicht und der Ölstrecke und kann eine synergetische Auswirkung mit einem starken Feld auslösen, indem sich der Verlustfaktor des Pressspan erhöht. Es wurde weiterhin herausgefunden, dass die Temperatur die Fehlertypen und Entladungsstärke unter konstanter oder stufenweise Beanspruchung beeinflussen kann, wobei die Art der Beanspruchung einen klar erkennbaren Einfluss auf die Fehlerart nur bei hohen Temperaturen hat. Abhängig von der Prüftemperatur und der Beanspruchungsform versagten die Prüflinge durch Grenzschichtüberschlag ohne Kriechwegspuren, langsame Kriechwegbildung und schnelle Kriechwegbildung. Ihre Teilentladungsgrößen wurden vergleichend ausgewertet. Darüber hinaus wurde herausgefunden, dass synchrone Teilentladungen und dielektrische Messungen eine gute Kennzeichnung für schnelle Kriechwegbildungsprozesse sind und es zeigt die Fähigkeit einer hohen Erkennungsempfindlichkeit und Entladungserkennung.

Die fortschreitenden Kriechentladungen bei Gleichspannung wurden in Abhängigkeit der Temperatur und der Ölflussstärke ermittelt. Die Temperatur beeinflusst die Gleichspannungsleitfähigkeit von beiden, Öl und Pressspan, das Widerstandsverhältnis von Pressspan und Öl, und die Relaxationszeit der Grenzschichtladungen Öl/Pressspan. Dementsprechend wurde die Grenzschichtfeldverteilung in Abhängigkeit der Temperatur mit Hilfe der Finite-Elemente Methode ausgewertet. Außerdem beeinflussten die Geschwindigkeit des Ölflusses und die Temperaturen die kurzzeitige Grenzflächenfeldstärke bei Gleichspannung und fortschreitenden Kriechwegentladung. Zwei Arten von Entladungen wurde bei ruhendem Öl gefunden. Sie zeigen deutliche Teilentladungsmerkmale und unterschiedliches Verhalten bei Temperaturänderungen. Sie waren vermutlich verbunden mit Entladungen im Öl und Pressspan. Es wurde weiterhin herausgefunden, dass forcierte Ölströmung das Verhalten der Kriechentladungen bei Gleichspannung drastisch verändert und einen besonderen Typ von Teilentladungen erzeugt (Pulsfolge). Die Erscheinung dieser Pulsfolge war abhängig von der Höhe der angelegten Spannung, der Temperatur und der Geschwindigkeit des Ölflusses. Es wurde ein theoretisches Modell zur Verdeutlichung der Pulsfolge vorgeschlagen, bei dem die Wechselwirkungen zwischen Raumladungen von verschiedenen Quellen behandelt wurden in Abhängigkeit der Spannungshöhe, des Ölflusses und der Temperatur.

Die vorliegende Arbeit erweitert die Kenntnis der fortschreitenden Kriechentladungen in der Anordnung Öl/Pressspan. Es wird erwartet, dass die Untersuchungsergebnisse als Basis für zukünftige wissenschaftliche Studien dienen und einen Beitrag mit hinweisenden Informationen für die praktische Anwendung zur Thematik fortschreitender Kriechentladungen liefern.

Schlagworte: Leistungstransformator, Öl/Pressspan, Kriechentladung, Teilentladung, Grenzflächenphänomene

1 INTRODUCTION

1.1 Problem Statement

As an integral part of any composite insulation structure, an interface is featured by its discontinuity in electrical, dielectric, and physicochemical properties. Unfortunately, the interface is ubiquitous in power and converter transformers and is deemed as a weak point of the entire insulation system. Among other interface-related issues, oil/pressboard creeping discharge is a particularly dangerous phenomenon, as it can fail the major insulation system even under normal operating conditions. A vast majority of the previous investigations in this field focus on the short-time behaviors of creeping discharges, e.g., interface flashover, interface electro-hydrodynamic motion, and pre-breakdown streamer. However, practical experiences have shown us that it is the long-term progressive creeping discharge that causes most failures of the oil/pressboard insulation system.

Thus far, the progressive creeping discharges, as well as their related failure mechanisms, have still not been fully understood, not to mention the development of effective monitoring and diagnostics methodologies toward them. This is largely due to the highly intricate nature of the progressive creeping discharge. On the one hand, it involves multiple materials, exhibits possibly varying discharge patterns, and features different accompanying phenomena. On the other hand, under the effects of critical influential factors, the oil/pressboard creeping discharges might generate distinct faults, and the insulation system could fail in utterly different manners.

A few of pioneering works have provided meaningful insights into this topic. However, some key issues pertinent to progressive creeping discharges still remain unsolved. Among others, the most pressing problems are listed as follows:

- No widely accepted definition of the progressive creeping discharge has been established. This problem causes great chaos in constructing defect models and selecting test arrangements. As a result, it is inconvenient to compare different investigation results, and a portion of researches has obviously deviated from practical scenarios.
- The nature, initiation conditions, and long-term trends of progressive creeping discharges shall be better clarified. Sound knowledge of these basic facts is essential to a valid and effective discharge severity assessment. Besides, from the perspective of practical operations, it is vital to distinguish the damage-free creeping discharges from really dangerous events.
- The effects of critical influential factors on progressive creeping discharges shall be systematically re-examined with deeper insights. Progressive creeping discharge involves both insulating oil and pressboard. In most cases, the same influential factor causes different variations to oil and pressboard properties and thus exacerbating the interface discontinuity further. Moreover, the degradation of the pressboard or oil is actually a multi-faceted phenomenon with mutually competing effects, rather than a single factor-dominated process as hypothesized in many previous investigations.
- The characteristics and mechanisms of insulation faults due to creeping discharges are still open questions. Dependent on environmental conditions and material properties, the progressive creeping discharge could result in different types of faults to oil/pressboard insulation. For different fault types, their developmental processes, accompanying phenomena, and physicochemical mechanisms are greatly varied from each other. For detecting and identifying the faults effectively, efforts must be made to reveal their underlying

mechanisms, elaborate the fault-to-failure evolution paths, and characterize their accompanying phenomena.

- No effective monitoring and diagnostics methodology is thus far available. Last but not least, it is found that the ongoing progressive creeping discharges could easily elude conventional detection techniques. This problem is due partly to a lack of relevant knowledge and due partly to an absence of advanced technology.

1.2 Research Objective

To address the above-mentioned problems, the present thesis carries out systematic and in-depth investigations on progressive creeping discharges. The primary objectives of the investigations are described as follows:

- To formulate a valid defect model of the progressive creeping discharge as well as to identify its discharge sources, discharge pattern, and discharge signals.
- To draw a clear line between damage-free creeping discharges and failure-inducing creeping discharges. For the creeping discharges-induced failures, their initiation conditions and evolution paths will be comparatively studied by various means, e.g., partial discharges, visual recording, online temperature monitoring, and gas analyses.
- To give clear illustrations and convincing explanations to the most representative accompanying phenomena of the dangerous creeping discharges, such as white marks, surface tracking, internal treeing, and bubbling effect. The results are supposed to shed light on the understanding of the insulation failure mechanism.
- To investigate the effects of critical influential factors on the inception and development of interface creeping discharges under AC voltage. Specifically, the test samples will be processed to different thermal ageing degrees, and the test environments will be configured to have varying voltage levels, temperatures, and stress waveforms.
- To propose a tentative methodology to detect and monitor the inception and development of dangerous creeping discharges in power transformers. Besides, it is also attempted to make possible improvements to conventional diagnostics and to test the applicability of relatively new detection techniques.
- To examine the progressive creeping discharges under the DC field based on the relevant knowledge obtained under AC voltage. The DC creeping discharges will be investigated in different temperatures and under forced oil flows. Prior to discharge tests, the basic properties of insulation materials under the DC field, e.g., DC conductivity, will be determined.

1.3 Thesis Structure

The present thesis consists of eight chapters. Chapter 1 gives a brief overview of research significance and research objectives.

Chapter 2 reviews the theoretical backgrounds and the existing literature on creeping discharges. First, it reports the transformer failure patterns and gives statistics of transformer failure modes and failure locations. Second, the insulation degradation mechanism and the major insulation structure of a transformer are presented. Third, the interface phenomena related to creeping discharges are discussed in detail. Fourth, it reports the history and status quo of the researches in this field.

Chapter 3 presents the test facilities and measurement techniques used in this thesis. Firstly, it shows

the specially designed electrode configurations. Afterwards, it illustrates the constructions of test cells and sample information. Subsequently, a detailed introduction of measurement techniques is presented. Lastly, the high voltage test circuits for various purposes are schematically depicted.

Chapter 4 investigates the influences of pressboard thermal ageing and the voltage level on oil/pressboard creeping discharges under AC voltage. In Chapter 4, the influences of thermal ageing on pressboard properties are firstly examined in terms of capillary water rise, absolute moisture, and fiber integrity. The interface field distributions versus voltage levels are studied by FEM simulations, where the emphasis is put on the triple-junction area. Afterwards, ramp-stress tests are carried out on different samples to determine their short-term electric strengths. Subsequently, the progressive creeping discharges are systematically studied via analyzing their partial discharge patterns, signal waveforms, and statistical distributions. Lastly, the effects of thermal aging and the voltage level on the inception and development of progressive creeping discharges are demonstrated, which is followed by a detailed interpretation of the dissolved-gas analysis.

Chapter 5 is dedicated to the tracking phenomena of pressboards due to progressive creeping discharges under AC voltage. Section 5.2 gives a detailed analysis of the internal treeing phenomenon, including its visual information, stage division criteria, and accompany phenomena. Section 5.3 revisits the accompanying phenomena of internal treeing and proposes their governing mechanisms. Section 5.4 reports the investigation results of the surface tracking phenomenon and summarizes the comparisons between internal treeing and surface tracking. Section 5.5 discusses the obtained results and presents a tentative monitoring and detection methodology of internal treeing.

Chapter 6 studies the influences of temperatures and stress types on oil/pressboard progressive creeping discharges under AC voltage. Section 6.2 focuses on the technical considerations of test temperature and voltage waveform selections and ends with an introduction of the test set-up and sample information. Section 6.3 presents all the experimental results. In Section 6.3, it firstly deals with the effects of temperature on pressboard dielectric properties. Subsequently, the influences of temperature and stress waveforms on progressive creeping discharge are studied, in which the emphasis is put on the failure mechanisms and PD characteristics. At last, a new detection method based on synchronous PD and online dielectric measurements is proposed and examined.

Chapter 7 investigates the influences of temperatures and forced oil flows on oil/pressboard progressive creeping discharges under DC voltage. Firstly, the DC conductivity, relative permittivity, and relaxation times of oil and pressboard are examined against different temperatures. Secondly, the interface DC field distributions under different temperatures are simulated via FEM methods. Thirdly, the influences of temperature on DC creeping discharges are studied under step-wise DC stress. The DC PD patterns and PD quantities are analyzed against temperature and voltage levels. Fourthly, the DC creeping discharges are investigated under three oil flowing levels. The DC PD patterns and PD quantities are analyzed against temperatures, voltage levels, and oil flowing speeds. Besides, the streaming currents due to forced oil flows are also measured and analyzed. Fifthly, a detailed discussion is carried out to explain creeping discharges under the DC field, which unravels the interactions between space charges from different sources.

Finally, Chapter 8 gives the conclusions of the present thesis.

2 THEORETICAL BACKGROUND AND LITERATURE REVIEW

2.1 Transformer Failure and Insulation System

2.1.1 Failure Pattern and Failure Cause of Transformer

Transformer is one of the most important as well as the costliest equipment of an electricity transmission network. The failures of an in-service transformer usually cause great problems and huge losses to utilities and consumers. For instance, only the output loss of an unplanned outage caused by transformer failures is counted in million dollars [1], not to mention the repair costs and possible hazards to other apparatus [2]. Moreover, under the economic pressures of electricity market liberalization, grid operators have to extract the maximum value of the capital-intensive assets and, in the meantime, secure their safe operations. To achieve this goal, therefore, it is imperative to study transformer failures and manage transformer health.

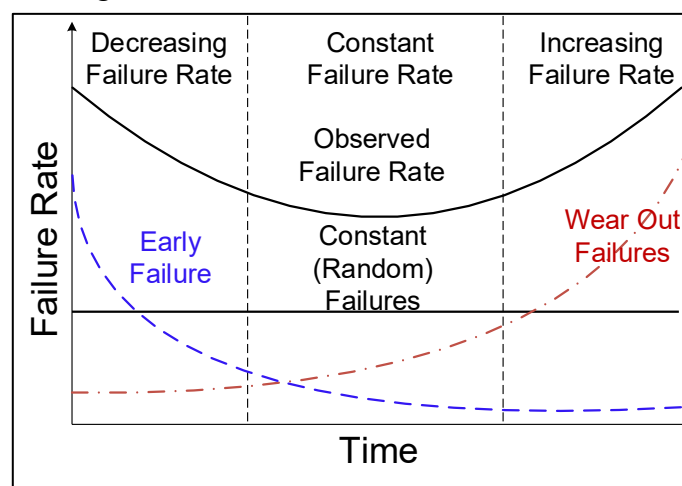


Figure 2.1 Traditional transformer failure pattern [3]

As shown in Figure 2.1, transformer failures follow the so-called “Bathtub Curve.” According to its failure rate, the lifecycle of a transform is subdivided into three consecutive stages. The first stage is known as the “infant-mortality” period. In this period, early failures predominate, and the total failure rate gradually declines with service time. Sequentially, the second stage is referred to as the “constant-failure” period. In this period, failures are mainly aroused by random causes, and the total failure rate does not vary greatly. Lastly, as a transformer approaches its life end, the number of ageing-related wearing-out failures soars, and this period is marked as the third stage of transformer failures [2, 3].

The root causes of transformer failures could be categorized as follows [4]:

- originally insufficient safety margin due to design deficiencies, manufacturing weaknesses, material defects, and so forth;
- operation stresses exceeding specified quantities, such as unusual events and operational error;
- critical deterioration of safety margin, such as inadequate maintenance and low-quality repair.

To summarize, a transformer fails when the stresses, either operational or abnormal, exceed its withstand strength. Therefore, the condition of a transformer can be evaluated by comparing its withstand strength with stress levels, as illustrated in Figure 2.2. It is noteworthy that failures can take place even without any fault, as the withstand strength itself of a transformer would be inevitably

prejudiced with operation time. On the other hand, a fault can accelerate the deterioration of transformer condition and thereby leading to premature failures.

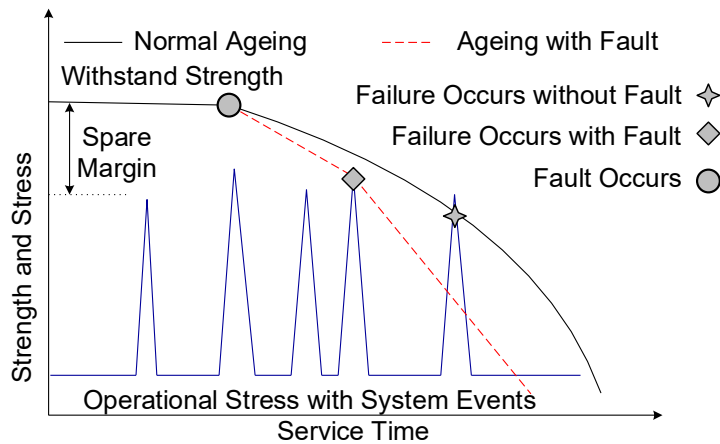


Figure 2.2 Transformer condition in its life cycle [5]

2.1.2 Failure Modes and Failure Statistics of Transformers

A running transformer is subject to a combination of various stresses, including electric stress, thermal stress, mechanical stress, and environmental stress. Accordingly, it may fail in different ways for miscellaneous reasons. According to Cigré working group A 2.18 [6], most transformer failures fall into the following modes : (1) Dielectric (Partial Discharge, Tracking, or Flashover) ; (2) Electrical (Open Circuit, Short Circuit, Poor Joint, Poor Contact) ; (3) Thermal (General Overheating, Localized Hotspot) ; (4) Physical Chemistry (Moisture, Particles, Gas, Corrosion) ; (5) Mechanical (Bending, Breaking, Displacement, Loosening, Vibration); and (6) Unknown.

Figure 2.3 displays the results of an international power transformer failure survey carried out by Cigré. As shown, dielectric-related failure is the most prevalent failure mode of substation transformers. Actually, dielectric failures make up more than 70 % of transformer failures in the extra-high voltage (EHV) class (500 kV– 700 kV). Mechanical failure and electrical failure are the second and third prevalent failure modes, respectively.

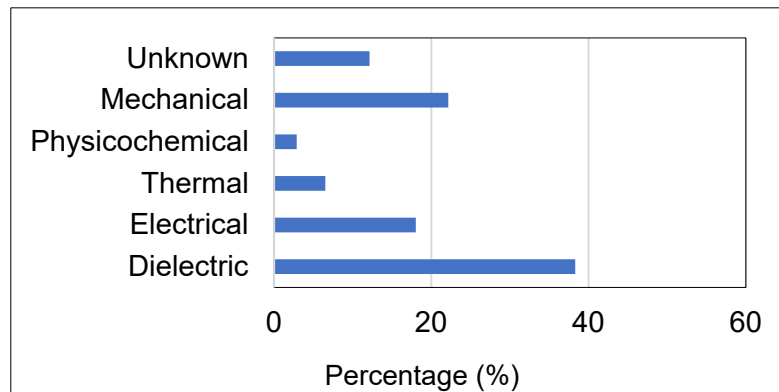


Figure 2.3 Failure mode analysis of 799 substation transformers [7]

Moreover, the statistics of transformer failure locations are displayed in Figure 2.4. As displayed, windings are the most vulnerable components: winding-related failures account for over 37 % of the total failures. Tap changer and bushing are other major failure locations, accounting for 31% and 17% of the total failures, respectively. Besides, HV parts are remarkably more inclined to fail than their LV counterparts. For example, over 50 % of winding failures occur on the HV side, and more than 80 % of bushing failures are related to HV bushings.

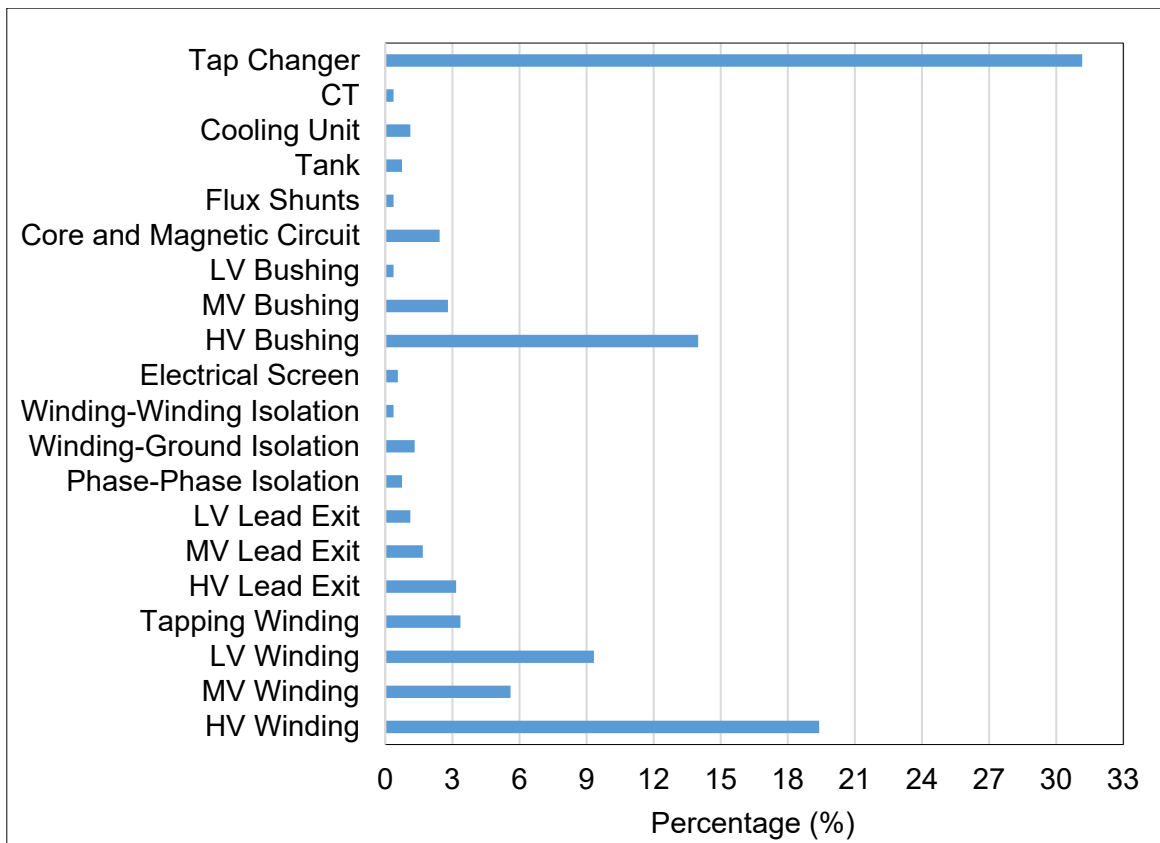


Figure 2.4 Failure location analysis (substation transformers, $U \geq 100$ kV, 536 failures) [7]

Slightly different from the scenario of power transformers, HVDC converter transformers usually fail due to the following causes [8]: (1) Mechanical; (2) Dielectric; (3) Thermal; (4) Induced Current; (5) Operational Error; and (6) Unknown. CIGRE advisory group B4.AG 04 has summarized the failure statistics of HVDC line-commuted converter (LCC) transformers from three consecutive international surveys, of which the timespans are years of 1972-1990, 1991-2002, and 2003-2013, respectively. The results regarding failure modes and failed components are depicted in Figure 2.5 and Figure 2.6, respectively.

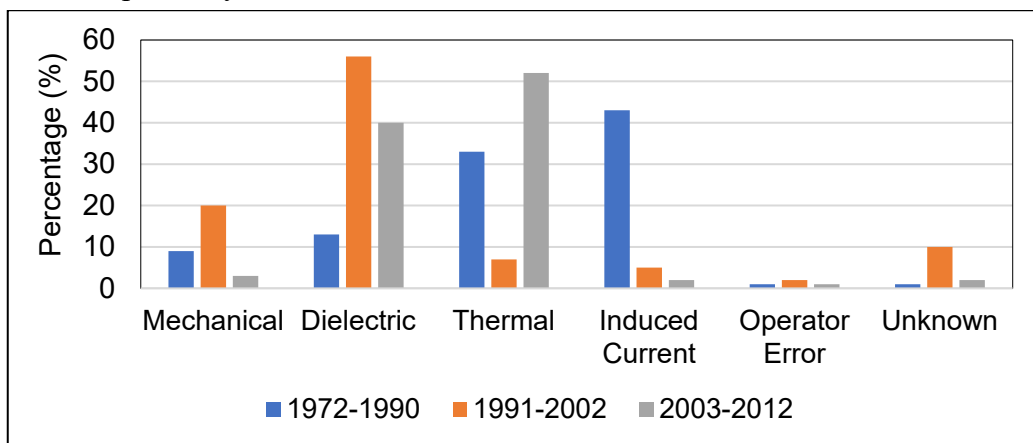


Figure 2.5 HVDC LCC converter transformer failure by modes [8]

Similar to the power transformer, dielectric failures and thermal failures are the most prevalent failure modes of converter transformers. More specifically, dielectric failures account for 56 % and 40 % of the total reported failures in 1991-2002 and 2003-2013, respectively; whereas, thermal failures account for 33 % and 52 % of the total reported failures in the periods of 1972-1990 and 2003-2012, respectively. Failures due to induced current used to make up a great portion in 1972-1990 but have

been remarkably diminished ever since. This change is probably a result of advancements in transformation protection techniques.

With regard to the failure components, valve winding is the most vulnerable part of the LCC converter transformer, and the connection is the second one. Core-related failures made up nearly half of the total failures in 1972-1990 and thereafter have been obviously mitigated. The vulnerability of valve winding is mainly due to the fact it has to withstand highly complex electric stresses in service.

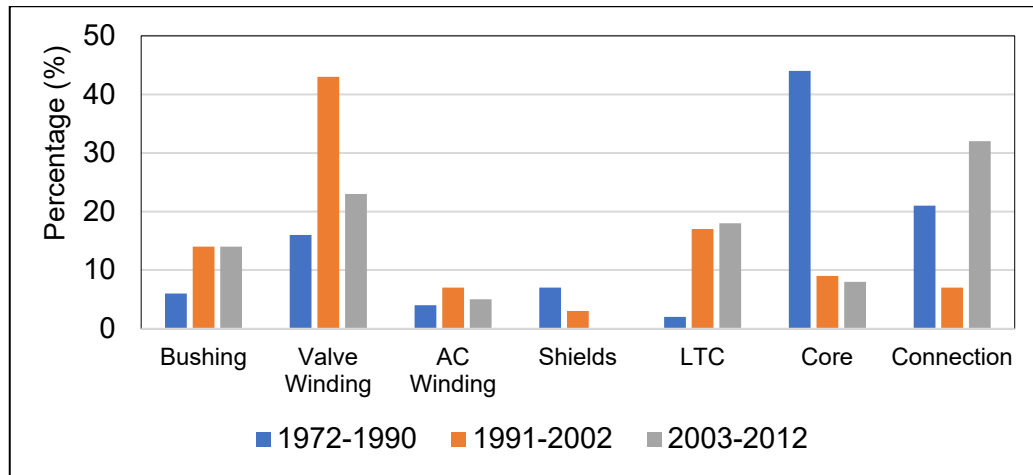


Figure 2.6 HVDC LCC converter transformer failure by components [8]

2.1.3 Physicochemical Properties of Insulation Materials

As probably the most important insulating liquid in the electric industry, mineral oil has been widely used in various types of electrical equipment, such as transformers, cables, capacitors, and circuit breakers. In essence, mineral oil is a mixture of hydrocarbons obtained from crude oil through fractional distillation. To make sure it possesses desired properties, moreover, mineral oil has to be refined through the following processes [9]:

- distillation: to eliminate the “light ends” and heavy fraction and produce a suitable feedstock;
- de-waxing: to eliminate n-paraffinic type hydrocarbons that precipitate under low-temperature;
- solvent extraction: to remove undesired aromatics and hetero-aromatic compounds;
- hydrogenation: to transform the unsaturated hydrocarbons by the reaction of hydrogen and oil over a fixed catalyst bed.

The hydrocarbon molecules of mineral insulating oils generally fall into three groups: paraffin, naphthenes, and aromatics. The paraffin is saturated hydrocarbons with chain-like backbones of single-bonded carbon atoms. The chains may be linear or, more often, with several branches. The naphthenes are also saturated hydrocarbons with one or several ring-like structures of single-bonded carbon atoms. The aromatics are unsaturated hydrocarbons with C=C double bond ring-like structures [10].

Table 2.1 enlists several representative hydrocarbons present in mineral insulating oils.

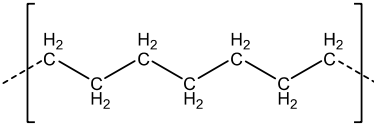
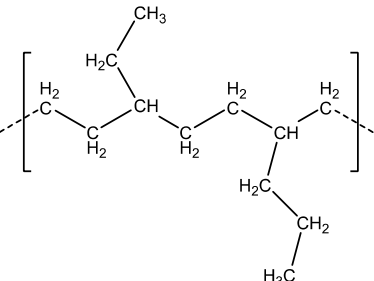
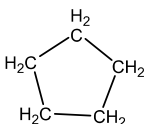
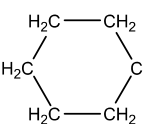
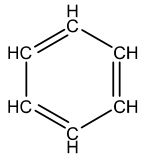
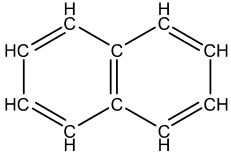
The properties of mineral insulating oil are highly dependent on the compositions. For instance, the paraffin and naphthenes affect the physical properties of mineral oil, such as density, viscosity, and pour point; whereas, the aromatic compounds influence the oxidation resistance, the gassing tendency, and impulse strength [9]. As a result, compromises must be made when facing varying and specific requirements. In a power transformer, mineral insulating oil is expected to serve three main

purposes:

- provide electric isolation between metal parts of different potentials;
- cool windings and core through heat transfer via natural convection or forced flowing;
- fill the pores and voids in solid insulating materials.

Therefore, the dynamic viscosity, the electric strength, and the compatibility with solid insulating materials are the three principal parameters in choosing transformer insulating oil [11].

Table 2.1 Hydrocarbon molecules in mineral insulating oil [12]

Saturated Hydrocarbon	Unsaturated Hydrocarbon	
<p>Linear Paraffin</p>  <p>Branched Paraffin</p> 	<p>Naphthene 1</p>  <p>Naphthene 2</p> 	<p>Aromatics 1</p>  <p>Aromatics 2</p> 

An overwhelming majority of solid insulating materials in a transformer are made from unbleached wood pulp, which is refined by the so-called “Kraft” process. Therefore, the insulating paper/pressboard obtained through this manner is referred to as kraft paper/pressboard. The major contents of the Kraft wood pulp are cellulose (75 % - 85%), hemicellulose (10% -20%), lignin (2-6%), and other inorganics (<0.5%) [13]. Cellulose is a natural linear high polymer that comprises a chain of cellobiose units linked by 1,4- β -glucosidic bonds. A cellobiose unit is composed of two β -D-levoglucose units of inverted conformations [14]. The structure of the cellulose molecule is shown in Figure 2.7, where n denotes the degree of polymerization (DP). The DP of new insulating paper/pressboard (before the factory drying) normally ranges from 1000 to 1200.

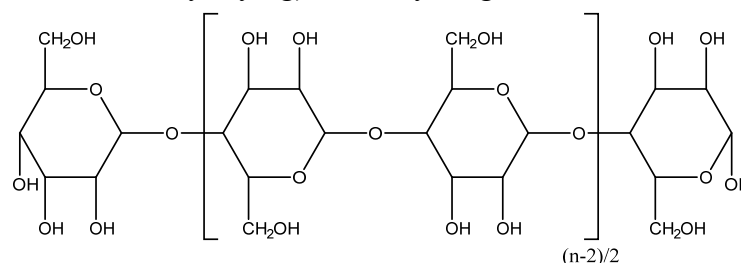


Figure 2.7 The chemical structure of cellulose molecule [14]

Figure 2.8 shows the structure of cellulose fibers. Hemicellulose is one kind of polysaccharide that has a much lower DP (50-250). It plays an important role in forming cellulose fiber sheets and hydrogen bonding, thus having a great influence on the mechanical integrity of insulating paper/pressboard. Lignin is a complex molecular structure containing cross-linked polymers of

phenolic monomers. It can provide protection to cellulose molecules.

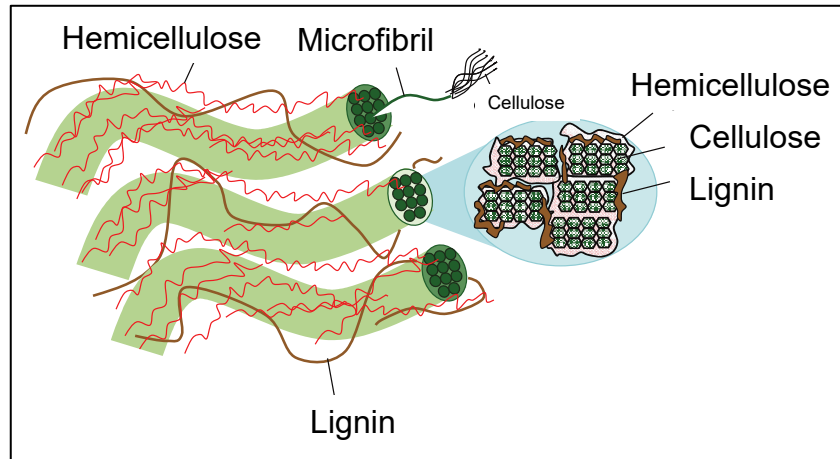


Figure 2.8 Strands of cellulose molecules embedded in a matrix of hemicellulose and lignin [15]

2.1.4 Degradation of Insulation Materials

From the commissioning of a transformer on, its insulation materials are incessantly subject to multiple ageing stresses, including electrical stress, thermal stress, mechanical stress, and environmental stress. These stresses can bring about intrinsic and/or extrinsic degradation to materials and eventually result in insulation failures. To make it worse, the ageing of transformer insulation is an immensely complex process, which involves various influential factors that have great yet obscure interplays. Figure 2.9 presents the degradation processes and failure mechanisms of transformer oil/cellulose insulation.

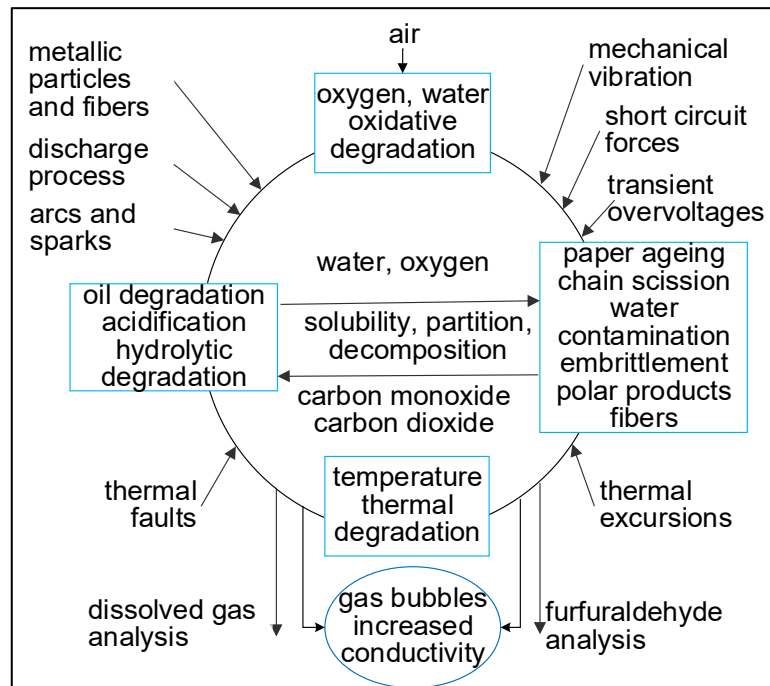


Figure 2.9 Degrading factors and fault mechanisms of oil/paper insulation [16]

As displayed, the major causes of oil degradation are electrical discharges, oxidation, contamination (water and particles), and temperature. The degradation of insulation oil could be considered somewhat reversible, as aged oil in a transformer can be rehabilitated to restore its insulation strength or be replaced by a retro-filling process [17]. On the contrary, there is no commercially feasible way to restore the insulating properties of aged cellulosic materials. In consequence, it is the cellulose

insulation that determines the lifespan of a transformer insulation system. Therefore, the emphasis is put on the ageing phenomena of cellulosic insulation in the following paragraphs.

The degradation of cellulosic insulation in a transformer is mainly ascribed to three processes: hydrolysis, oxidation, and pyrolysis [18]. The degradation mechanisms of cellulosic insulation are shown in Figure 2.10. The hydrolysis of cellulose is an auto-accelerated chemical reaction that is catalyzed by soluble acids, e.g., formic acid and acetic acid. In hydrolysis, each cleavage of glucosidic bond consumes one water molecule and produces three new ones, thereby generating two net water molecules. Nonetheless, rather than the amount of water, it is the concentration of hydrogen ion (H^+) that really matters in controlling the hydrolysis rate. Water, on the other hand, causes carboxylic acids to dissociate into hydrogen ions, thereby exerting profound effects on the ageing process [19].

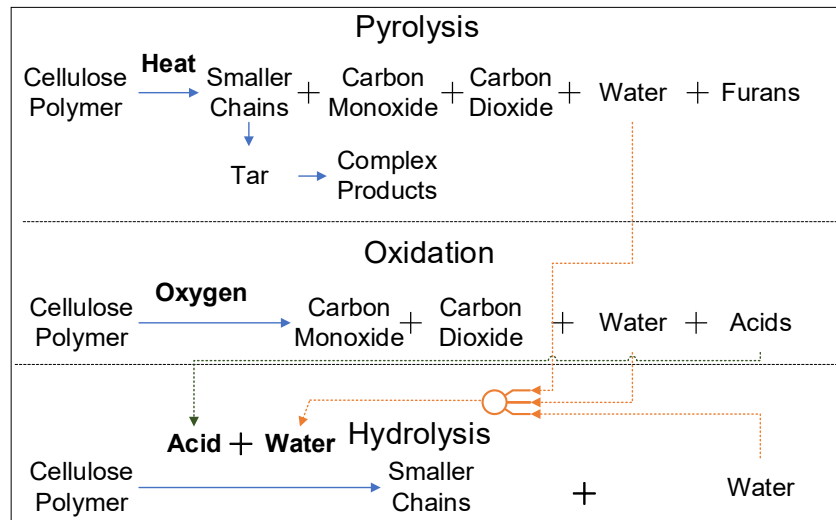


Figure 2.10 The degradation mechanisms of cellulosic insulation [20]

The oxidation of cellulose is catalyzed by the radical hydroxyl group ($-OH$), which is a decomposition product of hydrogen peroxide (H_2O_2) and organic hydroperoxides ($-ROOH$). The oxidation of cellulose facilitates the accumulation of ageing agents for hydrolysis, such as carboxylic acids. Nevertheless, the oxidation process is retarded in an acid environment, indicating an antagonistic effect with acid hydrolysis in deteriorating cellulose molecules [13]. The pyrolysis under $140\text{ }^\circ\text{C}$ is a degradation of the cellulose molecule, which can produce carbon dioxide, carbon monoxide, water, and furans.

2.1.5 Oil-barrier Insulation Structure

Solid insulation in a transformer falls into two categories: minor insulation and major insulation. The minor insulation refers to the materials that insulate individual coil conductors and isolate different layers and sections, such as wrapped papers and spacers. The major insulation refers to the materials that serve as inter-winding, inter-phase, and winding-to-ground insulations, including pressboard cylinder, pressboard barrier, angle ring, cap, and so forth. The typical major insulation system of a core-type transformer is shown in Figure 2.11.

In general terms, solid insulation in a transformer is supposed to fulfill triple purposes: to form electric isolation between metal parts of different potentials, to provide mechanical support to heavy components, and to construct oil flowing ducts. Therefore, various kinds of solid insulation are manufactured and then carefully selected for different purposes. Due to its low shrinkage and high resistance to pressure, pre-compressed pressboard is a perfect barrier structure for short-circuit

protection in the vertical area of the main gap; whereas, the components made out of wet pressboard are ideal insulating structures in horizontal and intermediate radial areas of the end insulation because they can be readily shaped to conform the equipotential contours for alleviating field distortions [21].

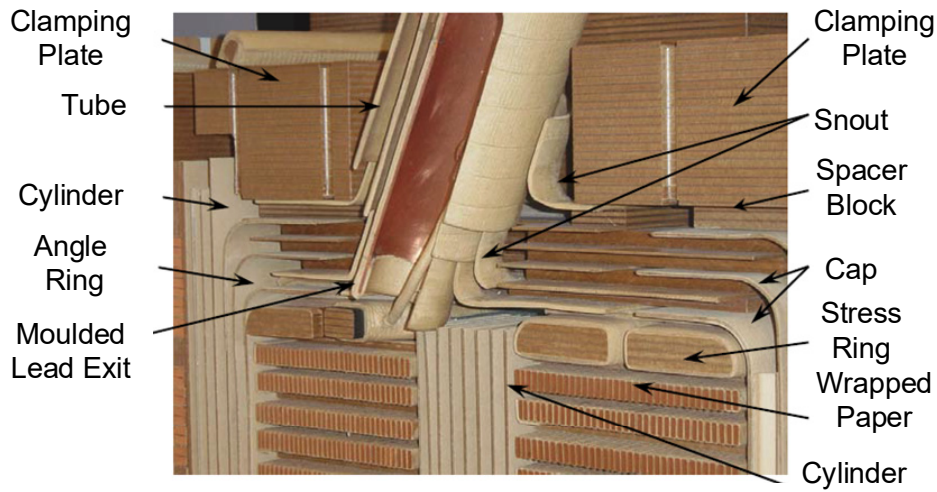


Figure 2.11 Cross-sectional view of a 400 kV transformer major insulation (220 kV-side) [13]

In particular, the oil-barrier structure is of vital importance to the entire insulation system of the transformer. In divergently stressed regions in transformers, such as inter-winding, winding-to-tank, and winding-to-core areas, pressboards are inserted into oil gaps for subdividing long oil gaps into several smaller ducts. In theory, the highest electric strength of oil gaps can be achieved as long as the oil-barriers structures are properly arranged. This technology was introduced into the transformer industry in the 1960s and still remains the predominant means of constituting transformer major insulation structures[22]. The pronounced effect of oil-barrier structure in enhancing the electric strength of the transformer insulation system is depicted in the industry-proven “Weidmann Design Curve,” as shown in Figure 2.12.

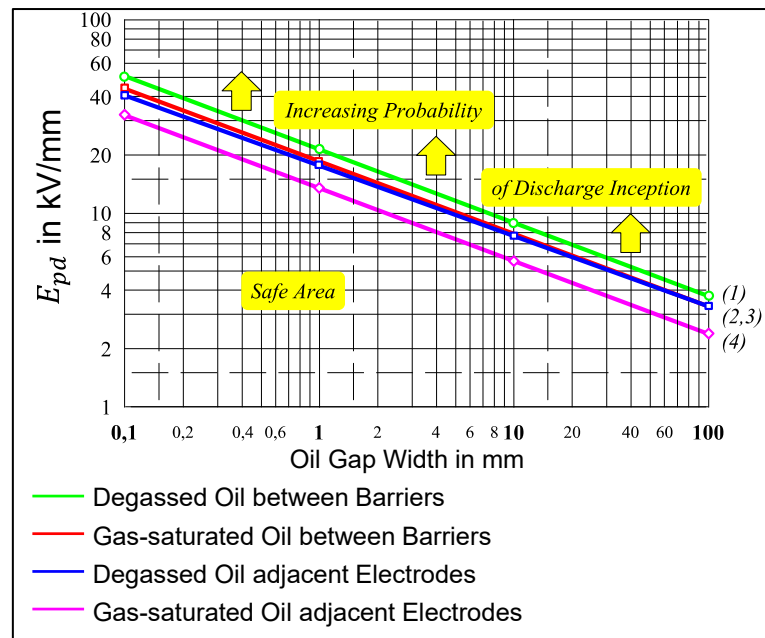


Figure 2.12 Weidmann design curve [23]

It is clearly seen that the electric strength of the insulation system is inversely proportional to the oil gap width for all concerned scenarios. However, it is noteworthy that the oil-barrier structure increases the electric strength of the entire insulation system rather than that of an individual oil duct.

As a matter of fact, the individual oil duct withstands greater electric stress than a barrier, as the relative permittivity of the pressboard is almost twice that of oil. To make a trade-off, therefore, the industry adopts a thin-barrier and wide-duct oil-barrier structure for large transformers, in which the barriers are made as thin as possible while the oil gaps are made as wide as possible [23].

Moreover, higher electric strength of the insulation system, as required by transformers of higher rated voltages, can be simply achieved by increasing the number of barriers. Figure 2.13 illustrates the typical inter-winding oil-barrier structures of transformers operated under different voltage classes.

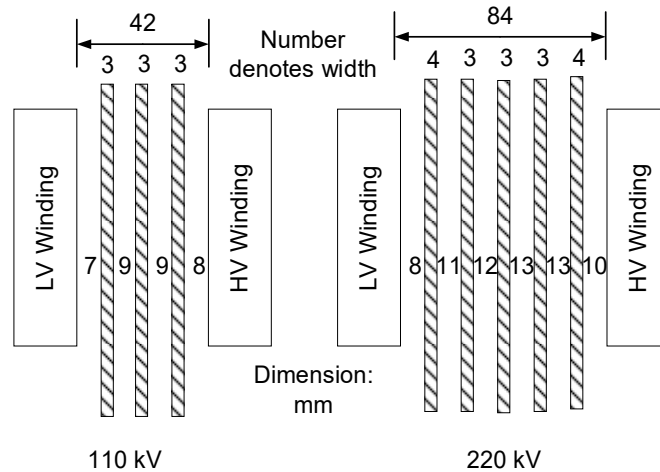


Figure 2.13 Inter-winding oil-barrier structure of transformers [24]

2.2 Interface Phenomena

However, the oil-barrier structure produces a disadvantageous factor as well, i.e., the oil/pressboard interface. As a transition region between pressboard and oil, the interface is featured by a discontinuity of dielectric and physicochemical properties. In reality, the problems pertinent to the oil/pressboard interface have posed a great challenge to transformer designers, manufacturers, and operators. On the one hand, the oil/pressboard interface is ubiquitous inside an oil-filled transformer; on the other hand, it is a weak point of the entire insulation system because the electric strength of an oil-pressboard interface is proven lower than that of either constituent material. Numerous interface-related transformer failures have been witnessed across global utilities during either factory testing or service [25]. Moreover, in spite of a great number of investigations, the oil/pressboard interface phenomenon is still not well understood. Rather than providing an exhaustive description of all interface phenomena, the following paragraphs would deal with several special interface properties that are closely related to the thesis topic.

2.2.1 Interface Morphology

The morphology of an oil/pressboard interface is probably much more complex than one might think. Figure 2.14 shows the surface topography of a pre-compressed pressboard sample. The pressboard surface is full of specially arranged wire marks. The dimpled surface texture is above all for enlarging the contact surface of the pressboard to oil, thus improving its oil adsorption. In addition, to prevent the formation of a long surface discharge channel, the layout of wire marks is carefully controlled to segregate the dimples from one another. With the help of a high-resolution optical microscope, the dimpled texture of the pre-compressed pressboard becomes more discernible, as shown in Figure 2.14 b). Surrounding the dimples are interwoven ruptured fibers, of which the ends are stretching into all

directions. It indicates there is no clear-cut boundary between the pressboard surface and oil.

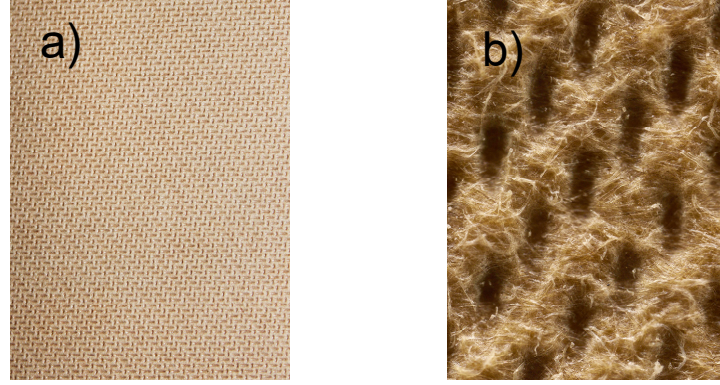


Figure 2.14 Pressboard surface topography; a) pressboard surface wire marks; b) dimples

Furthermore, by means of a 3D laser microscope, one can examine the surface profile of the pressboard in a quantitative way, as shown in Figure 2.15. The colors indicate the heights relative to the very bottom of the surface. More specifically, the yellow-to-orange areas denote the interwoven fibers; whereas, the green-to-blue areas denote the dimples. Besides, the surface profile of the dashed line-crossed area is given in Figure 2.15 (c). As can be seen, the relative height ranges from 54.7 μm to 103.9 μm , and the lowest point is certainly at the dimple. The information expressed in Figure 2.15, which echoes the previous statements, indicates that the oil/pressboard interface is neither homogeneous nor clear-cut.

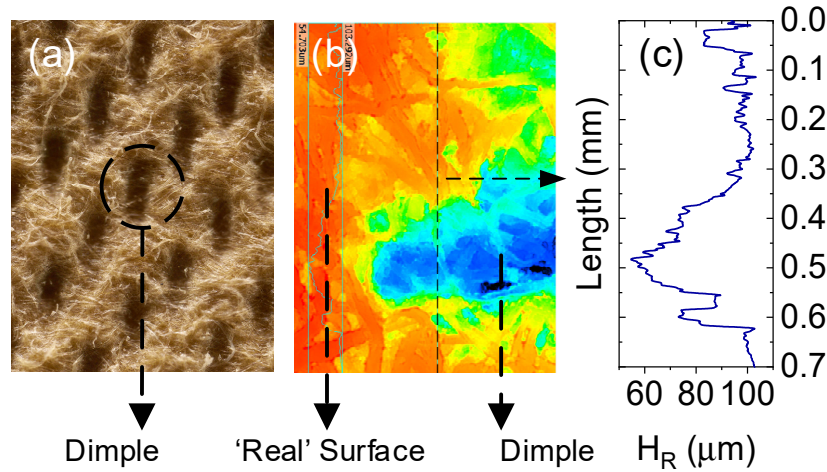


Figure 2.15 Pressboard surface morphology; a) pressboard surface under an optical microscope; b) dimple structure under a 3D laser scanning microscope; c) surface profile of the dimple cut-line

2.2.2 Permittivity Mismatch

In electrostatic or quasi-electrostatic fields, the behavior of a linear dielectric is governed by the following equations:

$$\begin{aligned}\vec{D} &= \varepsilon_0 \vec{E} + \vec{P} \\ \vec{P} &= \varepsilon_0 \chi_e \vec{E} \\ \chi_e &= \varepsilon_r - 1\end{aligned}\tag{2.1}$$

where \vec{D} is the displacement vector or electric flux density vector, \vec{E} is the electric field, \vec{P} is the polarization vector, ε_0 is the electric permittivity of free space, χ_e is the electric susceptibility of dielectric, and ε_r is the relative permittivity. From Equation 2.1, it begets a fundamental constitutive

relation of static electromagnetism:

$$\vec{D} = \varepsilon_0(1 + \chi_e) \vec{E} = \varepsilon_0 \varepsilon_r \vec{E} \quad (2.2)$$

Besides, the relation between \vec{E} and electric potential φ follows Poisson's Equation:

$$\vec{E} = -\nabla\varphi \quad (2.3)$$

Moreover, for an ideal composite dielectric in a static field, its interface has to satisfy two boundary conditions: the continuity of electric potential φ and the continuity of normal component of electric flux density \vec{D} [26].

Suppose an ideal composite dielectric composed of materials A and B in an electrostatic field, where the relative permittivity of A ε_A is half of that of B ε_B . The configuration is illustrated in Figure 2.16 and, where the effects of volume conduction and surface conduction are neglected.

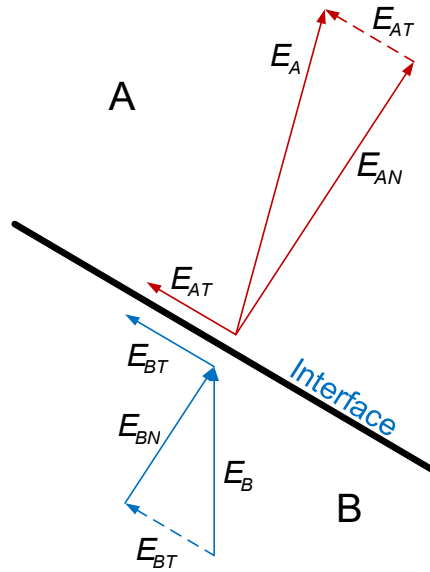


Figure 2.16 Composite dielectric in the electrostatic field [27]

The electric field is decomposed into normal component and tangent components,

$$\vec{E}_A = \vec{E}_{AN} + \vec{E}_{AT} \quad (2.4)$$

$$\vec{E}_B = \vec{E}_{BN} + \vec{E}_{BT}$$

Complying with the continuity of electric potential, the potential of the interface shall be identical everywhere. From Equation 2.3, it therefore begets:

$$\vec{E}_{BT} = \vec{E}_{AT} \quad (2.5)$$

In addition, considering the continuity of the normal component of electric flux density, it can be derived from Equation 2.2:

$$\varepsilon_0 \varepsilon_A \vec{E}_{AN} = \varepsilon_0 \varepsilon_B \vec{E}_{BN} \quad (2.6)$$

$$\varepsilon_B = 2 * \varepsilon_A$$

$$\vec{E}_{AN} = 2 * \vec{E}_{BN}$$

The normal component of the electric field in material A is twice that in material B. Accordingly, the total electric field \vec{E}_A would be distorted as well, as shown in Figure 2.16. This phenomenon is also referred to as dielectric refraction.

With respect to the oil-barrier insulation, the electric distortion due to permittivity mismatch is of great negative influence on its interface electric strength. Taylor has investigated the influence of permittivity mismatch on interface flashover voltage under power frequency ramp voltage [28]. Figure 2.17 shows the relation of permittivity ratio and spacer efficiency of different kinds of liquid-solid combinations, where the permittivity ratio ε_s and spacer efficiency E_s are defined as:

$$\varepsilon_s = \frac{\varepsilon_{li}}{\varepsilon_{so}} \quad (2.7)$$

$$E_s = \frac{V_{LF}}{V_{LB}} \quad (2.8)$$

where ε_{li} and ε_{so} are the relative permittivity of liquid and solid, respectively; V_{LF} is the interface flashover voltage and V_{LB} is the breakdown voltage of liquid alone.

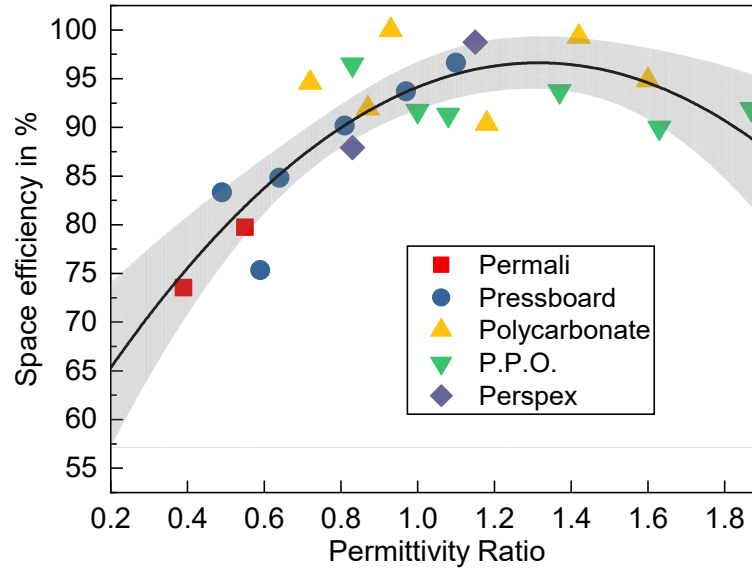


Figure 2.17 Variation of spacer efficiency with interfacial permittivity ratio [28]

It is found the electric strength of a liquid-solid interface is generally lower than that of an open oil gap, and the weakening effect is closely linked to the degree of permittivity mismatch. In addition, this weakening effect due to permittivity mismatch is also observed under impulse voltage [29].

2.2.3 Triple Junction Effect

The interface phenomena are further complicated when the interface contacts an electrode surface. The interface-electrode contact point is often referred to as a “triple-junction point,” where three media, i.e., two dielectrics and a conductor, meet each other. The triple-junction point could be very harmful to an insulation system, as it can cause field intensifications and thus facilitating the inception and propagation of electric discharges [30, 31].

The triple junction effect is essentially governed by two major factors: the contact angle between the electrode surface and dielectric interface α and the permittivity ratio of dielectrics ε_s . The most representative conditions of contact angle in an insulation system are illustrated in Figure 2.18, where A and B are dielectrics, and φ and P denote the electric potential and the contact point, respectively.

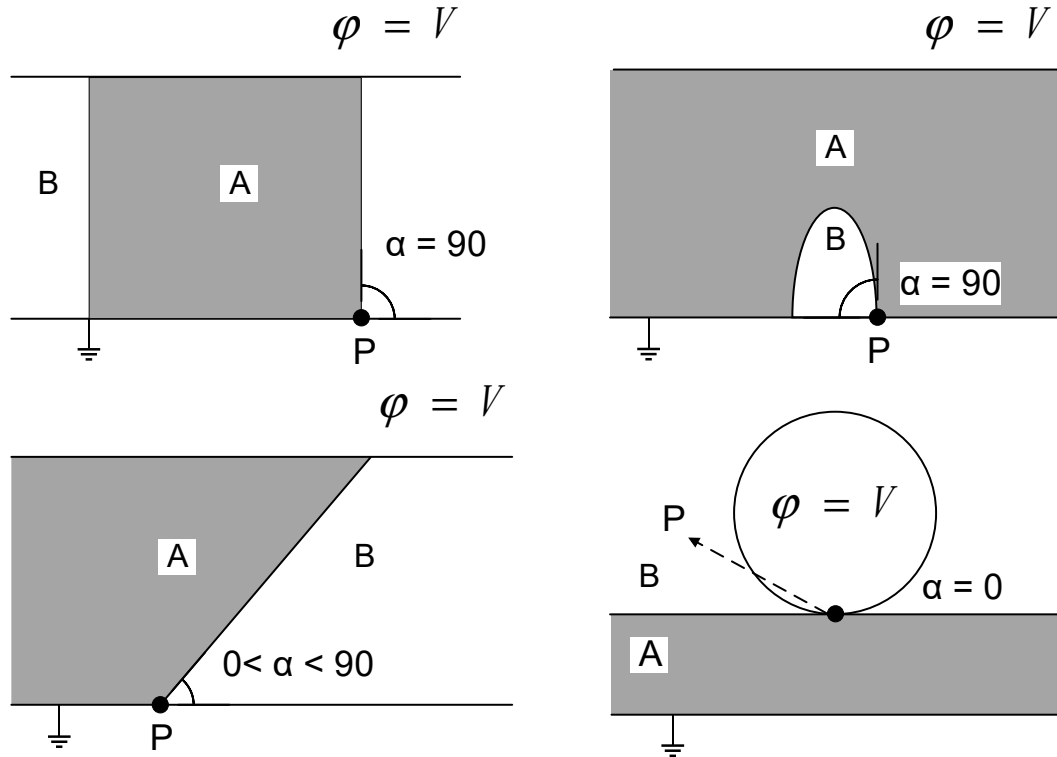


Figure 2.18 Triple-junction contact angles in composite dielectrics [30]

As displayed, the triple-junction contact angles could be sorted into three categories [26]:

- $\alpha = 90^\circ$,
where the dielectric interface is perpendicular to the electrode surface. Theoretically, there is neither field distortion nor field intensification in this case, regardless of the permittivity ratio. However, this ideal scenario barely exists in practice because of the rough surface of the solid dielectric;
- $0^\circ < \alpha < 90^\circ$,
where the dielectric interface and pressboard surface constitute an acute angle. Depending on the dielectric configuration and the permittivity ratio, the field intensity could be theoretically infinite or null at the contact point [30];
- $\alpha = 0^\circ$,
where either the interface or the electrode surface has a rounded shape to make a common tangent line at the contact point. Under this configuration, the field of interface near the contact point could be enhanced to a considerable extent. As the smooth contact of special interest to this thesis, the emphasis will be put on the zero-contact angle configuration.

Figure 2.19 presents the interface electric field distribution in a typical sphere-to-plane electrode configuration for varying permittivity ratios. The sphere electrode is energized by an electric potential of V and has a radius of R . Dielectrics A and B are split by a horizontal interface. The permittivity ratio ε_s is defined as:

$$\varepsilon_s = \frac{\varepsilon_B}{\varepsilon_A} \quad (2.9)$$

In addition, r denotes the horizontal distance from the triple-junction contact point P , E_t denotes the interface tangent field and E_1 equals to V/R . Two conclusions can be drawn from Figure 2.19. Firstly,

the interface tangent fields increase from null at the contact point to a peak value at a certain distance from the contact point and then gradually decline as the distance continues to increase. It infers the most electrically vulnerable point at a dielectric interface is somewhere away from the contact point rather than the contact point itself. Secondly, the triple junction effect is clearly influenced by permittivity mismatch as well. More specifically, the permittivity ratio can determine not only the degree of field intensification but also the location of the maximum field.

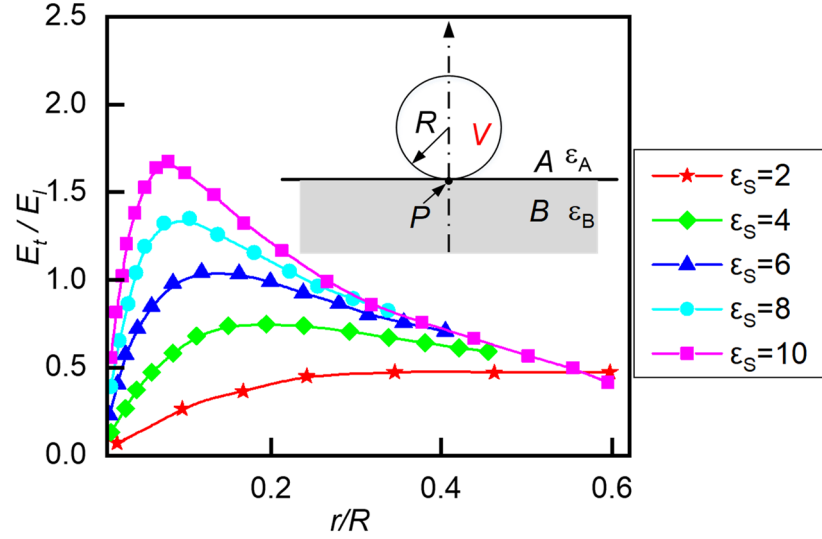


Figure 2.19 Interface field intensification for a zero-contact angle triple junction point [26]

2.2.4 Electrohydrodynamic Motion

When a pure insulating liquid is stressed by a strong electric field, a large number of charge carriers can be generated via three processes: field emission at the liquid-metal interface, field ionization of liquid molecules, and field-assisted dissociation of impurities. These charge carriers can yield a Coulomb's force under certain circumstances and cause hydrodynamic instability of liquid. In turn, an electro-convection of liquid is generated, which is also referred to as electro-hydrodynamic (EHD) motion [32]. The electric force density that governs the EHD motion is expressed as [33]:

$$\vec{F}_e = q\vec{E} - \frac{1}{2}E^2\nabla\epsilon + \nabla\left[\rho\frac{E^2}{2}\left(\frac{\partial\epsilon}{\partial\rho}\right)_T\right] \quad (2.10)$$

where \vec{F}_e is the electric force density, q is the charge density, \vec{E} is the electric field, ϵ is the permittivity of liquids, and ρ is the mass density. The first term on the right part of Equation 2.10 denotes Coulomb's force and the second term denotes the dielectric force. For a homogenous liquid, $\nabla\epsilon$ can be taken as null so that only the Coulomb's force presides the motion. The EHD motion alters the electric field distribution in the stressed volume of liquid and augments the conduction passage. Besides, it also affects the local pressure of oil and thus facilitating gas formation [12, 34, 35].

The introduction of a liquid/solid interface into an oil gap can modify the flow pattern of liquid EHD motion. Figure 2.20 illustrates the interface flow patterns as a function of the DC field intensities. Under low field, there are columnar vortices within the gap, which appear unaffected by the interface. However, under the intermediate field, the outer vortices begin to force the liquid to enter the gap. In consequence, a directed laminar flow passes along the interface. The laminar flow is present only in a gap bridged by a liquid/solid interface. Under high field, a stable flow pattern called cellular vortices emerges, which normally signifies an imminent breakdown. To conclude, the interface can promote

the flow pattern transition from stable columnar vortices to cellular vortices and thus lowering the breakdown voltage.

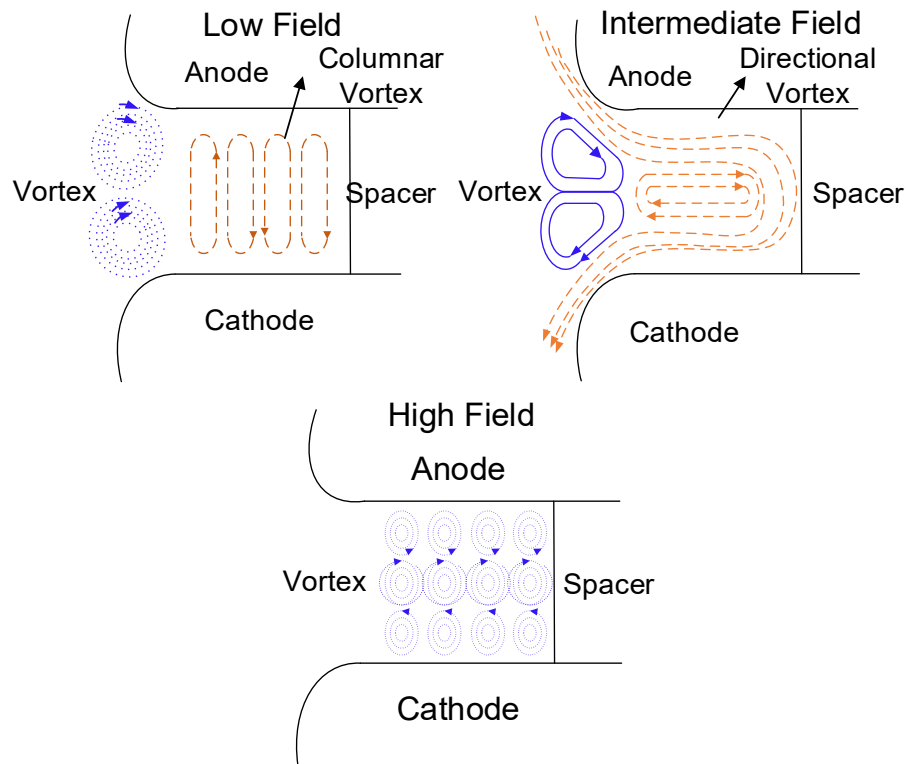


Figure 2.20 The flow pattern of EHD motion near a liquid-solid interface [36]

2.2.5 Moisture Migration and Bubbling

Excessive moisture can exert manifold detrimental effects on transformer insulation system, e.g., lowering PD inception field, exacerbating dielectric dissipation, accelerating solid degradation, and increasing risk of bubbling. Unfortunately, moisture is omnipresent in transformers and originates mainly from three sources [37]:

- residues moisture in insulation materials due to imperfect dehydration and impregnation;
- ingress from the ambient atmosphere during installation and service;
- decomposition of solid materials.

The hazardous effect of moisture is correlated with its physical state. For instance, free water in insulating oil is clearly more dangerous than oil-dissolved water. Water in insulating oil generally falls into three categories, i.e., dissolved water, dispersed water, and bound water [38]. The states of water in cellulosic materials, however, are much more complex. As shown in Section 2.1.3, cellulose is a highly polar and hygroscopic polymer with six hydroxyl groups on each of its repetition units, i.e., the cellobiose. In consequence, water molecules can be readily bound by cellulose molecules via hydrogen bonding. Besides, cellulosic paper/pressboard is also a porous fiber material. In addition to providing free spaces for water diffusion, the pores in the inter-fiber and intra-fiber areas also act as capillaries and thus enabling water adsorption via capillary effect [39–41]. Therefore, from the perspective of its interaction with cellulosic fibers, water in solid insulating materials exists in the following states: vapor, absorbed as a monolayer, absorbed as poly-layer, condensed in capillaries, and free [38].

Water absorption and water desorption in cellulosic materials take place mainly in the micro-capillaries, which are small channels in the microstructures of cellulose fibers and cannot be

impregnated by oil. Figure 2.21 gives a schematic illustration of water adsorption in micro-capillaries of cellulosic fibers. Firstly, water molecules are absorbed by surface polar groups of cellulose (active sites), generating the so-called ‘monolayer.’ Afterwards, as water content increases, water is absorbed through capillary force and thus forming a ‘polylayer.’ Finally, after reaching the saturation limit, water molecules will be condensed in micro-capillaries.

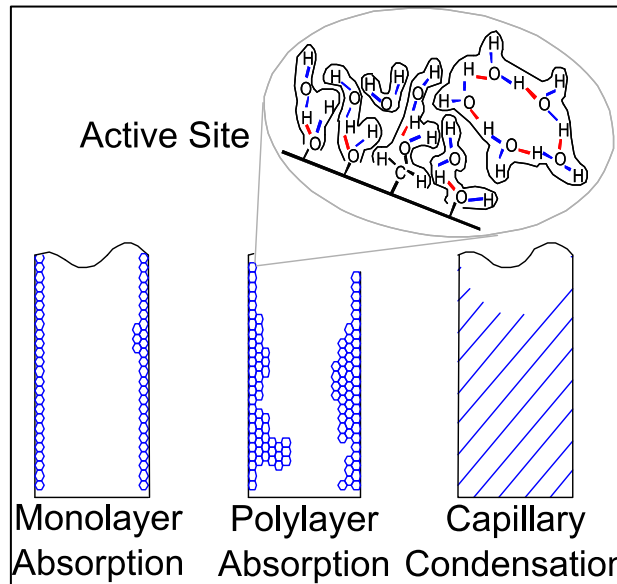


Figure 2.21 Adsorption of water molecules at active sites in micro-capillaries of cellulose [42]

The remarkable discrepancy in hydrophilicity between cellulosic material and mineral oil leads to a strikingly disproportionate moisture distribution in the transformer insulation system. Take a 25 MVA transformer as an example. An overwhelming majority of water reside in its solid materials (99.7 % at 40 °C and 97.3% at 80 °C), notwithstanding the great oil-to-solid mass ratio [43]. In this respect, solid insulation is like a water reservoir, whereas liquid insulation is but a moisture conveyer. However, the distribution is not static. Indeed, water migrates incessantly between oil and solid, and therefore the moisture distribution might reach a certain dynamic equilibrium. The migration process is subject to a couple of factors, among which the decisive ones are temperature and paper ageing degree [44–46]. Aiming for non-intrusive measurements of water content in solid materials, a number of moisture equilibrium curves have been proposed to assess water partitions under different conditions, such as Fabre-Pichon Curve [47], Oommen Curve [48], MIT Curve [49], and Perrier-Lukic Curve [50]. However, the proposed curves have their own inherent limitations and could lead to erroneous results if inappropriately used [51].

Under certain circumstances, the migration of water from solid to oil could come about in a very hazardous way, i.e., the bubbling effect. When the bubbling effect occurs, water on a solid surface, either vapor or condensed, is evaporated and then driven out of the inter-fiber macro-capillaries of cellulosic fibers, which ends up with the emission of free bubbles into insulating liquid [40, 52]. The bubbling could have double negative effects on the insulation system: diminution of interface electric strength and de-impregnation of cellulosic insulation [42].

The fundamental factor that governs the formation of bubbles is the water vapor pressure P_{WV} , an intrinsic property of pure water that increases with temperature. For enabling bubble formation and emission, the water vapor pressure P_{WV} has to conquer all external pressure and hampering forces [42], which includes atmospheric pressure P_A , hydrostatic pressure P_H , interfacial tension of oil F_{IT} , and bounding force of cellulosic fibers F_B :

$$P_{WV} > P_A + P_H + F_{IT} + F_B \quad (2.11)$$

A schematic illustration of bubble formation on the solid surface is given in Figure 2.22, where p_i is the equivalent of P_{WV} in Equation 2.11; p_e equals to the sum of P_A and P_H ; Δp denotes a function of F_{IT} and F_B ; R is the radius of bubble and r is the radius of the macro-capillary. From left to right in Figure 2.22, it depicts the evolutionary stages of a bubble in a macro-capillary on a solid surface with an increasing water vapor pressure, i.e., the inception stage, the expansion stage, the compression stage, the emission from the solid surface, and the movement in oil. Moreover, a steep temperature rise is indispensable in initiating bubbling, as water might migrate slowly into oil and get dissolved if the rising velocity of temperature is not sufficiently high [41].

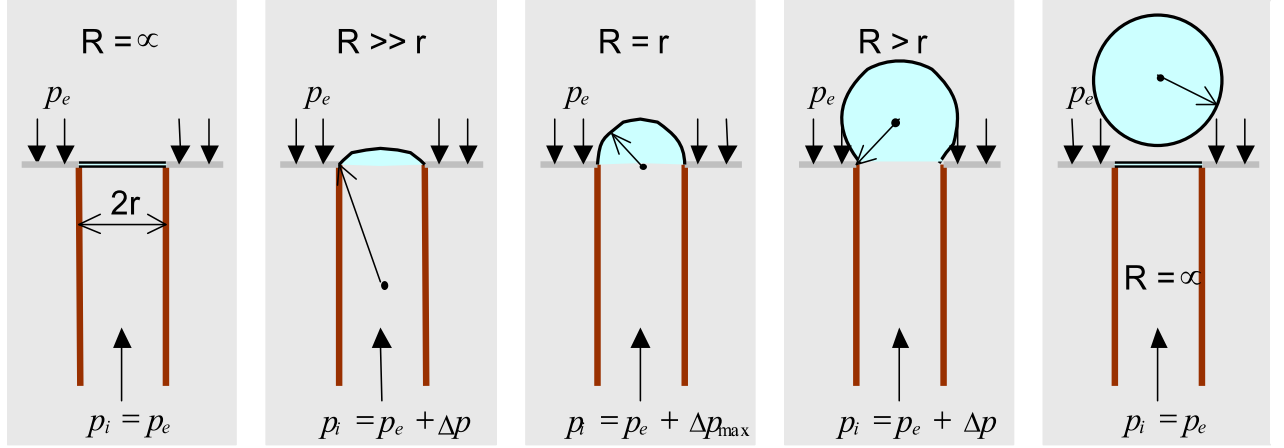


Figure 2.22 Bubble evolution from a macro-capillary on the solid surface [42]

The bubbling phenomenon in a transformer insulation system, its inception temperature, in particular, is also influenced by many other factors, e.g., water content and ageing condition of paper [41, 53], the chemical composition of oil [54], and dissolved gas in oil [42]. The primary cause of bubbling in a transformer is believed to be the overheat of winding conductors due to an overload of the transformer [55–57], and the dielectric dissipation of solid materials also shows a contributive effect [58]. Besides, inception temperature also determines bubble compositions [59, 60].

2.2.6 Streaming Electrification

Another dangerous phenomenon pertinent to the oil-solid interface in a transformer is streaming electrification, which is sometimes referred to as flow electrification or static electrification. Streaming electrification is a by-product of the modernization in transformer design and manufacturing technologies. As the rated voltage and capacity of the transformer increased, the forced oil flow cooling method was adopted for more efficient heat dissipation; better drying and purification techniques were introduced to generate high-resistivity oil and pressboard, and computer-aided design was utilized for a much more sophisticated oil duct design. Accordingly, the effects of streaming electrification have been greatly augmented. As a result, a high DC potential is possibly built up in the transformer and thus triggering electric discharges [61, 62]. Streaming electrification became a major concern of industry and academia in the 1970s when two catastrophic power transformers failures were reported in Japan. Moreover, as estimated by Crofts in 1988, there were at least 12 transformer failures in the US that can be ascribed to streaming electrification since 1983, with which oil/pressboard interface long-gap flashover was believed to be the predominant failure mode [63].

The oil/pressboard interface plays a key role in the process of streaming electrification in the transformer, for it is the place where charge separation and charge accumulation occur. When the oil in large-capacity power transformers is forced by a pump to flow into the oil ducts and pass along the pressboard surface, charge separation occurs. This process is schematically illustrated in Figure 2.23. As shown, due to its abundant polar groups of high electron affinity, the pressboard surface can absorb a number of negative ions, thus generating a fixed layer of adsorbed charge carriers. On the contrary, the net positive charges continue to flow upstream and build up a diffuse layer. This layer structure is often referred to as an electric double layer (EDL) [61].

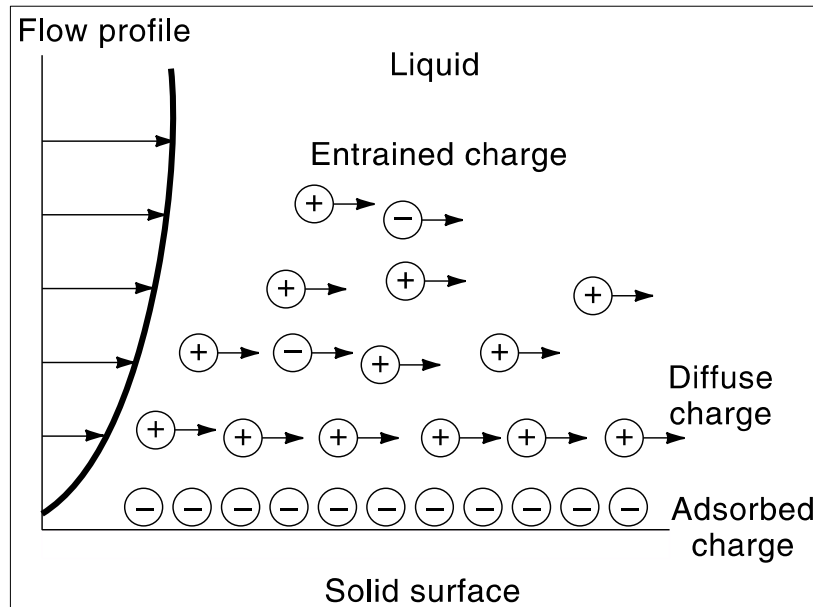


Figure 2.23 Charge separation at oil/pressboard interface [64]

However, streaming electrification in a transformer is a complex phenomenon, which involves various processes and various influential factors. In general terms, the process of streaming electrification could be divided into four distinct stages: charge generation, charge transport, charge accumulation, and charge leakage [65, 66]. For an intuitive illustration, an engineering model for a shell-form transformer streaming electrification analysis is presented in Figure 2.24, which is adapted from the work of Roach and Templeton [67].

- Charge Generation

As mentioned in Section 2.2.4, space charge in insulating liquids comes from three processes, i.e., field emission, field ionization, and field-assisted dissociation. Besides, mechanical friction can also lead to charge separation, and the pump is therefore suspected to be an important source of separated charges. Nevertheless, the oil/pressboard interface is still the foremost supplier of charges;

- Charge Transport

In natural-cooling transformers, the oil flow is primarily driven by the natural convection process, and the flow pattern is usually laminar. In this case, the streaming current is linearly proportional to the flow rate. In forced-cooling transformers, on the contrary, the oil flow is driven by the mechanical forces of pumps, and the flow pattern is usually turbulent. It is believed that turbulent flow can enhance the charge separation at the interface;

- Charge Accumulation

Charge accumulation is a key stage of the formation of a strong DC potential. If the majority of the net positive charges accumulate at a bare conductor surface, they will be immediately dissipated or neutralized, and no significant DC field can be built up. A strong DC field is possibly generated only when the majority of positive charges accumulate at the surface of the covered conductor or pressboard at a comparatively high rate;

- Charge Leakage

The net positive charge can be leaked through any metal part of earth potential in a transformer, such as tank, heat radiator, and pumps. Moreover, charge leakage also happens at the surface of a covered electrode or pressboard but at a much slower speed. The accumulation rate and the leakage rate of positive charges determine the steady-state potential distribution.

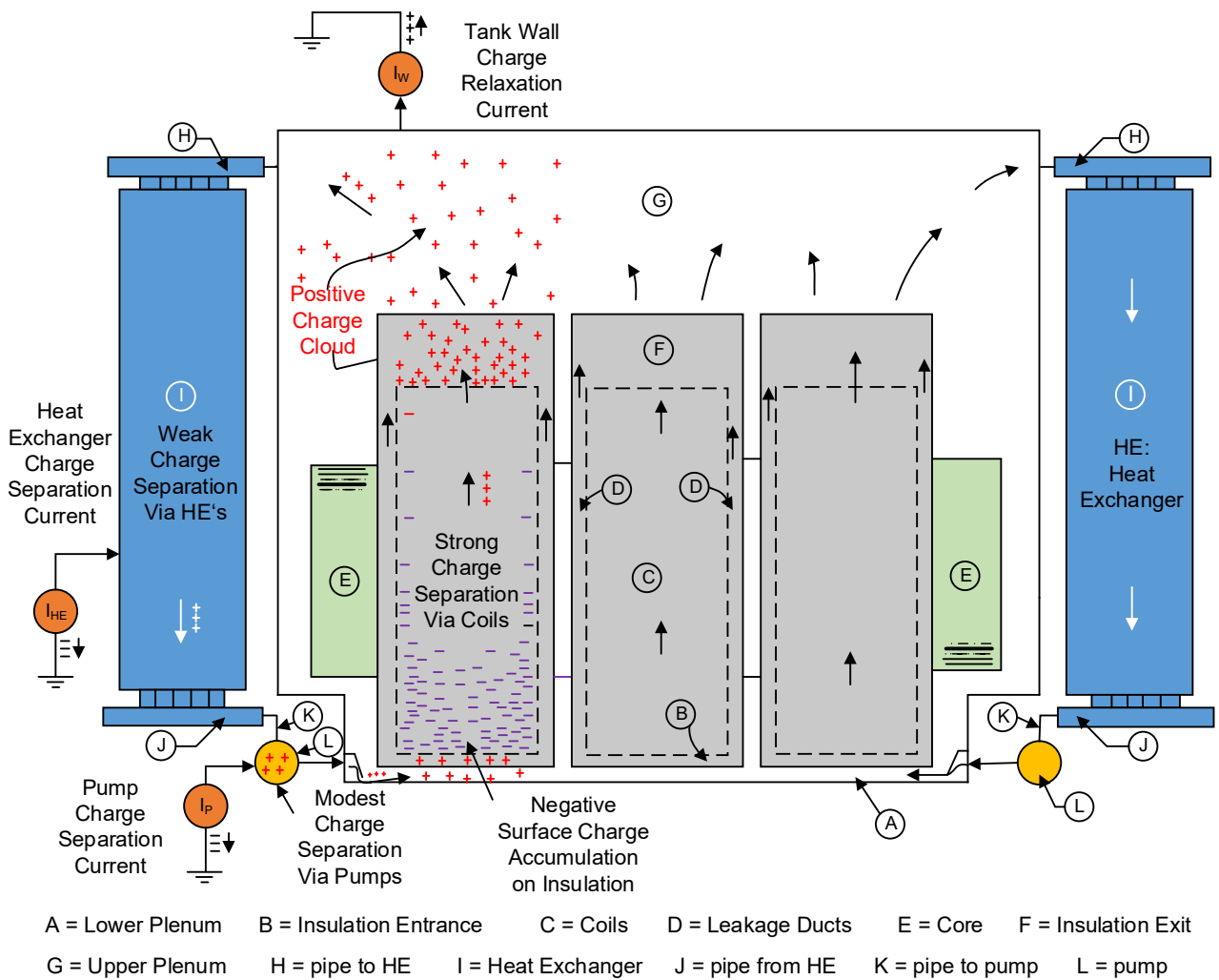


Figure 2.24 Model of shell-form transformer for streaming electrification analysis [67]

Furthermore, streaming electrification in the transformer is dependent on a number of factors. The verified major influential factors are listed below, and a comprehensive review is given by Crofts [63]: oil temperature, oil velocity, oil ageing degree, pressboard surface roughness, and electric field. The counter-measures of streaming electrification include oil flow reduction and transformer retro-filling [63]. However, for the transformers that have already been commissioned, it is almost impossible to change the insulation structure or to decrease the flow velocities, which makes the retro-filling with new insulating liquid the only economically plausible way [68]. Among others, the use

of additive BTA (1,2,3- benzotriazol) in mineral oil appears to be the most effective means in refraining the electrostatic charging tendency (ECT) of oil and thus mitigating the streaming electrification in the transformer [69].

2.3 Creeping Discharges at Liquid/Solid Interfaces

2.3.1 Liquid/Solid Interface Flashovers

Numerous researches have been dedicated to the breakdown and pre-breakdown phenomena of liquid/solid interfaces. Taylor found that the effects of permittivity mismatch on liquid/solid flashovers are consistent with a field intensification process at the surface irregularities along with the solid/liquid interface. Therefore, he recommended cleaning the liquid as well as matching the permittivity of the solid and liquid to improve the interface flashover strength [28]. Anker reported the pressboard calender direction could affect the impulse interface flashover voltage. Moreover, the copper particles resting on the solid dielectric surface can reduce the flashover voltages up to about 20 percent in average values with both power frequency and impulse voltages [29].

Cherney and Cross studied the role of electro-hydrodynamic (EHD) motion on the field distortion at the liquid/solid interface and argued that the field distortions at interfaces are due to liquid motion, independent of spacer materials and applied voltages [36]. Kelley and Hebner found no space charge or surface charge field enhancements on the oil/pressboard interface at room temperature and only a slight difference in field intensity between interface and oil under 125 °C. They suggested it is the microscopic phenomena, e.g., geometric factors and dielectric mismatch, rather than the macroscopic field enhancements due to surface charge accumulation that determine the strength of an interface parallel to the field in an oil/pressboard system [70, 71].

Schering Institute of the Leibniz University of Hannover has carried out systematic researches on liquid/solid flashover phenomena. It is found out that the liquid/solid interface flashover voltages can be significantly improved by a reduction of the relative oil humidity, i.e., by an increase of the temperature or by a diminution of the oil humidity [72]. The interface flashover voltages in carbonized oil can be higher than those in clean oil under certain circumstances [73]. Carbon particles in oil can lower the interface flashover voltages under negative lightning impulse, but they have no significant impact under positive lightning impulse. Moreover, surface tracking is more prone to be generated under negative lightning than under positive lightning impulse [74]. Carbonized oils exhibit a better interface electrical strength in the presence of high absolute water contents than clean oil [75].

Okubo et al. investigated the oil/pressboard creeping flashover characteristics using models equivalent to an actual transformer. They concluded that the flashover voltages are subject to both the electric field strength of the high-voltage electrode surface and the stressed oil volume [76]. Wilson et al. revealed the cumulative effects of successive interface flashovers [77], affirmed the detrimental effects of the interface in shortening the delay times to breakdown, and reported that a faster voltage rise could increase interface flashover voltages [78].

2.3.2 Liquid/Solid Interface Pre-breakdown Phenomena

The researches on streamer propagations on liquid/solid interfaces can be dated back to the 1950s when Andersen and Liao studied the streamer propagations over oil-immersed surfaces under impulse voltage [79]. It is revealed in their investigations that the negative impulse interface streamers propagate in a manner analogous to the propagation of stepped streamers in the air under natural lightning, whereas the positive impulse interface streamers propagate by a series of discrete discharges. Negative and positive interface streamers differ from each other in both propagation modes and channel potentials.

Devins and Rzad compared the propagations of positive streamers in open oil and on the oil/pressboard interface [80]. They found out the threshold voltages for streamer propagation in oil alone and over pressboard surface are approximate to each other in a point-plane electrode geometry. However, the pressboard surface can accelerate the streamer velocity considerably under higher voltages. Atten and Saker put their emphasis on the electrical characteristics of streamer channels during interface creeping discharges [81, 82]. They argued there is a definite potential gradient along the streamer channel, which increases when going from needle tip to the header of a streamer. The findings challenged the then presumptions that the interface streamers are extremely conductive.

Lundgaard et al. studied the inception and propagation of streamers in a point-plane gap (gap: 150 mm and tip radius: 190 μm), with and without pressboard interface parallel to the field [83]. They found that the breakdown voltage in the extremely divergent field is not affected by a parallel pressboard surface. Nevertheless, the oil/pressboard interface can definitely facilitate the inception of fast event streamers. The easier formation of fast event streamers was thought to be correlated with the destruction of streamer spheres by pressboard surface, as shown in Figure 2.25, which could result in a more inhomogeneous field close to the surface.

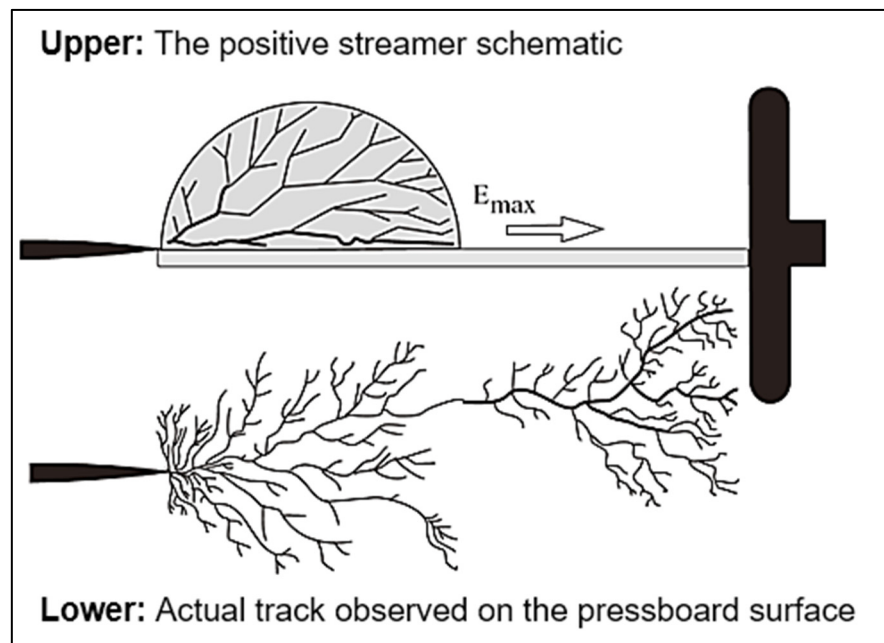


Figure 2.25 Positive streamer propagation along solid interface [83]

Xiao studied the creeping discharges streamers on the pressboard surface in an inhomogeneous AC field with three insulating liquids [84]. Figure 2.26 shows the images of positive streamers in an open oil gap and on the pressboard surface. She concluded that the introduction of a parallel pressboard surface in the oil gap could promote the development of negative discharges, which in turn increases

the probability of flashover failure. The discharge promotion effect is more pronounced in esters than in mineral oil.

Furthermore, Nakao et al. have carried out a series of investigations on creeping discharge streamers on an oil/pressboard interface with a back-electrode [85–87]. Beroual et al. studied the creeping discharges on liquid/solid interfaces using a vertical pressboard surface under various conditions [88–90]. The major evaluated parameters in their investigations are stopping length of the streamer, morphology of streamer channel, and current waveforms.

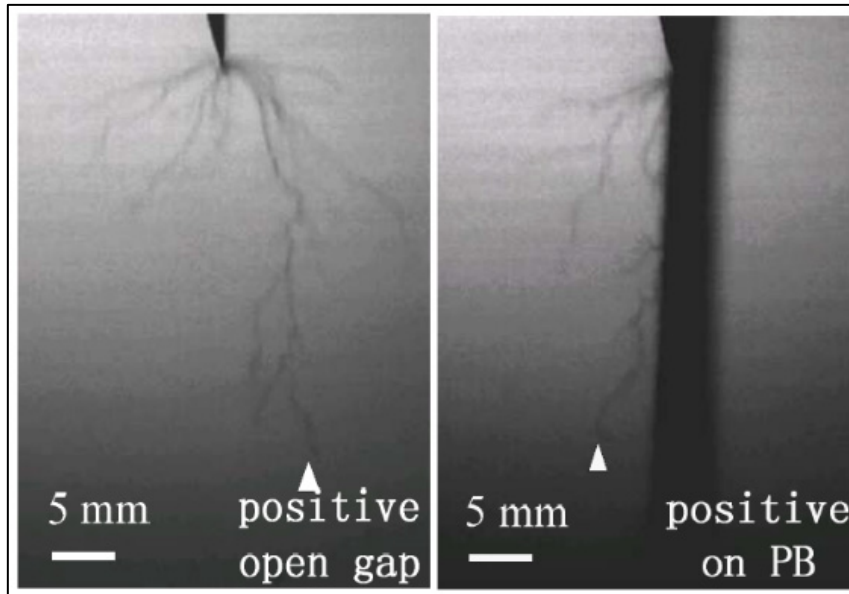


Figure 2.26 Positive streamers in the open gap and on the pressboard surface in mineral oil [84]

2.3.3 Creeping Discharges-Induced Failures in Power Transformer

Creeping discharge is probably the most dangerous failure mode of a power transformer that typically results in catastrophic failures under normal operating conditions [91]. It is worthy of mentioning that the term “creeping discharge” in this thesis refers exclusively to the long-term progressive discharge that creeps along the oil/pressboard interface, if not otherwise defined. Creeping discharge can last from minutes to months or even to years till the final breakdown, and it could occur to almost all components of oil-barrier insulation structures, including inter-phase barrier, inter-winding cylinder, and winding-to-core cylinder. Figure 2.27 displays several creeping discharge-related failures found in high-voltage and extra-high voltage power transformers.

V.V. Sokolov assumes that the complete fault-to-failure path of creeping discharges involves five consecutive steps [92], as shown in Figure 2.28. In Sokolov’s model, creeping discharge is initiated by a partial breakdown of the oil gap between winding and its nearest barrier, which is an aftermath of multiple processes, such as contamination of pressboard, bubbles, and distortion of winding geometry. Afterwards, a sliding discharge is formed at the oil/barrier interface. As a result, water and oil in the vicinity of the sliding discharge channel are driven out of pressboard pores, which in turn results in microscopic sparking within the pressboard. Sparking discharge facilitates the generation of hydrocarbons and carbonized treeing paths. Eventually, the whole process ends up with calamitous breakdown events in a transformer.

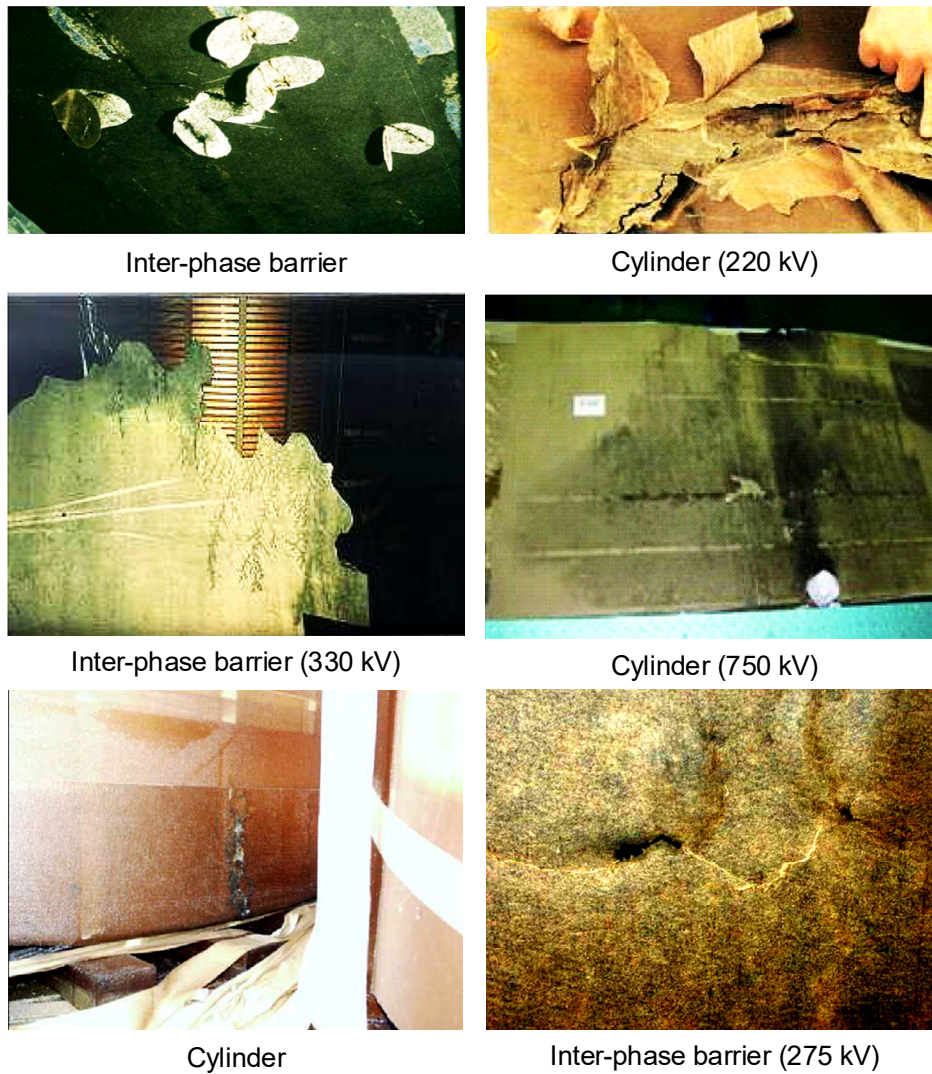


Figure 2.27 Creeping discharge-induced pressboard failures in power transformers [93–95]

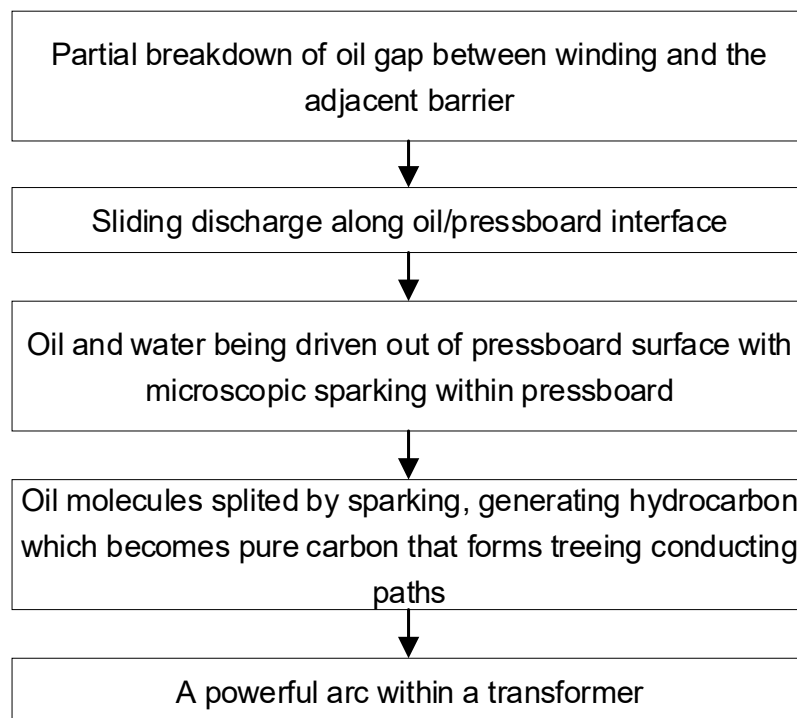


Figure 2.28 Progressive steps of creeping discharge of oil-pressboard insulation [92]

Although the mechanism of progressive creeping discharge is still not well-understood, the following factors are believed to probably have profound influences on creeping discharge [93, 96]:

- **Mechanical distortion of the winding geometry**
Mechanical force due to short-current can distort winding geometry, thereby altering the field distribution in the oil-barrier structure and causing overstressing in the oil gap. In the worst scenario, the mechanical force can puncture the wrapping papers and make oil having contact with bare conductors, which can jeopardize the electric strength of the oil gap considerably.
- **Contaminants**
The metal particles and ageing products of oil/cellulose insulation could deposit on the pressboard surface. The deposits can act as local discharge sources to initiate the occurrence of creeping discharge.
- **Tangential overstress**
The presence of a significant magnitude of a tangential electric field is critical to stimulate creeping discharges. Such high tangential stress arises from either imperfect insulation design or mechanical abrasion of winding. According to Sokolov [91], the magnitude of the tangential component of the electric field shall exceed 1.0 kV/mm to trigger creeping discharges.
- **High temperature**
High temperature due to sudden or sustained overload can promote the deterioration of paper and gas bubble generation, thus increasing the partial discharge rate and magnitude.
- **Moisture**
The presence of excessive moisture can stimulate vapor bubble formation, which can generate gases that may be trapped in pressboard cavities and thus exacerbating void discharge.

Furthermore, to generate steadily progressing creeping discharges at oil/pressboard interface in a power transformer, it has to satisfy three conditions [91]:

- a critical local discharge source;
- an imperfect insulation structure;
- a high tangential electric field.

2.3.4 Long-term Progressive Creeping Discharges under AC Voltages

Unfortunately, far too little attention has been paid to the long-term progressive creeping discharges of oil/pressboard interface under AC voltage. Thus far, the progressive creeping discharge and its related faults have still not been fully understood, which impedes the development of effective monitoring and diagnostics methodologies.

Little agreement has been made on the defect mode and initiation conditions of long-term creeping discharge in power transformer, as it usually occurs under ‘normal operating conditions.’ A great number of previous investigations treated the long-term creeping discharges as a short-gap phenomenon under either semi-homogenous or inhomogeneous fields. However, the short-gap electrode configuration tends to produce puncture of pressboard bulk rather than interface failures, such as surface tracking. Mitchinson et al. proposed a needle-to-bar electrode configuration to study long-term creeping discharges, as shown in Figure 2.29. This configuration is able to generate the localized field and thus having sustained interface creeping discharges. However, the inter-electrode

spacing of this electrode configuration should be carefully controlled. As reported by Dai [97], a minimum gap of 30 mm is needed to generate sustained creeping discharges without causing undesired interface flashovers. It indicates the long-term progressive interface creeping discharges are a long-gap phenomenon.

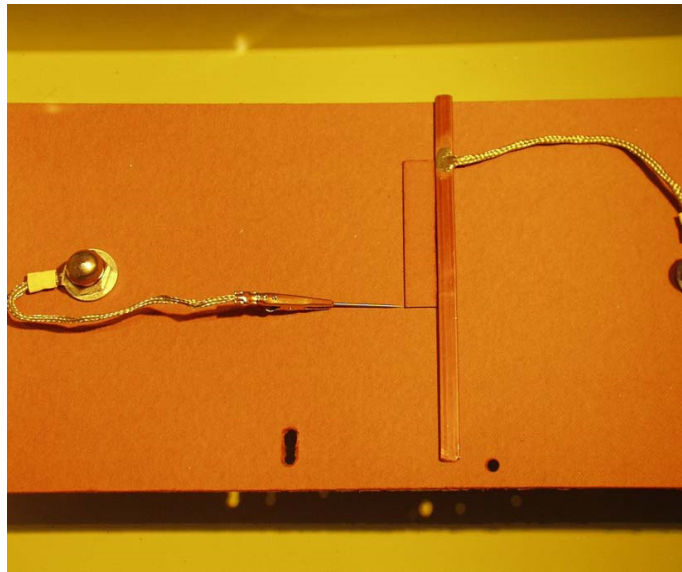


Figure 2.29 Needle-bar electrode proposed by Mitchinson [98]

One of the most inspiring works in this field has been carried out by Mitchinson. Following Sokolov's model of creeping discharges (see Figure 2.28), Mitchinson has constructed a large-scale test facility to simulate the creeping discharges and surface tracking of inter-phase barriers in a transformer [99]. The test facility enabled the interactions between a global phase-varying field and an independent local field. He concluded that the space charge on the pressboard surface is a major driven force of creeping discharge, and the discharges are enhanced by the polarization of the interface electric double layer (EDL). Moreover, a two-path model based on EDL theory was proposed in [100] to depict the electric processes of the oil/pressboard interface, in which one path is associated with surface discharges as well as tracking, and the other path is associated with interface flashover. However, most of his investigations were implemented qualitatively and substantiated evidence is hence needed to support his presumptions.

Dai has carried out comparative studies on interface flashovers as well as creeping discharge-induced failures between new and aged pressboard samples [97]. Pressboard surface carbonization and white marks were observed with new and aged pressboards, respectively. He concluded that increased water content in aged pressboards is probably the greatest facilitating factor of creeping discharge failures. Moreover, it is assumed that the formation of white marks is a result of the evaporation of oil and water in pressboard surface pores due to the overheat of interface streamer channels. Such expositions are not fully satisfactory, as they overlook the competing multi-faceted effects of pressboard ageing and fail to explain the massive bubbling effect during severe creeping discharges. In fact, a contradictory conclusion has been made in [101] that the formation of white marks on the pressboard surface is subsequent to bubbling and is actually a result of pressboard internal treeing.

Zainuddin has proposed a four-stage process of creeping discharges [102, 103], which comprises the initiation of arcing/glow at the needle electrode tip (Stage 1), formation of white marks (Stage 2), expansion of white marks, and micro-arcs near the grounding electrode (Stage 3), and a full discharge event, i.e., flashover (Stage 4). Despite its success in clearly depicting the inception-to-failure

mechanism of creeping discharge, this model has failed to give due considerations to the accompanying phenomena, such as bubbling, smokes, and internal treeing. Moreover, the proposed formation mechanism of white marks in this model appears to be too speculative.

Xiao and Wang have conducted an insightful investigation of the creeping discharge-induced surface tracking phenomenon [104]. They provided a holistic image of the long-term creeping discharges in mineral oil as well as esters, found two types of partial discharge in the process of creeping discharges (liquid type and gas type), and confirmed the gaseous nature of white marks. However, this study suffers an overemphasis on the white marks and tends to attribute all related phenomena to white marks without showing concrete evidence, e.g., the temperatures within the white marks areas.

Furthermore, Murdiya et al. have investigated the characteristics of creeping discharge over the ester/pressboard interface [105]. Due to a back-rod electrode, the composite insulation failed due to pressboard puncture rather than interface flashover. Nevertheless, tracking and white marks were still observed. They considered the formation of white marks as a result of oil decomposition near the streamer channel, which forced the bubbles to enter into the pressboard due to the Maxwell stress. However, the validity of this explanation should be questioned in case of no back electrode. Azcarraga et al. reported that the PDIV of creeping discharges increases with both oil speed and temperature and the forced oil flow could modify the PD patterns [106].

To summarize, much uncertainty over the nature of interface creeping discharges still exists, and no large-scale quantitative studies have been performed to examine the effects of relevant critical influential factors, such as ageing and temperature. Moreover, another major unsolved issue in this field concerns the accompanying phenomena of creeping discharges, which mainly include white marks, bubbling effect, smokes, internal treeing, and surface tracking [93]. To date, no clear illustrations or convincing explanations have been provided to unravel their respective mechanisms and to elucidate their possible interrelations. Owing to the lack of sound relevant knowledge and the absence of advanced detection devices, the ongoing creeping discharges and tracking in power transformers frequently remain undetectable, even with regularly scheduled PD measurements and DGA analysis [107, 108]. To address the challenges, an in-depth investigation of long-term progressive creeping discharges is therefore of vital significance.

2.3.5 DC Creeping Discharges in HVDC Converter Transformers

Since its first commercial operation in Gotland in the 1950s, high-voltage direct current (HVDC) transmission has gained ever-greater popularity in the modern electricity network. Compared with the conventional high-voltage alternating current (HVAC) system, HVDC technology shows unparalleled technological merits in various applications, such as integration of renewable energies into grid, inter-connection of asynchronous AC networks, the connection of offshore wind farms, and building long-distance cable systems [109]. Moreover, in spite of the comparatively expensive converter stations, the total costs of an HVDC system can be lower than those of an equivalent HVAC system, provided that the transmission distance is great enough. The critical distance, often referred to as ‘break-even distance,’ may vary depending on project contexts. Nevertheless, it is generally accepted that the break-even distance is 500 to 800 km for overhead lines and around 50 km for underground cables [110, 111]. A costs comparison between HVAC and HVDC transmission systems is schematically illustrated in Figure 2.30.

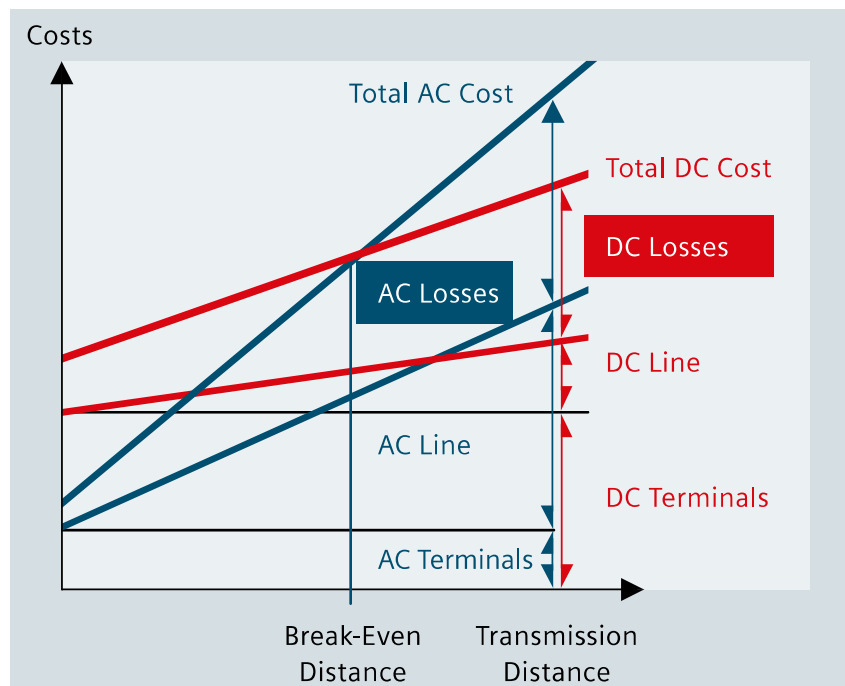


Figure 2.30 Costs comparison between HVAC and HVDC transmissions [110]

The converter transformer, acting as an interface between the AC network and rectifier converters, is one of the pivotal components in an HVDC system. In addition to providing correct voltages to converters, an HVDC converter transformer is also supposed to serve the following purposes: to provide galvanic isolation between AC and DC systems for preventing the DC potential from intruding into the AC system; to limit the effects of steady-state AC voltage change on converter operating conditions (tap-changer); to provide reactive impedance for reducing fault current; to generate a 30° phase shift for reducing low-order (5^{th} and 7^{th}) current harmonics [112].

In most of the existing HVDC projects, especially in the ultra-high voltage (UHV) class, the converter transformer is directly connected to thyristor-based line-commutated converters (LCC). As a result, the valve-side windings of converter transformers have to withstand a combination of various stresses, including [113]:

- power frequency (50 or 60 Hz) AC voltage;
- DC voltage;
- harmonic voltages of fundamental frequency;
- high-frequency transients due to converter commutation;
- high-order current harmonics.

Moreover, in case of a fault, they are also subject to:

- DC voltage polarity reversal;
- short-current due to commutation failures.

Such complex stress conditions have posed a great challenge to the insulation system of the converter transformer. Although the insulation design of converter transformers has made remarkable progress in the past decades, the safety of the converter transformer insulation system still remains a major concern to relevant stakeholders. Due to its particularly intricate stress conditions, the valve winding is probably the most vulnerable part of an HVDC converter transformer. In fact, a vast majority of valve winding failures are associated with insulation systems, in which flashover and overheat appear

to be the primary causes [114]. For instance, the hot-spot of the converter transformer valve winding could reach up almost to 160 °C at a continuous full load [115]. As indicated by field experience, plenty of converter transformers failures could be ascribed to interface flashover, pressboard tracking, and wrapped paper carbonization [116–118].

Ohshima et al. examined the effects of stressing time, high voltage electrode curvature, and voltage polarity on DC breakdown strengths of the oil gap, respectively. They presumed space charge is a decisive factor in governing DC breakdown of oil [119]. Kurita et al. studied the effects of oil/pressboard interface direction on the oil/paper breakdown strengths and observed surface tracking after flashovers. They concluded that the DC flashovers involve not only discharges in oil but also discharge in pressboards along with the layers [120]. Krause and Woschitz carried out both puncture and flashover tests under DC voltages at three temperatures [121]. However, they reported that the creeping strength of the oil/pressboard interface is determined by oil and independent of pressboard conditions. Ebisawa et al. investigated the DC creeping breakdown characteristics of oil/pressboard insulation using element and full-scale insulation models [122]. They affirmed the detrimental effects of the bare electrode on oil/pressboard creeping strength and revealed the role of creeping distance in decreasing the creeping strengths. Raghuvver et al. compared the pressboard surface strengths under impulses, AC, DC, and combined AC-DC voltages [123]. They have found the surface strength is the greatest under lightning impulse voltage, followed by switching impulse, DC, and AC voltages. The oil/pressboard interface lowers the breakdown voltage under impulses and AC voltages while increases the breakdown voltage when a DC component is present. However, contradictory results were reported in [124] that the spacer could reduce interface breakdown strength under DC voltage. Moreover, it was reported that the fraction of DC voltage could also influence the flashover locations under superimposed voltages [125].

Similar to the scenarios under AC voltage, limited attention has thus far been paid to the long-term progressive creeping discharge under DC voltage. Qi et al. studied fundamental characteristics of DC creeping discharge with a plate-to-plate electrode under a combined AC-DC field [126]. The failure processes were investigated by analyzing the related PD parameters and dissolved gas concentrations. Using a sphere-to-plate electrode, Zhou et al. examined the effects of pressboard thermal aging on creeping discharges under AC and combined AC-DC fields [127]. Their emphases were put on the inception of creeping discharge as well as the statistical distribution operators of partial discharges. Using a needle-to-plate electrode configuration, Li et al. compared creeping discharges characteristics under AC and combined AC-DC fields [128]. They reported that the DC components could increase the inception voltage of interface creeping discharges, and it is hard to induce tracking failures under combined AC-DC field due to a presumed joint effect of DC field distribution and space charges.

However, no literature pertinent to long-term creeping discharges under the pure DC field was reported. In fact, the field behaviors in oil/pressboard composite insulation under AC and DC stresses are conspicuously different from each other. Moreover, the oil/pressboard interface field distribution is more susceptible to environmental factors under DC voltage than under AC voltage, such as temperature [129] and oil flowing [130]. Therefore, it might be of no avail to study long-term creeping discharges in the converter transformer if the investigations under pure DC voltage are still absent.

3 TEST FACILITIES AND MEASUREMENT TECHNIQUES

3.1 Electrode Geometry and Electrode Configuration

3.1.1 Vertical Needle-Plate Electrode Configuration

To generate steadily progressing creeping discharges at an oil/pressboard interface in a power transformer, it has to satisfy three conditions: a critical local discharge source, an imperfect insulation structure, and a high tangential electric field [91]. Most of the previous researches on creeping discharge adopted a cylinder-to-plane electrode configuration, as shown in Figure 3.1 a). This configuration is revised from the electrode arrangement in IEC 60243-1:2013 [131], which is originally for determining the bulk electrical strength of solid insulating materials. However, this electrode configuration suffers several major drawbacks in investigating long-term creeping discharges. Firstly, the field is not local enough. Accordingly, most of the recorded partial discharges would come from discharges in the pressboard rather than from the interface. Secondly, the failures are more correlated to pressboard bulk than to interface. As the voltage increases, it probably leads to a pressboard puncture or a surface flashover instead of a local discharge that steadily creeps along with the interface without any undesirable premature breakdown events. Lastly, as a result of the first two reasons, it is almost impossible to observe interface tracking with this electrode configuration.

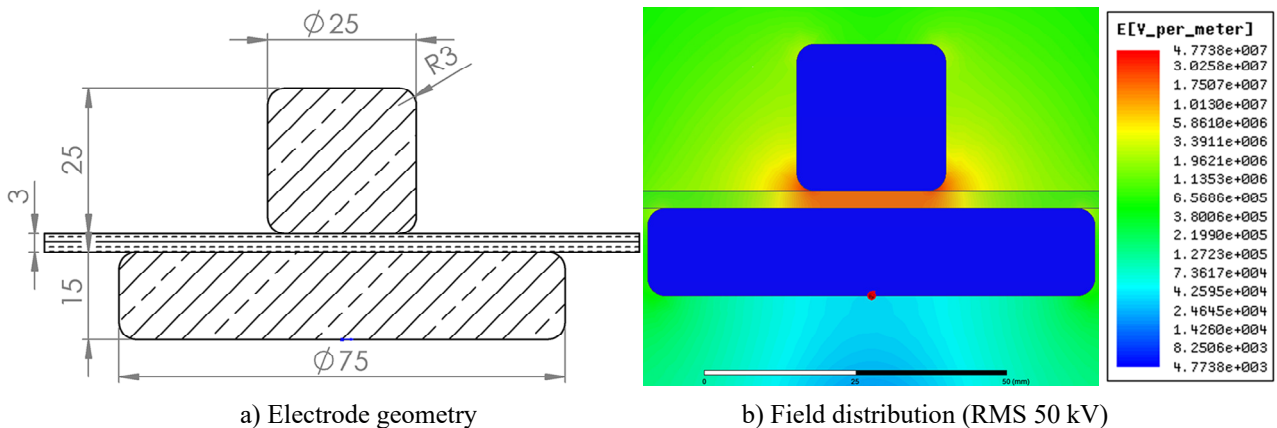


Figure 3.1 Electrode for determining electric strength of solid insulating materials

Mitchinson and Dai used a horizontally arranged needle-plate electrode to obtain sustained creeping discharge [97, 98]. However, this arrangement needs mechanical support to fix the pressboard sample, which can somewhat distort the electric field distribution. To overcome the shortcomings of the above-mentioned electrodes, this thesis proposes a vertical needle-plate electrode configuration to study the progressive creeping discharge at the oil/pressboard interface. The geometry and dimension of the proposed electrode configuration are illustrated in Figure 3.2 and Figure 3.3, respectively.

The proposed vertical electrode configuration consists of a high voltage needle electrode and a grounded plate electrode. For better contact between the needle tip and pressboard surface, the angle between the needle axis and pressboard surface is set to be 15° . More details of the needle electrode will be presented in Section 3.1.2. The plate electrode is made of brass and possesses a circular shape with a diameter of 140 mm. It is 15 mm high and has a curved edge on its upper surface: the edge radius is 10 mm. To ensure the oil/pressboard interface is perpendicular to the surface of the ground electrode, the pressboard sample is erected in a 10 mm-deep slot on the ground electrode.

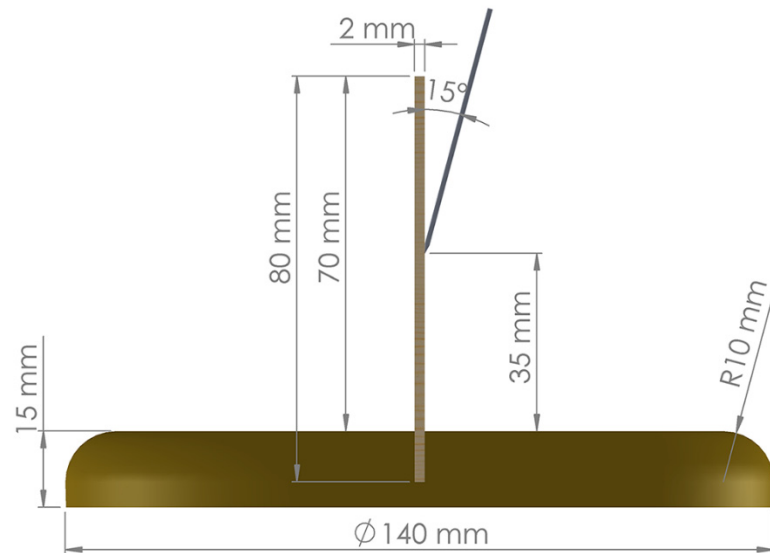


Figure 3.2 Electrode configuration for AC tests

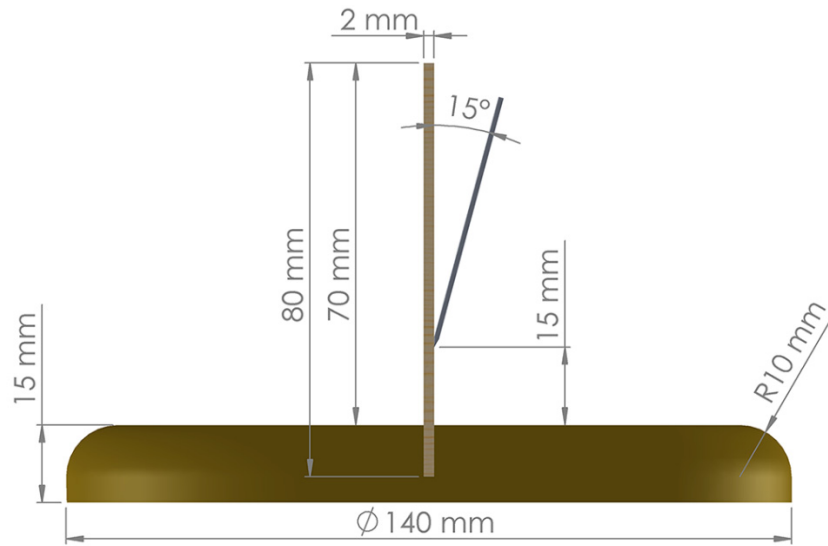


Figure 3.3 Electrode configuration for DC tests

The selection of inter-electrode spacing is a result of multiple factors. Firstly, it is reported that 30 mm is the minimum inter-electrode spacing to generate sustainable creeping discharge under AC voltage [97]. Secondly, oil withstands larger field intensity under AC field, whereas pressboard withstands larger field intensity under DC field. Lastly, oil has a much smaller withstand strength than pressboard. Based on the considerations, therefore, the gap widths are set to be 35 mm and 15 mm for AC and DC tests, respectively.

3.1.2 Needle Electrode

Ogura® treeing needle is utilized as the high voltage electrode. The needle electrode is made of tungsten carbide and has a tip radius of 15 μm . In spite of the superb mechanical strength of tungsten carbide, the needle is particularly vulnerable to any external force due to its sharp tip. Therefore, utmost care must be taken when handling the needles. A special design has been made in this thesis to ensure the needle has a possibly closest contact to the pressboard surface and, in the meantime, to protect it from any mechanical collision to the surface. The layout of the needle electrode is illustrated in Figure 3.4 a), and a magnified image of the needle tip is shown in Figure 3.4 b).

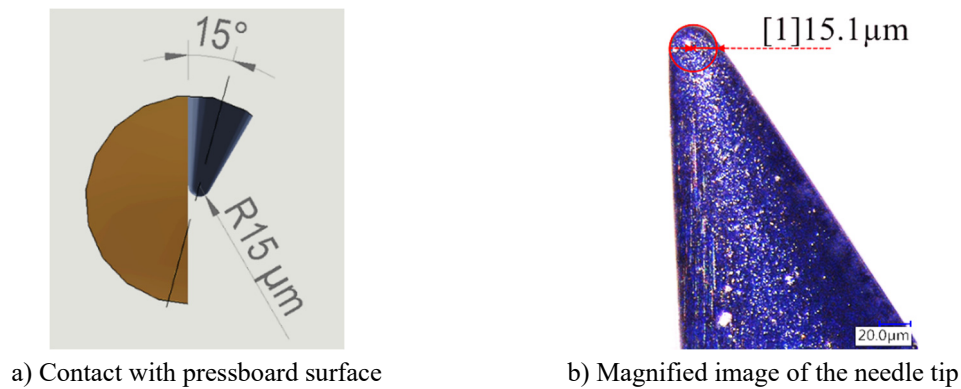


Figure 3.4 Ogura treeing needles

3.1.3 Triple Electrode for PDC Measurement

A triple-electrode was designed in this thesis to carry out polarization and depolarization current (PDC) measurements, as displayed in Figure 3.5.

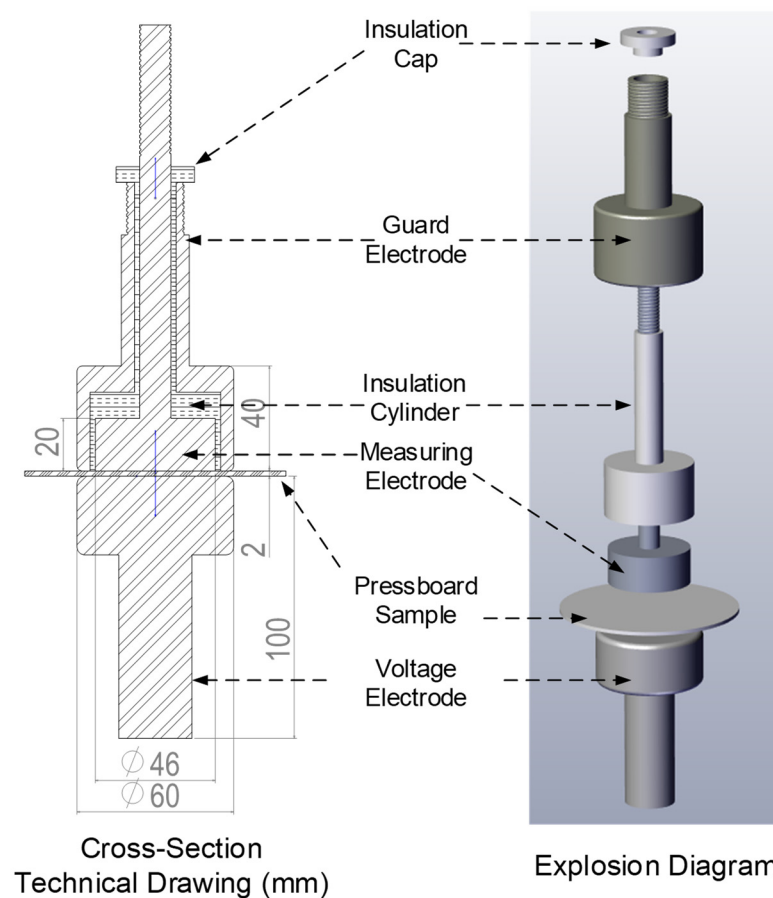


Figure 3.5 Triple electrode for PDC measurement

The triple electrode consists of three major parts: a voltage electrode, a measuring electrode, and a guard electrode. In PDC measurement, a DC voltage is applied on the pressboard sample through the voltage electrode, and the induced DC current is measured from the measuring electrode by an electrometer. The guard electrode is grounded and is intended for eliminating the influence of leakages current that passes along the pressboard surface. An insulation cylinder and an insulation cap, made of Teflon[®], are used to isolate the measuring electrode from the guard electrode and any other grounded metal parts.

3.1.4 Grounding Electrode for Oil Flowing Tests

Aiming to investigate the influences of oil flowing on creeping discharge under DC voltage, this thesis designed a special ground electrode to simulate the forced oil flowing in a power transformer. As shown in Figure 3.6, it consists of three major parts: a brass upper plate with a curved edge, a brass lower plate with a sharp edge, and a Teflon® tube. The two plates have an identical circular shape and are concentrically assembled using bolt fasteners. The tube is fixed on the lower plate. Moreover, an oil duct is constructed within the ground electrode, thereby driving oil flows passing along the pressboard surface.

The oil flowing duct comprises three parts: the tube, an oil reservoir, and a through-hole matrix. The tube is connected to an external liquid transfer pump and serves as the inlet of forced oil flows. A 5 mm-deep rectangular recess is made on the rear face of the upper plate. It serves as an oil reservoir and diverts the oil flow from the tube into the through-hole matrix. The through-hole matrix is made on the upper plate and is comprised of 5 x 3 through-holes. It is located quite close to the slot where the pressboard sample is erected, thereby generating an efflux of oil flows along the pressboard surface. The complete oil flow path is denoted by the red solid arrow lines in Figure 3.6.

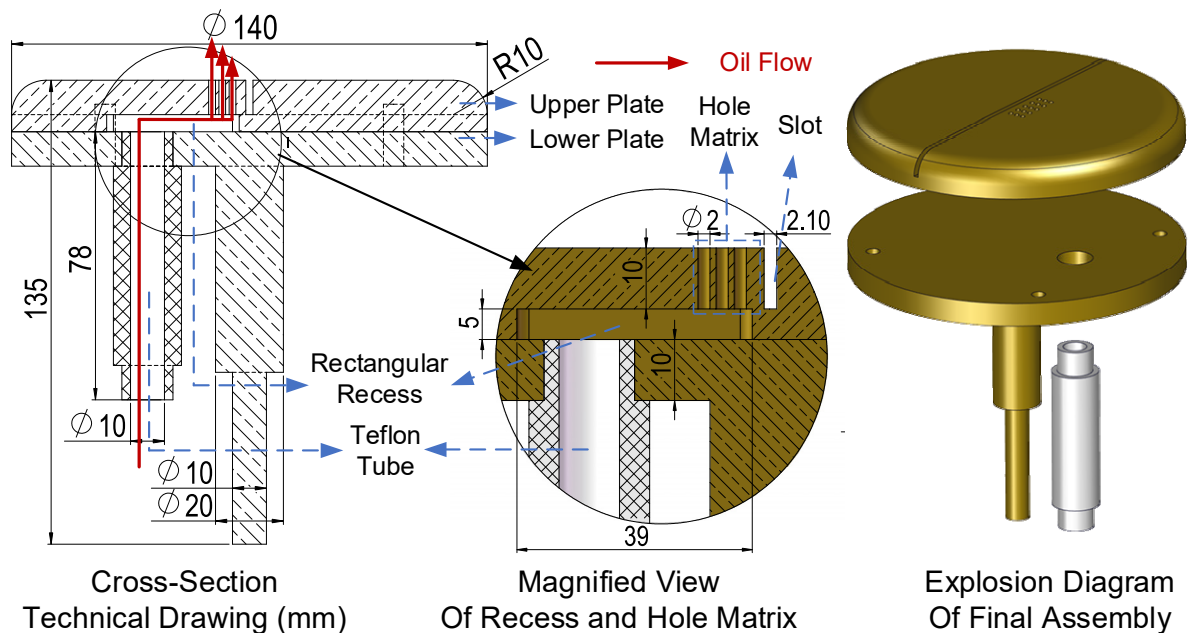


Figure 3.6 Grounding electrode for oil flowing tests

3.2 Construction of Test Cells

3.2.1 Test Cell for Creeping Discharge of Thermally Aged Pressboard

Figure 3.7 shows the test cell for the creeping discharge tests of aged pressboard samples. The cell vessel is made of transparent Perspex®, due to its light-weighted nature, high impact strength, and, more importantly, excellent light-transmitting capability, which enables a clear observation of discharge progression with video-recording tools. Its cover and bottom plates, made of Perspex® as well, are hermetically sealed with rubber O-rings and fastened with plastic bolts and nuts.

The cell can accommodate a large volume of insulating oil (> 10 L), making it an appropriate facility for breakdown tests as well. Four brass cylinder bars are installed on its cover to bridge the high voltage wire and the needle electrode. By changing the vertical locations of the bars, the inter-electrode spacing can be readily adjusted. Moreover, there are four slots on the ground electrode to

erect pressboard samples, which enables several consecutive breakdown tests without opening the test cell and thus mitigating the moisture ingress.

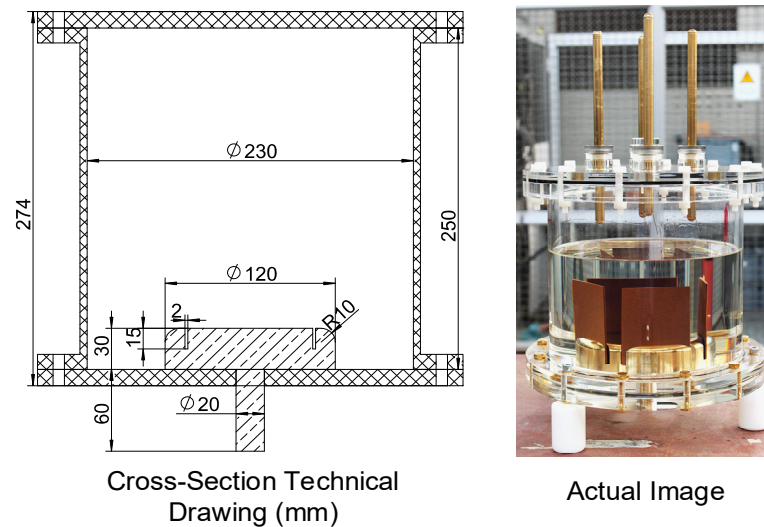


Figure 3.7 Test cell for creeping discharge for thermally aged pressboard

3.2.2 Test Cell for Temperature and Oil Flowing

Figure 3.8 shows the test cell for investigating the influences of oil temperature and oil flowing on creeping discharges. It consists mainly of four parts, i.e., a cover plate, a cell vessel, a bottom plate, and a movable high voltage electrode base. The cell vessel is made of glass, and the other three parts are made of Teflon®. To ensure a hermetic environment, all part conjunctions are sealed with rubber O-rings and fastened with plastic bolts and nuts.

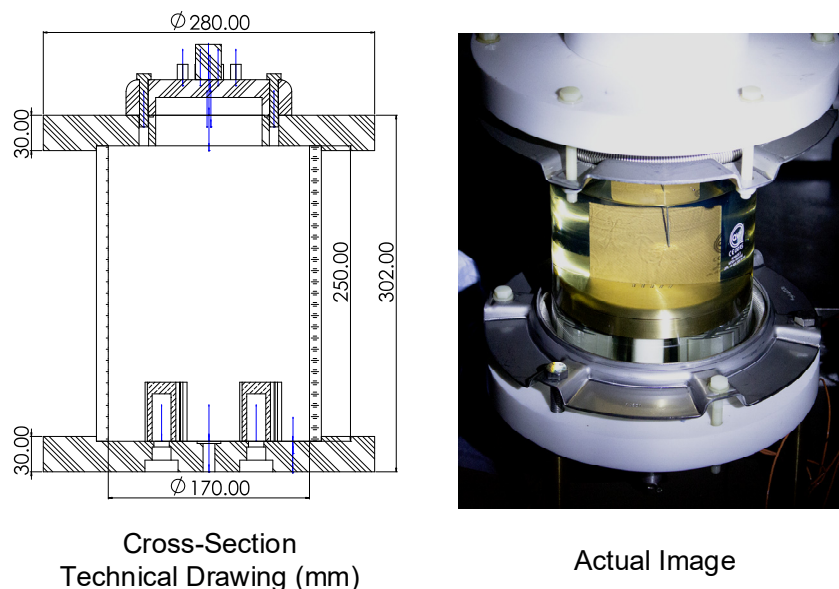


Figure 3.8 Test cell for temperature and oil flowing tests

The test cell is intended for fulfilling three specific functions. At first, different oil temperatures can be achieved using a pair of cartridge heaters. Thanks to the use of Teflon®, the heaters can be directly installed on the bottom plate, which can isolate the heaters from the brass ground electrode. At second, oil can be forced to pass along the oil/pressboard interface to generate streaming electrification using the specially designed ground electrode displayed in Section 3.1.4. At third, the positive space charges during streaming electrification can accumulate on the Teflon® cover plate rather than being immediately dissipated.

3.3 Sample Information and Sample Processing

3.3.1 Basic Information

Table 3.1 Basic information of oil sample

Property	Units	Method	Value
Density at 15 °C	kg/m ³	ISO 3675	882
Density at 20 °C	Kg/m ³	ISO 3675	879
Kinematic Viscosity at 40 °C	mm ² /s	ISO 3104	11.5
Kinematic Viscosity at -30 °C	mm ² /s	ISO 3104	1700
Flashpoint	°C	ISO 2719	140
Pourpoint	°C	ISO 3016	-57
Neutralization Value	mg KOH/g	IEC 62021-1	<0.01
Corrosive Sulphur		IEC 62535	Not corrosive
Breakdown Voltage (as delivered)	kV	IEC 60156	>70
Dissipation Factor at 90 °C		IEC 60247	0.002

Table 3.2 Basic information of pressboard sample

Property	Unit	Method	Value
Apparent Density	g/cm ³	IEC 60641-2	1.2
Tensile Strength (Machine Direction)	MPa	IEC 60641-2	76
Tensile Strength (Cross-Machine Direction)	Mpa	IEC 60641-2	57
Elongation (Machine Direction)	%	IEC 60641-2	7.7
Elongation (Cross-Machine Direction)	%	IEC 60641-2	8.8
Ply Adhesion	N/30 mm	IEC 60641-2	370
Moisture Content	%	IEC 60641-2	≤ 8.0
Ash Content	%	IEC 60641-2	0.3
Shrinkage (Thickness)	%	IEC 60641-2	3.6
Shrinkage (Machine Direction)	%	IEC 60641-2	0.7
Shrinkage (Cross-Machine Direction)	%	IEC 60641-2	0.9
Conductivity of Aqueous Extract	mS/m	IEC 60641-2	2.3
ph of Aqueous Extract		IEC 60641-2	7.0
Oil Absorption	%	IEC 60641-2	30
Electrical Strength in Oil	kV/mm	IEC 60243-1	46

The uninhibited mineral oil Shell Diala S2 ZU-I Dried is selected as the oil sample. It is featured by its natural resistance to oxidation degradation, non-corrosiveness to copper, and good low-temperature heat transferring capability. Moreover, it is already specially dried before delivery, thus requiring no further treatment for many applications. The basic information of Shell Diala S2 ZU-I Dried is summarized in

Table 3.1.

The 2 mm-thick Weidmann Transformerboard T IV (IEC B4.1 type) is selected as the pressboard sample. It is an uncalendered pressboard with light wire marks on the surface and made of 100% sulphate wooden pulp with pure water. Moreover, it is featured by its good oil absorption and capability of being shaped to highly bent components, which makes it a superb choice to construct the major insulation of oil-filler transformers, such as cylinder barriers, angle rings, and caps. The basic information of Weidmann Transformerboard T III is summarized in Table 3.2.

3.3.2 Dehydration and Degassing of Oil Sample

Although the oil sample is already well dried before delivery, to reach the possibly minimum water content and gas residue, it is nevertheless further processed using a self-assembled oil dehydrating and degassing system. Figure 3.9 shows the schematic diagram of the processing system.

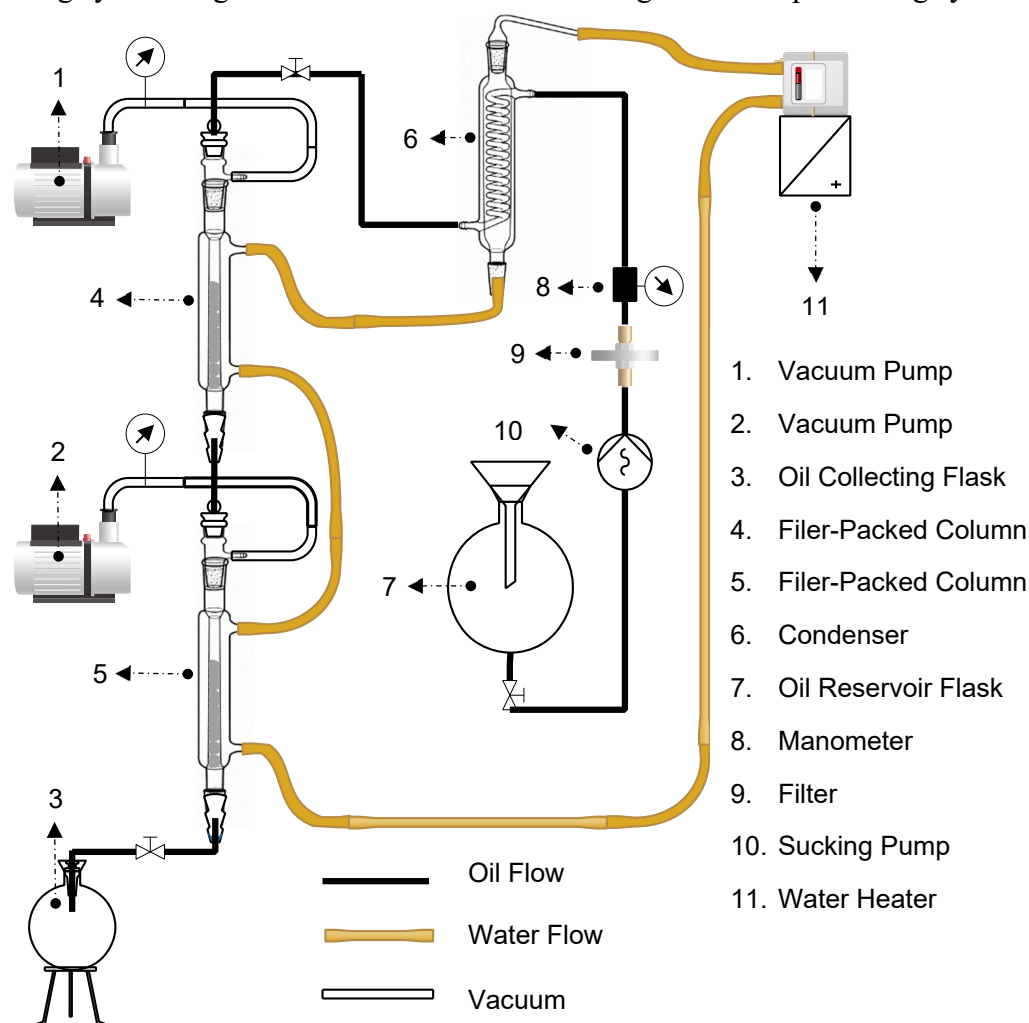


Figure 3.9 Oil processing system

The system functions based on three units that work in parallel. The oil unit feeds the system with un-processed oil sample and fills the hermetic collecting flask with processed oil. The water unit controls the flowing of heated water, and the vacuum unit connects the vacuum pumps with the central tubes of filler-packed columns. Prior to processing the oil sample, water is heated up to 55 °C and then circulated all the glassware that the oil passes through. The sucking pump controls the speed of oil influx from the reservoir flask, the filter excludes any particles in the oil sample, and the manometer monitors the pressure that the oil influx brings to the system.

Firstly, the oil sample enters into the spiral central tube of the condenser, where it is heated by the

surrounding heated water. Afterwards, the heated oil sample flows into the central tube of the first filler-packed column (0.3 mbar) and then the central tube of the second column (0.3 mbar), where it has massive contacts with borosilicate glass-made Raschig rings. Since the columns are heated as well, the trace moisture in the oil sample can be readily evaporated and then exhausted by the pump. Resultantly, the processed oil has moisture content below 5 ppm and a gas content less than 1% by volume.

3.3.3 Dehydration and Impregnation of Pressboard Sample

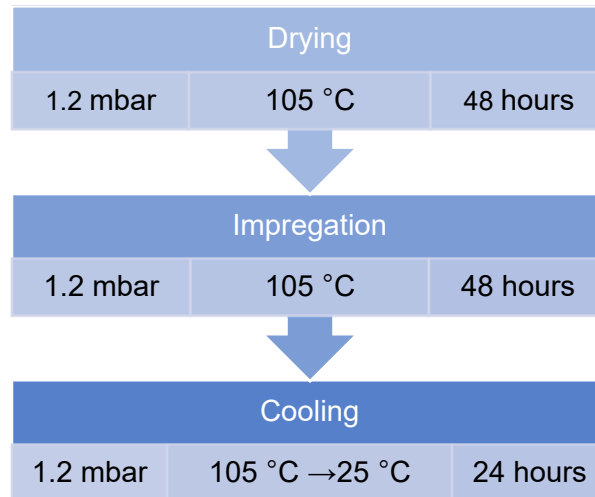


Figure 3.10 Flowchart of pressboard processing

Pressboard is a porous material of hydrophilic nature. Therefore, it has to be carefully processed before being used as a test sample. Figure 3.10 shows the flowchart of pressboard processing carried out in this thesis.

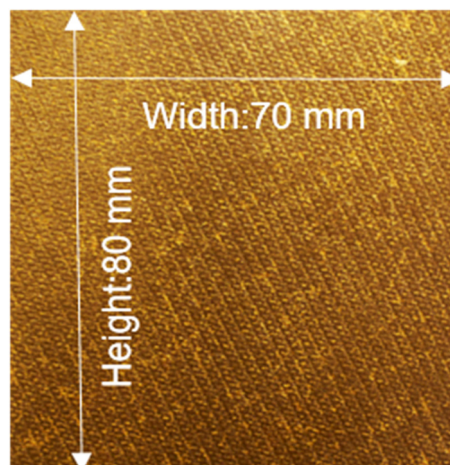


Figure 3.11 Newly impregnated pressboard sample

At first, pressboard samples were cut into a proper size of $80 \times 70 \times 2$ mm and then put into a thermal vacuum oven. The drying phase lasted for 48 hours and is intended for diminishing moisture in the pressboard. The temperature and pressure of drying are set to be 105 °C and 1.2 mbar, respectively. Afterwards, the dehydrated and degassed oil was used to impregnate the dried pressboard samples. The impregnation phase lasted for 48 hours and is intended for filling the voids and pores of the pressboard with oil. The temperature and pressure of the impregnation phase were the same as those in the dry phase. Finally, the cooling phase lasted for 24 hours and is intended for achieving certain moisture equilibrium between pressboard and oil. During the cooling phase, the temperature was

gradually decreased to room temperature, but the pressure still remained about 1.2 mbar. After processing, pressboard samples were sealed with oil in air-tight stainless-steel vessels for further treatments or use. An example of the newly impregnated pressboard sample is given in Figure 3.11.

3.4 Measurement and Analytic Techniques

In general terms, the used techniques in this thesis can be sorted into four categories:

- electrical;
- physicochemical;
- optical;
- finite-element method.

The following paragraphs will provide an overview of these techniques as well as the working principles of their corresponding test facilities.

3.4.1 Conductivity of Insulating Oil

The DC conductivity measurements of insulating oil are conducted using Baur Oil Tester DTL C. The assembly of the test cell is identical to that illustrated in Figure 3 of IEC 60247: 2004 [132]. The capacitance of the empty and clean test cell is 71.3 pF. The test temperatures range from 30 °C to 110 °C with an interval of 10 °C, and the applied electric field is maintained at 250 V/mm. Three measurements are carried out at each temperature to diminish probabilistic errors.

3.4.2 Conductivity of Pressboard

The polarization and depolarization current (PDC) method is used to estimate the DC conductivities of the pressboard under different temperatures. The working principle of the PDC method is illustrated in Figure 3.12.

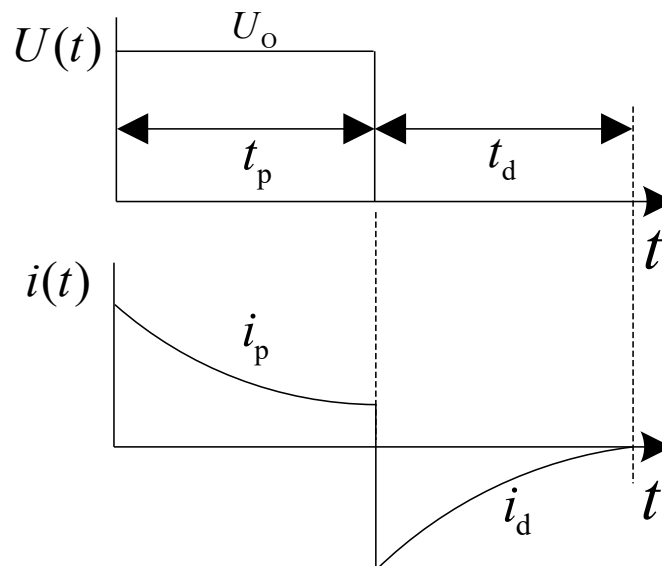


Figure 3.12 Waveform of polarization and depolarization currents [133]

When a step voltage U_0 is applied on a linear dielectric, it induces a current in material named polarization current i_p . Actually, the polarization current comprises two fractions: current due to polarization and current due to conduction. After a certain period of time t_p , the step voltage is cut off, and the test object is short-circuited. Subsequently, the dipoles arising from the polarization process disappear or return to a non-orientated state, which results in another current named

depolarization current i_d . The depolarization current is due exclusively to the depolarization process. Therefore, the conductivity of the pressboard can be estimated using equation [134]:

$$\sigma \approx \frac{(i_p - i_d)}{U_0} \cdot \frac{d}{A} \quad (3.1)$$

where σ denotes DC conductivity, i_p denotes the polarization current, i_d denotes the depolarization currents, d is the sample thickness, A is the electrode area, and U_0 is the applied voltage. The measurements are implemented using Omicron DIRANA with the triple electrode shown in Section 3.1.3.

3.4.3 Off-line Pressboard Dielectric Dissipation Measurement

The off-line dissipation factor measurements of the pressboard are conducted using the triple-electrode depicted in Section 3.1.3 and Omicron CPC 100 with CP TD1. CPC 100 is a high-precision data acquisition unit. CP TD1 consists mainly of a voltage transformer, a reference capacitor, and a relay matrix. CP TD1 applies an AC voltage up to 12 kV on the test sample and measures the leakage currents that flow through the reference capacitor and test sample simultaneously.

3.4.4 On-line Pressboard Dielectric Dissipation Measurement

The test setup is intended for online monitoring of the dielectric properties of the pressboard sample. As shown in Figure 3.13, the test setup comprises a reference capacitor, two Omicron TANDO 700 units, and an Omicron MCU1 unit. TANDO 700 is a high-precision current measuring system. It can work in an HV environment with a dynamic measuring range from 5 μ A to 1A. Omicron MCU1 is a digital control unit used for data acquisition. Two TANDO 700 units are connected in parallel to measure the leakage currents from the reference capacitor and the test object, respectively. Afterwards, the recorded current signals are transmitted to MCU1 via an optic fiber cable.

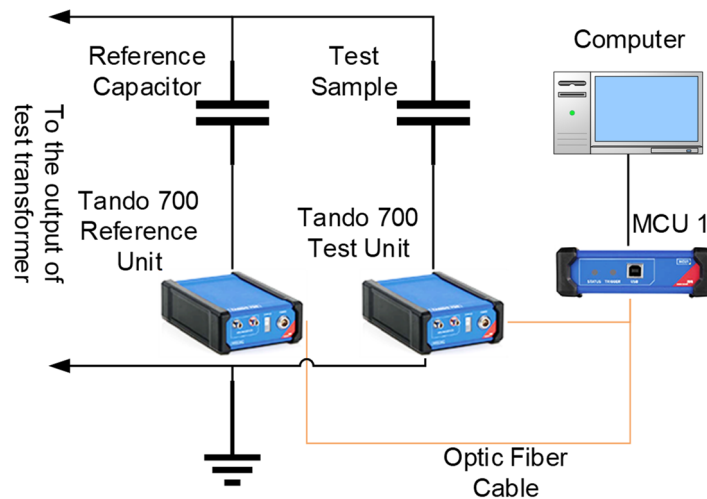


Figure 3.13 Schematic illustration of online dielectric dissipation measurements

The dissipation factor of the test object can be obtained by comparing the test object current with the reference current. Moreover, this system can be synchronized with the partial discharge (PD) measuring system, which enables a holistic investigation of progressing creeping discharges. The test circuit using this setup will be presented in Section 3.5.2.

3.4.5 Partial Discharge Measurements

Figure 3.14 shows a schematic diagram of the PD measuring system. As displayed, the system is

composed of the below-listed parts: a coupling capacitor (1200 pF), a calibrator (Omicron CAL 542), a measuring impedance (Omicron CPL 542), a data Acquisition unit (Omicron MPD 600), and an optic fiber controller (Omicron MCU 502).

MPD 600 is connected to MCU 502 via an optic fiber cable, thus providing galvanic isolation between the high voltage area and the personnel operation area. Independent of the type of applied voltages, all measurements comply with IEC 60270:2000 [135] and adopt the wide-band mode with a bandwidth of 300 kHz and a mid-band frequency of 250 kHz. To alleviate the disturbance of environment noise, all tests are carried out in a well-shielded room, and the measurement system is calibrated prior to each test.

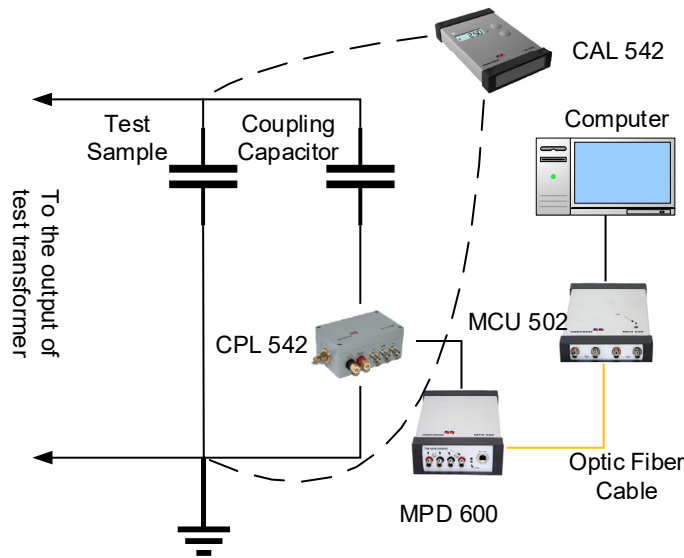
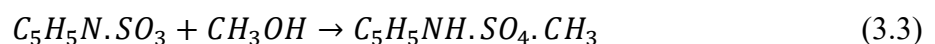
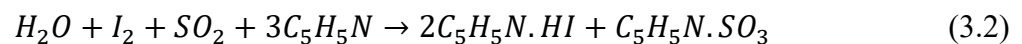


Figure 3.14 Schematic illustration of partial discharge measurement

3.4.6 Water Content Measurement of Insulating Oil

The water contents in insulating oil and oil-impregnated pressboard are determined using the coulometric Karl Fischer titration (KFT) method that complies with IEC 60814:1997 [136]. The chemical reactions involved with KFT can be expressed as:



where the sample is mixed with a base/alcohol solution of iodide ion and sulphur dioxide. Iodine is generated directly in the electrolyte by electrochemical means, in which the generation of iodine is proportional to the quantity of electricity. According to Faraday's law:



where one mole of iodine reacts with one mole of water stoichiometrically so that 1 mg of water is equivalent to 10.72 C (number of coulombs). Based on this principle, it is possible to determine the amount of water directly from the quantity of electricity (number of coulombs) required for the electrolysis.

Metrohm 831 KF Coulometer is used for this measurement, and the assembly of its titration cell is shown in Figure 3.15 [137]. The titration cell consists mainly of a drying tube for preventing moisture

ingress, an electromagnetic stirring bar for ensuring accurate dispersion of sample and reagent, a septum stopper for sample injection, and two Pt reaction electrodes. The test cell can automatically determine the endpoint of titration by monitoring the voltage difference between the Pt wires of the indicator electrode. Three measurements are carried out for each sample.

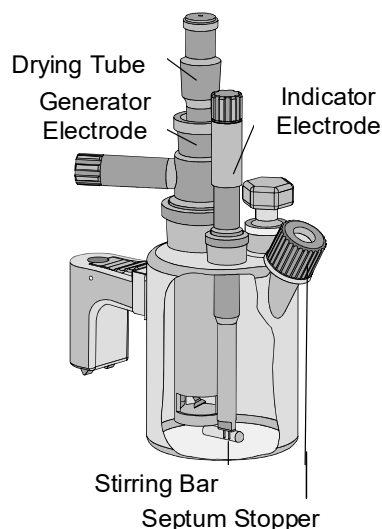


Figure 3.15 Titration cell of Metrohm 831 KF Coulometer [137]

3.4.7 Water Content Measurement of Oil-Impregnated Pressboard

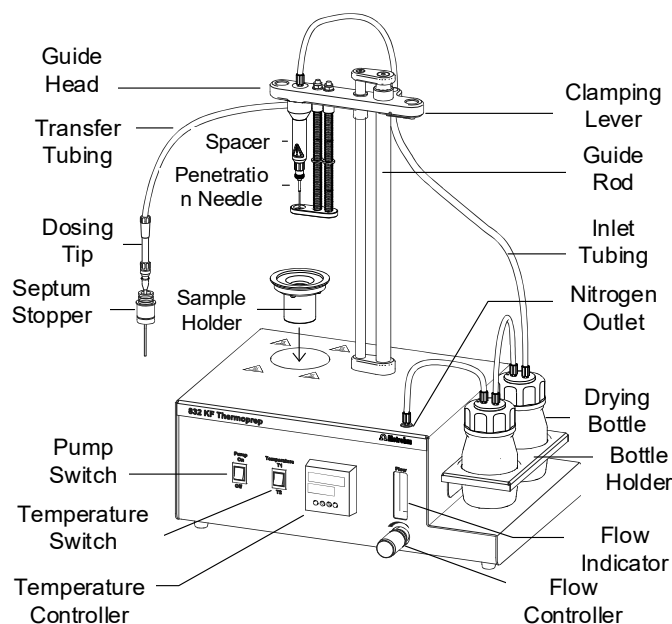


Figure 3.16 Construction of Metrohm 832 KF Thermoprep [138]

In addition, as prescribed in IEC 60814:1997, it needs a thermal oven to measure the water content in pressboard samples. The oven is used for evaporating moisture in the pressboard sample and transferring the vapors into the titration vessel by a carrier gas. Therefore, Metrohm 832 KF Thermoprep is integrated into the titration coulometer. Figure 3.16 gives an illustration of the construction of 832 KF Thermoprep [138]. The operation parameters and procedures are set according to Section 4.4 in IEC 60814:1997 [136]. Nevertheless, some parameters are revised based on practical experiences [139, 140]. For instance, IEC 60814:1997 recommends the heating temperature shall be 130 °C to 140 °C, whereas it is suggested in [140] that the optimal heating temperature should at least be 180 °C.

3.4.8 Capillary Water Rise Test

The capillary water rise can be used to evaluate the water adsorption capability of pressboard samples. Therefore, capillary water rise tests are conducted according to ASTM D202-08 [141]. The schematic diagram and actual construction of the test setup are shown in Figure 3.17. Ten specimens of the same sample are put under investigation simultaneously for obtaining the average value. Each test lasted for 8 hours, and the heights of water rise are recorded for every 1 hour.

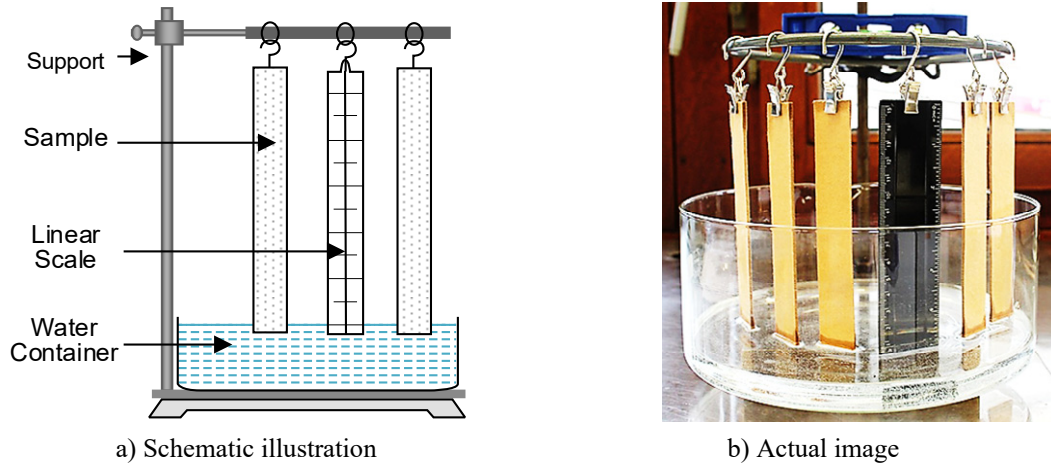


Figure 3.17 Experimental setup of water adsorption test

3.4.9 Gas Analysis

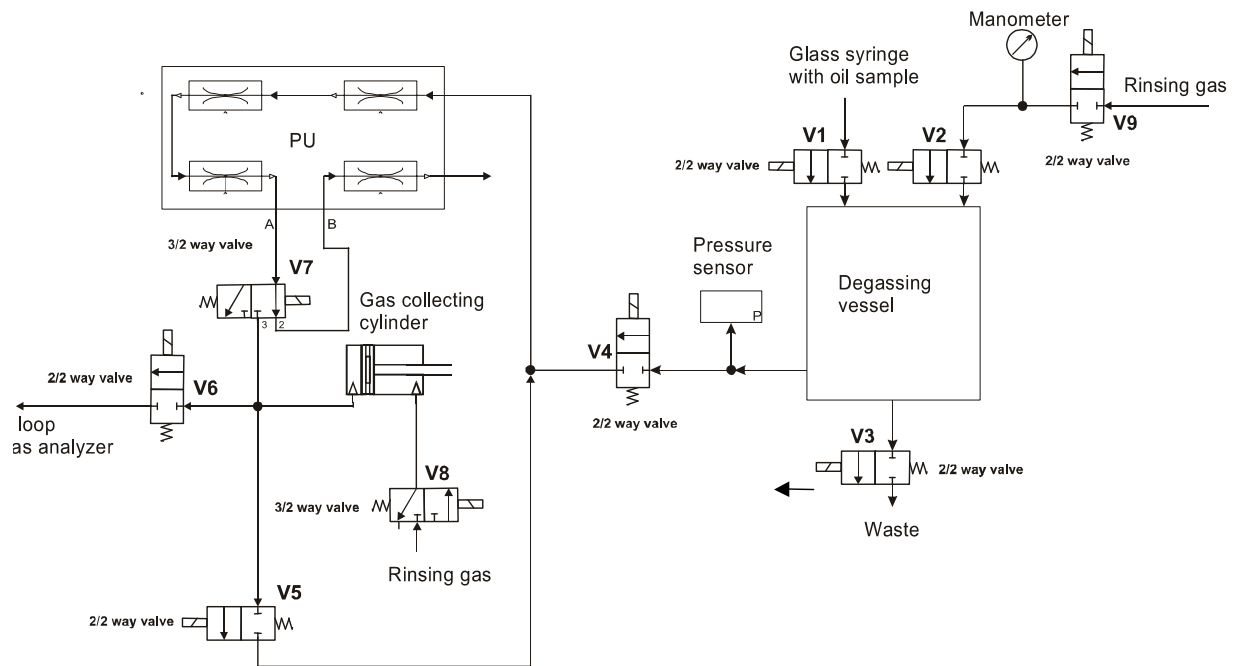


Figure 3.18 Scheme of gas supply and oil-degassing system [142]

TOGA GC from Energy Support GmbH is used to implement dissolved gas and free gas analyses. TOGA GC consists mainly of a gas supply system, a vacuum degassing system, and a gas analyzer. The gas supply feeds other systems with high-purity gases. Hydrogen (H₂) with a purity level of 4.0, argon (Ar) with a purity level of 5.0, and argon (Ar) with a purity level of 4.6 are used as fuel gas, carrier gas, and rinsing gas, respectively. Figure 3.18 shows a schematic diagram of the gas supply and oil-degassing system.

At first, the oil samples are injected into a vacuum degassing vessel, where dissolved gases are extracted and separated. Afterwards, the separated gases, driven by a diaphragm vacuum pump, enter a pressure sensor and then are released to atmospheric pressure. The total gas content is determined by the pressure sensor. At last, the gases are contained in a gas collecting cylinder and then transferred to the gas analyzer via a sample loop. The entire degassing process is controlled by 9 solenoid valves. The gas analysis system is shown in Figure 3.19. At first, gas samples are feed into the sample inlet, with which a dosing valve controls the gas quantity. Afterwards, the gas mixtures are transferred into a double capillary column for gas separation. Due to their small diameters and great lengths, the capillary columns exhibit considerably higher separation capacity than traditional packed columns. Lastly, the compositions of gas mixtures can be determined according to their respective retention times in the separation columns [143].

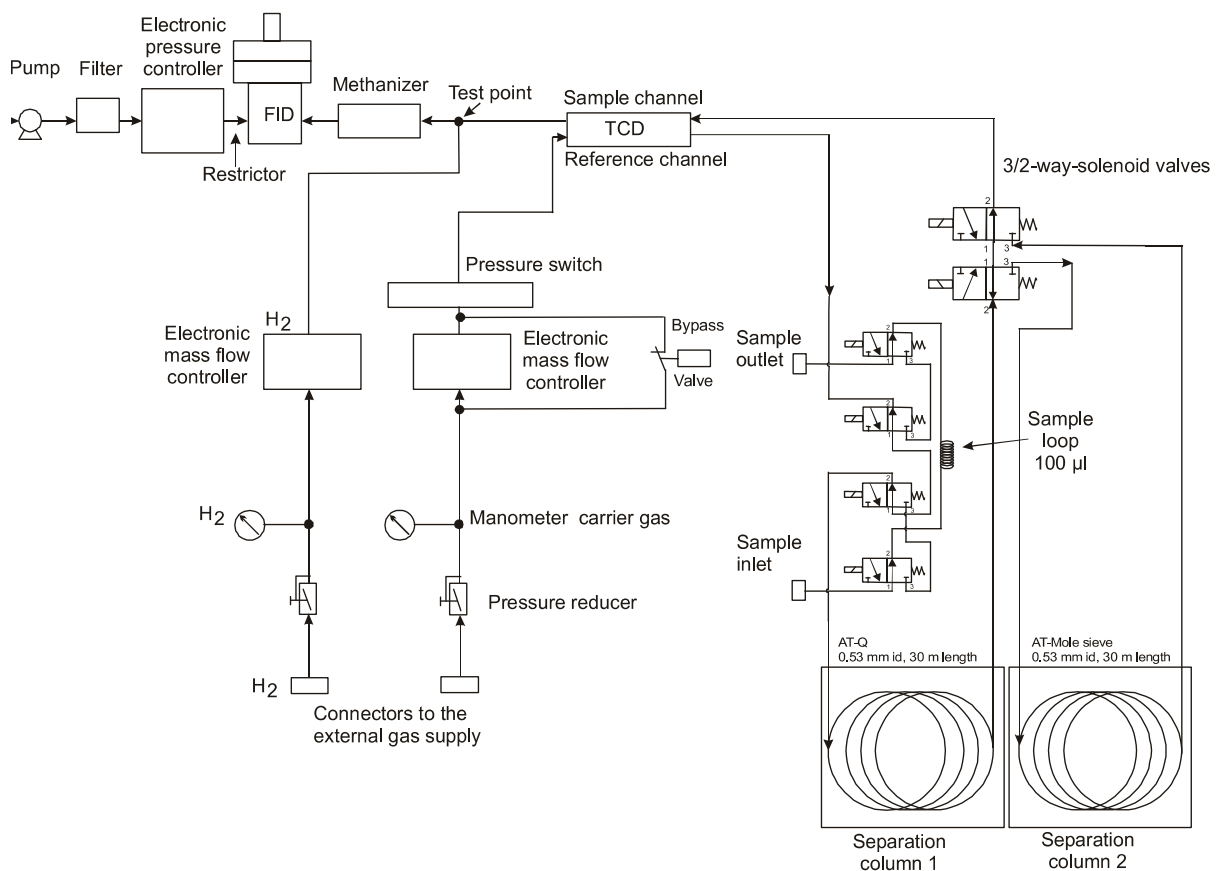


Figure 3.19 Schematic diagram of gas analysis system [142]

The separated gases travel with the carrier gas Ar 5.0 into a thermal conductivity detector (TCD) and a flame ionization detector (FID). The TCD detector uses a non-destructive methodology with comparatively low sensitivity and is therefore normally used for detecting permanent gases, such as hydrogen (H₂), oxygen (O₂), and nitrogen (N₂). In comparison, the FID uses a destructive methodology with high sensitivity and is therefore preferentially used for detecting hydrocarbon and carbon oxides. In the FID channel, the gas is warmed by a hydrogen flame, thereby emitting a weak current. The generated current signal is used to quantify the concentrations of gases. However, it is necessary to convert carbon monoxide (CO) and carbon dioxide (CO₂) into methane (CH₄) before they enter into the FID detector. This conversion reaction is realized using a methanizer tube. Moreover, TOGA GC can be configured to implement free gas analysis as well if the vacuum degassing mode is deactivated.

3.4.10 Pressboard Surface Temperature Measurements

The pressboard surface temperature is measured using an optic fiber thermometer system. The system consists mainly of a Neoptix T1 optic fiber temperature probe, Neoptix Reflex™ signal conditioner, and Neoptix OptiLink™ software. The Neoptix™ T1 optic fiber probe is a field-proven temperature sensor, which can measure the temperatures ranging from $-270\text{ }^{\circ}\text{C}$ to $+250\text{ }^{\circ}\text{C}$ with an uncertainty of $\pm 0.1\text{ }^{\circ}\text{C}$. Moreover, it is immune to the electromagnetic field and exhibits good compatibility with insulation oil.

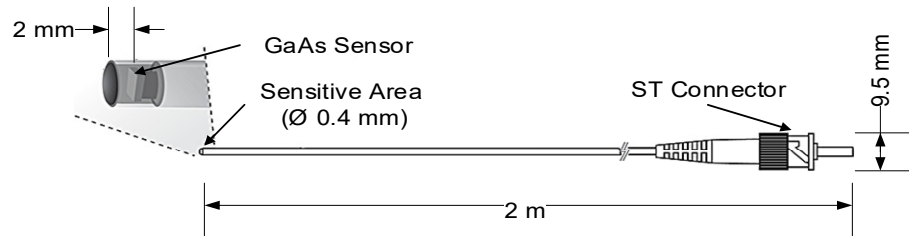


Figure 3.20 Basic structure of a GaAs optic fiber thermometer

Figure 3.20 shows the basic structure of the T1 optic fiber probe [144]. The probe has a gallium arsenide (GaAs) sensor at its tip. GaAs is a compound semiconductor with a direct energy gap. The energy gap decreases as environment temperature increases, which in turn results in a shift in its absorption spectra. In consequence, the environment temperature can be inferred through analyzing the absorption spectra of the GaAs sensor using a spectrometer. In addition to recording the temperature variations on the pressboard surface during creeping discharge, this system is also used to control the oil temperature whenever precise oil heating is required.

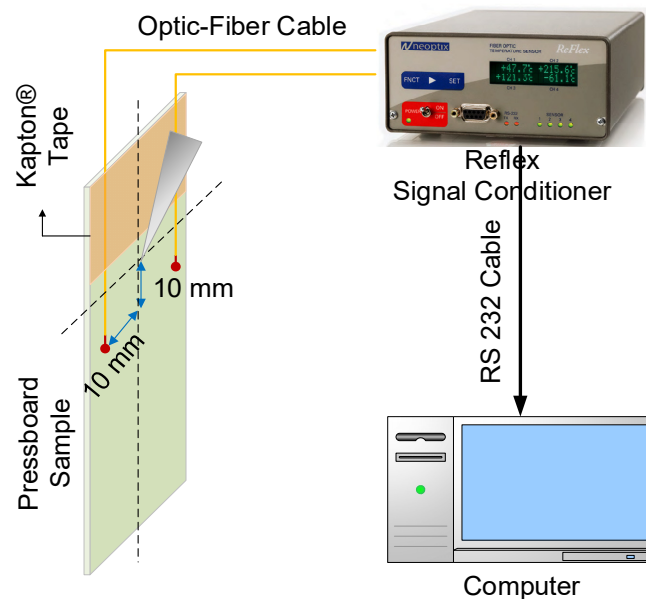


Figure 3.21 Schematic illustration of surface temperature determination

Figure 3.21 gives a schematic illustration of pressboard surface temperature measurement. Two optic fiber sensors are mounted on the pressboard surface. Since it is impossible to predict surface hot spots, the sensors are located 10 mm away, both vertically and horizontally, from the needle electrode tip. The PD-free and heat-resistant Kapton® tape are used to fix the sensors to ensure they have close contact with the pressboard surface. The sensors are connected to a signal conditioner via optic fiber cables. The signal conditioner digitalizes the reflected light signals and transmits them to a computer via RS-232 communication.

3.4.11 Scanning Electron Microscopy and 3D Laser Scanning

A scanning electron microscope (SEM) produces images of a sample by scanning the surface with a focused beam of electrons. The electrons interact with atoms in the sample, producing various signals that contain information about the sample's surface topography and composition [145]. Therefore, SEM is taken advantage of in this thesis to investigate the fiber structure of thermally-aged pressboards and to implement a post-mortem of the pressboard samples failed by creeping discharge. Moreover, the fiber diameters of the pressboard were also obtained using embedded software. An SEM image of the 60 days-aged pressboard sample is given in Figure 3.22.



Figure 3.22 SEM image of a 60-days aged pressboard

A colored 3D violet laser scanning microscope Keyence VK 9710 is used to investigate the surface morphology of the pressboard sample. Employing two light sources, i.e., a laser source and a white light source, the laser scanning microscope generates rich information on laser intensity, color, and height. Therefore, a fully-focused color image and height contour of the pressboard sample can be constructed. Working with a controller VK 9700, this system can also implement a series of detailed analyses, such as surface profile measurement, 3D display of surface height, surface roughness measurement, and so forth [146]. Figure 3.23 displays the height-color map of a 60 days-aged pressboard sample, in which the color contours indicate relative heights of different areas on the pressboard surface.

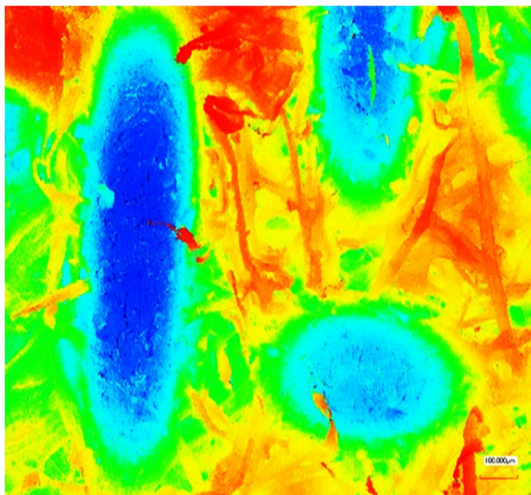


Figure 3.23 Surface image of aged pressboard by 3D laser scanning microscope

3.4.12 Finite Element Method (FEM) Simulation

All FEM simulations in this thesis are carried out with Ansys Maxwell® 2D. Electrostatic solver and DC Conduction solver are selected in the thesis to investigate potential contours, field distribution, and current intensity of oil-pressboard interface under AC and DC stresses, respectively. The flowchart of implementing a 2D FEM with Maxwell® is shown in Figure 3.24.

The electrostatic solver solves the electric potential $\varphi(x, y)$ in the field equation [147]:

$$\nabla \cdot (\varepsilon_r \varepsilon_0 \nabla \varphi(x, y)) = -\rho \quad (3.5)$$

where, ε_r denotes the relative permittivity, ε_0 is the vacuum permittivity (8.854×10^{-12} F/m) and $\rho(x, y)$ is the charge density. Resultantly, the electric field \vec{E} and the electric displacement field \vec{D} can be obtained using the following equations:

$$\vec{E} = -\nabla \varphi(x, y) \quad (3.6)$$

$$\vec{D} = \varepsilon_r \varepsilon_0 \vec{E} \quad (3.7)$$

The electrostatic solver treats the material as a perfect insulator, and the electric field is completely capacitive, whereas the DC Conduction solver treats the materials as lossy dielectrics with certain levels of electric conductivity. A conduction current is induced when a potential difference is applied to the materials:

$$\vec{J}(x, y) = \sigma \vec{E}(x, y) = -\sigma \nabla \varphi(x, y) \quad (3.8)$$

where, $\vec{J}(x, y)$ is the current density, $\vec{E}(x, y)$ is the electric field, σ is the conductivity (S/m) and $\varphi(x, y)$ is the electric potential. Resultantly, the electric potential $\varphi(x, y)$ can be obtained using the following equation:

$$\nabla \cdot (\sigma \nabla \varphi(x, y)) = 0 \quad (3.9)$$

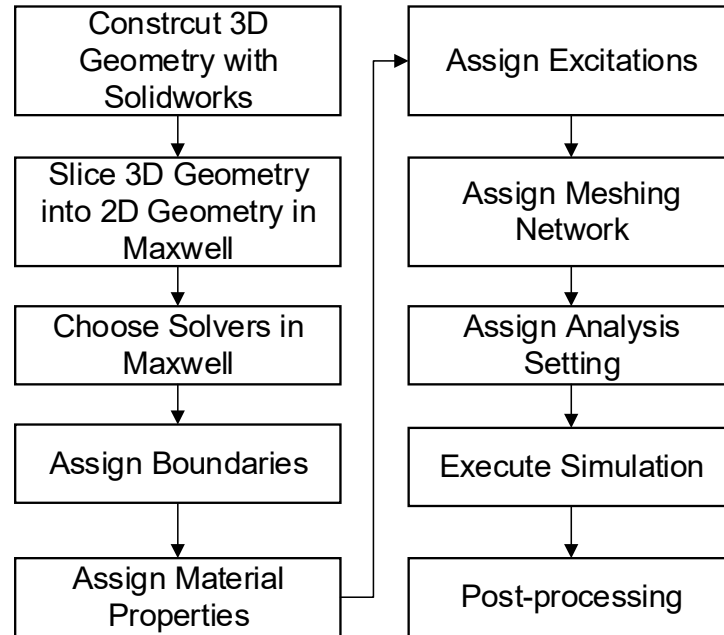


Figure 3.24 Flowchart of 2D FEM simulation with Maxwell®

Moreover, one should bear in mind that the validity of a FEM simulation is determined by the quality of its meshing network. Despite that Maxwell provides a self-adaptive meshing scheme, the meshing parameters are manually set in all simulations to achieve the possibly maximum accuracy. Figure

3.25 gives an example of the meshing network of the needle-plate electrode with a pressboard sample.

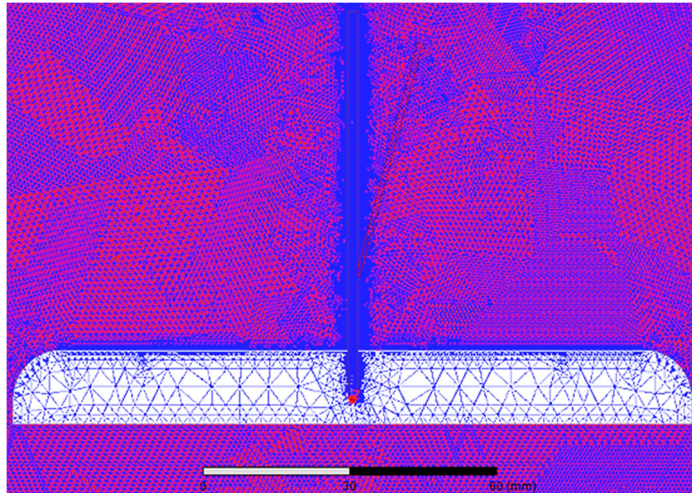


Figure 3.25 Meshing network of the needle-plate electrode geometry

3.5 Test Set-up

3.5.1 AC Creeping Discharge Test on Aged Pressboard Samples

Figure 3.26 shows the high voltage test circuit of creeping discharge tests with thermally aged pressboard samples. The system is energized by the main power source (230 V, 50 Hz), and the high voltage is generated via a test transformer with a maximum output of 70 kV. A manual variac and a motor variac are installed between the main power source and test transformer for adjusting voltage level and voltage rising steepness. A resistor (60 Ω) is used to limit the inrush current when the system is tripped, which will be short-circuited immediately after energization. A resistor (50 k Ω) is installed between the test transformer and the high voltage needle electrode to protect the test transformer from breakdown events. A voltage divider, comprising two capacitors (100 pF and 100 nF), is used to measure the applied voltage.

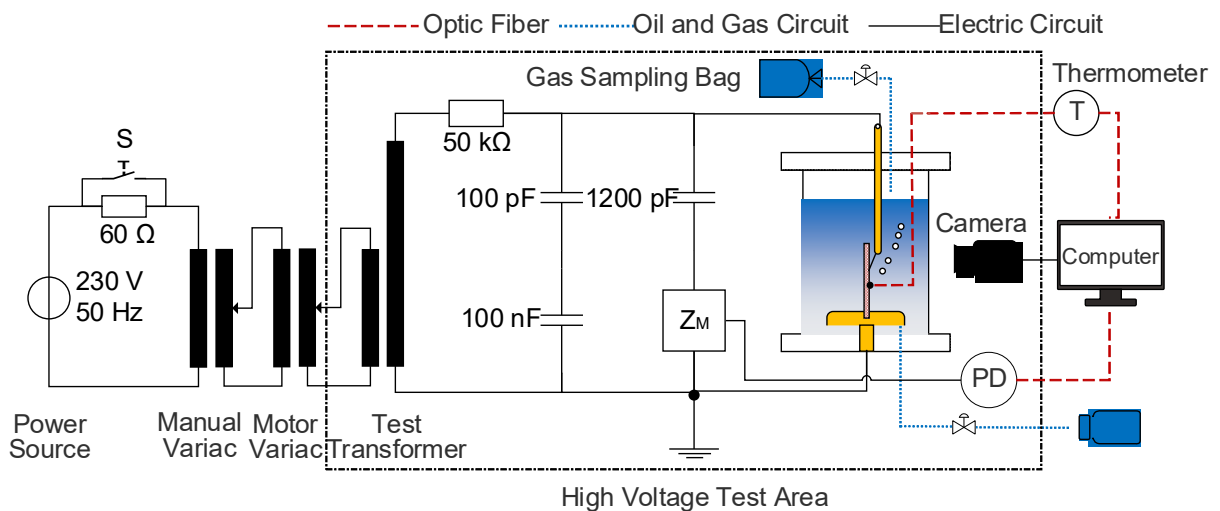


Figure 3.26 High voltage test circuit for ac creeping discharge for differently-aged pressboard

The vertical electrode configuration is employed to apply an extremely divergent AC stress on the oil/pressboard interface. The PD measurement is carried out using a coupling capacitor (1200 pF) and a measuring impedance Z_M (50 Ω), which are connected in parallel to the test object. The PD signals are transmitted from the measuring impedance to a PD detection device via BNC cable and further to a computer via optic fiber cable. In the meantime, three optic fiber temperature probes are inserted

into the test cell to record the real-time temperature variations on the pressboard surface and in oil bulk. In addition, a translucent Teflon® gas sampling bag is mounted on the test cell to collect any potential free gas during the discharge process, and an air-tight aluminum bottle is used to obtain oil samples. The collected gas and oil samples are thereafter analyzed using gas chromatography. Aiming to analyze the progression process of creeping discharge, moreover, a well-shielded high-resolution camera is used to capture the visual information.

3.5.2 AC Creeping Discharge Test with Different Oil Temperatures

Figure 3.27 shows the high voltage test circuit of creeping discharge tests with different oil temperatures. Its layout is almost identical to that shown in Figure 3.26. Besides, a reference capacitor (37.1 pF) is connected in parallel to the test sample. Two high-precision leakage current measuring devices (I1 and I2) are connected in series to the reference capacitor and test sample, respectively. With the help of this system, the leakage current, as well as the dielectric dissipation of the test object during creeping discharge, can be recorded in real-time. Moreover, this system can be synchronized with the PD measuring system, thereby correlating the variations of leakage current with PD patterns.

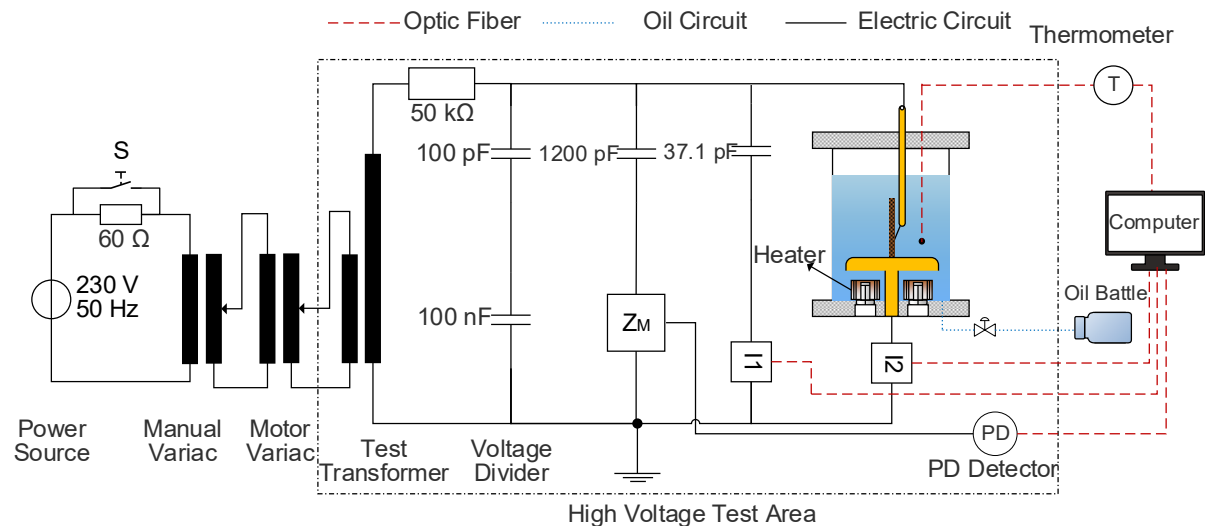


Figure 3.27 High voltage test circuit for ac creeping discharge at different temperatures

Furthermore, two compacted cartridge heaters are located underneath the brass grounding plate to obtain desired oil temperatures. The heaters are energized by an external isolating transformer, and the heating effect is controlled by adjusting the output of the isolating transformer. For homogeneous liquid heating, the heaters are sheathed by circular radiators. The liquid temperature is monitored by an optic fiber thermometer.

3.5.3 DC Creeping Discharge Test with Different Oil Temperatures

Figure 3.28 shows the high voltage test circuit of DC creeping discharge tests with different oil temperatures. Its layout at the primary side is identical to those shown in Figure 3.26 and Figure 3.27. The rectifying system comprises a diode (140 kV, 100 kΩ) and a smoothing capacitor (6000 pF). The generated DC voltage has a ripple factor of around 3%. A resistive voltage divider, comprising two resistors (1 GΩ and 1 MΩ), is used to measure the applied DC voltage. The heating system and PD measuring system are identical to those illustrated in Section 3.5.2. It is noteworthy that a blocking resistor (100 MΩ) is installed between the smoothing capacitor and the coupling capacitor. This arrangement aims to inhibit the high-frequency PD signals from propagating into the smoothing capacitor.

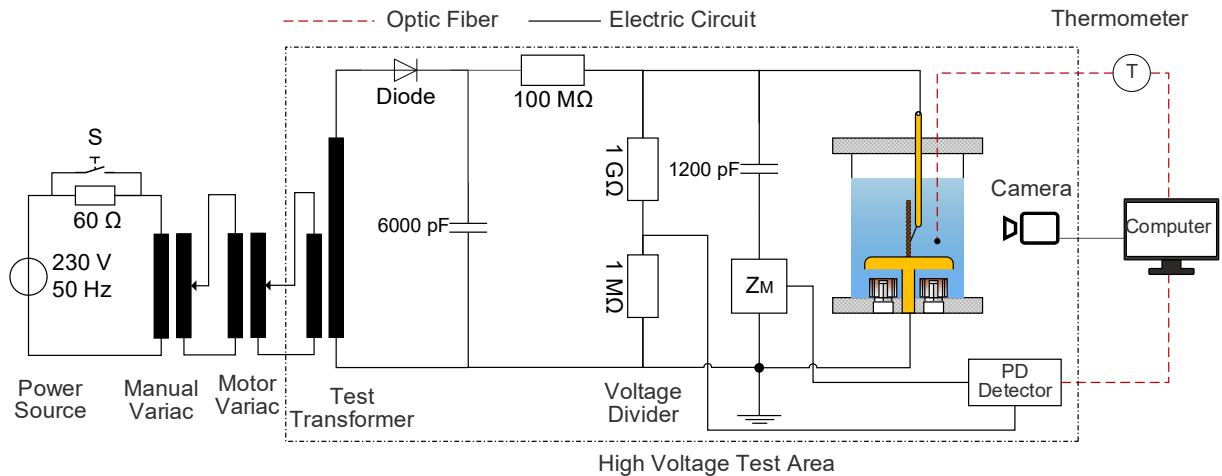


Figure 3.28 High voltage test circuit for DC creeping discharge at different temperatures

3.5.4 DC Creeping Discharge Test with Different Oil Flowing Speeds

Figure 3.29 shows the high voltage test circuit of DC creeping discharge tests with forced oil flows. Its basic layout is identical to that shown in Figure 3.28. Besides, it incorporates an oil flowing circuit and a streaming current measuring system as well. The oil flowing circuit consists mainly of four parts: a test cell, a relaxation tank, a liquid transfer pump, and an oil reservoir. The structures of the test cell and the specially designed ground electrode have been illustrated in Section 3.1.4 and Section 3.2.2, respectively. The relaxation tank is made of a hermetic metal vessel and connected to a picoammeter. The oil reservoir is a glass vessel filled with insulating oil. A spiral heater is installed in the oil reservoir to heat the oil sample up to a certain temperature, and an optic fiber thermometer is used to monitor the oil temperature at the outlet point. The liquid transfer pump is a diaphragm pump. It can withstand a liquid temperature up to 80 °C and has 11 flow rates. It transfers heated oil from the oil reservoir to the test cell, thereby driving oil circulating in the whole system.

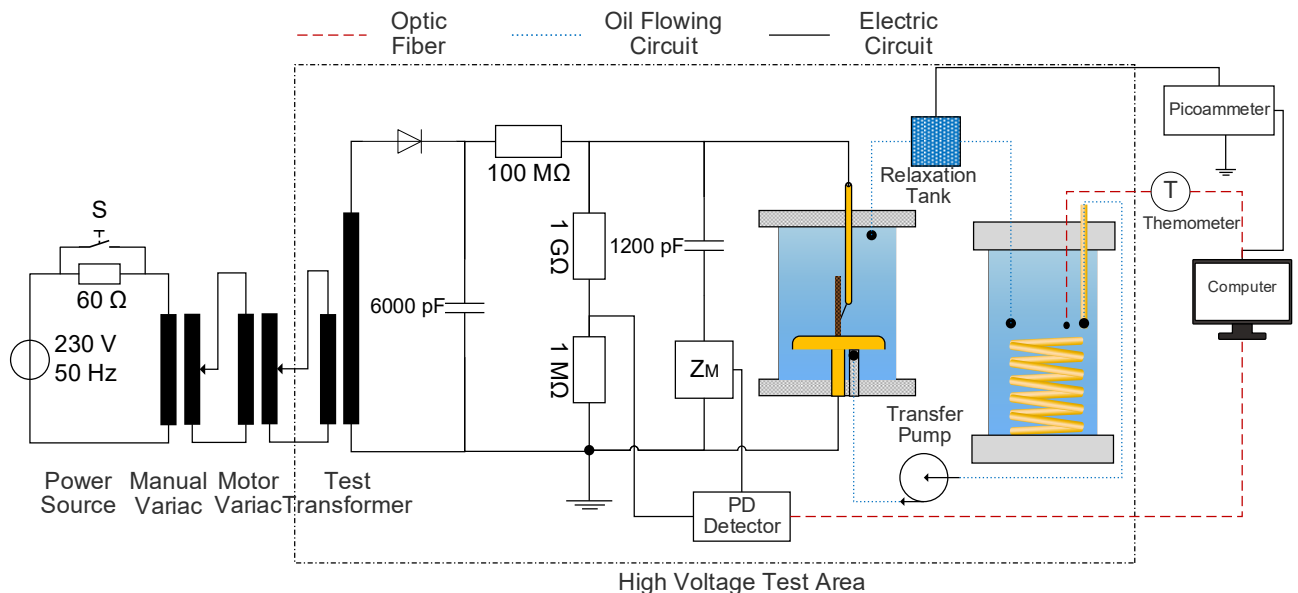


Figure 3.29 High voltage test circuit for DC creeping discharge for oil flowing tests

The streaming current measuring circuit is composed of the relaxation tank and a Keithley Model 6485 picoammeter. For a better dissipation of net charges that are generated from the streaming electrification, multiple layers of metal grids are installed inside the relaxation tank for enlarging the contact surface of oil with metal parts. The grid layers are electrically connected to the sheath of the

relaxation tank and eventually to the picoammeter. In consequence, the streaming current can be measured by the picoammeter and then recorded by a computer.

4 INFLUENCES OF AGEING AND FIELD INTENSITY ON AC CREEPING DISCHARGES

4.1 Introduction

As an inevitable degrading process for transformer insulating materials, thermal ageing has complex and multi-faceted effects on pressboards, such as destroying the fiber structure and producing polar substances. Consequentially, the irreversible prejudices to pressboard properties could exert a profound influence on the oil-pressboard interface phenomenon. Moreover, the interface creeping discharges in a transformer are also susceptible to stress conditions. The interface field intensity can not only influence the progression of creeping discharge but also determine the final failure mechanism. Therefore, it is of vital importance to reveal the impacts on pressboard thermal ageing and field intensity on oil-pressboard interface creeping discharges.

However, most of the previous researches in this field only focus on either a single individual outcome of ageing or the short-time electric strength of the interface. Thus far, the long-term creeping discharge behaviors in an aged transformer have not been soundly reproduced under laboratory conditions, not to mention being thoroughly understood. In consequence, an evident gap still exists between investigation works and practical applications. To address the problem, one has to revisit the correlations between long-term creeping discharges and their influential factors and examine them with deeper insights. Therefore, a systematic investigation was carried out in this chapter to study the influences of pressboard thermal ageing and field intensity on the long-term oil-pressboard interface creeping discharges.

This chapter is subdivided into five sections. Section 4.2 presents the information on sample preparation and experimental setup. Section 4.3 reports the results of the preliminary tests. The emphases in Section 4.3 are put on the influences of thermal ageing on pressboard physicochemical properties and the influences of the voltage level on interface field distribution. Section 4.4 reports the results of long-term creeping discharge tests. Section 4.5 gives the concluding remarks of this chapter.

4.2 Sample Preparation and Experimental Setup

4.2.1 Preparation of Test Samples

Thermally accelerated ageing tests were carried out to simulate the natural ageing process of transformer pressboards in practical service. Firstly, the pressboard and oil specimens were processed following the procedures depicted in Section 3.3. To prevent the ingress of ambient moisture and oxygen, the impregnated pressboard samples were immersed in oil-filled hermetic stainless-steel vessels. The mass ratio of oil to pressboard is 10:1. Aiming to maintain constant pressure during ageing, overhead space is left in the vessels to accommodate the thermal expansion of oil. Afterwards, the metal vessels were put in a forced air-circulated thermal oven for accelerated ageing. The ageing temperature was 130 °C and the ageing periods were 20, 40, and 60 days, respectively. According to IEEE Std C57.91-2011 [148], the ageing times are equivalent to, in terms of insulation loss-of-life, natural ageing of 2152, 4304, and 6457 days, respectively, given an average winding temperature rise of 55 °C and an average ambient temperature of 30 °C. For the sake of conciseness, the varyingly aged pressboard samples are referred to as #00, #20, #40, and #60, respectively.

In addition, a set of non-impregnated pressboard samples was prepared for investigating the influences of thermal ageing on pressboard water absorption capability. The pressboard sample is shown in Figure 4.1. According to ASTM D202-08 [141], the pressboard samples were firstly cut into a proper size of $150 \times 25 \times 2$ mm, in which half were cut parallel with machine direction and the other half cut parallel with cross-machine direction. Afterwards, samples were put into a vacuum thermal oven for drying. The drying environment is identical to that of ‘normal’ pressboard samples, except that the impregnation step is omitted. After drying, they were taken out of the vacuum oven for accelerated ageing. The ageing environment is identical to that of normal pressboard samples.



Figure 4.1 Pressboard samples for capillary water rise tests

Due to the limitation of laboratory conditions, substitute samples had to be prepared for determining the absolute water contents of differently aged pressboards. The pressboard samples are shown in Figure 4.2. The pressboard samples were cut into the size of $5 \times 5 \times 2$ mm. The impregnation and ageing processes of the substitute samples are almost the same as those of normal pressboard samples. Newly processed mineral oil was used as the test specimen, and its water content is around 7 ppm.

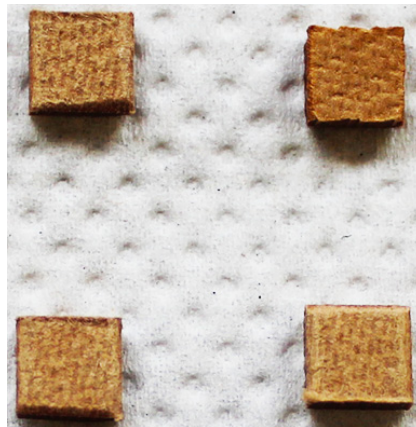


Figure 4.2 Substitute pressboard samples for absolute water content determination

4.2.2 Test Contents and Experimental Setup

The tests can be broadly divided into two groups. The first group of tests is referred to as preliminary tests. The investigations in preliminary tests focused on influences of thermal ageing on pressboard physicochemical properties, the impacts of the voltage level on interface field distribution, and the short-time electric strengths of the oil/pressboard interface. The second group is referred to as the long-term creeping discharge tests.

In long-term creeping discharge tests, the influences of thermal ageing and voltage levels on interface creeping discharge would be directly evaluated. The electrode geometry, the test cell, the partial discharge test-up, and the HV test circuit were illustrated in Section 3.1.1, Section 3.2.1, Section

3.4.5, and Section 3.5.1, respectively. All high-voltage tests were carried out in a well-shielded room, and the actual arrangement of the needle-to-plate electrode at the interface is shown in Figure 4.3.



Figure 4.3 The actual arrangement of the needle-to-plate electrode at the interface

4.3 Results of Preliminary Tests

4.3.1 Capillary Water Rise of Aged Pressboard Samples

The setup and procedure of capillary water rise tests were depicted in Section 3.4.8. Figure 4.4 displays the test results. No significant differences in water capillary rise are detected among the varyingly aged samples within the first hour. As tests proceed, however, the differences become ever more apparent, and the capillary water rise is clearly negatively correlated with pressboard ageing degree. At the end of the tests, the capillary water rise of #0 sample is almost 50 mm, whereas that of #60 sample is merely 20 mm. Nevertheless, the capillary water rises of aged samples do not differ much from one another. Moreover, the capillary water rise is not very sensitive to cutting directions: the rises in both directions are quite approximate to each other for all samples.

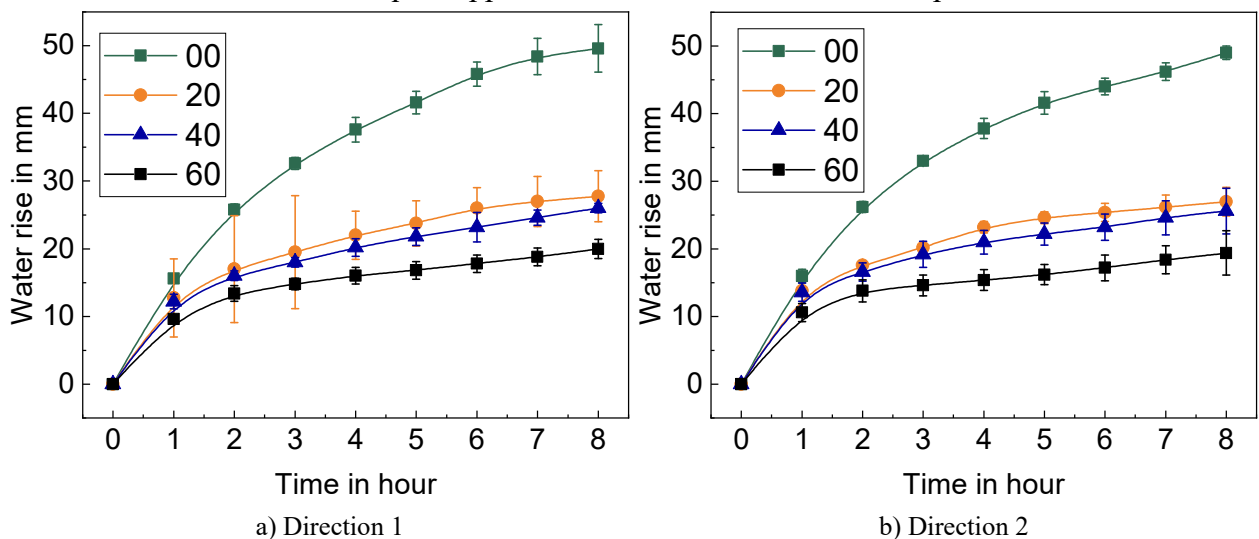


Figure 4.4 Capillary water rise of aged pressboard samples

As explained previously, the capillary water rise is highly indicative of pressboard water absorption capability. The results infer that the aged pressboards have a weaker bonding force to water molecules. As a possible consequence, water might diffuse more vibrantly in aged pressboard cellulosic fibers, and the moisture migration between oil and pressboard can be facilitated as well.

4.3.2 Absolute Water Content of Aged Oil-Pressboard Samples

The test setup for absolute water determination was depicted in Section 3.4.7. Figure 4.5 shows the colors of oil-pressboard samples of varying degrees (from left to right: new, 20 days-aged, 40 days-aged, and 60 days-aged). Five measurements were carried out for each sample to obtain the average values. The results are shown in Figure 4.6.



Figure 4.5 Oil colors of aged oil-pressboard samples

The absolute moisture contents in both oil and pressboard samples increase steadily with the ageing degree. With respect to the new sample, the moisture contents in oil and in pressboard are 6.3 ppm and 0.11 % by weight, respectively, indicating both materials are well dry. In contrast, the oil and pressboard moisture contents of sample #60 increase to 15.4 ppm and 0.57 % by weight, respectively. According to IEC 60641-2: 2004 [149], the # 60 sample can be taken as ‘wet.’ The results reveal an interesting fact of pressboard ageing. On the one hand, water in the pressboard steadily increases with the ageing degree; on the other hand, the water absorption capability of the pressboard gradually declines. It can be deduced that the moisture distribution equilibrium would change as the ageing time increases. Moreover, the phenomenon could result in severe problems under extreme conditions. For instance, if the aged pressboard is subject to a sudden overheat, water in the pressboard would emigrate abruptly into oil, whereas the water solubility of oil is not proportionately enhanced. As a result, the migration of water could probably end up with bubbling.

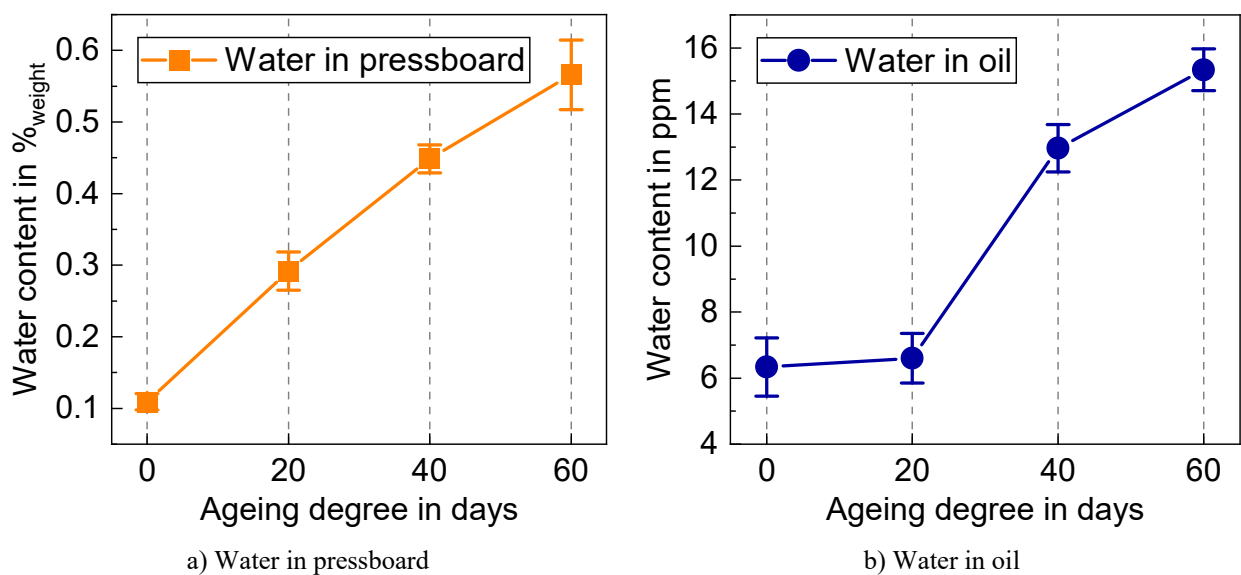


Figure 4.6 Absolute water contents of aged oil and pressboard samples

4.3.3 Fiber Integrity of Aged Pressboard Samples

The influences of ageing on the fiber integrity of pressboard were evaluated by means of SEM (see Section 3.4.1.1). The magnification is set to be 700, and five specimens of each sample were selected for investigations. All the sampling points, as denoted by the blue dots in Figure 4.7, are placed along the pressboard surface centerline, where the maximum tangential field is supposedly present.

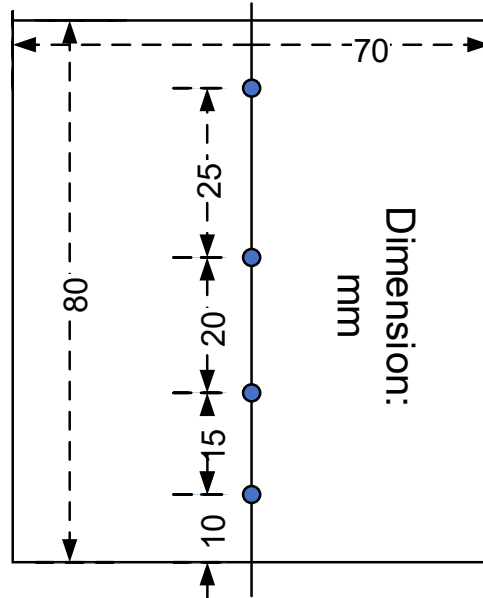


Figure 4.7 Locations of SEM sampling points on pressboard surface

The SEM images of pressboard samples are shown in Figure 4.8.

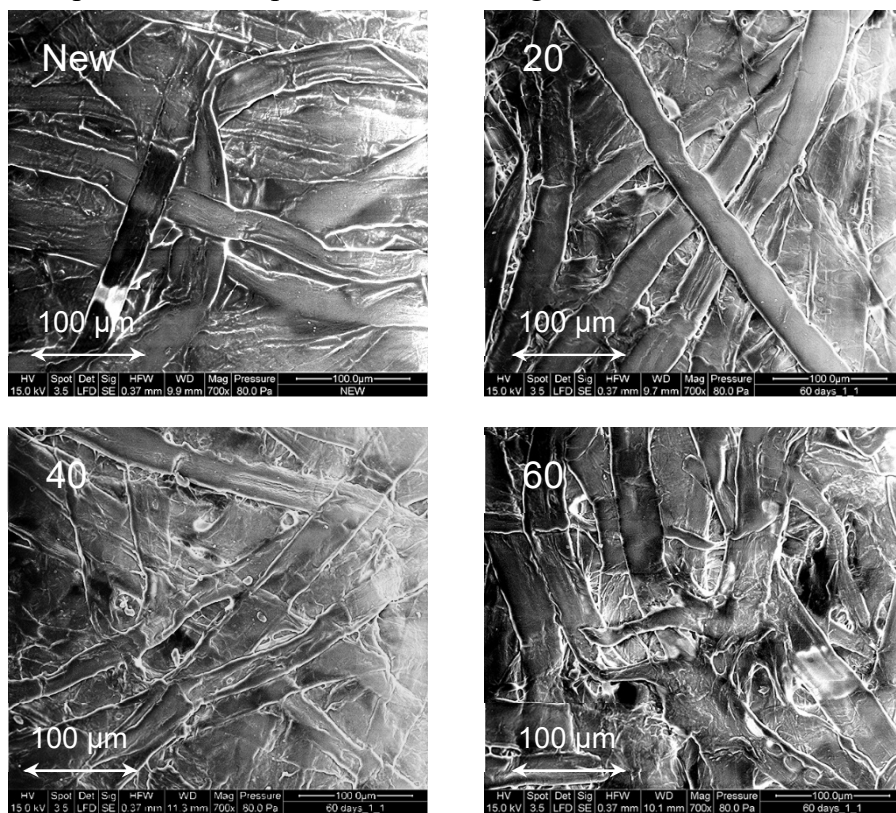


Figure 4.8 SEM images of aged pressboard samples

As displayed, the new sample has a sound fiber structure: no obvious fiber rupture or cracks. Besides, no holes are found in inter-fiber regions either, indicating the ‘bonding substances’ of cellulose

fibers, i.e., hemicellulose and lignin, are intact as well. Some inter-fiber holes are detected with #20 sample, indicating the hemicellulose and lignin have been degraded to a certain extent. Nevertheless, the cellulose macro-fibrils of #20 sample are still good enough, but #40 sample exhibits more and larger inter-fiber holes. Moreover, some embryo cracks are also found on the cellulose macro-fibrils of #40 sample, and particles also emerge. For the #60 samples, ever more and larger inter-fiber holes are observed. More importantly, the cracks on fibers are considerably enlarged, and some fibers are even ruptured, indicating the fiber structure of the #60 sample has been severely damaged.

Moreover, around 400 measurements have been made to each sample to determine the pressboard fiber width. The measurement results are shown in Figure 4.9.

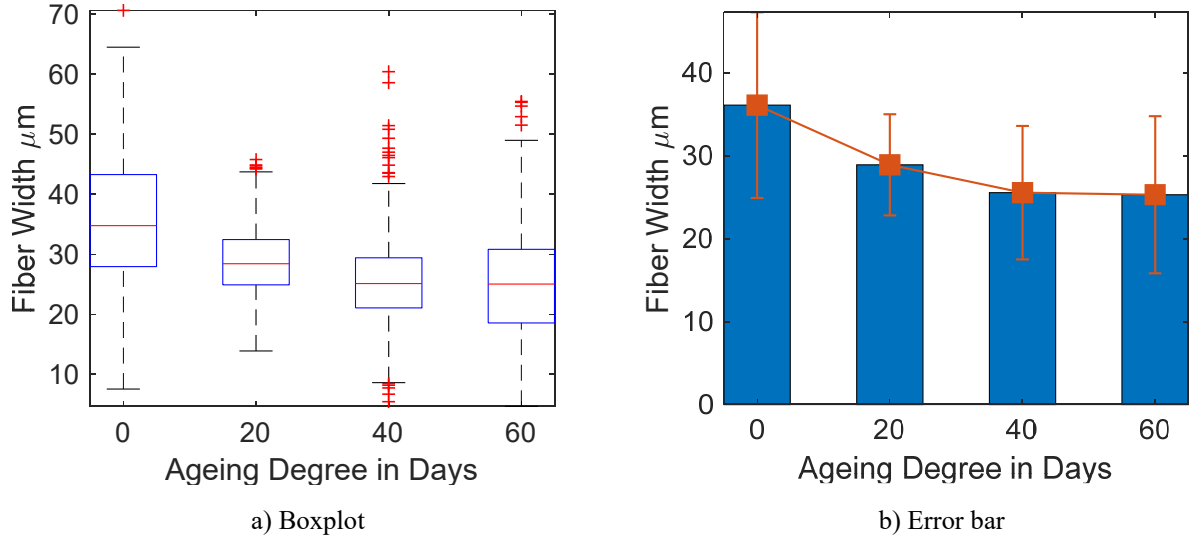


Figure 4.9 Fiber widths of aged pressboard samples

In spite of the great scattering tendencies, the median values of pressboard fiber width exhibit clearly negative correlations with the ageing degree. Besides, the mean value of fiber width steadily declines as ageing time increases: from 36 μm of #0 to 25 μm of #60. The information revealed by SEM investigations could explain the decline of water absorption capability of aged pressboard samples. As a porous cellulosic fiber, the pressboard absorbs water via the capillary effect. According to Jurin's Law, the relation between capillary size and water absorption capability can be described as [150]:

$$h = \frac{2\gamma \cos \theta}{\rho g r} \quad (4.1)$$

where h is the liquid height, γ is the surface tension, θ is the contact angle of the liquid on the capillary tube wall, ρ is the liquid density, r is the radius of the capillary tube, and g is the gravitational force.

As shown, the capillary water height is inversely proportional to the radius of the capillary tube. As indicated by SEM measurements, aged pressboard samples have enlarged inter-fiber regions and weakened fibers, which in turn cause an increment in their micro-capillary sizes. According to Jurin's law, the capillary effect of pressboard is diminished by thermal ageing, which in turn leads to a declined water absorption capability. Moreover, the reduction in hydroxyl groups of aged pressboards is another important factor of water absorption capability decline.

4.3.4 PD Inception Voltage (PDIV) and Flashover Voltage

An AC ramp voltage, starting from null with a rising steepness of 1 kV/s, was used to determine the PDIV and flashover voltage of oil/pressboard interface. The PD measurements were carried out according to IEC 60270:2000 [135] and the PD threshold magnitude was set to be 20 pC. Ten measurements were carried out for each sample to obtain the average values. In flashover tests, a waiting period of 3 minutes was held between consecutive tests to eliminate the effects of residual space charge and hydrocarbon bubbles. Aged pressboards and newly dried oil were used as test specimens. The results are shown in Figure 4.10.

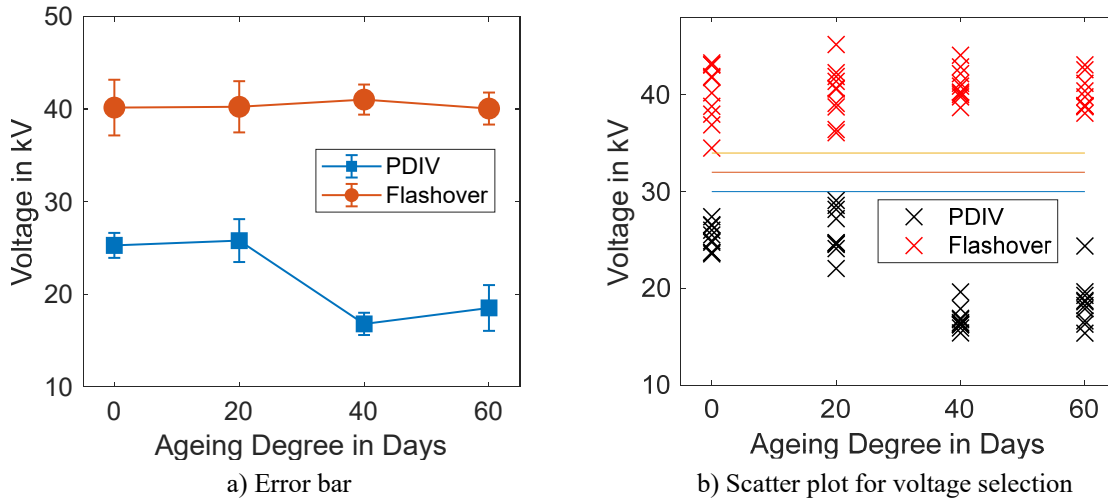


Figure 4.10 PDIV and flashover voltages of oil/pressboard interface

Irrespective of pressboard ageing degree, the mean interface flashover voltages of different samples are approximate to each other: around 40 kV. The results indicate that the short-time electric strength of the oil/pressboard interface under an extremely divergent field is hardly influenced by pressboard conditions. Instead, it is probably the oil condition that really matters in this case.

Previous researches have obtained similar results. It is reported in [97] that the creeping discharge is mainly determined by the oil quality when the pressboard is dry and clean. Besides, as argued by Cherney in [36], the oil/solid interface flashover is a liquid-controlled phenomenon. Moreover, a high-speed camera was utilized to record the interface flashover process. As revealed in the recorded video, the flashover arc channel is in the oil bulk rather than exactly at the interface. A snapshot of the flashover process is shown in Figure 4.11.

However, pressboard ageing does have an impact on interface PDIV. The PDIVs of #40 and #60 samples are significantly lower than that of the new pressboard. Nevertheless, it is difficult to build up a linear relation between PDIV and ageing degree. Two major factors, i.e., water content and pressboard surface finish, are probably responsible for the phenomenon. On the one hand, an aged pressboard has more water content, thus facilitating the occurrence of discharge. On the other hand, aged pressboard has a smoother surface finish [151], which results in a reduction of electric field distortion, thus increasing the inception field of discharges. Under the interplay of the two factors, the interface PDIV exhibits no strict linear relations to the ageing degree.

The results of PDIV and flashover voltages were also used to select the appropriate voltage levels for long-term constant-stress creeping discharge tests. The criteria for selecting voltage levels were as follows: they shall be great enough to generate repetitive discharges to the strongest sample without

any premature flashovers. Accordingly, the voltage levels (Root Mean Square) are determined: 30 kV, 32 kV, and 34 kV. A comparison between the selected voltage levels and the short-time electric strengths is given in Figure 4.10 b), where the solid lines denote the voltage levels for long-term tests.

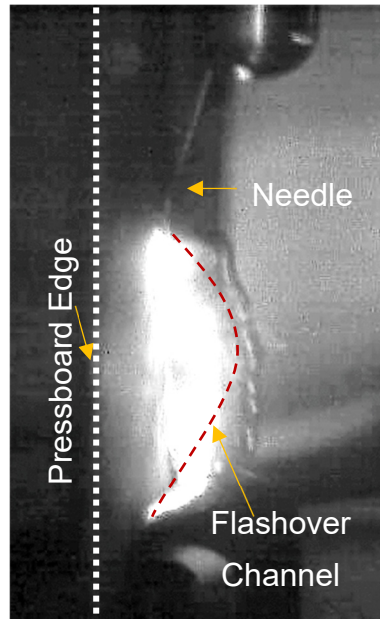


Figure 4.11 Flashover arc channel at the oil-pressboard interface

4.3.5 FEM Simulation of Interface Field Distribution

Subsequently, electrostatic FEM simulations were performed to investigate the effects of the voltage level on oil-pressboard interface field distribution. The technique and flowchart of FEM simulations were explained in Section 3.4.12. The applied voltages are the peak values of selected voltage levels, i.e., $30 \times \sqrt{2}$ kV, $32 \times \sqrt{2}$ kV, and $34 \times \sqrt{2}$ kV, respectively. Figure 4.12 shows the simulation geometry and the meshing network of the triple-junction area of the FEM simulations.

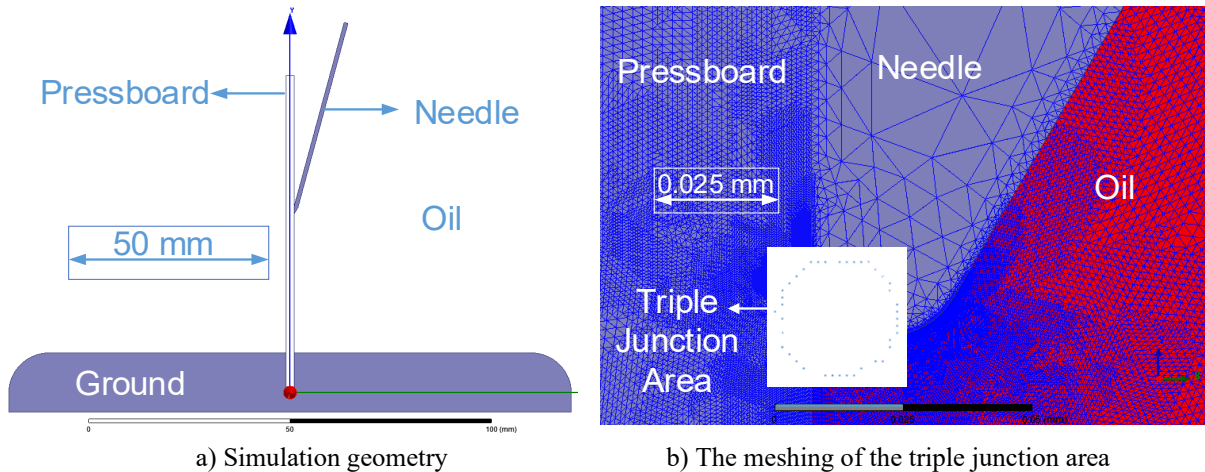


Figure 4.12 FEM design setting of the needle-to-plate electrode

Figure 4.13 a) displays the global electric potential contour under 34 kV. For voltages of 30 kV and 32 kV, the scenarios of potential distributions are almost the same. Figure 4.13 b) presents the local field distribution at the critical triple-junction areas under 34 kV. As displayed, the field distribution is considerably distorted, and the triple junction areas exhibit extremely high field intensity. Expect for the values of maximum field intensity, the scenarios of field distributions under 30 kV and 32 kV are identical to those under 34 kV.

whereas the tangential field intensity E_{tan} contains the information of direction as well. Therefore, some of the tangential fields are of negative values. Secondly, the maximum total field is at the interface, whereas the maximum tangential field is in the oil bulk. Considering the results in Section 4.3.4, it is, therefore, inferred that the inception of partial discharges is mainly affected by the total field at the interface, whereas the flashover is determined by the tangential field in the oil bulk.

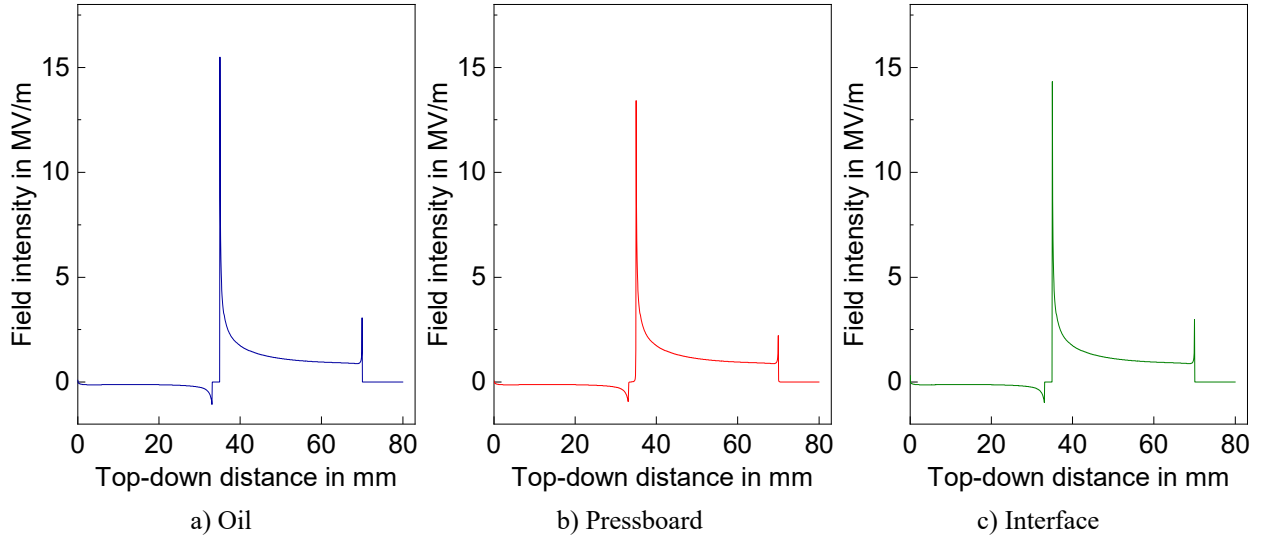


Figure 4.15 Tangential field intensity of interface at 34 kV

Furthermore, the maximum values of total and tangential fields of all regions are plotted versus the voltage levels, as shown in Figure 4.16. Besides, the global maximum field intensities are added as well. It is noteworthy that the global maximum field is not present at the exact interface. Indeed, it is located within the wedge of the triple junction area and does not move with voltage levels.

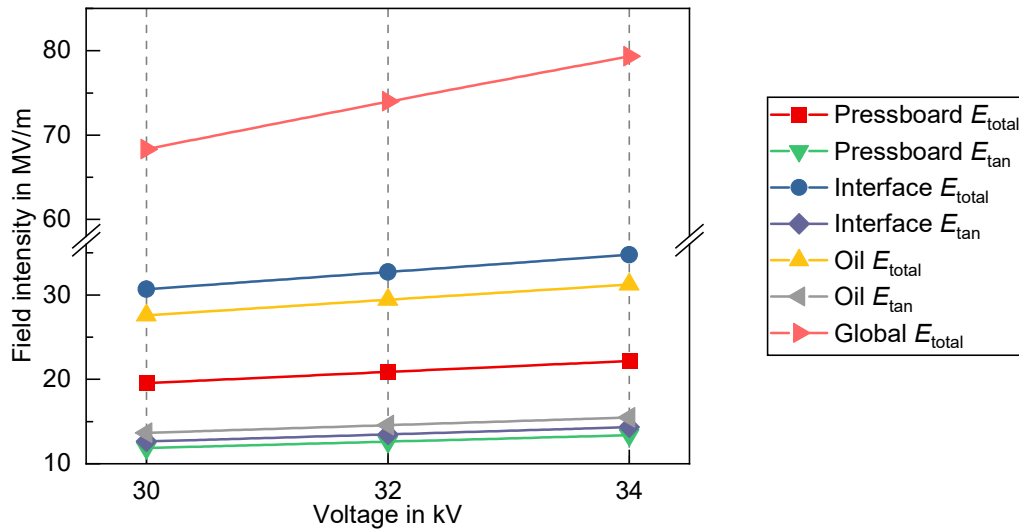


Figure 4.16 Maximums fields versus voltage

4.4 Results of Long-term Constant-Stress Creeping Discharge Tests

Long-term constant-stress tests were carried out with the aged oil-pressboard samples. The selected voltage levels (RMS) were 30 kV, 32 kV, and 34 kV, respectively. Each run of tests lasted for 180 minutes. The PD signals were recorded for 3 minutes after every 15 minutes. In the meantime, the visual information of creeping discharges was recorded using a high-resolution camera, and the temperatures of the pressboard surface were obtained via optic fiber thermometers. Lastly, the oil samples were periodically taken for dissolved gas analysis.

4.4.1 Partial Discharge Patterns

In general terms, three kinds of PD patterns are commonly used for PD evaluation [152]:

- Phase-resolved Pattern

In the phase-resolved PD (PRPD) pattern, the PD incidents within a given test period are plotted versus the sinusoidal waveform of the applied voltage. The horizontal denotes phase of PD occurrence, and the vertical coordinate denotes PD magnitude. Depending on how the information of discharge density is expressed, the PRPD pattern can be constructed in either 2D and 3D forms.

- Time-resolved Pattern

The waveform of a PD pulse contains rich information regarding its discharge nature. The time-resolved PD pattern can display the true shape of a PD pulse, which in turn enables a further detailed signal analysis, such as Discrete Wavelet Transform (DWT) and Fast Fourier Transform (FFT).

- Pattern without Phase/Time Information

In this pattern, the information pertinent to phase or time is absent. Alternatively, the voltage difference between consecutive PD incidents is investigated in detail, as the occurrence of PD pulse is determined by the external field and the local field together.

Owing to its intuitive and versatile representation of partial discharges, PRPD is widely used for PD investigations. A typical 2D PRPD pattern of oil-pressboard interface creeping discharge is shown in Figure 4.17.

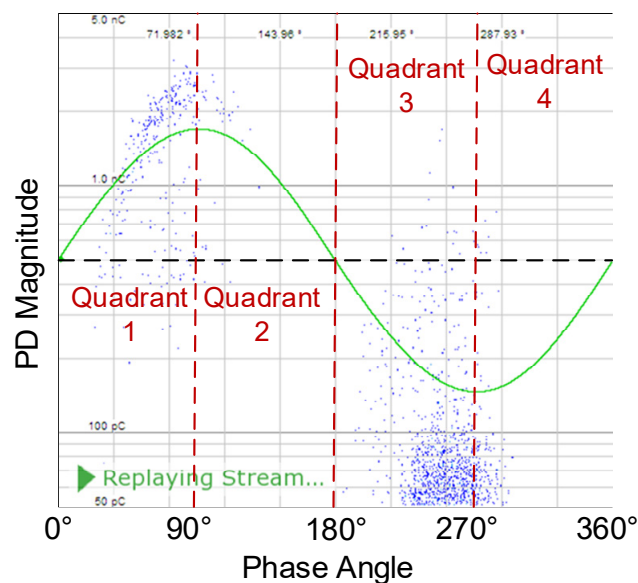


Figure 4.17 Typical PRPD pattern of oil-pressboard interface creeping discharge

The interface creeping discharges have a peculiar PRPD pattern. Firstly, the positive pulses are obviously larger in magnitude but smaller in density than negative ones. A great number of positive pulses exceeds 1 nC, whereas the overwhelming majority of negative pulses have magnitudes ranging from 50 pC to 500 pC. Positive pulses are recorded in both Quadrant 1 and Quadrant 2. More specifically, the repetitive positive pulses start at the phase angle around 20° and vanish around 120°. The magnitude of positive pulses rises with voltage level in Quadrant 1 and reaches the maximum near the positive crest (90°). Similarly, the negative pulses are found in both Quadrant 3 and Quadrant 4, ranging from around 200° to around 300°.

The PRPD of interface creeping discharges reminds one of the oil corona discharge and surface discharge. Their PRPDs are shown in Figure 4.18. As displayed, the positive pulses of oil corona discharge have comparatively great magnitudes and low intensity; whereas, the negative pulses have almost constant magnitudes. Besides, both positive and negative pulses are concentrated around the crest areas and span two quadrants. With respect to the surface discharge, either positive or negative pulses are confined within only 1 quadrant and vanish immediately after voltage crests. Moreover, the starting phase of surface discharge is smaller, and the repetitive positive pulses appear shortly after the voltage zero-crossing point. Therefore, it is inferred that creeping discharge is a multi-sourced discharge phenomenon that is composed of oil corona discharge and surface discharge.

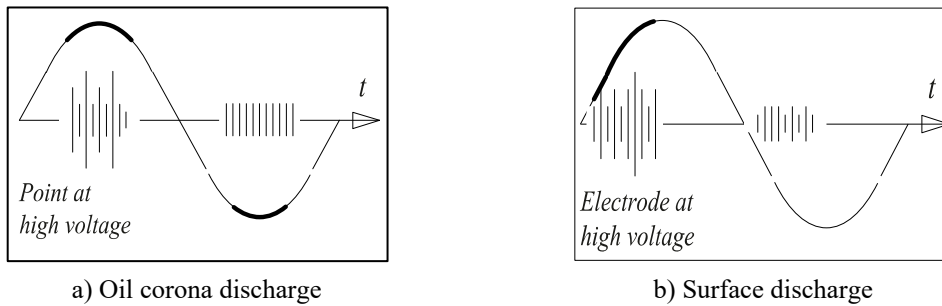


Figure 4.18 Representative PRPDs of typical PD types [153]

Furthermore, the PRPD pattern is found almost consistent with all samples, irrespective of the voltage level or pressboard conditions. The PRPDs of different samples versus voltage levels are presented in Figure 4.19 to Figure 4.21. For succinctness, only three time points (0 minute, 90 minutes, and 180 minutes), two samples (#00 and #60), and two voltage levels (30 kV and 34 kV) are selected for demonstrations.

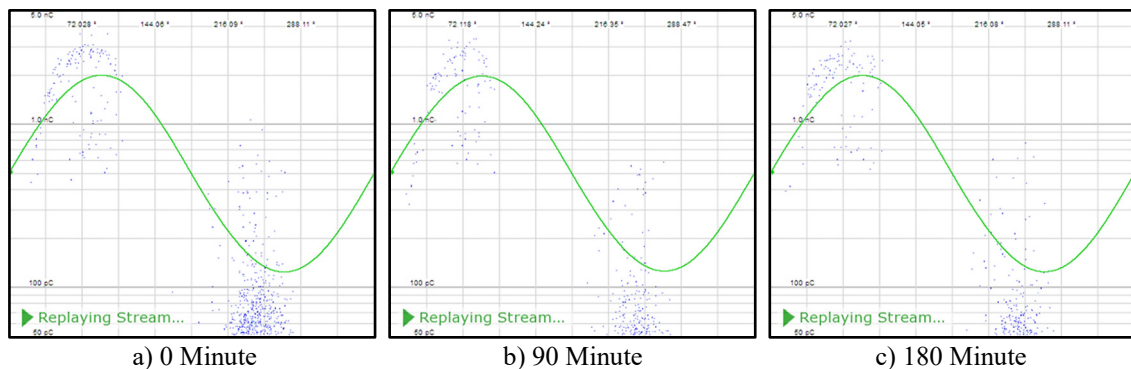


Figure 4.19 PRPD of sample #00 at 34 kV

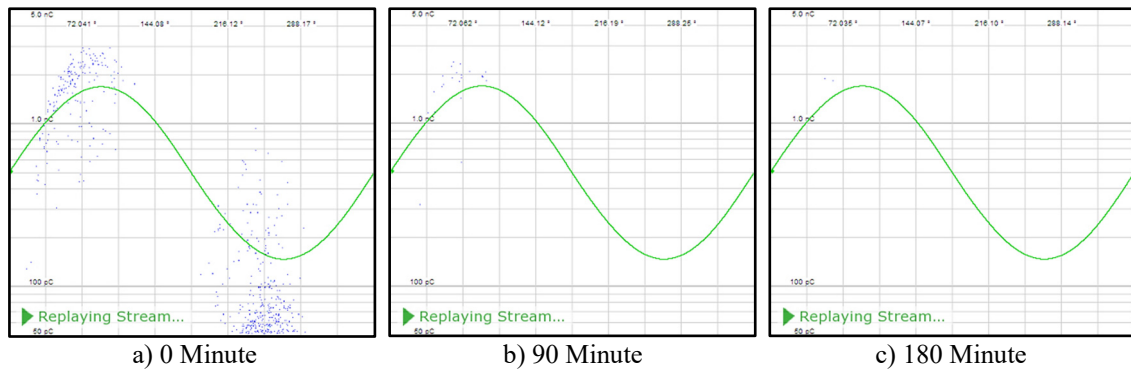


Figure 4.20 PRPD of sample #60 at 30 kV.

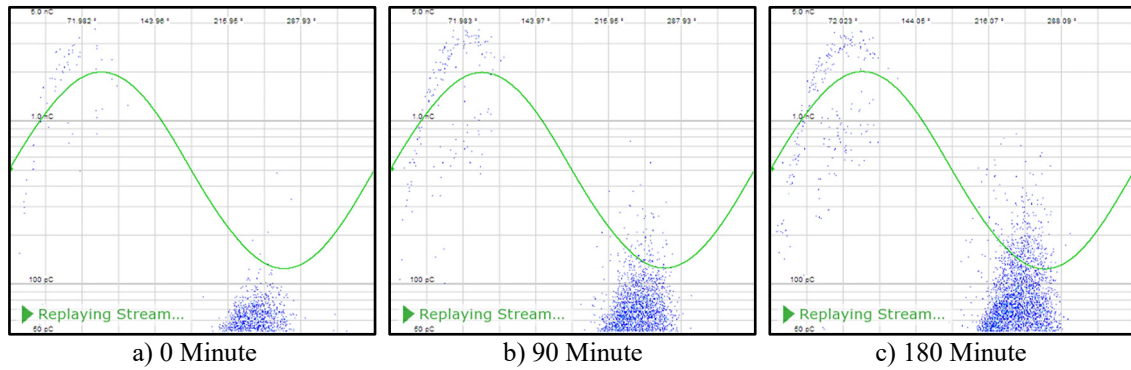


Figure 4.21 PRPD of sample #60 at 34 kV

The occurrence of partial discharge is jointly governed by an external electric field and a local electric field. The external field is determined by the applied voltage, geometrical dimension, and constituent materials; whereas, the local field is aroused by the accumulation of space charges inside the discharge site. The space charges, i.e., the charge carriers generated by previous discharge events, can build up a DC field that has a quite the opposite direction to the external field. The resultant DC field could cancel the external field and thus impeding the following discharges until the external field is raised high enough again to conquer the local field. Therefore, the partial discharges, especially for those within an enclosed space, exhibit a nature of intermittence.

Aiming to provide a better understanding of the physical process of partial discharges, pulse sequence analysis (PSA) emphasizes the roles of space charge and local field on initiating discharges. The basic principle of PSA is illustrated in Figure 4.22, where $\Delta\phi$ and Δu denote the phase difference and instantaneous voltage difference between consecutive discharges, respectively.

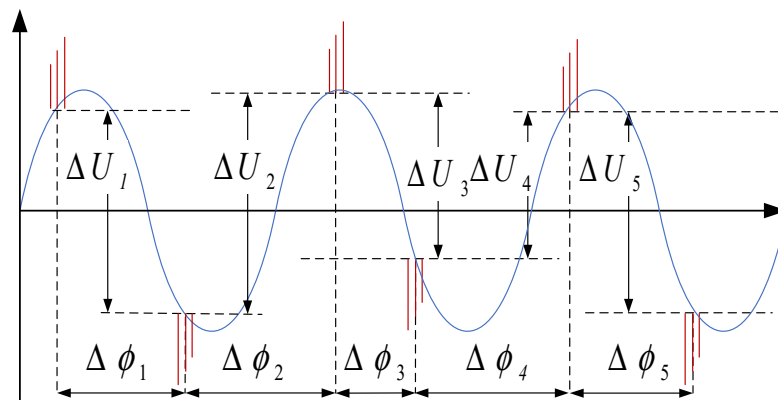


Figure 4.22 Basic principle of PSA method [154]

Several kinds of patterns can be made based on the statistical results obtained from Figure 4.22, among which the most commonly used ones are:

- $n-\Delta\varphi$ Histogram
where n denotes the counts and $\Delta\varphi = \Delta\varphi_{n+1} - \Delta\varphi_n$ ($\Delta\varphi > 0$);
- $\Delta U_n - \Delta U_{n-1}$ Pattern
where ΔU_n is the voltage difference between a specific PD pulse and its succeeding pulse and ΔU_{n-1} is the voltage difference between the PD pulse and its preceding one. The typical $\Delta U_n - \Delta U_{n-1}$ pattern of oil-pressboard surface discharge is shown in Figure 4.23;
- $\Delta\varphi_n - \Delta\varphi_{n-1}$ Pattern
where, $\Delta\varphi_n$ is the phase difference between a specific PD pulse and its succeeding pulse, and $\Delta\varphi_{n-1}$ is the phase difference between the PD pulse and its preceding one.

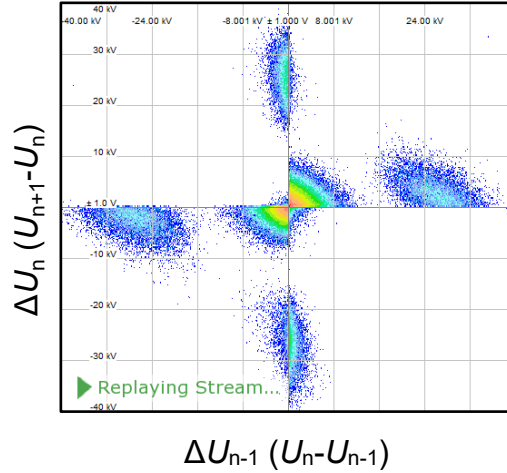
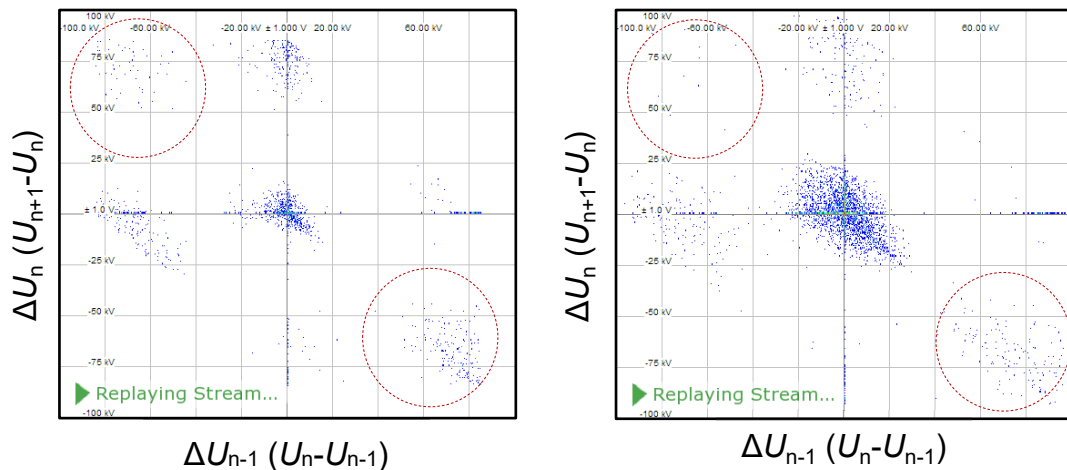


Figure 4.23 The typical $\Delta U_n - \Delta U_{n-1}$ pattern of oil-pressboard surface discharge

A number of examples regarding the above-listed patterns of typical partial discharge types can be found in [3]. The typical $\Delta U_n - \Delta U_{n-1}$ PSA pattern of oil-pressboard interface creeping discharge is given in Figure 4.24. For the sake of succinctness, only two images are presented.



a) Sample #00 at 30 kV (0 Minute)

b) Sample #60 at 34 kV (180 Minute)

Figure 4.24 Typical $\Delta U_n - \Delta U_{n-1}$ pattern of creeping discharge

As shown, no significant variations in $\Delta U_n - \Delta U_{n-1}$ patterns were found between samples #00 at 30 kV and #60 at 34 kV. It indicates that the partial discharge pattern of creeping discharge is independent of pressboard ageing, voltage level, and even test time. Moreover, a certain degree of similarity in the $\Delta U_n - \Delta U_{n-1}$ pattern can be found between creeping discharge and typical surface discharge; on the other hand, they are clearly distinguished from each other by the presence of some ‘peculiar’

discharges. The ‘peculiar’ discharges, located within the dashed circles in Figure 4.24, have great voltage differences to their neighboring discharges, almost double the voltage crest values, implying the consecutive pulses occur in opposite crests of applied voltages. This kind of discharge behavior is usually found in sharp point oil corona discharges [155].

In addition, the typical PSA $n-\Delta\varphi$ histograms of oil-pressboard interface creeping discharge are shown in Figure 4.25. As seen, the shape of the histogram has one peak at the center and two nearly symmetrical low crests aside. Through referencing the $n-\Delta\varphi$ pattern of typical single-sourced discharge types presented in [3], it is believed that the central peak could be ascribed to surface discharge and oil corona discharge combined, whereas the two low crests are solely caused by the surface discharge. Moreover, it suggests that the oil corona discharge is probably more susceptible to a voltage level rise than the surface discharge when one takes the difference between Figure 4.25 a) and Figure 4.25 b) into consideration.

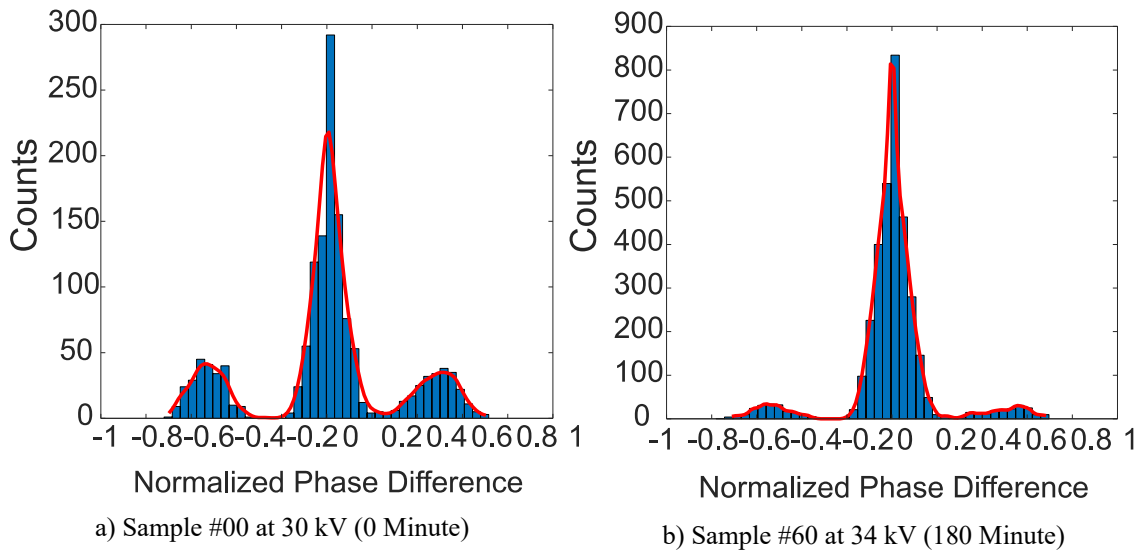


Figure 4.25 Typical $n-\Delta\varphi$ pattern of creeping discharge

The typical statistical distributions of interface creeping discharge are shown in Figure 4.26. Moreover, the temporal variations of PD statistical distributions are shown in Figure 4.27 to Figure 4.29. For succinctness, only sample # 60 at 34 kV is selected for demonstration.

The typical statistical distributions of interface creeping discharge are shown in Figure 4.26. The statistical distributions were made to explore the relations between phase and three PD quantities, i.e., the PD number ($H_n(\Phi)$), PD average magnitude ($H_{qn}(\Phi)$), and PD maximum magnitude ($H_{qmax}(\Phi)$), respectively. The statistical distributions and their derived statistical operators, such as skewness, kurtosis, phase asymmetry, discharge asymmetry, and cross-correlation factor, have been proven useful for PD identifications in practical applications. As a matter of fact, they have laid the very foundation of the PD diagnosis expert system in some commercial products [156–158].

In general, the shape of PD statistical distributions does not vary greatly with voltage level or pressboard ageing. In both cases, the center phases of positive and negative pulses are around 70° and 245° , respectively. The magnitude of positive pulse grows steadily with rising voltage value and reaches a peak around 90° ; on the contrary, it is hard to define the relationship between negative pulse amplitude and voltage instant value. Nevertheless, a minor difference is observed in respect of the starting phase of positive pulses. Repetitive positive pulses of sample #00 at 30 kV appear around 15° , whereas those of sample #00 at 34 kV appear immediately after the zero-crossing point.

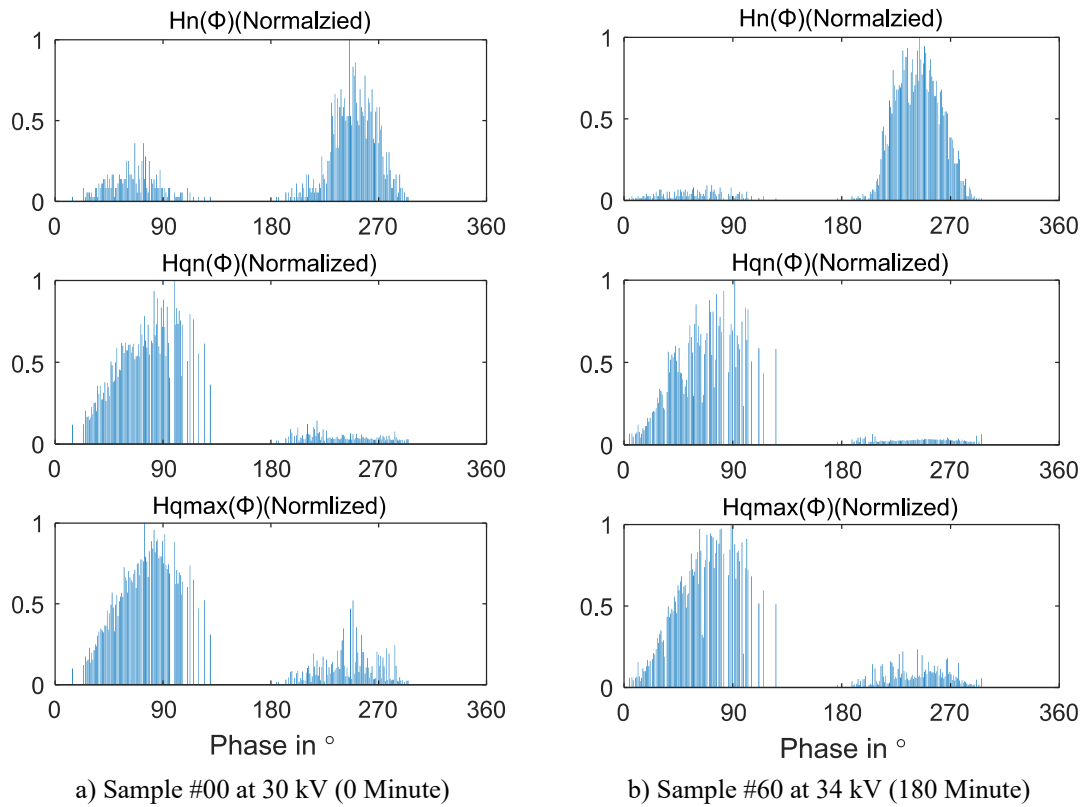


Figure 4.26 Typical PD statistical distributions of creeping discharge

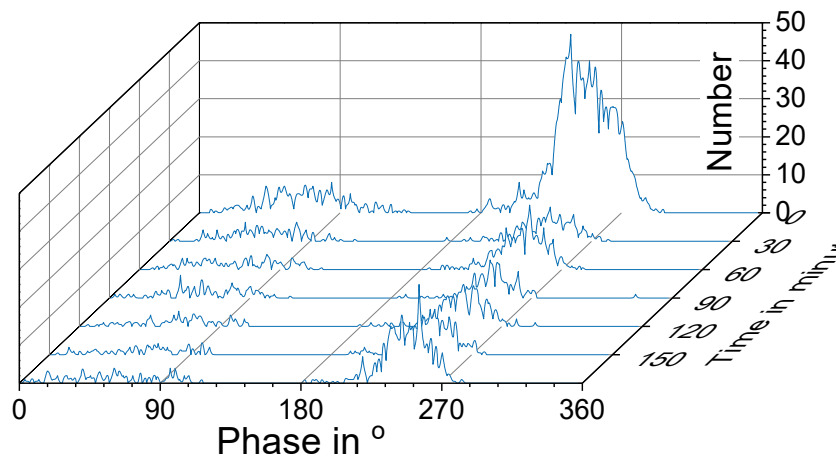


Figure 4.27 Temporal variations of PD number distribution ($H_n(\Phi)$)

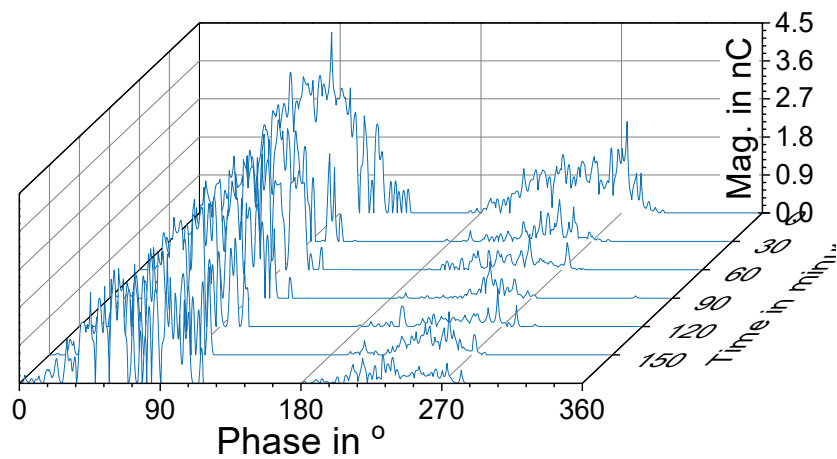


Figure 4.28 Temporal variations of PD maximum magnitude ($H_{qmax}(\Phi)$).

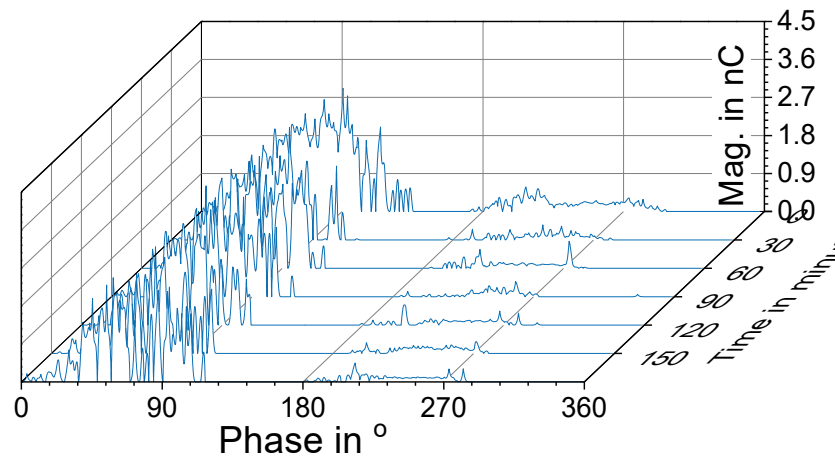


Figure 4.29 Temporal variations of PD average magnitude ($Hqn(\Phi)$)

4.4.2 PD Signal Analysis

In addition to the above-displayed patterns, the waveform of a PD pulse is also thought to be closely correlated to discharge nature. Pulse peak value, pulse rise time, pulse decay time, pulse width, and frequency spectrum are the most used parameters to characterize a PD signal in time-frequency domains [152, 159]. In this chapter, the time-domain PD signals were captured by an RLC type measuring impedance, and the sampling frequency is 64 MHz. Each single sampling period lasts for $32 \mu\text{s}$ and consists of 2048 sampling points. The typical waveforms of PD pulses of interface creeping discharges are shown in Figure 4.30. For a closer look at the pulse shape, the sampling points of no pulse information are omitted in the plot.

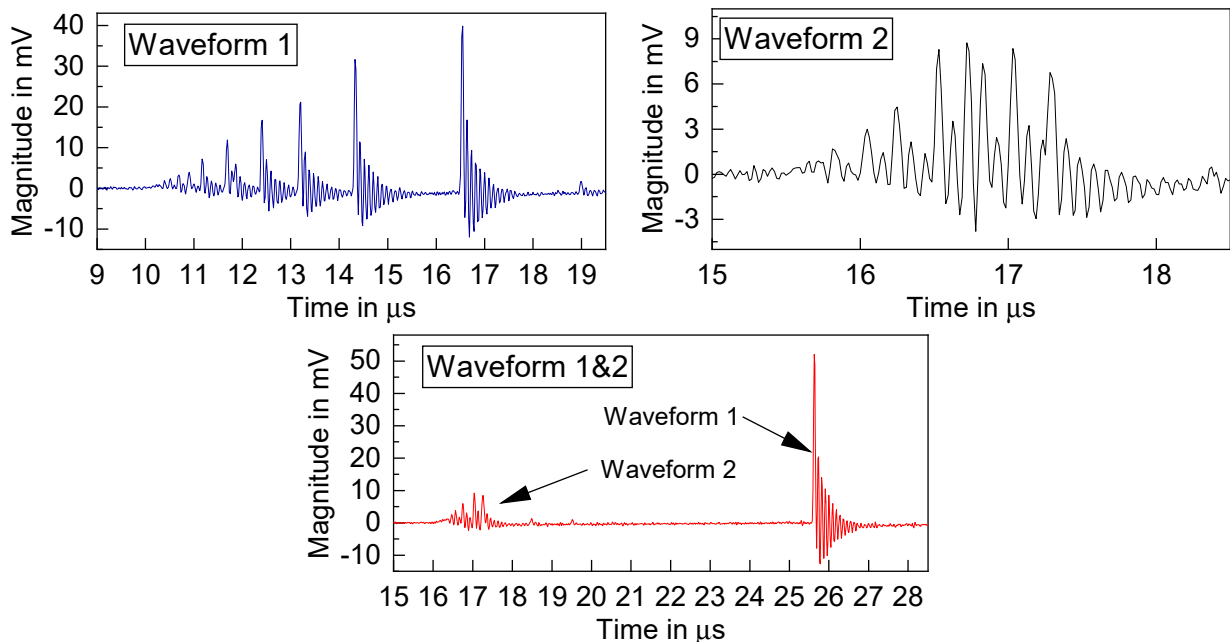


Figure 4.30 Typical waveforms of creeping discharge PD pulses

Two distinct PD waveforms were captured during interface creeping discharges. From top to bottom in Figure 4.30, it shows the PD Waveform 1, PD Waveform 2, and them both, respectively, in one sampling period. As seen, either Waveform 1 or Waveform 2 possesses a damped oscillatory shape, which is typical for the PD signals captured by an RLC circuit [160]. The Waveform 1 PD pulse usually occurs in a manner of the pulse train, and several PD pulses can be found in the same single sampling period. Moreover, the peak amplitudes of pulses increase steadily with time: from 6 mV of the first pulse to 36 mV of the last one in this case. With respect to PD Waveform 2, only one pulse

can usually be found in a single sampling period. Besides, compared with PD Waveform 1, the peak amplitude of Waveform 2 is much smaller: around 8 mV.

As stated previously, space charge has a significant role in initiating partial discharges. Regarding the PD pulses of Waveform 1, they are featured by the large-magnitude pulse trains, implying that the occurrence of PD pulse is barely inhibited by the space charges generated by preceding discharges. Therefore, the PD pulses of Waveform 1 are presumably attributed to the discharges in an open gap, where the space charges can be dissipated comparatively fast. On the contrary, the PD pulses of Waveform 2 are featured by the low-amplitude single pulse, implying a non-trivial impeding effect of space charges in the process. Therefore, the PD pulses of Waveform 2 are presumably attributed to the discharges in an enclosed or semi-enclosed space, where the space charges cannot be readily dissipated.

Moreover, the frequency-domain information of these two typical PD pulses is analyzed as well. However, it is of vital importance to implement signal de-noising prior to the frequency-domain analysis, as it is impossible for the recorded PD signals to be completely immune from the external interference even in a well-shielded test area. This chapter adopts the discrete wavelet transform (DWT) techniques to process the PD signals. The basic principle of DWT multi-scale signal decomposition (MSD) and relevant critical issues of de-noising are given in [160, 161]. In general, the process of DWT signal de-noising could be divided into three steps:

- Decomposing the original signal into approximation and detail coefficients

One should select the optimum mother wavelet and the appropriate decomposition levels n . Thereafter, the original signal is decomposed into approximation coefficients and detail coefficients to n levels. The approximation coefficients contain low-frequency components of the original signal, whereas the detail coefficients contain the high-frequency components;

- Thresholding the coefficients

Thresholding is carried out to the detail coefficients of all levels because noises are usually embedded in the high-frequency components. The critical issues in this step are the selections of the thresholding method and the threshold values for each level;

- Reconstructing signal using the processed coefficients

in this step, the de-noised signal is reconstructed using the approximation coefficient of the n th level and all the processed detail coefficients.

This thesis adopts Daubechies 8 (db8) as the mother wavelet, as it proves the best choice for the damped oscillatory PD pulse captured by an RLC impedance detector [162]. The wavelet function of db8 is shown in Figure 4.31.

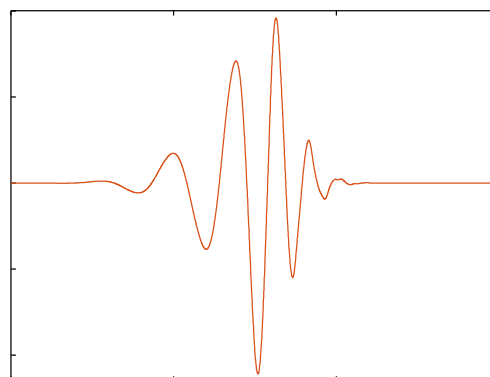


Figure 4.31 Wavelet function of db8

The technique of selecting the appropriate decomposition level is expressed as [163]:

$$J_{\max} = \text{fix} \left(\log_2 \left(\frac{n}{n_w} - 1 \right) \right) \quad (4.2)$$

where n is the length of the original signal, n_w is the length of the decomposition filter of the selected mother wavelet, and J_{\max} is the maximum decomposition level. In this case, n equals 2048 and n_w is 16 for mother wavelet db8. As a result, it begets that the maximum decomposition level is 6. Subsequently, 6-level db8 DWT decompositions are carried out to the PD pulses. The DWT decomposition coefficients of the PD signal of Waveform 2 are shown in Figure 4.32.

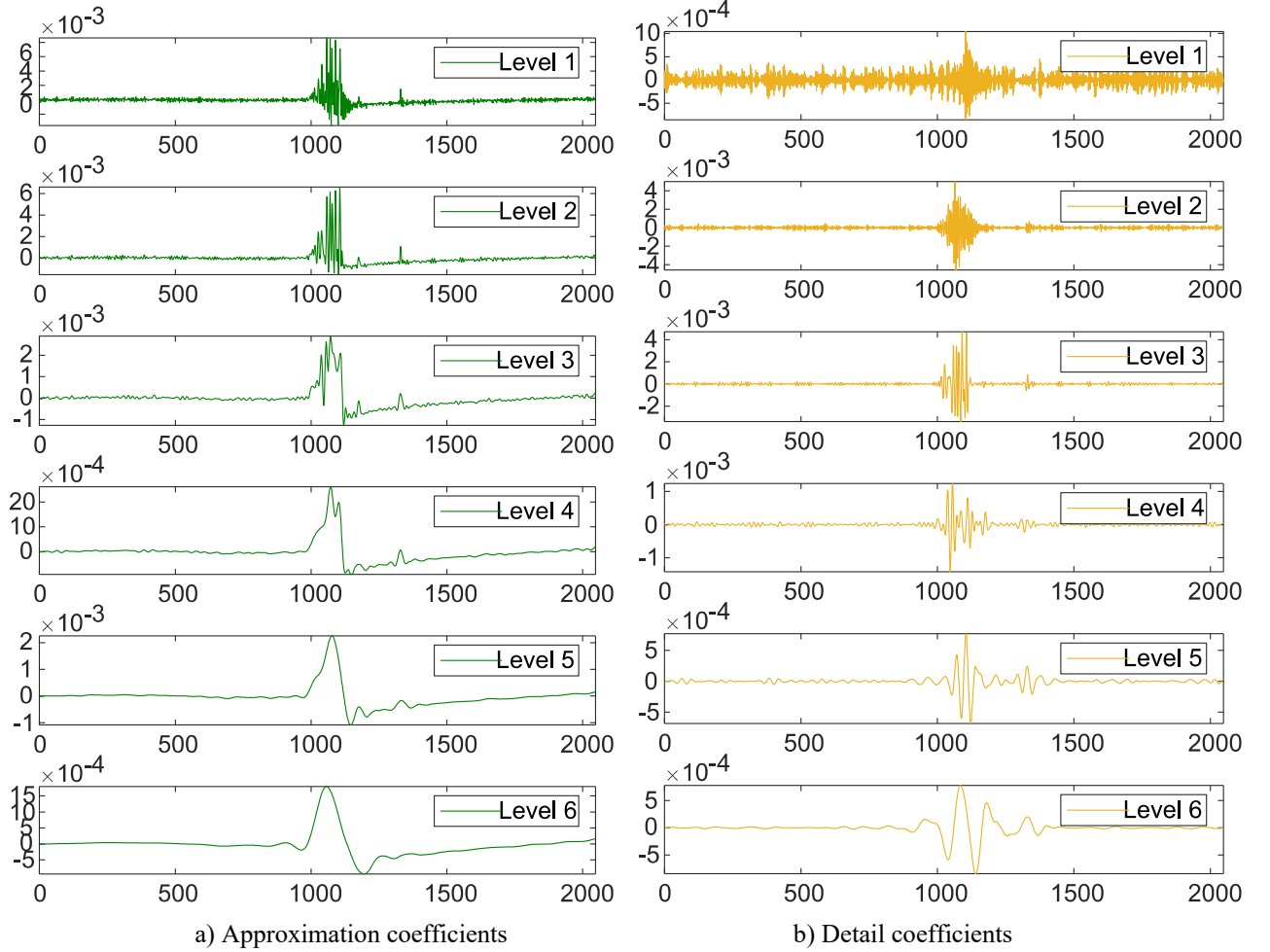


Figure 4.32 The DWT approximation and detail coefficients of Waveform 2 signal

Figure 4.33 displays the comparison between an original PD signal of Waveform 2 and its de-noised one. As displayed, the used DWT de-noising strategy is effective in excluding the external interferences, and in the meantime, can hold the essential information of the real PD pulses.

Lastly, the Fast Fourier Transform (FFT) algorithm was used to investigate the frequency information of the de-noised signals. The frequency spectra of the PD signals of Waveform 1 and Waveform 2 are shown in Figure 4.34 and Figure 4.35, respectively.

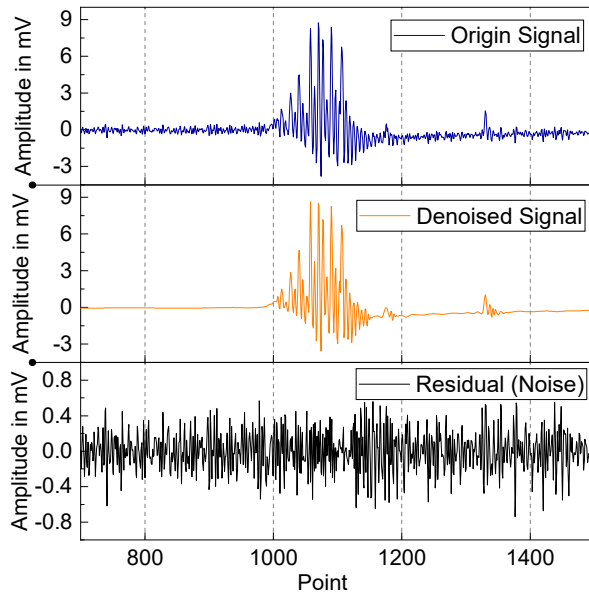


Figure 4.33 Comparison between original and de-noised Waveform 2 signal

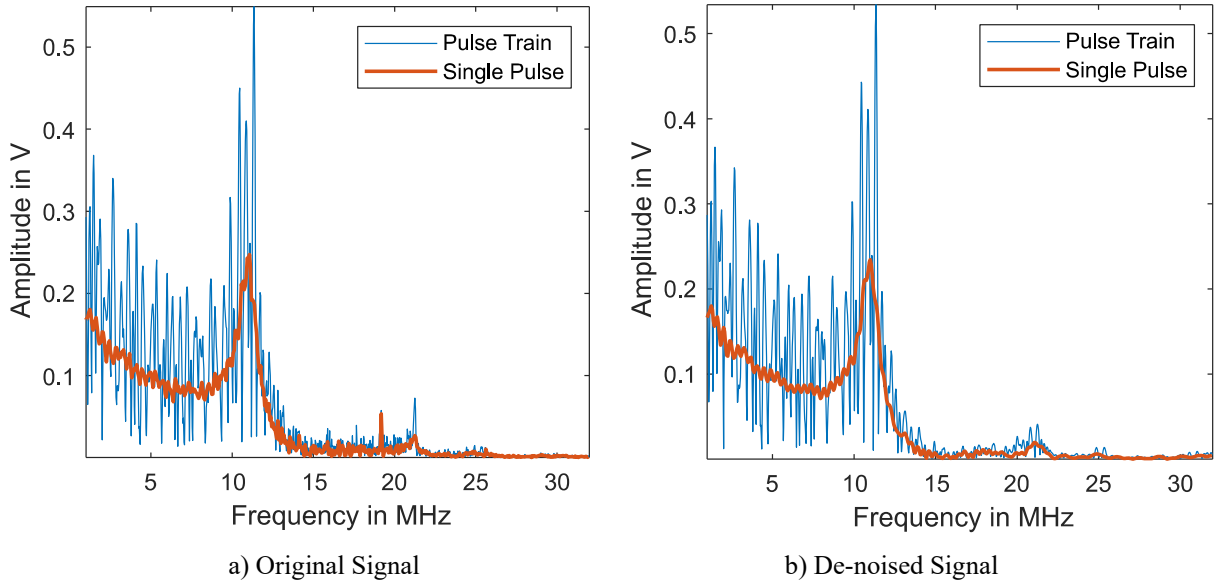


Figure 4.34 Frequency spectrum of waveform 1 PD signal

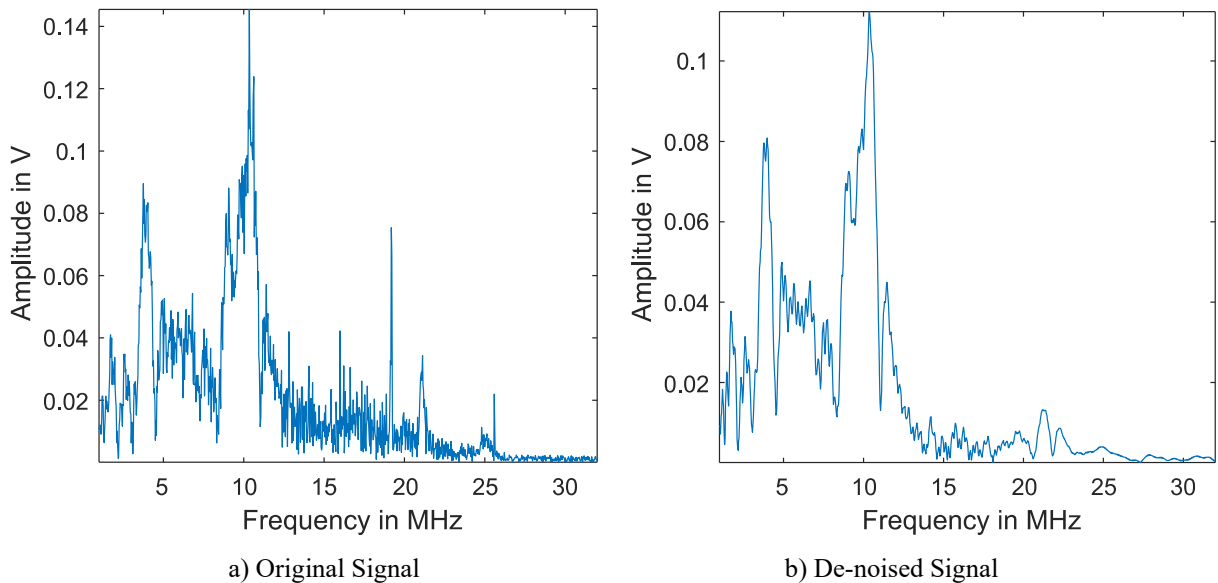


Figure 4.35 Frequency spectrum of waveform 2 PD signals

For the PD pulse Waveform 1, given that multiple pulses exist in one sampling, the frequency spectra of both pulse train and single pulse were analyzed. With respect to the Waveform 1 PD signal, the shape of its frequency spectrum is comparatively simple: a major peak is located at 11 MHz and a much smaller peak is located at 21 MHz. Besides, the resonant effect of multiple pulses is quite evident in the low-frequency regions. For the Waveform 2 PD signal, its frequency components are more complicated than those of Waveform 1. Multiple peaks are found in its frequency spectrum. In terms of amplitude, those peaks can be organized in descending order: 10.3 MHz, 4 MHz, 9 MHz, 11.5 MHz, and 21.3 MHz.

4.4.3 Partial Discharge Quantities

The following PD quantities are investigated in this section [135]:

- the pulse repetition rate of positive/negative pulse n^+/n^- :

$$n = \frac{\text{Number of Recorded PD Pulses}}{T_{\text{ref}}} \quad (4.3)$$

where T_{ref} denotes the chosen reference time interval and T_{ref} is 180 s.

- the average magnitude of positive/negative pulse q_a^+/q_a^- :

$$q_a = \frac{\sum_1^i q_i}{\text{Number of Recorded PD Pulses}} \quad (4.4)$$

where q_i denotes the individual apparent discharge magnitude.

The PD repetition rates n^+/n^- versus voltage levels are shown in Figure 4.36 to Figure 4.38. At 30 kV, creeping discharges would be weakened with test time irrespective of pressboard conditions. In particular, the negative pulse repetition rate n^- of all samples are almost halved within the first 30 minutes. Afterwards, the PD repetition rates decline at a comparatively slow pace and almost vanish at the end of the test. Moreover, the influence of pressboard ageing on PD repetition rate is only manifested at the initial stage of discharges: the repetition rates of the #60 sample are significantly greater than those of others.

Compared to those at 30 kV, the positive pulse repetition rates n^+ get slightly greater whereas the repetition rates of negative PD n^- at the initial discharge stages become smaller at 32 kV. Moreover, the voltage increment can change the creeping discharge behaviors of massively aged samples. Specifically, the PD repetition rates of the massively-aged samples, i.e., # 40 sample and # 60 sample, are no longer vanished at the end of the test. Instead, after steep drops within the first 30 minutes, both n^+ and n^- of sample # 60 stays somewhat stable and fluctuates with time. However, the creeping discharge behaviors of samples #00 and #20 still tend to diminish with time.

At 34 kV, the repetition rates of negative PD pulses n^- are increased remarkably, whereas the repetition rates of positive pulses n^+ do not vary much. Moreover, similar to the scenarios at 32 kV, the creeping discharges can be sustained with the massively aged samples but diminish with the new and slightly aged sample.

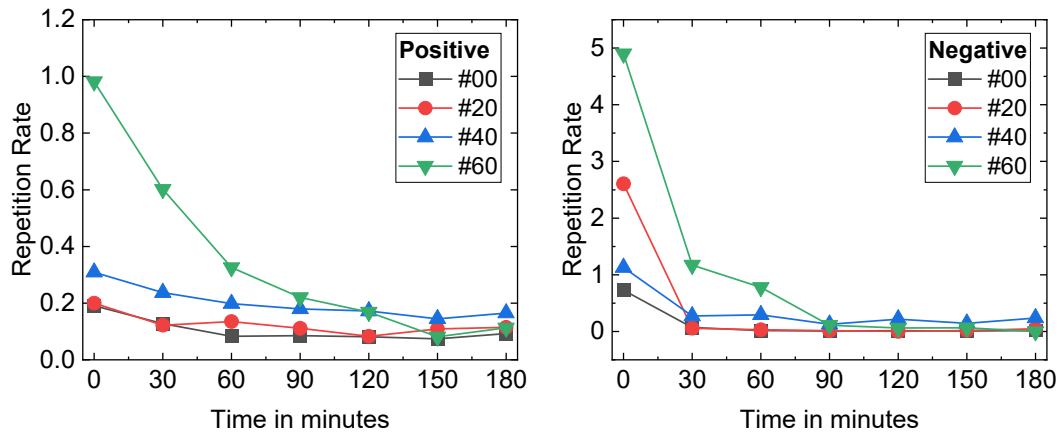


Figure 4.36 PD repetition rate at 30 kV

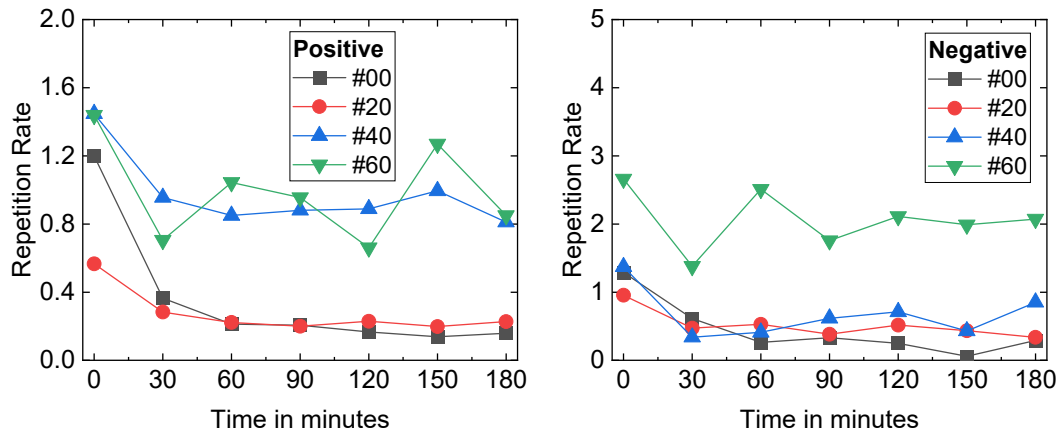


Figure 4.37 PD repetition rate at 32 kV

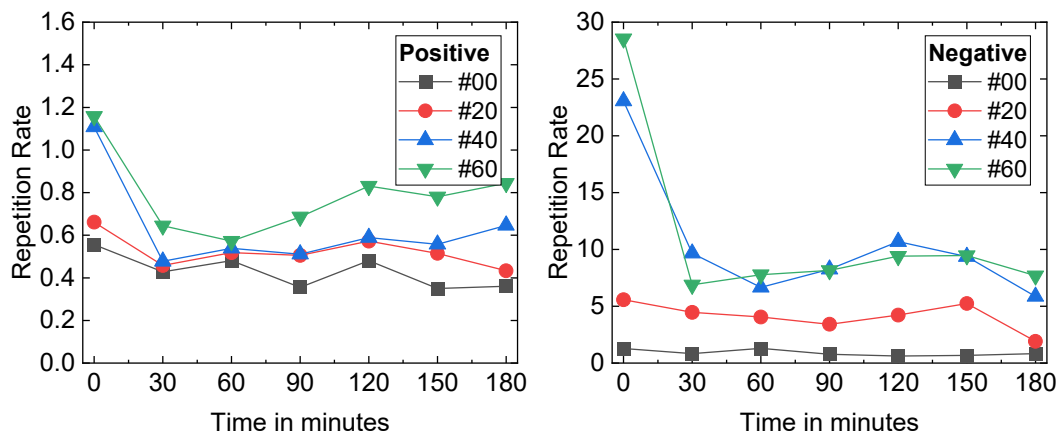


Figure 4.38 PD repetition rate at 34 kV

The PD average magnitudes q_a^+/q_a^- of varyingly aged samples are shown in Figure 4.39 to Figure 4.41. Firstly, at each level of voltage level, the average magnitudes of positive pulses q_a^+ are remarkably higher than their negative counterparts q_a^- , irrespective of ageing degree. Secondly, the influence of pressboard ageing on PD magnitudes is hardly discernible. At any voltage level, the average discharge magnitudes of all samples, either positive or negative, are approximate to each other. Thirdly, the influence of voltage level on PD magnitude is very limited as well. For each sample, either positive or negative PD discharges exhibit no significant variations with voltage levels.

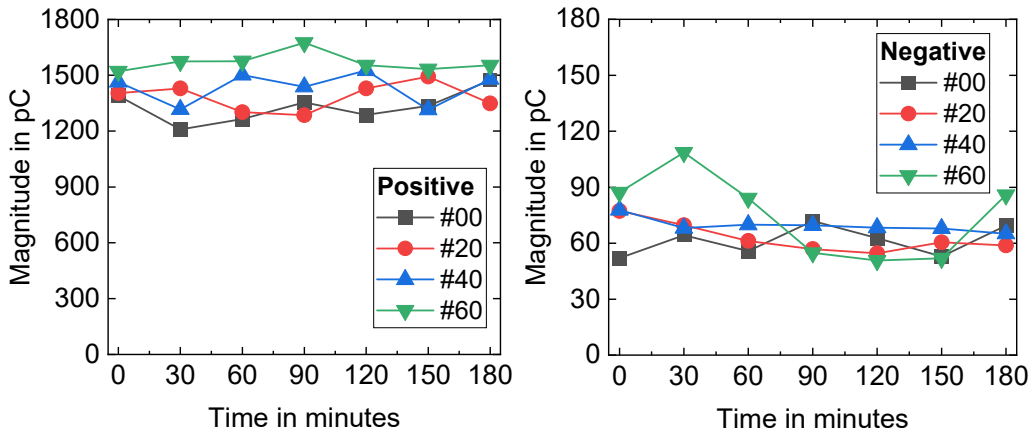


Figure 4.39 PD magnitude at 30 kV

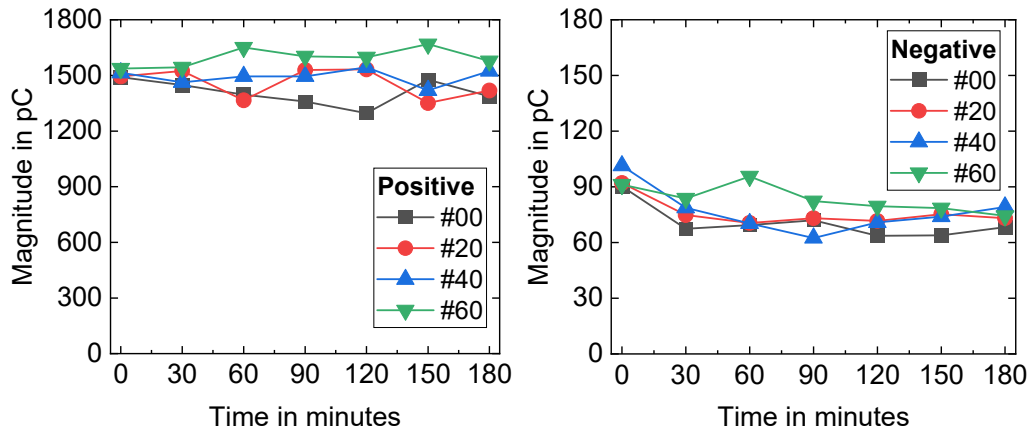


Figure 4.40 PD magnitude at 32 kV

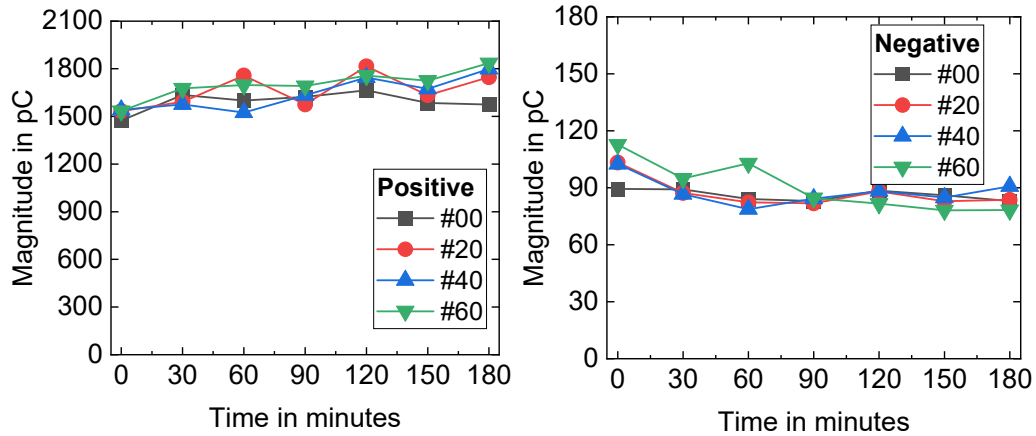


Figure 4.41 PD magnitude at 34 kV

The results of PD quantities reveal important traits of interface creeping discharges. At first, the creeping discharges, if not resulting in pressboard tracking, would be gradually weakened with test time, especially within the first 30 minutes after PD inception. At second, the discharge activities of massively aged pressboards (# 40 and # 60) can be sustained at relatively low levels under a strong field (32 and 34 kV). However, the discharge activities of new and slightly aged pressboards (# 00 and # 20) almost vanish, irrespective of voltage levels. At third, both voltage level and pressboard ageing can influence the PD repetition rates, but neither of them exhibits obvious effects on PD average magnitudes. At last, negative discharges appear highly susceptible to voltage rise, especially for those of the massively-aged pressboard samples. It suggests the intense negative discharges are probably the major cause of sustained discharges of massively aged pressboards under strong fields.

4.4.4 Interface Temperature and Gas Analysis

The temporal variations of pressboard surface temperature during creeping discharge have been obtained through optic fiber thermal sensors. The test facility and the test setup were illustrated in Section 3.4.10. An additional optic fiber thermometer was located in oil bulk to provide a benchmark for temperature investigations. For example, the temporal temperature variations of sample # 60 at 32 kV are shown in Figure 4.42. The temperatures of both interface and oil bulk were sampled for every 1 second in this case.

The temperature of either interface or oil bulk varies very limitedly during creeping discharges, regardless of the voltage levels or ageing degrees. As displayed, for different locations, the trends of temperatures variations are quite approximate to each other, indicating the temperature changes are merely due to environmental factors and independent of the discharge process.

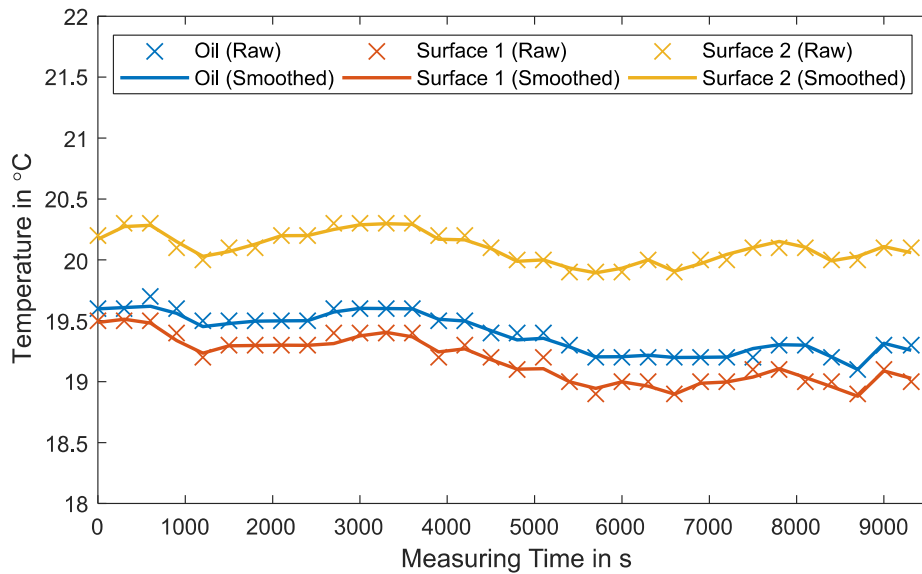


Figure 4.42 Interface temperature variations during creeping discharge (#60, 32kV)

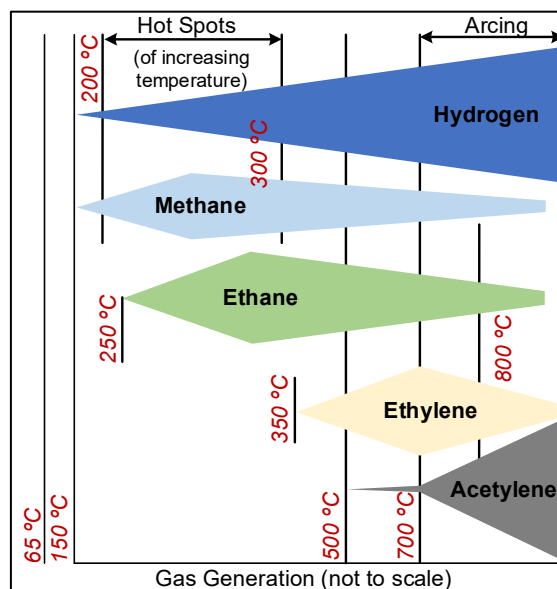


Figure 4.43 Hydrocarbon gas evolution in transformer oil [164]

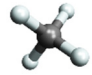
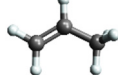
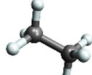
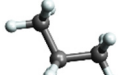
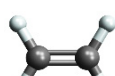



The principal causes of gas formation in oil-filled equipment are electrical discharges and heat. Each kind of dissolved gases can be correlated with specific discharge phenomena, temperature ranges, and discharge locations. The hydrocarbon gas evolution in transformer oil is schematically illustrated

in Figure 4.43. In addition to the hydrocarbon gases from oil deterioration, the decomposition of cellulosic materials generates carbon monoxide (CO) and carbon dioxide (CO₂), which are eventually dissolved in oil as well.

Eight oil-dissolved gases were analyzed in the thesis, as listed in

Table 4.1. The oil samples were taken every 3 hours, and two measurements were made for each sample to obtain the average values. The concentrations of oil-dissolved gases were analyzed using gas chromatography. The test facility and measuring techniques were illustrated in Section 3.4.9. The results are shown in Figure 4.44 to Figure 4.46.

Table 4.1 List of investigated gases

Name	Formula	Molecular Plot	Name	Formula	Molecular Plot
Methane	CH ₄		Propylene	C ₃ H ₆	
Ethane	C ₂ H ₆		Propane	C ₃ H ₈	
Ethylene	C ₂ H ₄		Carbon Monoxide	CO	
Acetylene	C ₂ H ₂		Hydrogen	H ₂	

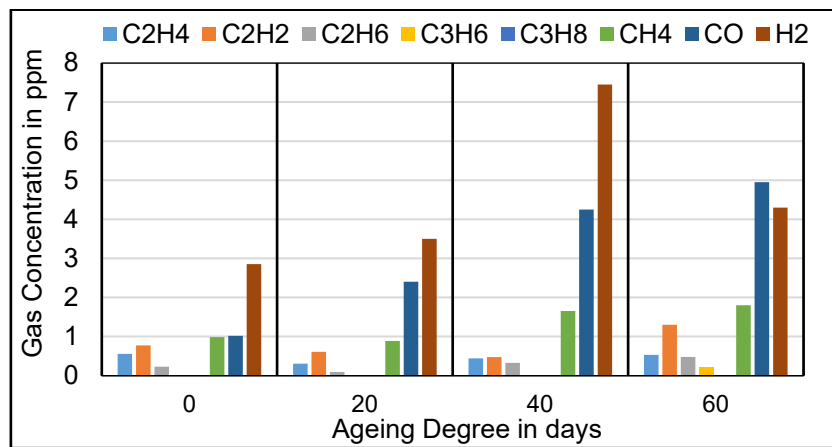


Figure 4.44 Gas concentrations at 30 kV

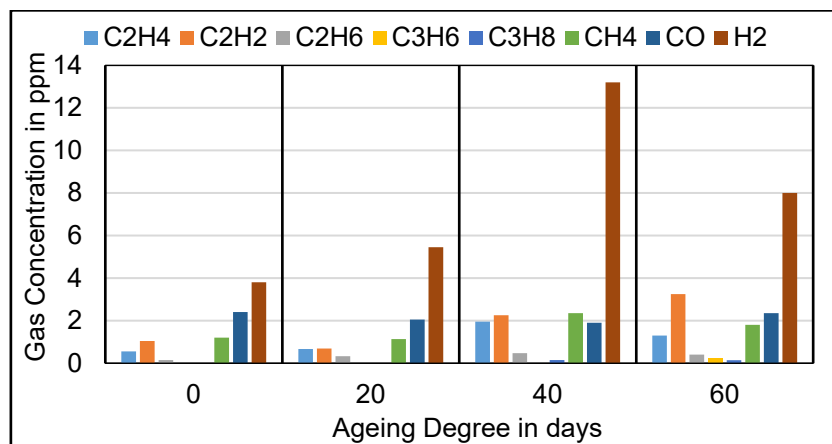


Figure 4.45 Gas concentrations at 32 kV

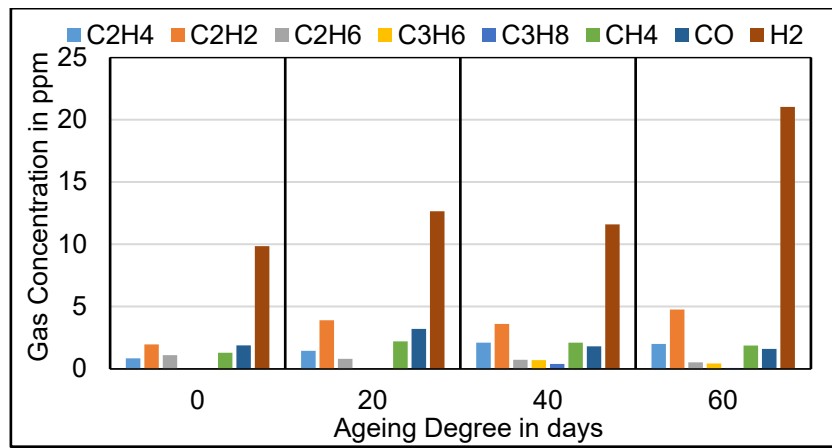


Figure 4.46 Gas concentrations at 34 kV

In spite of the low gas concentrations due to short discharge times, some remarks can still be made based on the findings. At first, the most indicative gas of interface creeping discharge is hydrogen (H_2), and the concentrations of hydrogen (H_2) of all samples grow in general with voltage levels. As known, hydrogen (H_2) is the principal gas of partial discharge in oil [165]. Therefore, it is inferred that oil corona discharges are the major parts of interface creeping discharges, and they are probably enhanced by voltage increment.

Another two noticeable gases are carbon monoxide (CO) and acetylene (C_2H_2). The presence of carbon monoxide (CO), a gas coming solely from cellulosic material, indicates the degradation of pressboards during interface creeping discharges. However, the concentrations of carbon monoxide (CO) at higher voltages are quite low, appearing independent of voltage level and pressboard ageing degree. Acetylene (C_2H_2), as a highly unsaturated hydrocarbon, is a representative gas of high-energy discharge activities. It is detected in all samples at each voltage level, and its concentration exhibits a positive correlation with voltage level. The result suggests the interface creeping discharges contain possibly high-energy discharge events, which will be intensified by raising voltage levels.

Besides the concentration of individual gas, the quantity of total dissolved combustible gases (TDCG) can also be used to assess the general gassing tendency of insulating materials. The combustible gases are defined in IEEE Std C57.104-2008 [165] and enlisted in

Table 4.2.

Table 4.2 List of combustible gases

Name	Formula	Name	Formula
Methane	CH_4	Acetylene	C_2H_2
Ethane	C_2H_6	Carbon Monoxide	CO
Ethylene	C_2H_4	Hydrogen	H_2

The results are shown in Figure 4.47. As displayed, the concentration of TDCG grows in general with rising voltage levels, indicating the entire discharge activities of creeping discharge have been enhanced by voltage increments. At the same voltage level, moreover, a coarse positive correlation between TDCG and pressboard ageing degree is also witnessed, which implies the promoting effects of thermal ageing on creeping discharge.

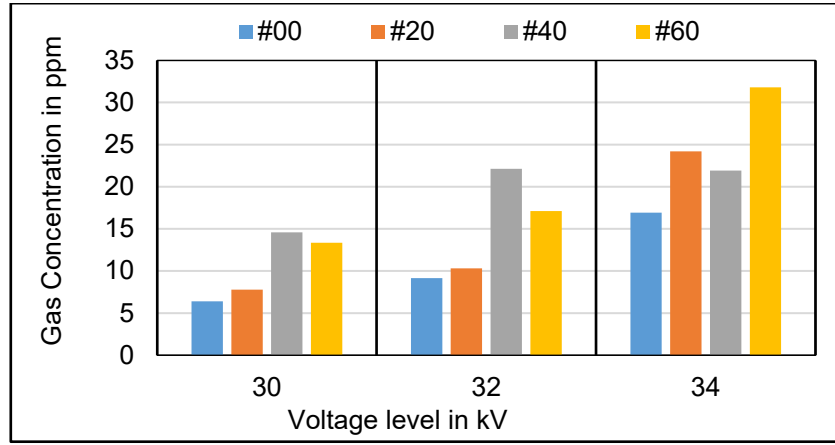


Figure 4.47 Concentrations of total dissolved combustible gases

To fulfill a fault diagnosis via DGA, one must select an appropriate method to interpret the measurement results. The existing interpretation methods of DGA results can be sorted into two broad categories: conventional methods and computational intelligence methods. Overviews of the conventional DGA interpretation methods are given in [143, 166]. The computational intelligence methods can be further divided into two sections: traditional artificial intelligence methods and data-driven statistical learning methods. In spite of the high performances of various methods as proclaimed by the authors, some fundamental issues, such as the class imbalance of training dataset and the generalization capability of classification models, shall be addressed with more care. A critical review of the existing statistical methods related to DGA analysis is given by Mirowski and Yann LeCun [167], in which 15 standard statistical learning algorithms are tested and evaluated.

This chapter adopts the classical Duval’s Triangle Method for DGA results interpretation, owing to its intuitive graphical illustration form and proven applicability in practice. The Duval’s triangle is essentially a clockwise ternary plot, in which the percentages of three hydrocarbon gases, i.e., acetylene (C_2H_2), methane (CH_4), and ethylene (C_2H_4), are analyzed. Accordingly, the coordinates of Duval’s triangle represent the respective percentage of each individual gases and can be obtained as follows [168]:

$$\begin{aligned} \%C_2H_2 &= \frac{100x}{x + y + z} \\ \%CH_4 &= \frac{100y}{x + y + z} \\ \%C_2H_4 &= \frac{100z}{x + y + z} \end{aligned} \quad (4.5)$$

where, x , y , and z stand for the absolute concentrations of acetylene (C_2H_2), methane (CH_4), and ethylene (C_2H_4), respectively.

The Duval’s Triangle for DGA interpretation of interface creeping discharges is shown in Figure 4.48. The plot is constructed using Origin[®] based on the coordinates given in [164]. As shown, all the diagnosis results are scattered around the D1/D2 zone edge. More specifically, a part of discharges is interpreted as low-energy discharges and the other as high-energy discharges. The scenario of creeping discharges is similar to those of tracking and sparking discharge, as presented in [169]. However, no identifiable trace of carbonization was found on the surfaces of all pressboard samples.

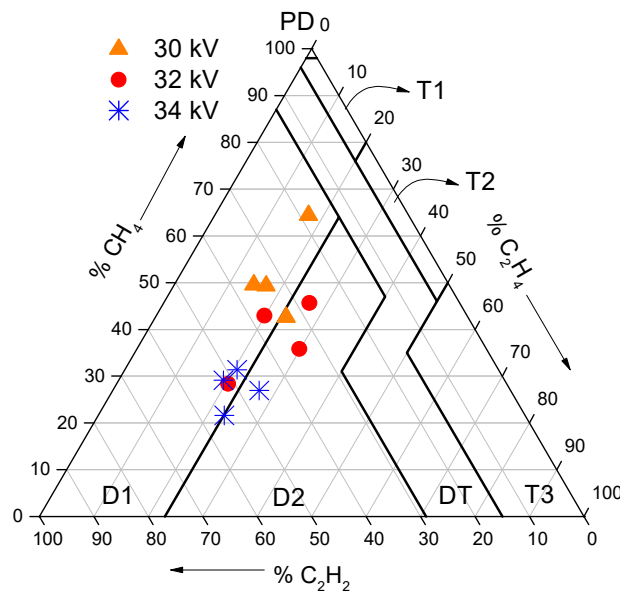


Figure 4.48 Duval's Triangle for interface creeping discharge

4.5 Conclusions

This chapter sets out to better understand the nature of interface creeping discharge as well as the influences of pressboard thermal ageing and voltage level on its long-term behaviors. At first, the influences of thermal ageing on pressboard properties and interface short-term electric strength were studied. Afterwards, FEM simulations were employed to investigate the interface field distributions versus voltage levels. Subsequently, the nature of interface creeping discharge was comprehensively studied. At last, the influences of pressboard ageing and the voltage level on creeping discharges were examined at a large time scale. Based on the obtained test results, the following conclusion can be drawn from the present study:

- Progressive creeping discharge is a compound discharge phenomenon that exhibits peculiar discharge patterns and various discharge signals. Oil corona discharge and surface discharge are believed to be the major discharge sources. Moreover, it is a highly localized discharge phenomenon that mainly concentrates around the triple-junction area. Pressboard ageing affects the inception voltage of creeping discharges but has no influence on the interface breakdown strength.
- The damage-free progressive creeping discharge exhibits a constant PRPD pattern but a diminishing PD intensity with time. At its inception stage, the PD repetition rates are positively correlated with both voltage level and pressboard ageing, whereas the average PD magnitudes are rarely affected by these factors. The long-term behaviors are jointly determined by voltage level and pressboard ageing. For new and slightly aged pressboards, the creeping discharges almost vanish with time at any voltage level. On the contrary, for massively-aged pressboards, the creeping discharges can be sustained under a strong field due to the intensified negative discharges.
- No significant temperature variations on the pressboard surface are observed during the damage-free progressive creeping discharge. Hydrogen is the principal indicative oil-dissolved gas, and its concentration is positively correlated with voltage level and pressboard age degree. Trace concentrations of carbon monoxide and acetylene are also detected. The damage-free creeping discharge is located around the edge regions between fault zones D1

and D2 in the classical Duval's Triangle.

- The general diminishing trend of damage-free progressive creeping discharge could be caused by the interface moisture migration. The aged pressboard sample has a greater moisture content; therefore, its discharge activities can be sustained at a certain level. The intensified negative discharges for massively-aged pressboard under stronger fields are probably facilitated by the pressboard surface moisture as well as the electrode electron emissions due to permittivity mismatch and triple-junction effect.

5 TRACKING PHENOMENA OF AC CREEPING DISCHARGES

5.1 Introduction

Chapter 4 focuses on the fundamentals of interface creeping discharges as well as the effects of critical influential factors. It is revealed that interface creeping discharges tend to diminish with time and are sustained only with massively-aged pressboards under strong fields. However, no creeping discharge-induced insulation failures are reported thus far. In reality, the real hazard of interface creeping discharge lies in the fact that it could generate permanent damages to the pressboard. In general terms, the resultant damages to the pressboard fall into two broad categories: surface tracking and internal treeing. In both cases, carbonized conductive paths are formed and thus leading to transformer major insulation failures. For different damages, their developmental processes, accompanying phenomena, and physical mechanisms are greatly varied from each other. As a consequence, the oil/pressboard insulation could eventually fail in different manners.

However, the current knowledge of these faults is hardly satisfactory. Up to now, they are still considered as one of the least understood phenomena pertinent to transformer insulation systems, the internal treeing in particular. This is largely due to the fact that the development of internal treeing is a highly intricate process, which involves multiple materials and features several physical phenomena. Aiming to have a thorough exposition of relevant issues, this chapter carries out systematic and in-depth investigations of both surface tracking and internal treeing. Using various characterization means, their initiation conditions, developments, and final failures are comparatively studied. Moreover, the underlying mechanisms and inter-relations of their accompanying phenomena are discussed in detail. Lastly, a tentative monitoring scheme of pressboard internal treeing is proposed.

This chapter is subdivided into six sections. Section 5.2 gives a detailed analysis of the internal treeing phenomenon. Section 5.3 revisits the accompanying processes of internal treeing and proposes several governing mechanisms. Section 5.4 reports the investigation results of the surface tracking phenomenon and summarizes the comparison between internal treeing and surface tracking. Section 5.5 discusses the obtained results and presents a tentative monitoring and detection methodology of internal treeing. Section 5.6 gives the concluding remarks of this chapter.

5.2 The Internal Treeing Phenomenon

Chapter 4 reported that oil/pressboard interface discharges tend to diminish with time and are sustained only with massively aged pressboards under strong fields. Under certain circumstances, the sustained creeping discharge can trigger a dangerous phenomenon, i.e., the internal treeing of the pressboard. The failure statistics of the tests carried out in Chapter 4 are summarized in Table 5.1.

On the one hand, the internal treeing is definitely a threshold phenomenon that occurs only to # 60 sample under 34 kV. On the other hand, the occurrence of internal treeing is also an issue of probability: there are in total eight specimens of #60 sample stressed under 34 kV, and only three of them are found to have internal treeing. Moreover, no surface tracking incident is observed in all the tests of Chapter 4. The following paragraphs report the internal treeing phenomena as well as their corresponding discussions.

Table 5.1 Failure statistics of normal pressboard samples

Sample	Surface tracking	Internal treeing	Time-to-Failure
New	No	No	Greater than 180 minutes
#20	No	No	Greater than 180 minutes
#40	No	No	Greater than 180 minutes
#60	No	No below 34 kV	Greater than 180 minutes
		Yes at 34 kV	Within 1 hour

5.2.1 General Information on Internal Treeing

The development of the internal treeing process, from the inception of discharges to the final breakdown event, can be divided into six consecutive stages. Its full process, stage division criteria, and concomitant phenomena are schematically illustrated in Figure 5.1. Moreover, Figure 5.2 shows a series of video snapshots of an internal treeing incident, where the two yellow stick-like objects on the pressboard surface are optic fiber thermal sensors.

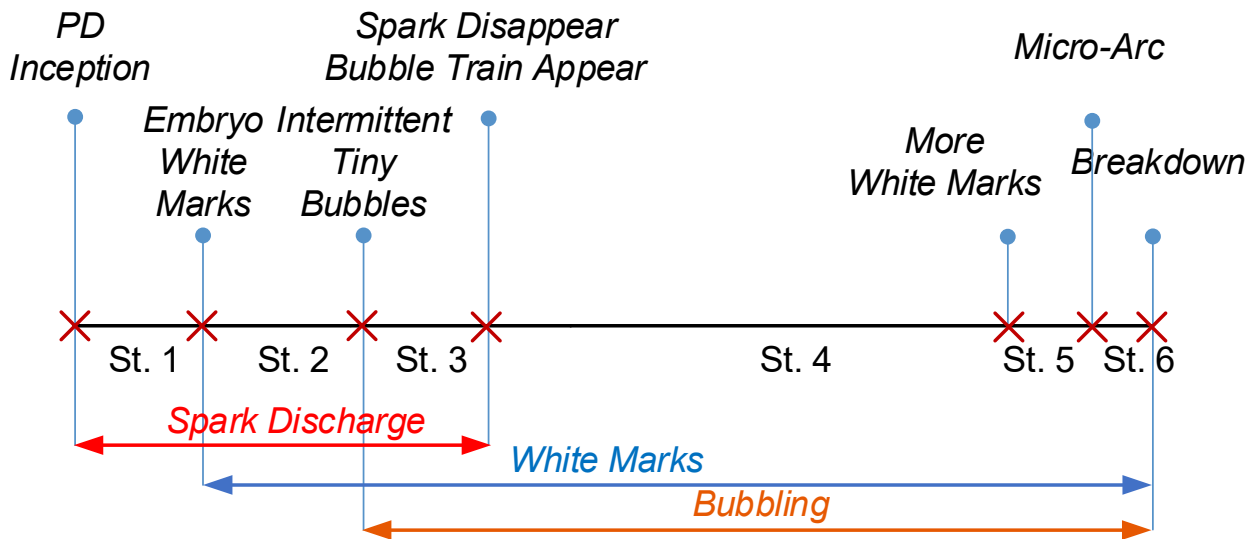


Figure 5.1 Full process, stage divisions, and concomitant phenomena of internal treeing

Stage 1 (St. 1) starts from discharge inception and ends when the first white marks emerge. In Stage 1, no particular phenomena except strong spark discharges are found. The discharge pattern is almost the same as that elaborated in Section 4.4.1, except that the discharge repetition rate is obviously higher.

The appearance of embryo white marks around the tip needle marks the beginning of Stage 2 (St. 2), as shown in Figure 5.2 b). In stage 2, strong spark discharges at the needle tip still exist (see Figure 5.2 c)), and no bubbles are observed.

Stage 3 (St. 3) starts when the first identifiable bubbles come in appearance, as shown in Figure 5.2 d). In this stage, some tiny bubbles are emitted from the pressboard surface. Nevertheless, the bubble emission occurs in an intermittent manner, and the bubbles in oil are either collapsed or driven away from the needle tip. Obvious spark discharge is maintained in Stage 3 as well.

Stage 4 (St. 4) begins with a sudden extinction of the spark discharge, which is coincident with an abrupt expansion of the embryo white marks. In this stage, a severe bubbling effect comes into emergence. Trains of bubbles are emitted from the periphery areas of white marks and steadily rise upwards. As the white marks expand quickly towards the grounded electrode, ever more trains of

bubbles are generated. Besides, some smog is also found in the middle areas of white marks. The initial bubble train, the expansion of white marks, and the smog are shown in Figure 5.2 e), f), and g), respectively.

Stage 5 (St. 5) has no essential difference from Stage 4 (St. 4). Nevertheless, a distinction can still be made considering the number of white marks. In Stage 4 (St.4), the expansion of white marks is realized by augmentation of the embryo white marks, whereas in Stage 5 (St. 5), new white marks emerge on surface locations that are certainly distant from the ever-augmenting embryo white marks.

Stage 6 (St. 6) signals the imminent breakdown event, as some micro-arcs are observed. These micro-arcs bridge the header areas of white marks and the ground electrode. This stage usually lasts for 1 minute and ends up with a sustained power-through arc, i.e., a breakdown.

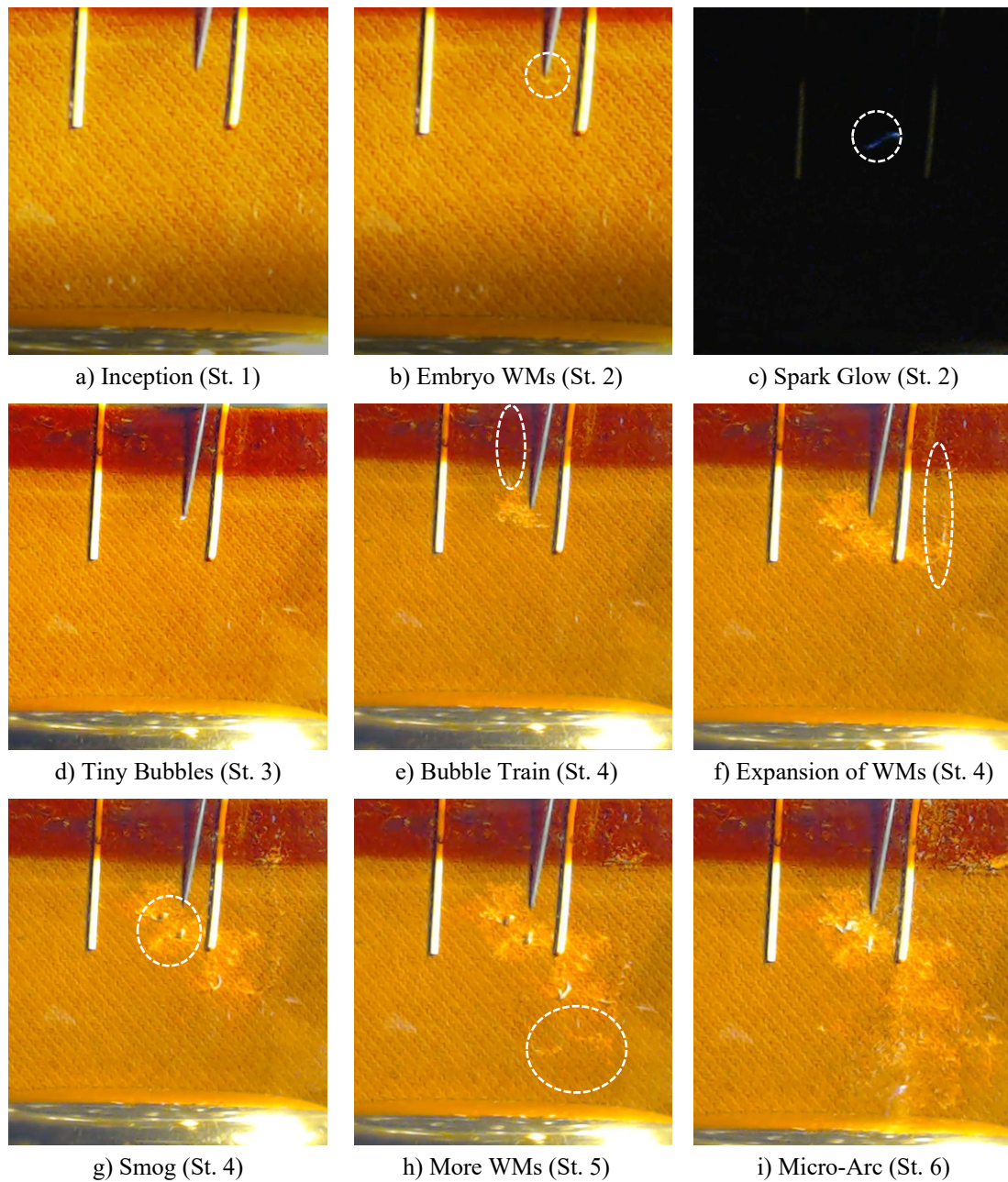


Figure 5.2 Visual information of internal treeing developmental stages (WMs denotes white marks)

5.2.2 PD Quantities of Internal Treeing

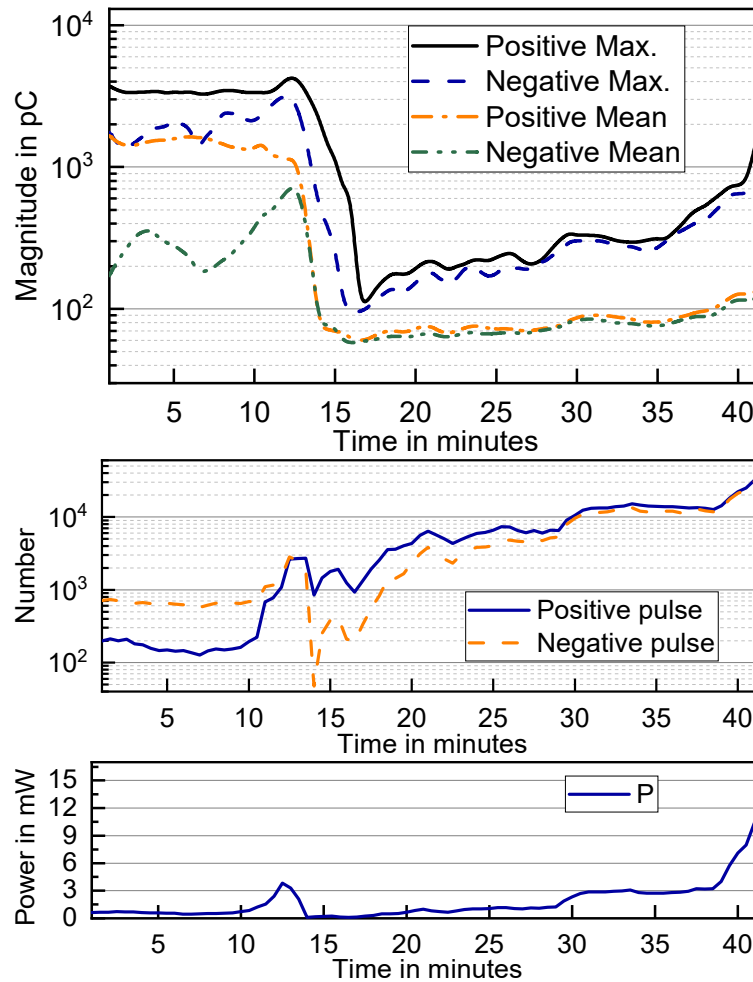


Figure 5.3 PD quantities of a full-cycle internal treeing event

For a detailed analysis of the temporal variations of PD quantities, a 42 minutes-long full-cycle internal treeing event was segmented into a set of consecutive steps. Each step lasts for 30 seconds. Statistics were made to each step, and the results are summarized in Figure 5.3. As shown, the trends of PD quantities of different stages are quite distinct from each other, which implies the discharge types are incessantly varying in the process of internal treeing.

In Stage 1 (St. 1), both the mean and the maximum magnitudes of positive PD pulses are significantly greater than their respective equivalents of negative pulses. In the meanwhile, the numbers of both positive and negative PD pulses gradually decline, similar to that of tracking-free creeping discharges elaborated in Chapter 4. Moreover, the PD power exhibits no obvious variations.

In Stage 2 (St.2), coinciding with the emergence of embryo white marks, the trends of PD quantities experience fundamental changes. For positive PD pulses, the maximum amplitude is maintained at a high level, whereas the mean magnitude begins to decrease. On the contrary, both the maximum and the mean magnitudes of negative PD pulses grow sharply. As a result, the mean magnitude of the positive pulse is only slightly greater than that of the negative pulse at the end of Stage 2. In the meantime, the numbers of both positive and negative pulses begin to soar at the beginning of Stage 2 and become almost identical to each other at the end of Stage 2. The PD power increases synchronously with the PD number and reaches a local maximum at the end of Stage 2.

In Stage 3 (St. 3), the trends are altered for another time. All magnitude quantities drop drastically.

In the meantime, the PD numbers decline sharply as well, the number of negative pulses in particular. Accordingly, the PD power falls from the local maximum to a very insignificant level.

In Stage 4 (St. 4), with the emergence of the bubble train and the disappearance of spark discharge, the trends vary again. The magnitude quantities continue to descend in the early period and then steadily ascend. However, no distinct differences can be identified anymore between positive and negative pulses. With respect to the PD numbers, in addition to the re-appearances of the soaring trends, a remarkable change occurs to the composition of PD pulses: the positive PD number is obviously greater than the negative PD number. Nevertheless, the gap is gradually narrowed with test time, and no difference can be found at the end of Stage 4. Regarding the PD power, it re-bounces from the low level and increases steadily again.

As mentioned previously, Stage 5 (St.5) can be considered as a continuation of Stage 4. Nevertheless, as more white marks are generated on the pressboard surface, all the PD quantities start to increase sharply again. For instance, the PD numbers increase almost exponentially with time, which results in a steep rise in PD power as well.

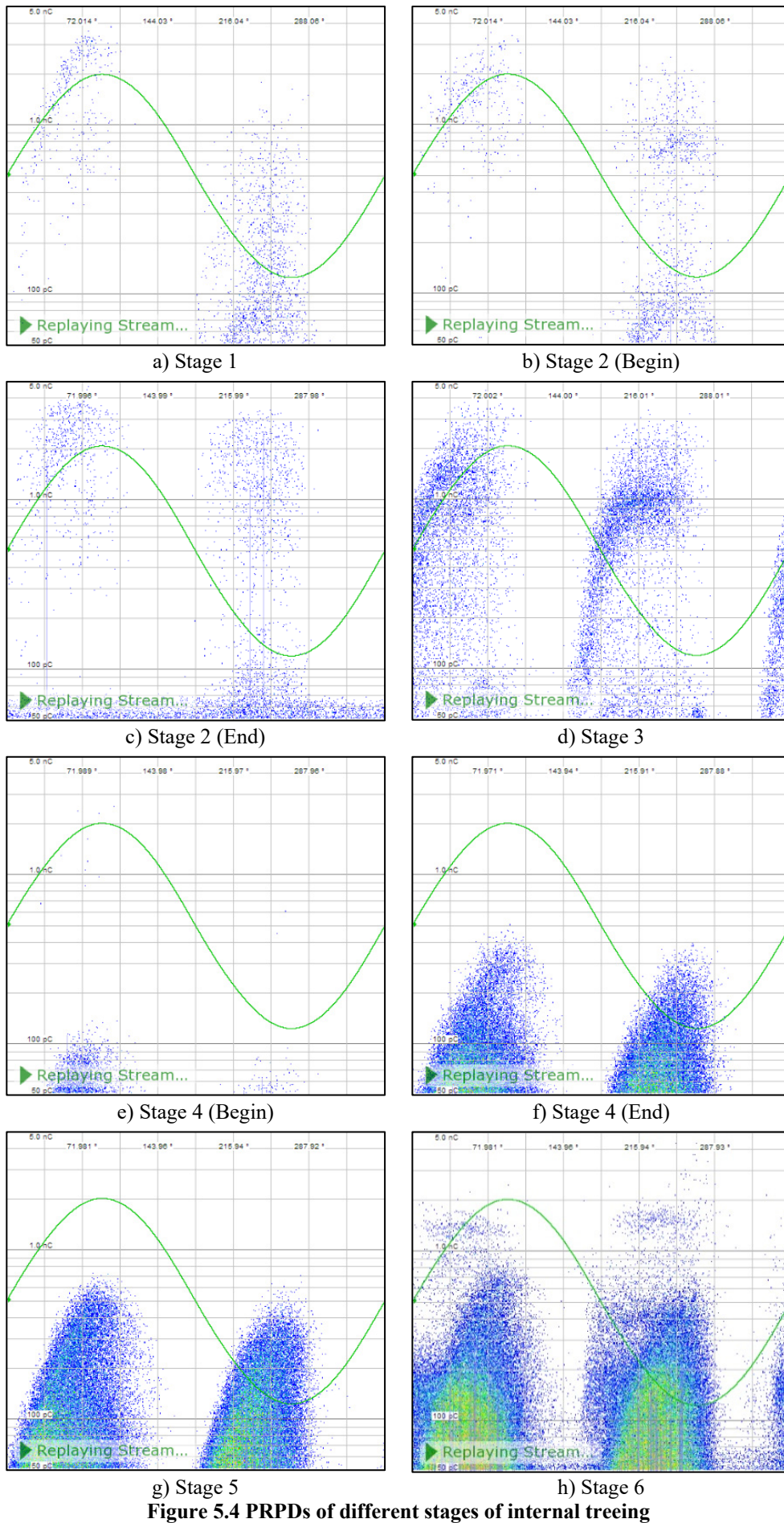
5.2.3 PD Patterns of Internal Treeing

The PRPD patterns, PSA patterns, and phase-related statistical distributions of different stages of internal treeing are shown in Figure 5.4, Figure 5.5, and Figure 5.6, respectively. The sampling period is 60 seconds in this case. The PD patterns of Stage 1 are approximate to those of creeping discharge without tracking. With respect to Stage 2, a cluster of large negative pulses begins to emerge in the early period and become quite clear at the end period. The PSA pattern fails to reflect these changes, but clear hints can be found in the phase-related statistical distributions, as shown in Figure 5.6 b) and Figure 5.6 c). Both the average and maximum magnitudes of negative pulses are obviously increased compared to positive pulses. The maximum positive pulse occurs around 60° - 70° . Lastly, the PD pulses are recorded throughout all phase angles at the end of Stage 2, which is presumably attributed to a certain kind of strong discharges.

The PRPD of Stage 3 is highly similar to that of large-sized spherical cavity discharge in solid materials [170] (see Figure 5.4 d)). Accordingly, its PSA pattern and phase-related statistical distributions are greatly varied. Compared to Stage 2, the phase width of PD occurrence is enlarged, and the phase center is further shifted towards the zero-crossing points. More specifically, the phase ranges of repetitive positive and negative PD pulses are 330° - 110° and 150° - 290° , respectively, which is highly indicative of discharges in enclosed space.

At the early period of Stage 4, the magnitudes of both positive and negative discharges polarities decline drastically. More importantly, the intensity of the positive pulse exceeds that of the negative one for the first time. This change is clearly reflected in its statistical distributions. Compared to that of Stage 3, the phase width is greatly shrunk as well: the phase ranges of repetitive positive and negative PD pulses are 30° - 130° and 200° - 300° , respectively. At the end of Stage 4, the magnitudes of positive and negative pulses are almost the same. Repetitive pulses of both polarities occur immediately after the zero-crossing points, and the pulse width is 120° for both polarities. The discharge patterns can remind someone of void discharges or surface discharges.

The PD patterns of Stage 5 are quite approximate to that of the end period of Stage 4, and the bizarre features of the PRPD pattern of Stage 6 are presumably due to the volatile micro-arcs.



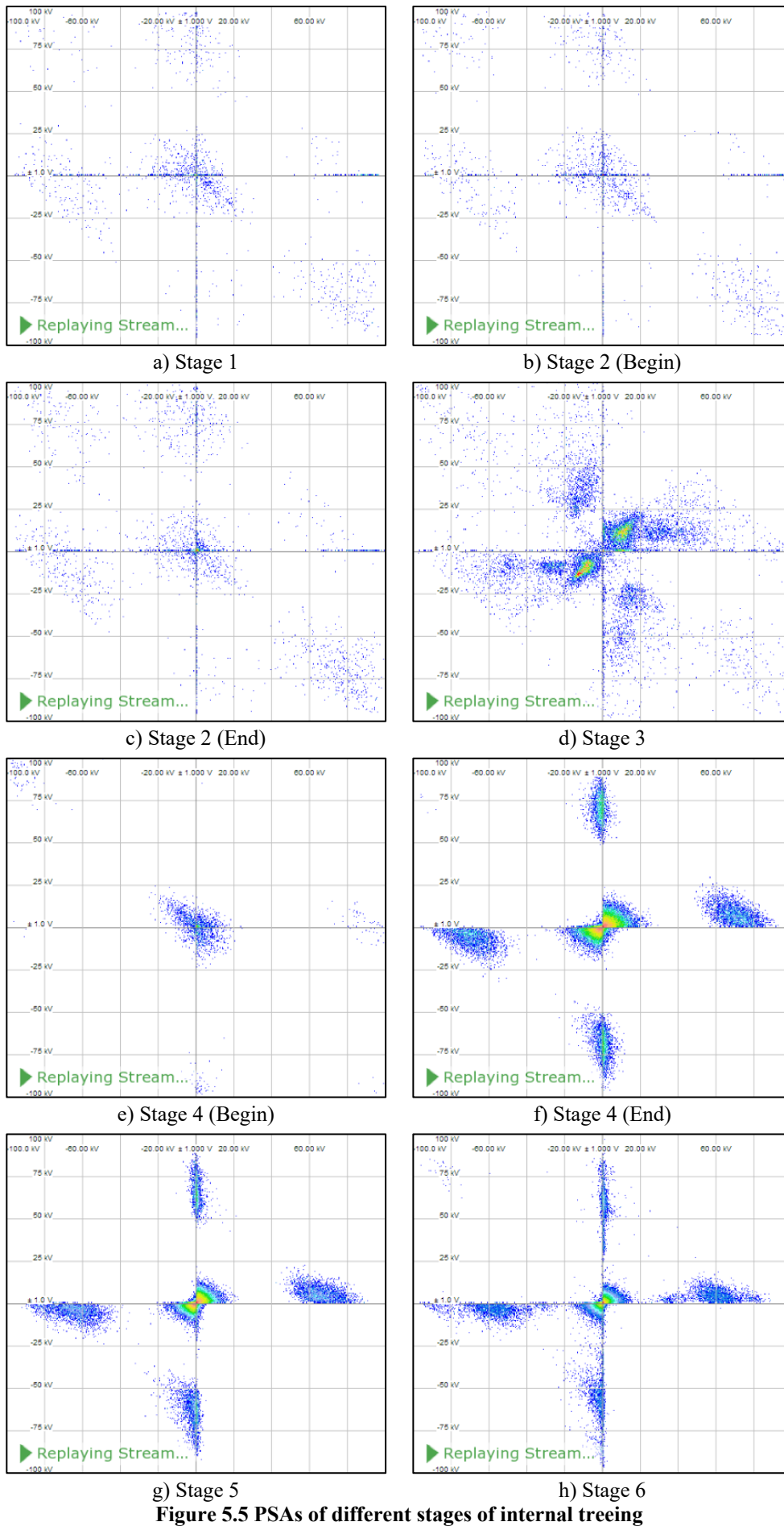


Figure 5.5 PSAs of different stages of internal treeing

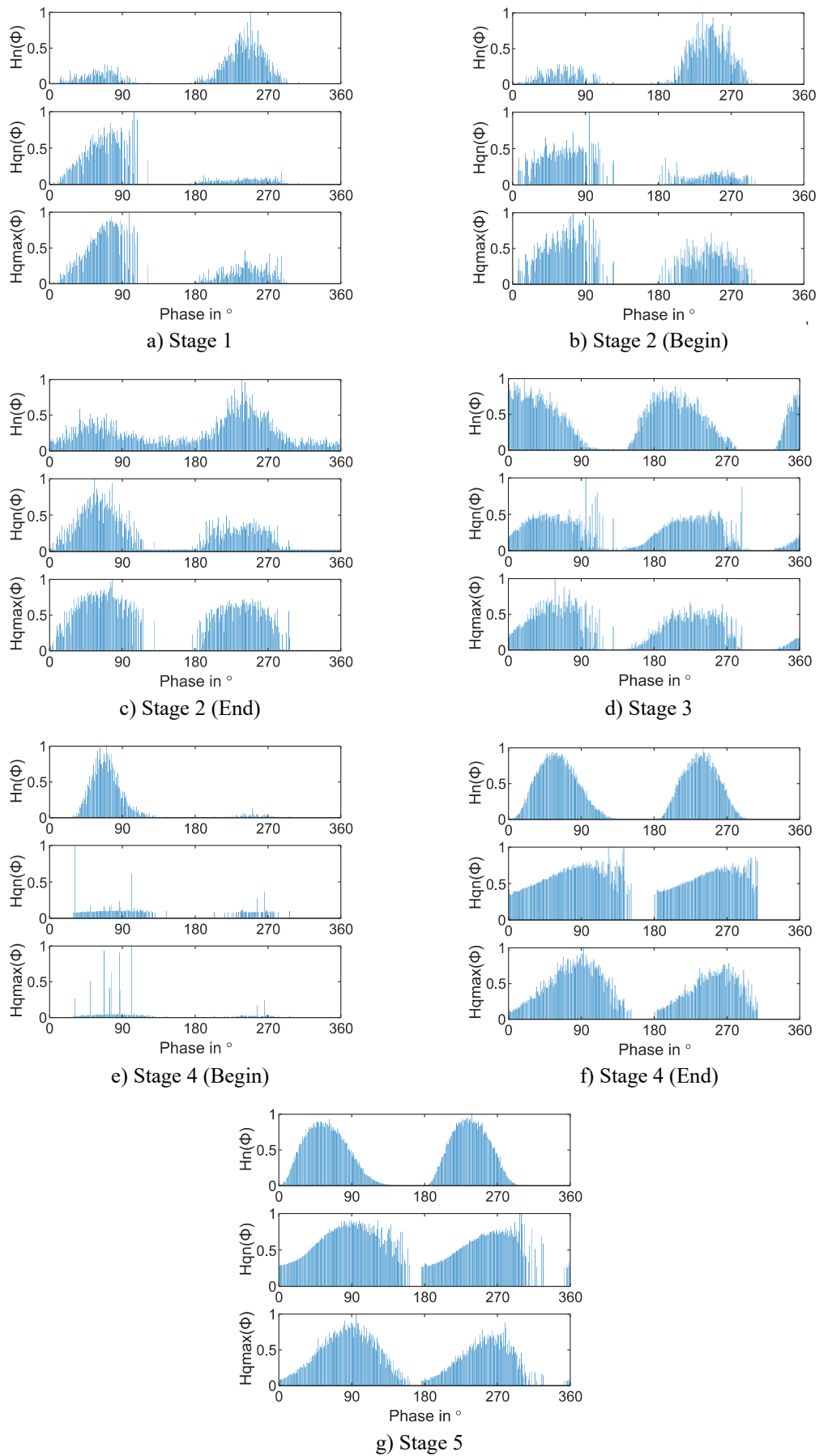


Figure 5.6 PD statistical distributions of different stages of internal treeing

5.2.4 PD Signals of Internal Treeing

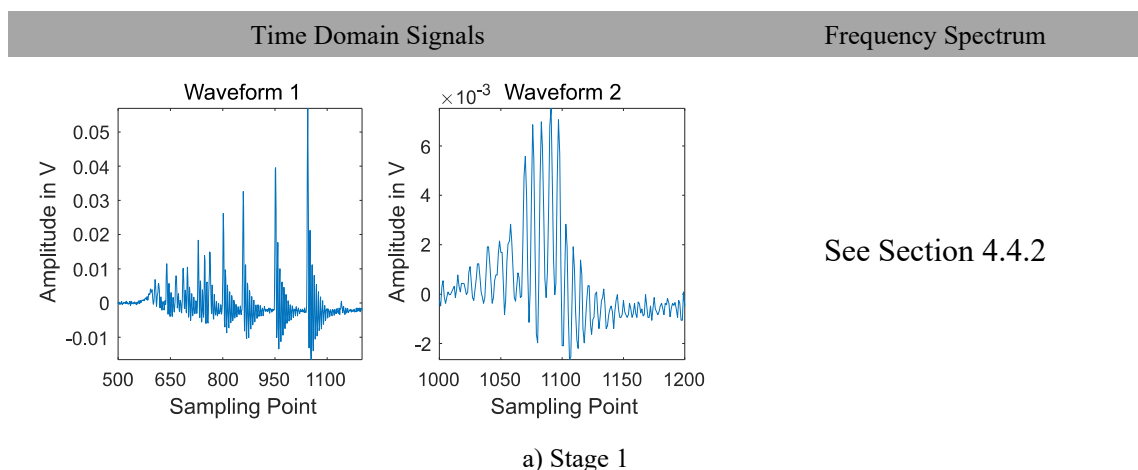
Furthermore, representative PD signals of each stage were captured for detailed investigations on their pulse shapes and frequency components. The sampling details and wavelet denoising techniques are the same as depicted in Section 4.4.2. The result is shown in Figure 5.7.

In Stage 1, the representative PD pulses are the same as those displayed in Section 4.4.2. As stated previously, the large-amplitude pulse-train signal (Waveform 1) is attributed to oil corona discharge, and the small-amplitude signal pulse (Waveform 2) is attributed to surface discharge.

In Stage 2, the large-amplitude pulse of Stage 1 (Waveform 1) can still be found. Besides, a new kind of PD signal of extremely large amplitude appears in Stage 2, as shown in Figure 5.7 b). Usually, only one such signal can be found in a single sampling period. At the early period of Stage 2, its amplitude scarcely exceeds 1 V: normally ranging from 0.4 V to 0.8 V. However, at the end of Stage 2, its amplitude is greatly enhanced. Most of the PD signals of this type have an amplitude over 1 V, and some of them even bigger than 2 V. Regarding the frequency spectra, three peaks are located at 10.5 MHz, 20.5 MHz, and 24.5 MHz, respectively.

In Stage 3, the corona discharge-induced pulse of Stage 1 (Waveform 1) can still be found, but its quantity is obviously diminished. The PD signal pulse shape is quite approximate to those of Stage 2, as shown in Figure 5.7 c). However, their amplitudes are obviously smaller compared with the PD signals in Stage 2. Moreover, the peak amplitudes of the PD signals at the early period are generally greater than those at the end period. Furthermore, regarding the frequency spectra, the PD signal at the early period exhibits some high-frequency components: peaks at 10.5 MHz and 20.5 MHz; whereas, the signal at the end period has lost the high-frequency components: only one peak at 10.5 MHz.

In Stage 4, the corona discharge-induced pulse of Stage 1 (Waveform 1) vanishes. Moreover, unlike Stage 2 and Stage 3, the peak amplitudes of PD signal stay almost unvaried throughout the whole period, and no great difference can be found between positive and negative pulses either (see Figure 5.7 d)). Only one peak is found in their frequency spectra, which is located at 10.5 MHz. In Stage 5, the scenario is almost the same as in Stage 4.



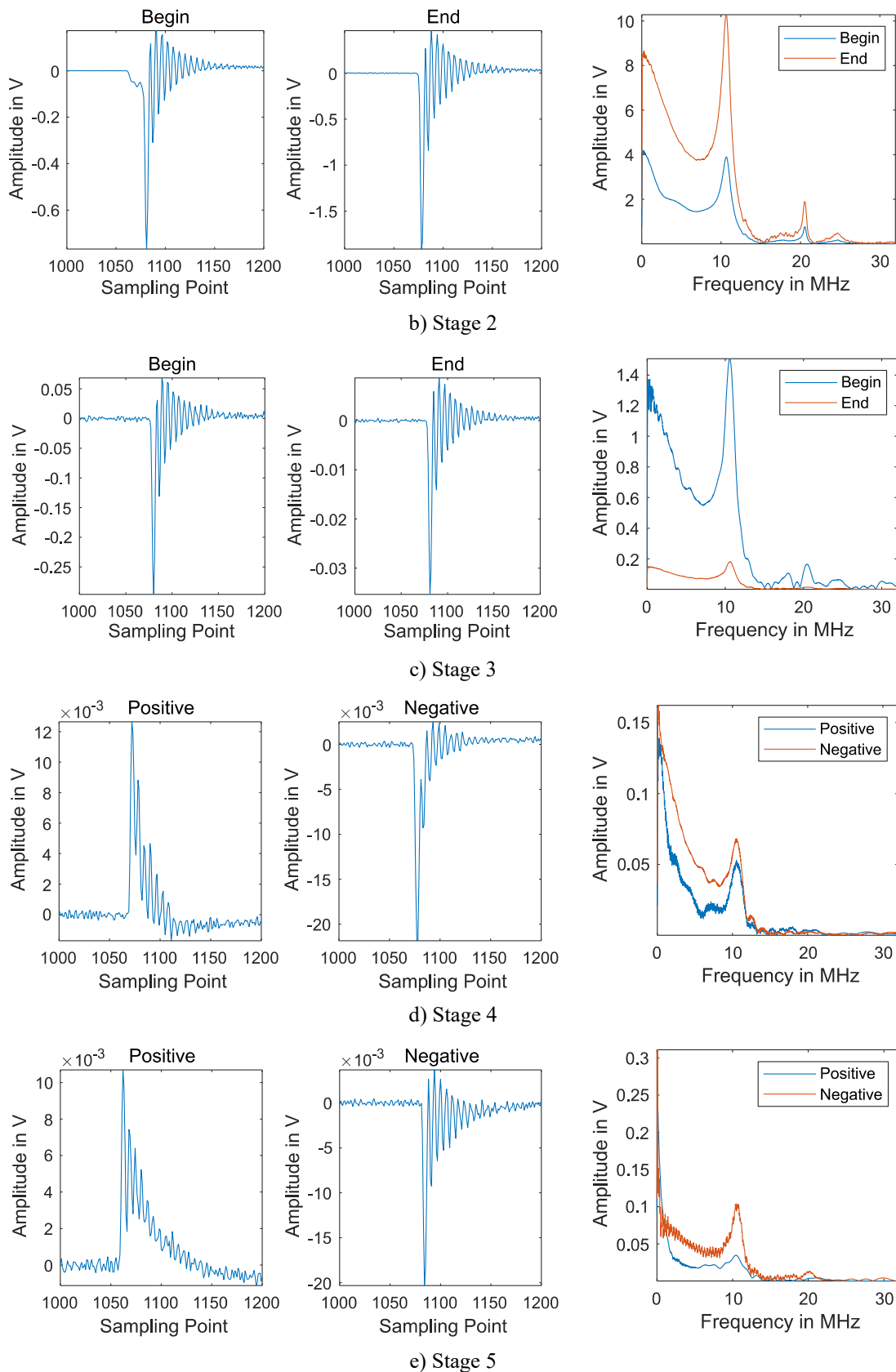


Figure 5.7 PD signal waveforms and frequency spectra of internal treeing

5.2.5 Interface Temperature and Gas Analysis of Internal Treeing

The pressboard temperature during the internal treeing process was obtained by optic fiber thermal sensors. The temperatures were recorded for every 0.1 s, and the results are shown in Figure 5.8.

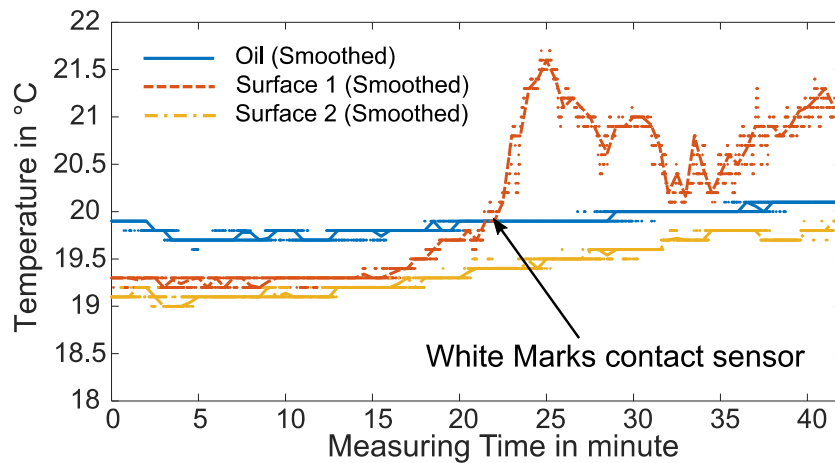


Figure 5.8 Pressboard surface temperature variations during internal treeing

As displayed, the temperatures of pressboard surface and oil bulk fluctuate within a very limited range (± 0.3 °C) at the first 15 minutes of the test. Afterwards, the pressboard surface temperature obtained by the sensor Surface 1 shows a slowly rising tendency from 15 minutes to 21 minutes and is thereafter steeply elevated to almost 22 °C within 4 minutes. From then on, the temperature of Surface 1 has experienced several up-and-downs but is always obviously greater than those of others. It is found in the recorded video that the white marks arrived at the measuring location of Surface 1 around 23 minutes after discharge inception, which is temporally coincident with the start of its steep temperature rise. In contrast, the temperatures of oil bulk and the other measuring point on the pressboard surface (Surface 2), which is located outside of the expansion path of white marks, exhibit no obvious changes throughout the entire test.

It is inferred that white marks are exactly the reason for the steep temperature rise. Therefore, the evolution and expansion of white marks on the pressboard surface could be potentially detected through monitoring the pressboard temperature, its rising steepness in particular. However, the results also reveal that temperatures of white marks are actually not strong enough to cause carbonization to pressboard. There must be an alternative process governing the formation and evolution of carbonization tracks.

Gas analyses were carried out to determine the compositions of bubbles generated during tracking. The oil-dissolved gases were also investigated as a benchmark. Three incidents of tracking were observed in the tests, and they are denoted as Sample 1, Sample 2, and Sample 3, respectively. The analysis results of oil-dissolved gases and free gases of bubbles are shown in Figure 5.9 and Figure 5.10, respectively.

The concentrations of oil-dissolved gases after internal treeing are greatly increased compared with those of tracking-free creeping discharges (see Section 4.4.4), the concentration of hydrogen (H_2) in particular. For instance, the concentration of hydrogen exceeds 50 ppm in Sample 2. The generation speed of hydrogen is truly impressive, especially when considering the comparatively short discharge time of the internal treeing.

The concentrations of fault gases are even greater in bubbles. The hydrogen concentration in bubbles is several times bigger than in oil. Moreover, the bubbles of Sample 1 also contain a large quantity of carbon monoxide (CO) and acetylene (C_2H_2). However, these two gases are not very much in the bubbles of Sample 2 and Sample 3, where hydrogen is the single dominant gas.

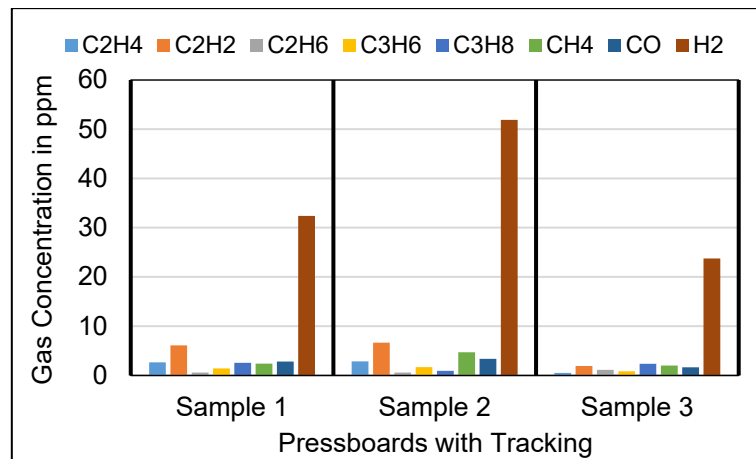


Figure 5.9 Concentrations of oil-dissolved gases after internal treeing

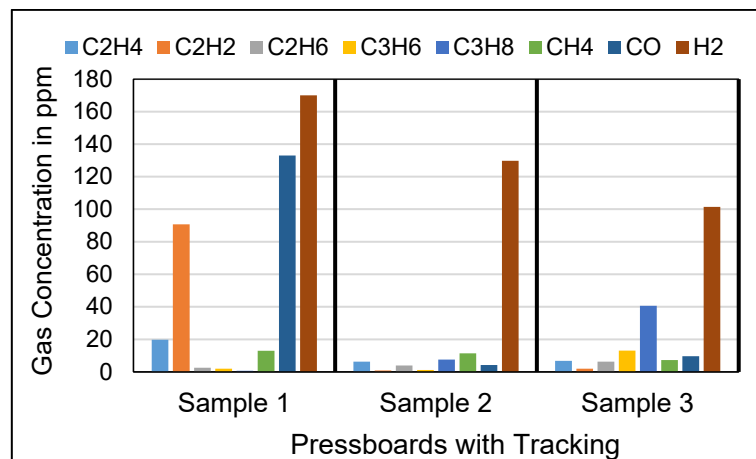


Figure 5.10 Concentrations of free gases after internal treeing

The fault gas diagnosis results of internal treeing using Duval's Triangle are shown in Figure 5.11. For all three incidents, the tracking phenomenon is classified as Fault D1 using oil-dissolved gases, i.e., low-energy discharge, similar to the diagnosis results of creeping discharge without tracking (see Section 4.4.4).

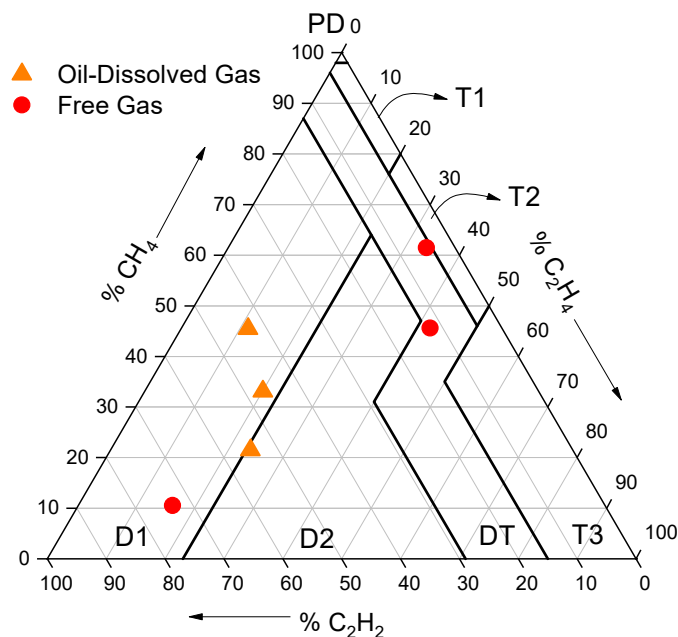


Figure 5.11 Duval's Triangle for internal treeing

However, if using free gases, two incidents (Sample 2 and Sample 3) are classified as Fault DT, i.e., mixed electrical and thermal faults. The discrepancy in diagnosis results suggests that the free gases, if found in an insulation system, could be a better choice for incipient fault diagnosis when a suspicious sign of tracking is detected by other means.

5.2.6 Post-Mortem of Pressboard Sample of Internal Treeing

Furthermore, the pressboard samples after internal treeing were dissected to unravel the fundamental causes of their failures. The post-mortem images are shown in Figure 5.12.

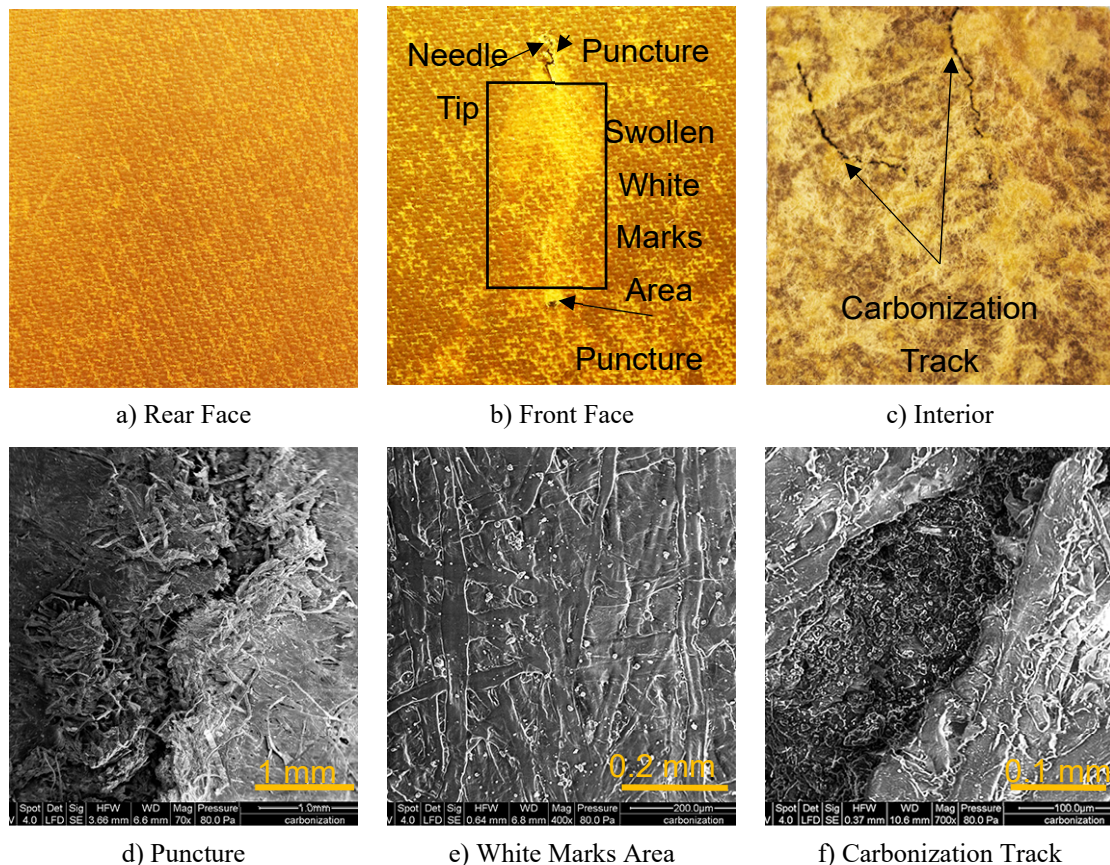


Figure 5.12 The Post-Mortem images of pressboard samples after internal treeing

The rear face of the pressboard, i.e., the surface having no contact with the needle electrode, is still intact after tracking; whereas, the front face shows evident signs of damages. At first, punctures are found in the areas near the needle tip and the grounding electrode edge. As revealed in the SEM image, see Figure 5.12 d), the fibers in the puncture area are completely ruptured, but no identifiable trace of carbonization is present. It indicates the formation of puncture is probably attributed to a certain kind of mechanical stress, i.e., the stress of strong spark discharge in this case.

At second, the white marks areas, especially the embryo white marks, are obviously swollen after tracking. The surface swelling can only be attributed to the mechanical burst force of severe bubbling. However, no carbonization traces are recognized within these areas. The SEM image (see Figure 5.12 e)) shows the fiber structures of the white marks areas can still be considered sound. However, the presence of some tiny particles indicates the pressboard fibers have actually deteriorated, and it needs further investigations to locate the deteriorated fibers.

After dissecting the pressboard samples, two filament-like carbonization tracks are found in the pressboard interior, as displayed in Figure 5.12 c). Two important remarks can be made on those

carbonization tracks. At first, they do not necessarily bridge the needle electrode and ground electrode. Instead, they are located in the middle region of the pressboard samples. At second, the paths of the carbonization tracks are quite narrow, which indicates the overheating process is confined within a very limited space. As can be seen in Figure 5.12 f), the width of the carbonization track is around 150 μm . The fibers in the carbonization tracks are utterly melting down while the fibers in the vicinity are still fairly good.

5.3 Revisiting White Marks, Carbonization and Bubbling of Internal Treeing

As a matter of fact, the same phenomena, including white marks, carbonization, bubbling, and even smokes, have been witnessed plenty of times. Accordingly, various theoretical presumptions have been made, aiming to expound the phenomena and to unravel their fundamental causes. In spite of the interesting findings and inspiring thoughts obtained thus far, no clear illustrations or convincing explanations to accompanying phenomena of internal treeing have been developed. The following paragraphs are dedicated to serving the purpose of filling the gap

To grasp the nature of the phenomena, the below-listed critical issues will be tackled in a priority:

- the essence of white marks;
- the formation of carbonization;
- the cause of bubbling;
- the inter-relations of the phenomena.

5.3.1 The Essence of White Marks

At least, a consensus has been made on some characteristics of white marks: they result from a dehydration and de-impregnation process of pressboard and are actually gaseous channels [97, 103–105]. The white marks would disappear after a re-impregnation process and emerge again even under a lower field [104]. According to the author's experience, the white marks would spontaneously disappear even without any intentional re-impregnation.

Now that the gaseous nature of white marks is widely recognized, the key question is the source of gas. As presumed by Dai [97] and Xiao [104], the gas originates from discharge-induced oil decomposition in pressboard surface pores and is trapped there due to oil-pressboard interfacial tension. Moreover, it is inferred by Murdiya [105] that the gas formation is also a result of interface streamer progression: the gas is generated at the header region of the pre-breakdown streamer and then partially captured by pressboard surface pores due to Maxwell stress.

However, neither argument seems completely valid in this case. As shown in Figure 5.2, the onset of rapid expansion of white marks is coincident with the extinction of strong spark discharge. Besides, as revealed in PD investigations, almost no large-magnitude PD pulses are detected during the rapid expansion stages (Stage 4 & Stage 5) of white marks. It indicates the absence of a strong pre-breakdown streamer in this case. Therefore, the pre-breakdown streamer is not very likely a major reason for white marks formation.

Moreover, the effect of oil decomposition in pressboard surface pores has probably been exaggerated as well. It is known that the decomposition of oil needs either high temperature or high-energy discharge. Unfortunately, neither of the conditions is satisfied in this case. At first, as shown in Figure 5.8, the temperature of the pressboard surface does not increase much when contacting white marks, in spite of its steep rise. It suggests the gas formation is not a result of high temperature on the

pressboard surface. At second, although a great quantity of PD pulses is detected during the rapid expansion of white marks, it is still hard to correlate the PD pulses with a massive gas decomposition, considering their low magnitudes and power. Furthermore, the FEM simulation results (see Section 4.3.5) reveal that the extremely high field only exists near the triple-junction area. Regarding other areas, nevertheless, the field, either total field or tangential component, is quite small and thus unlikely capable of generating sustained oil decompositions required for white marks expansions. Therefore, it can be concluded that oil decomposition in the pressboard surface pores is not a major cause of the gaseous white marks either.

To conclude, the formation of white marks cannot be mainly attributed to oil decompositions in oil bulk or in pressboard surface pores. Therefore, it is reasonable to claim that the majority of gases in the white marks are from the very interior of the pressboard bulk. The swollen surface of white marks areas (see Figure 5.12 b)) indicates the non-negligible mechanical burst stress due to massive gas formations inside of the pressboard samples.

5.3.2 Formation of Carbonization

The formation of carbonization has been thought to be a result of accumulative energies released from gas discharges in white marks because its appearance on pressboard surface is often subsequent to white marks, and its shape is somewhat similar to that of the area of the white marks [104, 105]. However, the sequence of appearance on the pressboard surface does not necessarily mean a sequence of occurrence. As shown in Figure 5.12, the carbonization track is located in the very interior of the pressboard, and no obvious carbonization trace has been found in the white marks areas even under the scale of the micrometer. Moreover, as revealed by temperature and PD measurements, neither the surface temperature of pressboard nor the power of partial discharges is sufficiently high to sustain a carbonization process of such a degree. Therefore, the formation of carbonization during creeping discharge is still an open question and needs to be further analyzed.

Unfortunately, compared with cable insulating materials such as polyethylene (PE) and cross-linked polyethylene (XLPE), the treeing phenomenon in pressboard is much less understood and even scarcely studied in a systematic way. It is partly due to the opaqueness of cellulosic materials, which makes direct observation of treeing in pressboard impossible, and partly due to an underestimation of the severity of treeing in transformers. Although cellulosic materials are quite different from those dense synthetic polymers in many aspects, the initiation and growth mechanisms of treeing in cable insulating materials can still shed some light on the understanding of carbonization in pressboards. Based on the treeing mechanisms of cable insulating materials, the assumed formation process of carbonization track in pressboard is proposed in Figure 5.13.

The assumed formation process consists of two stages: initiation and growth. As well-known, the inception of treeing is closely associated with charge injection into insulating materials by either a high field electrode or gas discharges in a cavity [171]. When a polymer contacts a needle of a high electric field, the charge carriers would conquer the metal-insulator potential barrier and thus being injected into polymer via tunneling effect. The nature of injected charge carrier is dependent on the needle field strength: the injected carriers are mainly electrons for a normally high field (< 1 MV/cm) and holes for an extremely high field (> 1 MV/cm), respectively [172]. According to the FEM simulation results (see Section 4.3.5), the maximum field of the needle-to-plate electrode configuration under 34 kV is around 0.8 MV/cm. Therefore, it can be inferred that electron emission is the predominant way in this case. Due to the small mean free path in polymer, the injected electrons

are usually trapped in insulators. However, some so-called “hot electrons” can be generated via an energy transferring mechanism termed the “Auger Process.” The hot electrons can bombard the chemical bonds of the polymer molecules and eventually result in their degradation. It is noteworthy that the injection and transport of charge carriers are clearly a field-threshold phenomenon, which means the dielectric polymer can have a virtually “infinite” lifetime below the field threshold and an inevitable treeing initiation above it [173].

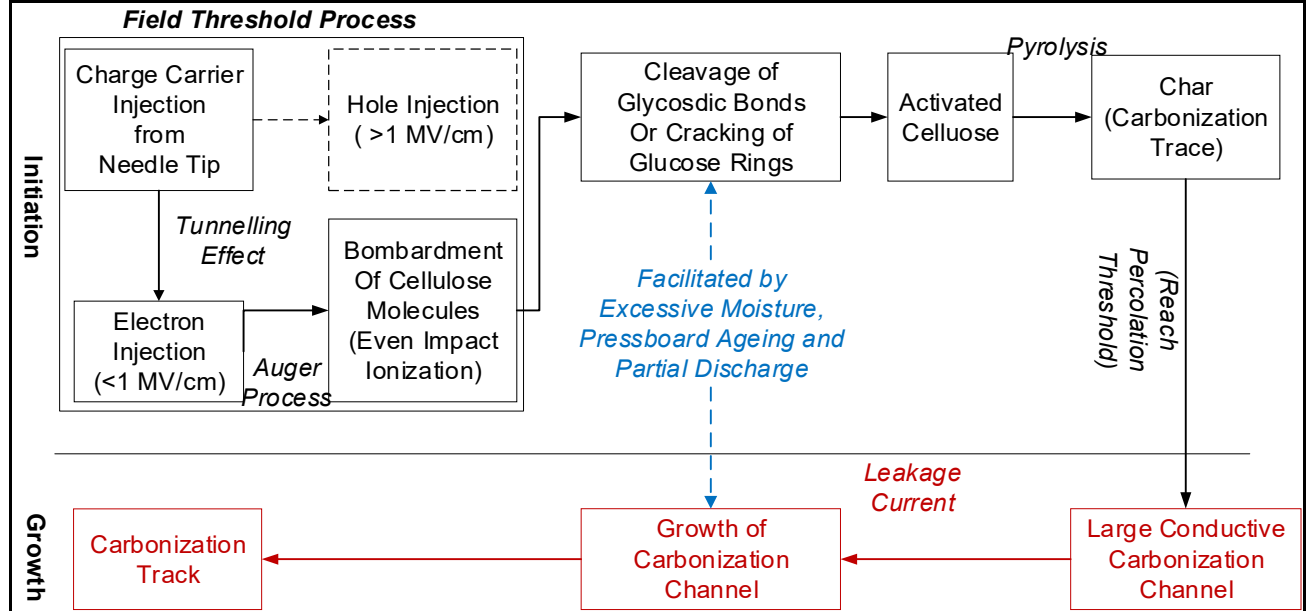


Figure 5.13 Assumed process of pressboard carbonization track

As a result of the cumulative hot-electron bombardments, an irreversible deterioration would occur to the polymer molecules, such as cleavage of the glycosidic bond (C-O) and crack of glucose ring (C-C). The deteriorating process is probably facilitated by the presence of excessive moisture, ageing-caused fiber degradation, interface spark discharge, and void discharges in pores. Subsequently, some of the polymer molecules, e.g., the cellulose molecules, become activated and are thereafter converted into chars via low-temperature pyrolysis. As postulated by Tang and Bacon [174], the low-temperature pyrolysis of cellulosic fibers comprises four consecutive stages: desorption of physically bonded water, splitting of structure water, chain scissions, and formation of graphite-like layers. The formation of chars was observed in the temperature range of 240 °C to 400 °C. Figure 5.14 shows a refined cellulose-to-char conversion mechanism proposed in [175].

The generated trace char and its surrounding cellulosic fiber matrix constitute a double-phase system (conductive phase and insulating phase) in the onset sites of carbonization. The conductivity of this double-phase system can be expressed as [176]:

$$\frac{\sigma_m - \sigma_c}{\sigma_m - 2\sigma_c} = \frac{(1 - \varphi)(\sigma_i - \sigma_c)}{\sigma_i + 2\sigma_c} \quad (5.1)$$

where, σ_m , σ_c and σ_i denotes the mean conductivity of the entire double-phase system, the conductivity of conductive trace, and the conductivity of the surrounding insulating matrix, respectively; φ denotes volume fraction of the conductive phase.

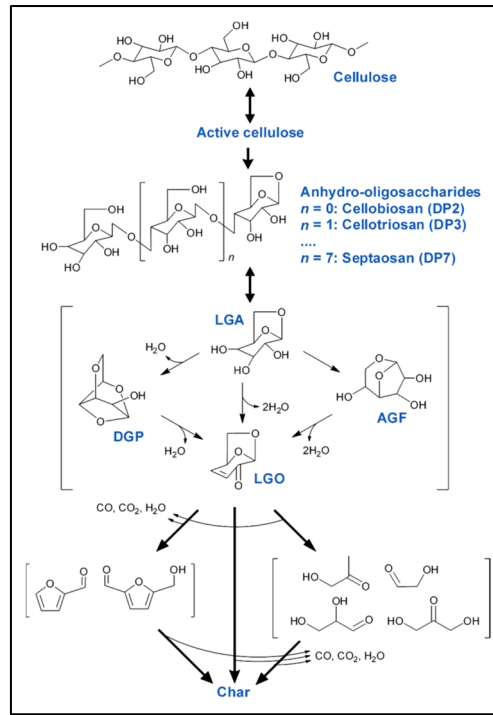


Figure 5.14 Mechanism of cellulose pyrolysis [175]

The volume fraction of conductive phase φ is steadily enlarged as ever more chars are generated. In consequence, the conductivity of the double-phase system would be sharply changed when the percolation threshold, i.e., the critical volume fraction of the conductive phase, is reached. The relation between σ_m and the critical volume fraction of the conductive phase φ_c can be described as follows [176]:

$$\sigma_m = \sigma_i \left(\frac{\varphi_c}{\varphi_c - \varphi} \right)^s \quad \text{for } \varphi < \varphi_c$$

$$\sigma_m = \sigma_c \left(\frac{\varphi - \varphi_c}{1 - \varphi_c} \right)^t \quad \text{for } \varphi > \varphi_c$$
(5.2)

where s and t are exponents which are dependent on system dimensionality and geometry. According to the percolation theory, the conductivity of carbonization onset sites would be dramatically increased when the generated chars accumulate to a certain level. The degraded regions of cellulosic fiber become sufficiently conductive to sustain a thermal process-governed growth in the carbonization channel.

Subsequently, the growth of the conductive carbonization channel is a self-sustained process, which is subject to multiple factors, such as voltage level, stress time, and dielectric dissipation factor. The dielectric dissipation factor is determined by the contents of impurities and water. More importantly, it is synergistic with dielectric temperature, which could result in an auto-accelerated heating process, provided that the cooling is not adequate or sufficient. For a homogenous dielectric under a uniform field, the real power loss P in dielectric can be estimated by [12]:

$$P = \varepsilon_0 \cdot \omega \cdot E^2 \cdot V \cdot \varepsilon_r \cdot \tan\delta$$
(5.3)

where V is the dielectric volume, ω is the angular frequency of applied voltage, and E is the electric field stress.

The growth speed of the carbonization channel is determined by heat generation and heat dissipation.

For the carbonization channel in the pressboard interior, i.e., internal treeing in this case, its growth can be much faster than the carbonization channel on the pressboard surface since oil is an excellent cooling medium. Furthermore, due to the porosity and inhomogeneity of aged cellulosic pressboards, it is hard to locate the “hot spot” and thus impossible to predict the growth path of the carbonization channel. As the carbonization track approaches the ground electrode, it acts as an extension of the high voltage electrode due to its high conductivity. Therefore, the micro-arcs and arcs can be ignited between the ground electrode and the header region of the carbonization crack.

The carbonization channel deep inside of the pressboards might be tiny enough to elude any visual inspections. Therefore, scrutiny of pressboard samples is indispensable for any suspicious creeping discharge-related faults because the tiny carbonization channels in the pressboard interior can re-grow at an ever-faster pace under an electric field and leads eventually to catastrophic failures.

5.3.3 Cause of Bubbling

The bubbling phenomena in the oil-paper insulation system have been extensively studied. However, the research emphasis has always been put on conductor wrapped papers, and little attention has been paid to pressboards. As a matter of fact, it is the cold-thin pressboards that possess the vast majority of moisture of the transformer insulation system. Therefore, provided the inception conditions, especially the temperature and its rising steepness, are satisfied, the bubbling effect in the transformer pressboard could occur on an unparalleled scale. In fact, severe pressboard tracking is often associated with a massive bubbling effect [108, 177], which, in some cases, can even result in alarm operations of gas relays [177].

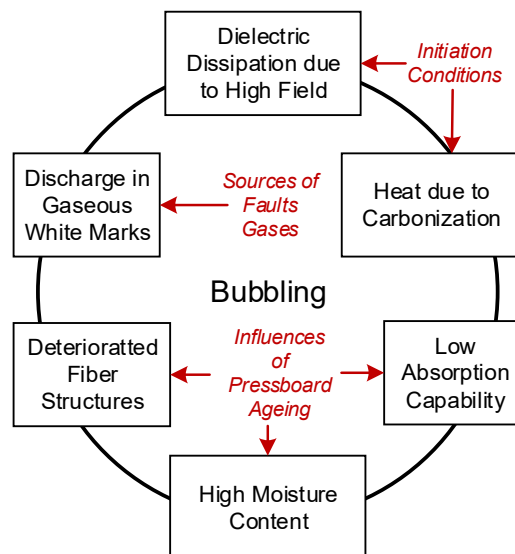


Figure 5.15 Influential factors of tracking-related pressboard bubbling

The bubbling of conductor papers is subject to a number of factors, such as moisture content, absolute temperature, temperature rise steepness, and ageing. With respect to the pressboard bubbling due to internal treeing, nevertheless, the effects of strong field and partial discharges have to be taken into consideration as well. The influential factors of tracking-related pressboard bubbling are schematically illustrated in Figure 5.15. Although strong corona discharge in oil can generate bubbles as well, its effect is apparently dwarfed by other factors in this case.

As stated in Section 2.3.5, the fundamentally governing factor of bubble formation is the temperature-dependent water vapor pressure P_{WV} . For P_{WV} conquering all the hampering forces, there must be a sufficient supply of heat. The overheat for paper bubbling is usually due to an overload-induced

temperature rise of conductors; whereas, the major heat source for pressboard bubbling is undoubtedly the carbonization track. Besides, high field dielectric dissipation and void discharges could probably take part in heat generation as well.

In the meantime, the ageing of pressboard exerts three-fold impacts in facilitating pressboard bubbling. At first, as shown in Section 4.3.2, the aged pressboard has a greater moisture content, which means more “raw materials” for bubbling. At second, as shown in Figure 4.3.3, ageing deteriorates the fiber structure of the pressboard and leaves more pores and macro-capillaries, which means more incubation sites for embryo bubbles. At third, as shown in Figure 4.3.1, ageing results in the weakening of water absorption capability of pressboard, which means a reduction of hampering forces of bubbling effect.

However, the compositions of the bubbles are not purely water. As shown in Figure 5.10, the bubbles also have appreciable concentrations of hydrocarbons and hydrogen. The hydrocarbons and hydrogens are presumably a result of oil decompositions in pressboard interiors near the carbonization track.

5.3.4 Inter-relations

Based on experimental phenomena and discussions, Figure 5.16 illustrates the evolution of creeping discharge-induced internal treeing as well as the inter-relations of its accompanying phenomena.

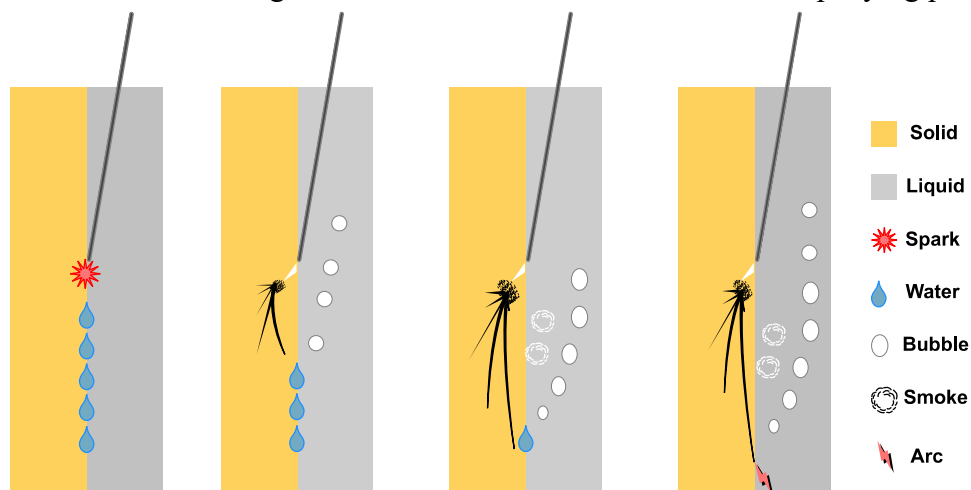


Figure 5.16 Evolution of internal treeing and its accompanying phenomena

Firstly, strong creeping discharges, comprising surface discharge and oil corona discharge, are initiated at the triple-junction point. It is only sustained for massively-aged pressboards under strong fields due to enhanced negative discharges. Secondly, spark discharges disappear, and some embryo carbonization cracks are generated in the pressboard interior. Due to the overheat generated in the carbonization process, the moisture in the pressboard is turned into bubbles and then driven out of the pressboard. This bubbling effect is greatly facilitated by pressboard ageing and leaves the sign of dehydration on the pressboard surface, i.e., the white marks. Thirdly, the carbonization cracks grow bigger and expand towards the grounded electrode. More bubbles, white marks, and even smoke are observed in this step. Lastly, the carbonization cracks have almost reached the grounded electrode and grow into the pressboard surface. Some arcs are generated between the tip of the highly conductive carbonized channels and the ground electrode.

Therefore, it can be concluded that the internal carbonization generates the bubbling effect, which in turn produces white marks on the pressboard surface. The bubbling effect and white marks are signs

of severe carbonization in the pressboard interior.

5.4 The Surface Tracking Phenomenon

Aiming to investigate the surface tracking phenomenon, another run of identical tests have to be carried out to a new type of pressboard specimens. The most distinct difference between the new specimen and the normal pressboard lies in the apparent density: the apparent density of the previous specimen is 1.2 g/mm³, while that of the new specimen is 0.9 g/mm³. The sample preparation, accelerated ageing, and HV test setup for the investigations with new pressboard specimen is completely the same as those used in previous tests. The new pressboard specimens were thermally aged with new mineral oil for 20, 30, 40, 50, and 60 days, respectively. A new pressboard is used as the benchmark. Thereafter, the samples were subject to constant-stress creeping discharges, in which the voltage levels are 34 kV and 36 kV, respectively. The test duration was 6 hours unless breakdown events occurred.

Table 5.2 summarizes the statistics of creeping discharge-induced failures of low-density pressboards. As shown, surface tracking phenomena were only observed with new and moderately aged samples, whereas internal treeing phenomena were only observed with massively-aged pressboard samples under 36 kV. Moreover, with respect to the samples suffered from surface tracking, the surface carbonization area appears negatively correlated with the thermal ageing degree. Figure 5.17 shows the surface carbonization of new and moderately-aged samples after 6 hours of creeping discharges.

Table 5.2 Failure mechanisms of low-density pressboards due to creeping discharges.

Sample	Group	Surface Tracking	Internal Treeing	Time-to-Failure
New	New	Yes	No	Greater than 6 hours
#20	Moderately Aged	Yes	No	Greater than 6 hours
#30		(small trace)		Greater than 6 hours
#40	Massively Aged	No	No under 34 kV Yes under 36 kV	Within 1 hour
#50				Within 1 hour
#60				Within 1 hour

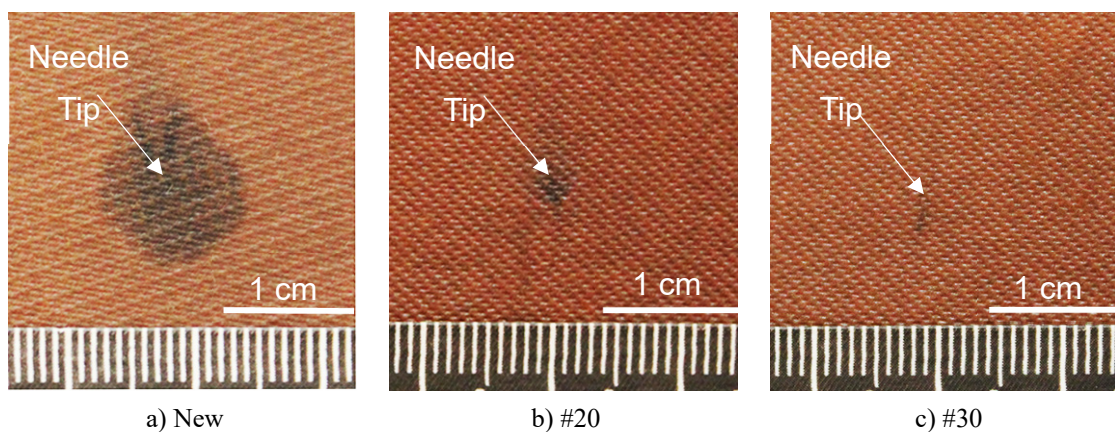


Figure 5.17 Surface carbonization of low-density pressboard samples after 6-hours of surface tracking

Another noteworthy phenomenon in surface tracking is the PD disappearance of the new sample. The PD numbers of surface tracking samples are given in Figure 5.18.

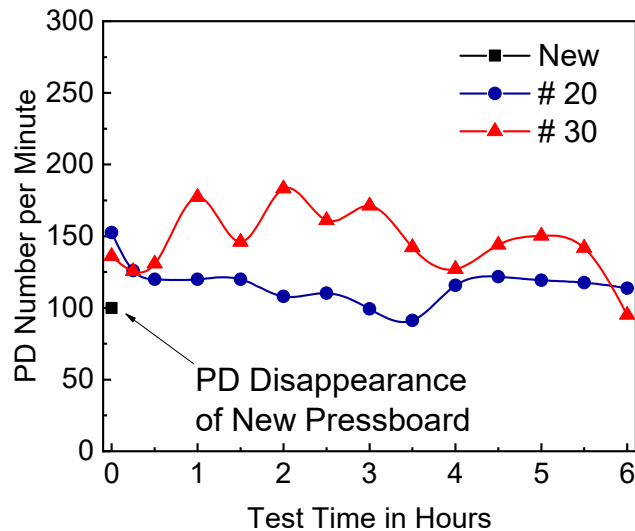


Figure 5.18 PD numbers of surface tracking samples versus test time (34 kV)

As shown, no PD signals are recorded after only about 5 minutes after the discharge inception with the new pressboard. In fact, the PD disappearance is almost temporally coincident with the emergence of obvious carbonization marks on the pressboard surface. In contrast, for the moderately-aged samples, the PD numbers fluctuate at comparatively high levels throughout the tests. The results suggest the surface carbonization is the major reason for PD disappearance. However, on the other hand, the PD signals would not be completely extinct if the carbonization area is not sufficiently large. Moreover, it also implies it could be very hard to detect the surface tracking process using the conventional electrical PD measuring technique.

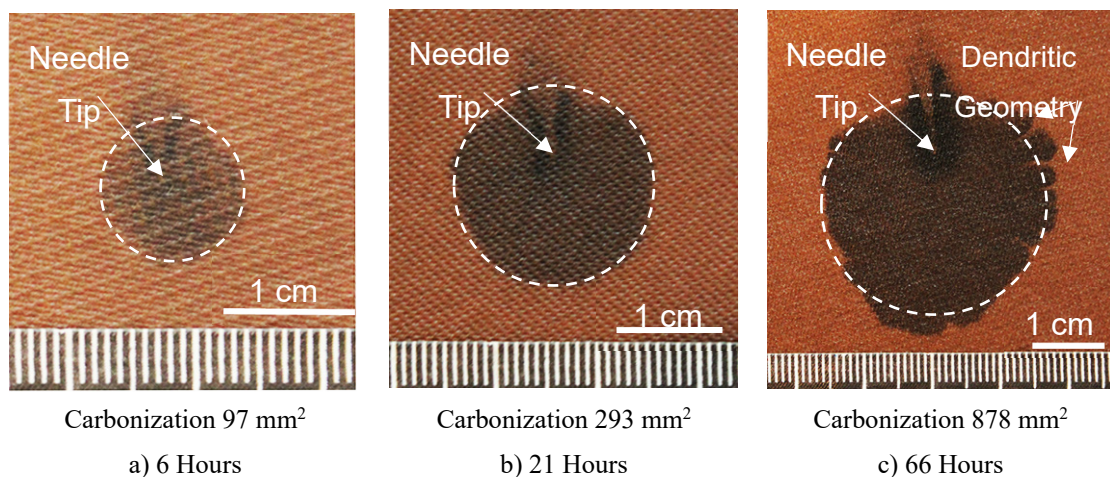


Figure 5.19 Temporal evolution of surface tracking of new low-density pressboard

Now that the samples of surface tracking would not fail soon, it is interesting to investigate the evolution of the surface tracking process on a larger time scale. Therefore, the stressing times have been considerably extended for the surface tracking-inflicted new samples. Figure 5.19 shows the temporal evolution of slowing tracking on the pressboard surface as a function of stressing time. The carbonization area is estimated using the image process package ImageJ.

The pressboard sample did not break down even after 66 hours of stressing. Nevertheless, the carbonization area steadily grows with stressing time. As shown, the carbonization areas after 6, 21

and, 66 hours are 97 mm², 293 mm², and 878 mm², respectively. In addition, the geometry of the carbonization area also varies with time. After 6 and 21 hours of stressing, the carbonization area exhibits a circular shape around the needle tip, where the triple-junction area shows the most severe deterioration. After 66 hours of stressing, however, the carbonization area exhibits an obvious dendritic shape at its periphery. It is believed that the dendritic geometry would eventually evolve into surface treeing, as witnessed in practical failures.

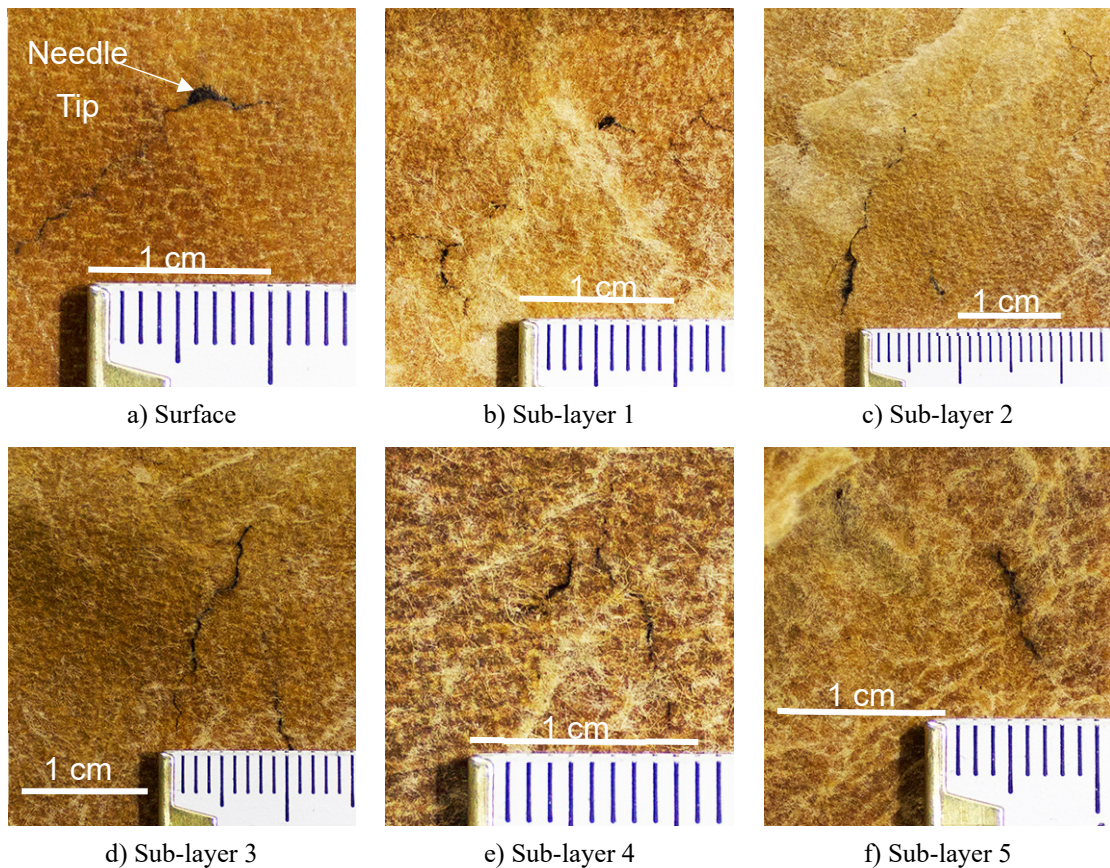


Figure 5.20 Cross-layer internal carbonizations of high-density pressboard after internal treeing

Compared with the slow and simple expansion of the carbonization area in a surface tracking process, the expansion of the carbonization channel in an internal treeing is much faster and more intricate. Figure 5.20 gives the post-mortem images of a dissected high-density pressboard sample after the internal treeing process. Although the carbonization trace on the pressboard surface after internal treeing is much smaller than that after surface tracking, the carbonization channels penetrate deeply into the pressboard interior and cross a number of layers. Besides varying in size, the filament channels are randomly located in the pressboard interior, rather than necessarily being connected with each other or initiated from the needle tip. The filament channels tend to grow along the tangential field lines, and some of them are found to have almost bridged electrodes.

Lastly, a qualitative comparison between slow and internal treeing phenomena is made based on the information gathered thus far, as shown in Table 5.3. From the information of Table 5.3, one can realize the effects of voltage level and pressboard condition in determining the failure mechanisms due to interface creeping discharges

Table 5.3 Comparison between slow and internal treeing phenomena

Prerequisites to Occur	Surface tracking	Internal treeing
Pressboard Type	Only Low Density	Both
Pressboard Conditions	New or Slightly Aged	Massively Aged
Threshold Voltage	Low	High
Characteristics	Surface tracking	Internal treeing
Growth Speed	Slow	Fast
Major Phenomena	Surface Carbonization	Internal Carbonization, White Marks, Bubbling
Mechanical Damage	No	Puncture, Swelling
Morphology of Carbonization	Initially, Circular Cluster Lastly, Dendritic Periphery	Cross-layer Filaments
PD Trend	Disappear in the worst cases	Soaring Numbers Varying Patterns
Flashover	No (up to 66 hours)	Yes (within 1 hour)

5.5 Discussion

5.5.1 Discharge Sources of Internal Treeing

Various discharge patterns and discharge signals were found in the process of internal treeing, which indicates multiple discharge types are involved. Although it is currently hard to differentiate their respective contributions in different stages, one can still make some remarks in a qualitative manner. In Stage 1, the major discharges are oil corona discharge and surface discharge in the triple-junction area. In Stage 2, oil corona discharge and surface discharge still exist. However, electron injection starts to have an effect on discharge behaviors. This statement is supported by the presence of large-dense negative PDs in the PRPD pattern and the appearance of large-amplitude PD signals. It is also believed that Stage 2 is the most critical period for the formation of internal treeing. In Stage 3, the partial discharges are dominated by discharges in large-sized cavities. The large size cavity is possibly generated in the puncture near the triple-junction area or in a large bubble. However, the large-sized cavity is very unstable and can be easily split by the electric field. Therefore, one can see a clear diminishing trend of PD quantities in Stage 3. In Stage 4 and Stage 5, the conductive carbonization path is eventually formed, and the bubble discharges in the white marks become the predominant discharges. As the sizes of the bubbles are largely determined by the radii of pressboard macro-capillaries, the amplitudes of PD signals do not vary greatly.

5.5.2 Detection of Surface Tracking

Due to the PD disappearance, it is still a great challenge to detect the evolution of surface tracking using conventional PD measurement techniques. A possible explanation for the PD disappearance is the phenomenon of so-called ‘Swarming Pulsive Micro-Discharges’ (SPMD). SPMD refers to tiny PD pulses of 1 pC or less and was thought to be correlated with the degradation process of epoxy specimen [178, 179]. Measurement devices with much greater frequency ranges, such as ultra-high frequency (UHF) detectors, could be a promising tool to detect the SPMD.

5.5.3 Detection and Monitoring of Internal Treeing

Based on the existing knowledge and obtained test results, a tentative detection and monitoring methodology of pressboard internal treeing due to creeping discharges is proposed in Figure 5.21.

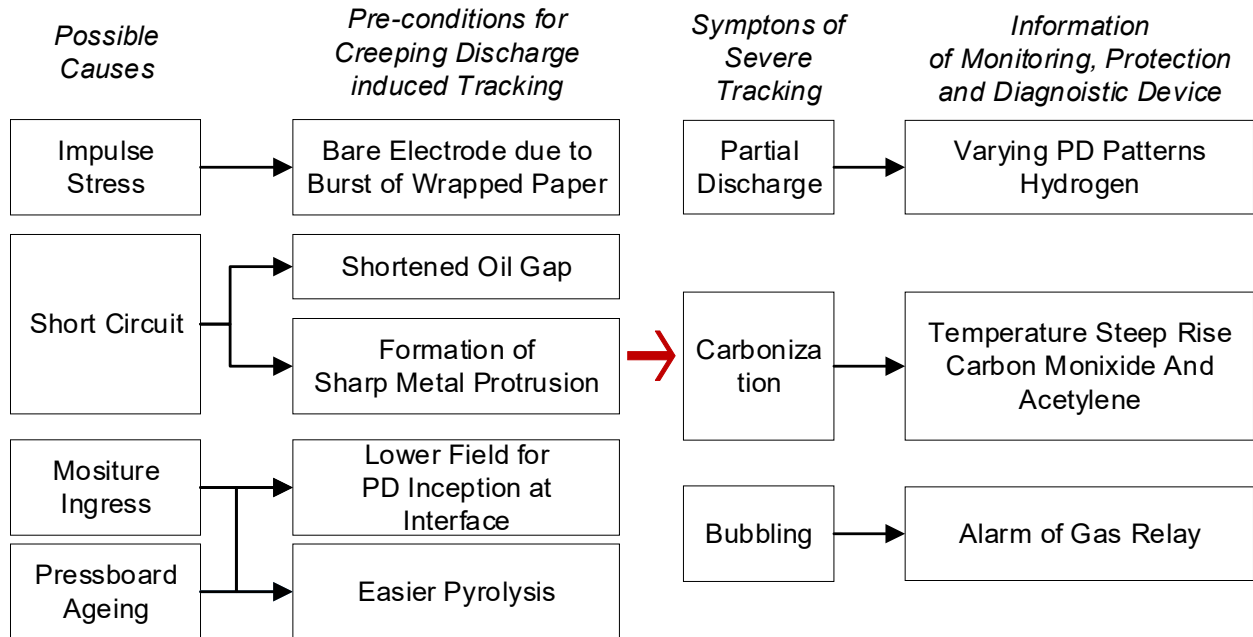


Figure 5.21 Proposed detection and monitoring methodology of pressboard internal treeing

Utmost care must be taken to the power transformers that have been subject to impulse voltages and short-circuit events, as they might result in winding distortion and/or burst of conductor wrapped papers. As a result, the field distributions in the oil/barrier structure could be greatly distorted, and the charge emissions from a metal protrusion enhanced, which in turn facilitates the inception of creeping discharges. Moreover, the transformers having long service history or accidental moisture ingress are more prone to be inflicted by the internal treeing, as the interface discharge inception field is lower and the pyrolysis of pressboard is easier.

Continuous PD measurements, online temperature monitoring, and gas analysis are believed the most effective means to detect an ongoing pressboard internal treeing in a transformer. It is recommended to install optic fiber sensors in pressboards where the maximum tangential field is expected to be present. The key indicator in online temperature monitoring is the abnormal steep temperature rise. The alarm operations of gas relays shall be treated with more caution. Both free gases and dissolved gas should be analyzed, and their results should be carefully compared.

5.6 Conclusions

This chapter sets out to better understand the creeping discharge-induced tracking phenomena of pressboards. Based on the obtained test results, the following conclusion can be drawn from the present study:

- The progressive creeping discharges could generate two distinct faults to the pressboard, i.e., internal treeing (internal treeing) and surface tracking (surface tracking). Massive ageing of pressboard and strong field are the prerequisites for the internal treeing to occur, whereas the surface tracking occurs only with new or slightly aged pressboard with a lower inception voltage. Besides, the fault type is dependent on pressboard density as well. Moreover, the two faults vary greatly from one another in the growth modes and the final failure mechanism.

- The developmental process of internal treeing can be divided into distinct consecutive stages according to the accompanying physicochemical phenomena (sparking, white marks, bubbling, and micro-arcs) and the varying PD characteristics (PD patterns, PD quantities, PD signals, and statistical distributions). By contrast, the development of surface tracking is a straightforward process that features only the augmentation of circular carbonization trace on the pressboard surface and the PD disappearance.
- A generalized four-stage model is proposed to explain the initiation and growth of internal treeing. It is believed that internal treeing is fundamentally driven by the filament-like carbonization tracks in the pressboard interior, which incurs the bubbling effect and the white marks. Moreover, a two-staged model is proposed to explain the onset and growth of the internal carbonization track, which takes into account the important roles of charge emission, pressboard pyrolysis, percolation theory, and electro-thermal process. Furthermore, the bubbling effects of internal treeing are qualitatively evaluated against pressboard aging and discharges.
- It is found the expansion of internal treeing could be characterized by a steep temperature rise on the pressboard surface. Hydrogen is the principal faulty gas in both oil samples and the bubbles. Nevertheless, the concentrations of hydrogen in free gases are much greater than those in oil-dissolved gases, and the interpretations of free and oil-dissolved gases using Duval's Triangle method direct to different diagnosis results. Accordingly, a tentative detection methodology of pressboard internal treeing is proposed. Continuous PD measurements, online temperature monitoring, and gas analysis (oil-dissolved and free gases) are believed the most effective means to detect an ongoing pressboard internal treeing in a transformer. However, due to the PD disappearance, it is still hard to detect a severe surface tracking fault using the conventional PD detection method.

6 INFLUENCES OF TEMPERATURE AND STRESS TYPE ON AC CREEPING DISCHARGES

6.1 Introduction

Temperature is a fundamental factor of the electrical insulation system. It not only induces insulation ageing but also influences the physicochemical, electrical, and dielectric properties of insulation materials. In fact, the major insulation system of a transformer operates in a temperature-varying environment. The typical temperature rise distribution model of an oil-natural cooled transformer is given in Figure 6.1 [180], where $\Delta\theta_b$, $\Delta\theta_{om}$, $\Delta\theta_w$, $\Delta\theta_o$ and $\Delta\theta_h$ denote the bottom-liquid temperature rise, average liquid temperature rise, average winding temperature rise, top-liquid temperature rise, and hot-spot temperature rise, respectively; H is the hot-spot factor, and g is the average winding gradient.

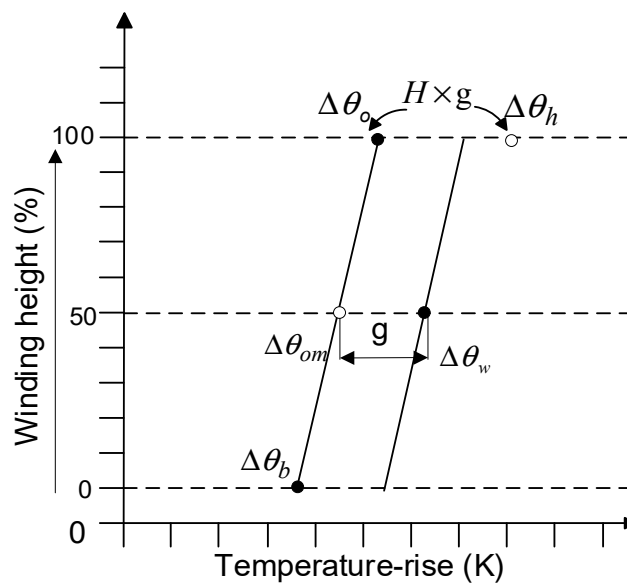


Figure 6.1 Temperature rise distribution model for ON cooling methods

Owing to the winding temperature gradient, it is inevitable for the transformer pressboard barriers, its surface, in particular, to be exposed to varying temperatures in service as well. Besides, temperatures have different effects on liquid and solid insulations. For instance, elevated temperatures can suppress the PD intensity in oil [181] whereas facilitating the PD inception of solid materials [182]. Moreover, it is revealed in Chapter 5 that the development of pressboard tracking is a thermally-governed process. Therefore, it is believed that the temperature inhomogeneity of transformer major insulation system could influence the interface phenomena and thus having a profound effect on interface creeping discharge as well as its related failures.

However, most of the previous researches in this field was confined to a limited scope: either a single homogeneous material or the short-time interface electric strength. Thus far, the influence of temperature on the long-term progressive oil-pressboard creeping discharges has been scarcely studied. To fill the gap, therefore, this chapter is dedicated to the investigations of interface creeping discharges at different temperatures. Moreover, it is hypothesized that the waveform of applied electric stress could also influence the governing processes of creeping discharge as well, e.g., the heat dissipation and discharge inception. Therefore, it is also of special interest to explore the effects of stress type on interface creeping discharge as well.

This chapter is subdivided into four major sections. Section 6.2 focuses on the technical considerations of test temperatures and stress waveforms and ends with a brief introduction of test set-up and sample information. Section 6.3 presents all the experimental results. In Section 6.3, it firstly deals with the effects of temperature on pressboard dielectric properties. Afterwards, the influences of temperature and stress waveforms on interface creeping discharge are studied, in which the emphasis emphases are put on the failure mechanisms and long-term PD characteristics. At last, a new method based on synchronous PD and online dielectric measurements is proposed to detect the initiation and growth of pressboard internal treeing. Section 6.4 discusses the test results, and Section 6.5 gives the concluding remarks of this chapter.

6.2 Experimental Setup and Measurement Techniques

6.2.1 Selection of Test Temperatures

The temperature rises of in-service transformers shall comply with specific requirements. The temperature rise limits of a transformer in steady conditions are given in Table 6.1 [180].

Table 6.1 Temperature rise limits (ambient temperature: 20 °C)

Requirements for	Temperature Rise Limits (K)
Top Insulating Liquids	60
Average Winding	65 (ON and OF Cooling Systems) 70 (OD Cooling System)
Hot-Spot Winding	78

As shown, the top-liquid temperature of a transformer with normal insulation materials shall not exceed 80 °C under continuous rated power. It is assumed that the temperature profile of the pressboard barrier is equivalent to that of oil bulk, considering their extremely intimate contact. Besides, as recommended in IEEE Std C57.100-2011 [183], a temperature interval of 20 °C is the priority option for thermal evaluations of oil-immersed transformer insulation systems. Accordingly, the test temperatures are determined: 20 °C, 40 °C, 60 °C, and 80 °C, respectively.

6.2.2 Selection of Stress Waveforms

Both constant stress and progressive stress are adopted for evaluating the electrical endurance of insulating materials under AC voltage. Either stress has its own pros and cons. The constant-stress test has an advantage in shortening test times over the progressive-stress test; whereas, the data of progressive-stress tests are of higher quality due to their comparatively low dispersions [184]. For a comprehensive study, therefore, it is necessary to employ both stresses to examine the electric strength of the oil/pressboard interface.

The waveforms of step-wise (progressive) and constant stresses are shown in Figure 6.2. The constant-stress voltage is mainly defined by the constant voltage level (U_C); whereas, the step-stress voltage is shaped by multiple parameters, i.e., the initial voltage level (U_0), the voltage increment (ΔU), the step duration time (t), and the voltage rise time (Δt). To select the appropriate parameters, one must know the test samples' short-time electric strengths [185]. Therefore, this research firstly determined the interface short-time strengths under ramp stress and then customized the voltage parameters for constant-stress and step-stress voltages at each temperature, respectively.

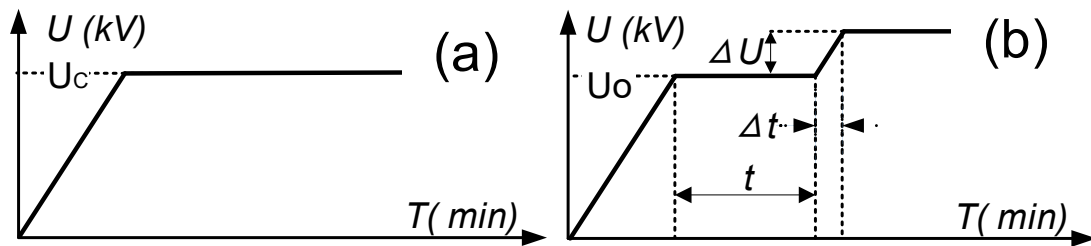


Figure 6.2 Test voltages; a) constant stress; b) step stress

To obtain the appropriate waveform parameters, however, one has to carry out a set of preliminary tests to determine the short-time electric strength of insulation materials [185]. In this context, the short-time electric strength of the oil/pressboard interface is characterized by two fundamental parameters: flashover voltage and PD inception voltage. Therefore, this chapter firstly implemented ramp-stress tests to determine the flashover voltages and PD inception voltages of the oil/pressboard interface at different test temperatures. Afterwards, the stress waveform parameters were customized for each individual test temperature.

6.2.3 Sample Preparation and Test Setup

All pressboard samples were processed following the procedures depicted in Section 3.3.3, and the oil samples were completely dehydrated and degassed.

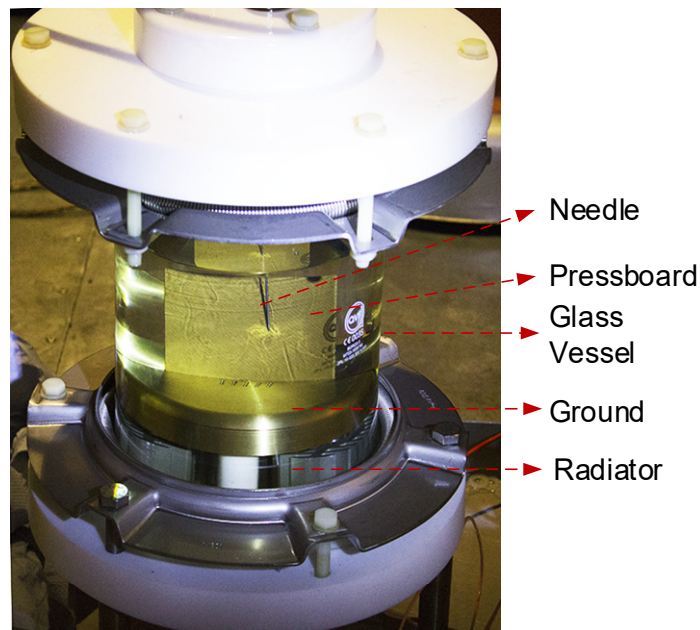


Figure 6.3 Test cell for creeping discharge tests under different temperatures

The electrode configurations shown in Figure 3.2 were adopted to apply high tangential stress on the oil/pressboard interface. PD signals were measured according to IEC 60270:2000, and the test circuit was constructed as shown in Section 3.4.5. The off-line dielectric properties of pressboard samples were measured prior to high voltage tests. Moreover, the test setup depicted in Section 3.4.4 was utilized to on-line measure the dielectric properties of the oil/pressboard interface during tracking. Furthermore, the high voltage test circuit, the oil heating system, and the temperature monitoring system were illustrated in Section 3.5.2. All tests were carried out in a well-shielded area. Figure 6.3 displays the actual image of the test cell used for creeping discharge tests in this investigation.

6.3 Test Results

6.3.1 The Influences of Temperature on Pressboard Dielectric Properties

The triple-electrode shown in Section 3.1.3 and Omicron CPC 100 were used to implement the measurements. The electrode and pressboard specimens were contained in an oil-filled hermetic glass vessel and then heated in an air-circulated thermal oven. The triple-electrode was connected to Omicron CPC 100 via an epoxy-resin wall bushing mounted on the thermal oven. Prior to measurements, the vessel was kept at the test temperature for at least 60 minutes for homogeneous temperature distribution. The test voltages range from 0.5 kV to 5 kV with an interval of 0.5 kV, and the test temperatures are 20 °C, 40 °C, 60 °C, and 80 °C. For eliminating probabilistic errors, five measurements were carried out at each measuring point, and the average values were used for evaluation. The capacitance c), leakage current a), and dissipation factor ($\tan\delta$) of pressboard samples at different temperatures are shown in Figure 6.4 to Figure 6.6.

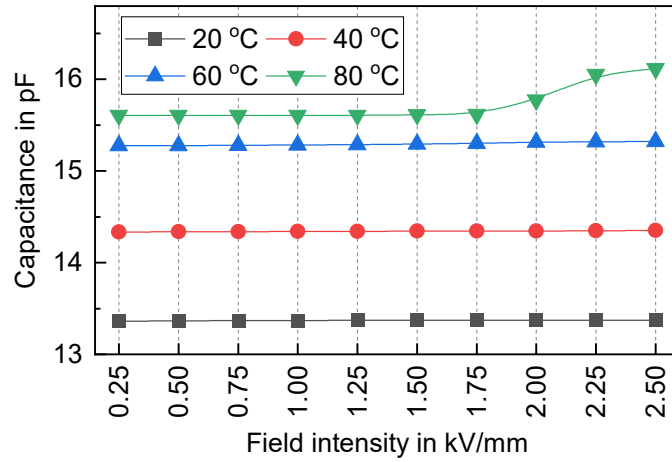


Figure 6.4 Capacitance of pressboard samples versus temperatures

As known, for a given insulation geometry, its capacitance C is solely determined by its relative permittivity:

$$C = \varepsilon_r \varepsilon_0 \frac{A}{d} \quad (6.1)$$

where, ε_r , ε_0 , A and d denote relative permittivity, vacuum permittivity, electrode area, and inter-electrode spacing, respectively. As shown in Figure 6.4, the capacitance of the pressboard increases with temperature, indicating a positive correlation between its relative permittivity and ambient temperature. Moreover, the pressboard capacitance is independent of field intensity at low temperatures. More specifically, at 20 °C, 40 °C, and 60 °C, the pressboard capacitance varies barely as the test voltage increases. Nevertheless, at a high temperature (80 °C), the pressboard capacitance stays constant under low field but changes abruptly when field intensity reaches 1.75 kV/mm. The results suggest the capacitance of pressboard is jointly determined by electric field and temperature, where the influence of temperature is readily observable, but the effect of electric field manifests itself only at high temperatures. In other words, there is probably a synergistic effect between high temperature and strong field in altering the dielectric properties of pressboard samples.

Moreover, as shown in Figure 6.5, the leakage current is linearly proportional to field intensity. At each test temperature, the leakage current grows steadily as field intensity increases. Besides, the inter-temperature differences in leakage current become ever greater as field intensity increases.

With respect to the dissipation factor, the synergy between high temperature and strong field is even

more pronounced. As shown in Figure 6.6, the dissipation factors of the pressboard appear independent of field intensity and are almost the same under low temperatures (20 °C, 40 °C, and 60 °C). At 80 °C, however, the dissipation factor is obviously higher and increases steeply when the voltage intensity exceeds 1.75 kV/mm. As stated in Chapter 5, the heat due to dielectric dissipation is an important promoting force of tracking. Therefore, it is postulated that the tracking phenomenon of pressboard might be more readily initiated under high temperatures.

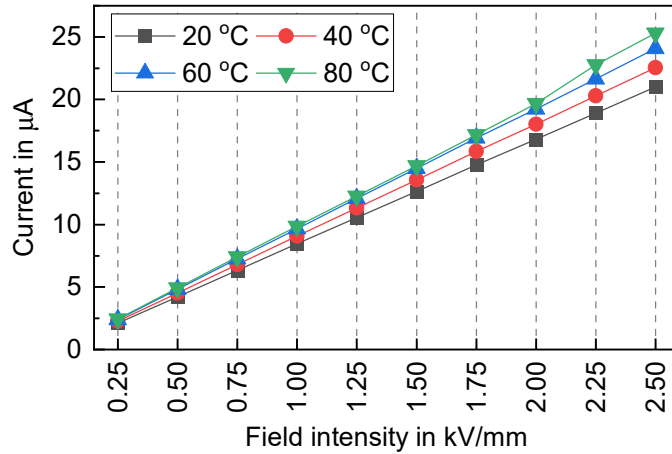


Figure 6.5 Leakage current of pressboard samples versus temperatures

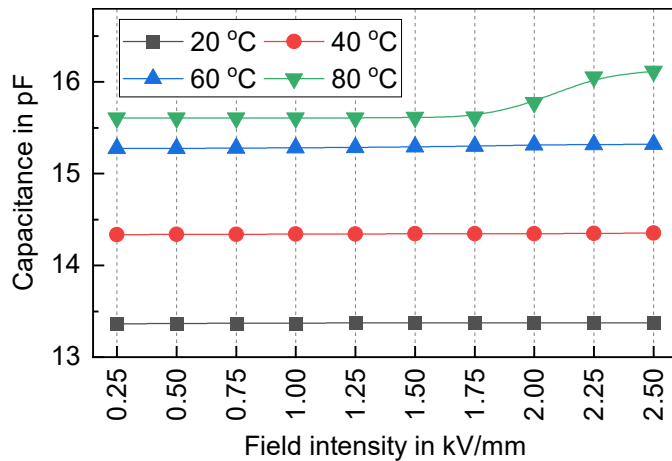


Figure 6.6 Dissipation factor of pressboard samples versus temperatures

6.3.2 Short-Time Electric Strength of Oil/Pressboard Interface under Ramp Stress

In the preliminary tests, an AC ramp stress, with a rising steepness of 1 kV/s, was applied on the oil/pressboard interface to determine its short-time flashover and PD inception voltages at different temperatures. The gap distance is 35 mm. Moreover, the breakdown voltages of the oil gap were measured as well for a comparative study. Nevertheless, the spacing of the oil gap is downsized to 30 mm because of the limited output capacity of the test transformer. In order to obtain a homogenous temperature distribution, the samples were kept at the test temperature for at least 30 minutes prior to tests. Besides, a waiting period of 5 minutes was held between consecutive tests to preclude the influences of previous events. Ten measurements were carried out at each test temperature, and the average values were used for evaluations. Test results are shown in Figure 6.7 and Figure 6.8.

As shown, the short-time electric strength of either oil-pressboard interface or pure oil gap is strongly dependent on temperature. The interface flashover voltage increases steadily with ascending oil temperature: from 40 kV at 20 °C to 60 kV at 80 °C. Similarly, in spite of some fluctuations at 40 °C and 60 °C, the interface PD inception voltage increases from 26 kV at 20 °C to 37 kV at 80 °C. The

same trend is also found in oil gap breakdown data: the pure oil gap breakdowns on average at 38 kV when the temperature is 20 °C and at 60 kV when the temperature is raised to 80 °C, respectively.

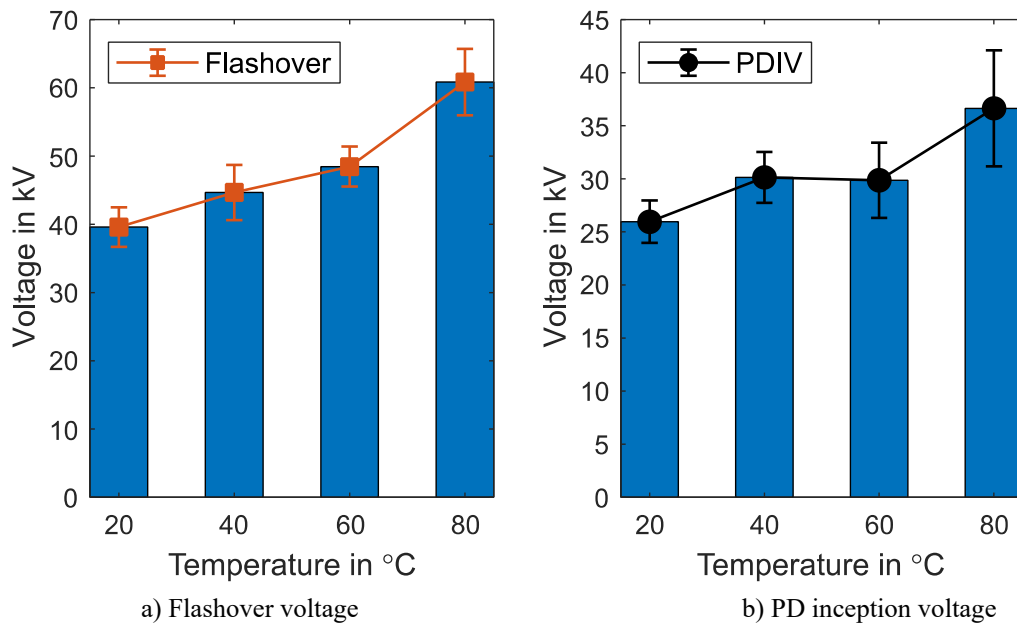


Figure 6.7 Short-time electric strengths of interface versus temperatures (35 mm)

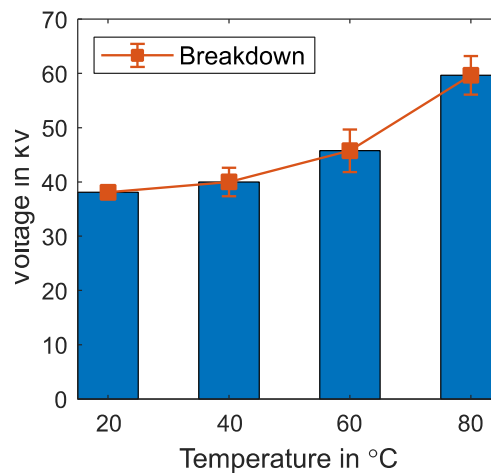


Figure 6.8 Short-time electric strengths of oil gap versus temperatures (30 mm)

As discussed in Section 4.3.4, interface flashover is, in essence, a liquid-controlled phenomenon, for the liquid phase is the weak point under the short-term stressing. Therefore, it is inferred that the increase in interface flashover voltage is a consequence of an electrically ever-stronger oil bulk with rising temperature. As known, the relative humidity of oil decreases with rising temperature. In turn, the declined oil relative humidity will offset other negative outcomes of high temperatures, such as smaller oil density, and thus leading to a higher breakdown voltage. However, as pointed out in previous researches, the positive correlation between oil electric strength and temperature is confined to a specific temperature range [186, 187] and shall not be simplistically extrapolated.

Moreover, it is declared in IEEE Std 930:2004 that the breakdown of liquids may follow the Gumbel distribution [188]. Like the renowned Weibull distribution, Gumbel distribution is a typical extreme value distribution and has been widely used for analyzing ageing failure and system reliability. Since the interface flashover, in this case, is mainly determined by oil strength, the Gumbel distribution is used for the statistical analysis of interface flashovers as well.

The probability density function (PDF) $P(x)$ and cumulative distribution function (CDF) $D(x)$ of Gumbel distribution are expressed as follows:

$$P(x) = \frac{1}{\beta} \exp \left[\frac{x - \alpha}{\beta} - \exp \left(\frac{x - \alpha}{\beta} \right) \right] \quad (6.2)$$

$$D(x) = 1 - \exp \left[-\exp \left(\frac{x - \alpha}{\beta} \right) \right] \quad (6.3)$$

where α is the location parameter, and β is the scale parameter. Under this context, x is the breakdown voltage, and the unit of α and β is Volt. The Gumbel probability plots of interface flashover and oil gap breakdown data are shown in Figure 6.9 and Figure 6.10, respectively. As displayed, the data of both interface flashover and oil gap breakdown fit Gumbel distribution quite well. Moreover, the shape of the Gumbel plot of interface flashover is somewhat similar to that of the oil gap breakdown, which suggests a close relation between the strength of the interface with that of oil.

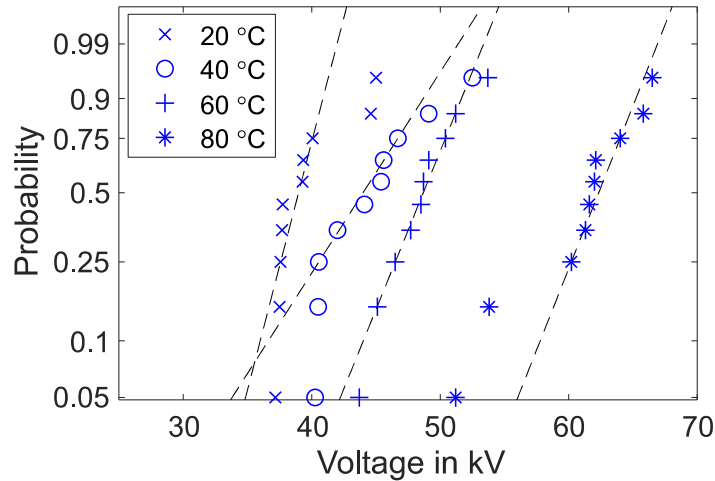


Figure 6.9 Gumbel plot of interface flashover voltage (35 mm)

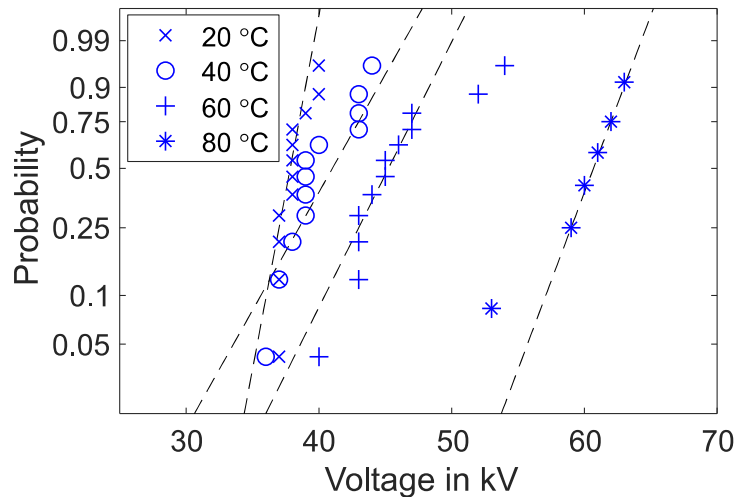


Figure 6.10 Gumbel plot of oil gap breakdown voltages (30 mm)

In addition, The Gumbel location and scale parameters of interface flashover and oil gap breakdown are summarized in Table 6.2. As test temperature rises, the location parameter α , i.e. the mode of breakdown voltage in this case, shows clearly an upward trend in both cases.

Table 6.2 Location and scale parameters of Gumbel distributions

Temp. (°C)	Oil Gap (30 mm)		Interface (35 mm)	
	α	β	α	β
20	38.6350	1.1043	41.1092	3.1063
40	41.2803	2.3623	46.6883	4.0432
60	47.7768	4.2065	49.8630	2.7112
80	61.0611	2.1511	62.9167	3.3824

6.3.3 Long-term Creeping Discharges under Constant Stress

Subsequently, constant-stress tests were carried out at different test temperatures. The desired constant voltage level (U_c) shall satisfy the following criteria: it suffices to generate sustained partial discharges for the electrically strongest sample (test sample at 80 °C) and, in the meanwhile, does not cause premature breakdowns for the weakest one (test sample at 20 °C). Therefore, through a comparative analysis of the short-time electric strength data obtained under ramp stress, the constant voltage level is set to be 35 kV. The AC voltage was raised from null to U_c with a rising steepness of 1 kV/s, and three repetitive tests were carried out at each test temperature. The failure statistics of constant-stress creeping discharge tests are presented in

Table 6.3.

Table 6.3 Creeping discharge failure statistics under constant stress

Temp (°C)	Specimen No.	Breakdown Time (Minute)	Failure Mechanism
20	1	27	Flashover
	2	8	Flashover
	3	18	Flashover
40	1	18	Flashover
	2	6	Flashover
	3	9	Flashover
60	1	>150	Surface tracking
	2	>150	Surface tracking
	3	>150	Surface tracking
80	1	24	Internal treeing
	2	51	Internal treeing
	3	35	Internal treeing

As displayed, the temperature has a decisive role in determining the failure mechanism. At low temperatures (20 °C and 40 °C), all specimens fail due to interface flashovers and no trace of tracking is detected; at 60 °C, on the contrary, all specimens fail due to surface tracking (surface tracking) but

do not breakdown even after 150 minutes of discharges; at 80 °C, all specimens fail due to internal treeing (internal treeing) and subsequent interface flashovers.

At low temperatures (20 °C and 40 °C), the withstand time is dependent on test temperature as well. In general, the specimens at 20 °C can withstand creeping discharges longer than those at 40 °C. This finding is particularly interesting when compared with the results of ramp-stress tests. Under ramp stress, the oil/pressboard interface has a lower electric strength at 20 °C than at 40 °C.

The contradictory results imply that the impact of temperature on interface electric strength would vary with stress waveforms. As explained previously, due to a lower relative humidity of oil bulk, the interface has a greater flashover voltage at a higher temperature under ramp stress. However, the ramp-stress tests evaluate only the intrinsic strength of insulating oil and do not take into consideration other processes. In contrast, more factors could come into effect in the constant-stress test because of its comparatively long stressing time. For instance, the raised temperature could enhance the gassing tendency of insulating oil and thus facilitating bubble formation, which in turn increases flashover probability and shortens the withstand time.

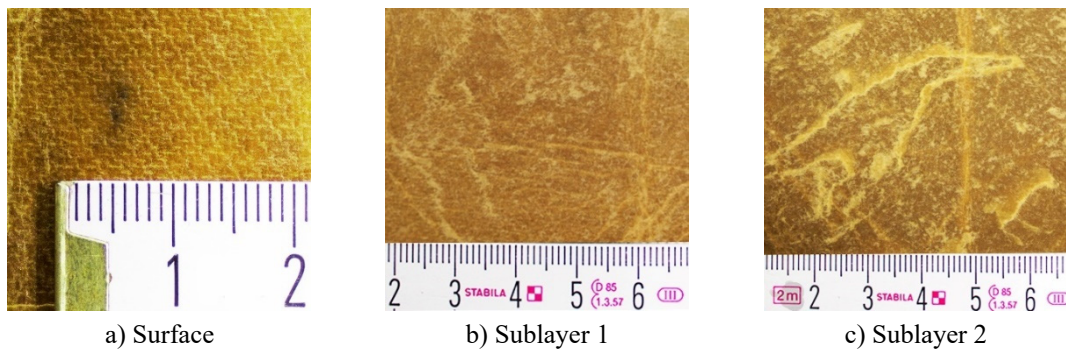


Figure 6.11 Failed pressboard specimen at 60 °C under constant stress

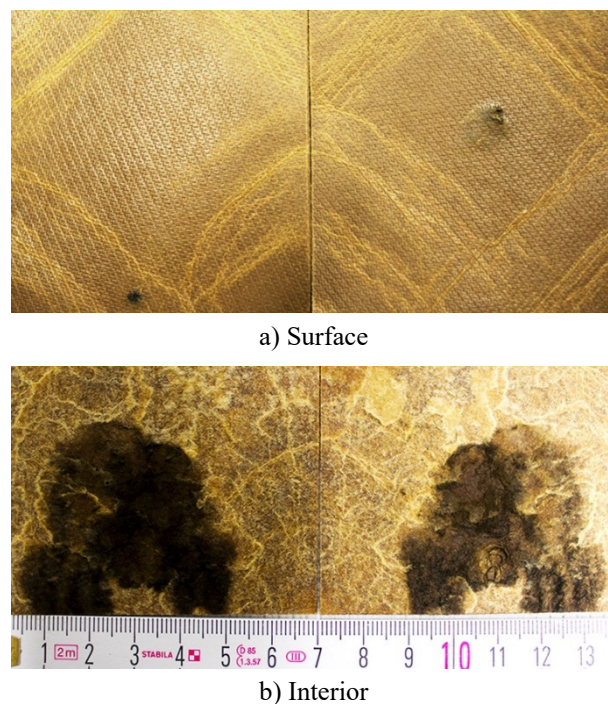


Figure 6.12 Failed pressboard specimen at 80 °C under constant stress

Besides, temperature also determines the severity of tracking. For an intuitive illustration, the post-mortem images of failed pressboards at 60 °C and 80 °C are shown in Figure 6.11 and Figure 6.12,

respectively. As shown, only a small carbonization trace emerges in the triple-junction area of the pressboard surface after 150 minutes of stressing at 60 °C. However, no carbonization is found in the interior after dissecting the pressboard samples, which indicates the creeping discharge-induced surface tracking is confined on the pressboard surface. Contrastingly, the carbonization area racking expands enormously in the interior of the pressboard specimens stressed at 80 °C.

As demonstrated in Section 6.3.1, high temperature, together with a strong field, can considerably change the dielectric properties of the pressboard sample, the dissipation factor in particular. Moreover, as discussed in Section 5.3.2, the growth of tracking is a thermal-electrical process that is subject to multiple factors, such as field intensity, stress time, and dielectric dissipation. Therefore, it can be concluded that the difference in tracking type and tracking severity is mainly due to the sharp rise of the dissipation factor of the pressboard at 80 °C. Besides, the weakened heat dissipation capability of oil could probably exacerbate the tracking even further.

Furthermore, with respect to the specimen stressed at 60 °C, although its dissipation factor is not significantly higher than those at 20 °C and 40 °C, its electric strength is definitely enhanced. The enhanced strength leads to a prolonged stressing time and thus enabling the accumulation of discharge energies on the pressboard surface. In consequence, tracking is eventually formed. However, the extent of tracking is insufficient to bridge electrodes but enough to lower the local field intensity. Therefore, none of the specimens stressed at 60 °C fail due to flashovers.

The PRPD pattern and PD quantities of a full creeping discharge incident at 20 °C are given in Figure 6.13 and Figure 6.14, respectively. The whole test lasts for 27 minutes, and every sampling point lasts for 30 seconds. As discussed in Chapter 4, a typical tracking-free creeping discharge is actually composed of two fundamental types of discharge: oil corona discharge and surface discharge. Accordingly, its PRPD pattern can be deemed as a superposition of those discharges: the distributions of both positive and negative PD pulses span two quadrants, and their respective peaks are located near the crests of voltage waveforms. Compared with positive pulses, the negative pulses exhibit smaller magnitudes but higher repetition rates.

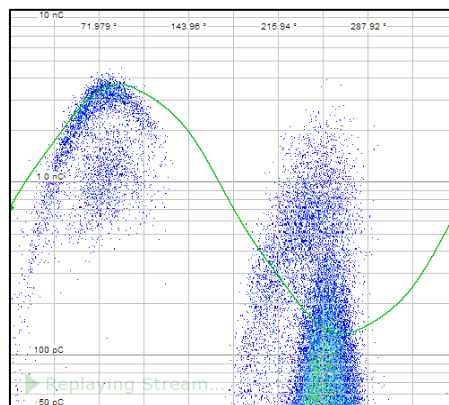


Figure 6.13 PRPD at 20 °C under constant stress

With respect to PD magnitudes, as displayed in Figure 6.14, the positive pulses are always stronger than their negative counterparts: the maximum positive pulses q_{max}^+ are in the order of 4 nC while the maximum negative pulses q_{max}^- are in the range of 2 nC to 3 nC. The difference becomes more pronounced in respect of average magnitude. In spite of fluctuations at the early stages, the average magnitudes of positive pulses q_{ave}^+ are eventually stabilized around 2 nC; whereas, the average magnitudes of negative ones q_{max}^- are around merely 150 pC: less than one-tenth of those of positive ones. However, negative pulses outperform positive ones in respect of repetition rate. The numbers

of negative pulses num^- are always 6 to 8 times of those of positive ones num^+ . Approaching the imminent flashover, nevertheless, the numbers exhibit a converging trend. Moreover, the PD power at 20 °C scarcely exceeds 0.5 mW during the test but abruptly increases to over 2 mW at the end stage, indicative of the forthcoming flashover. It is found the sharp rise of PD power can be solely ascribed to an intensification of positive discharges, for the magnitudes of negative discharges are constant, and their numbers are even diminished.

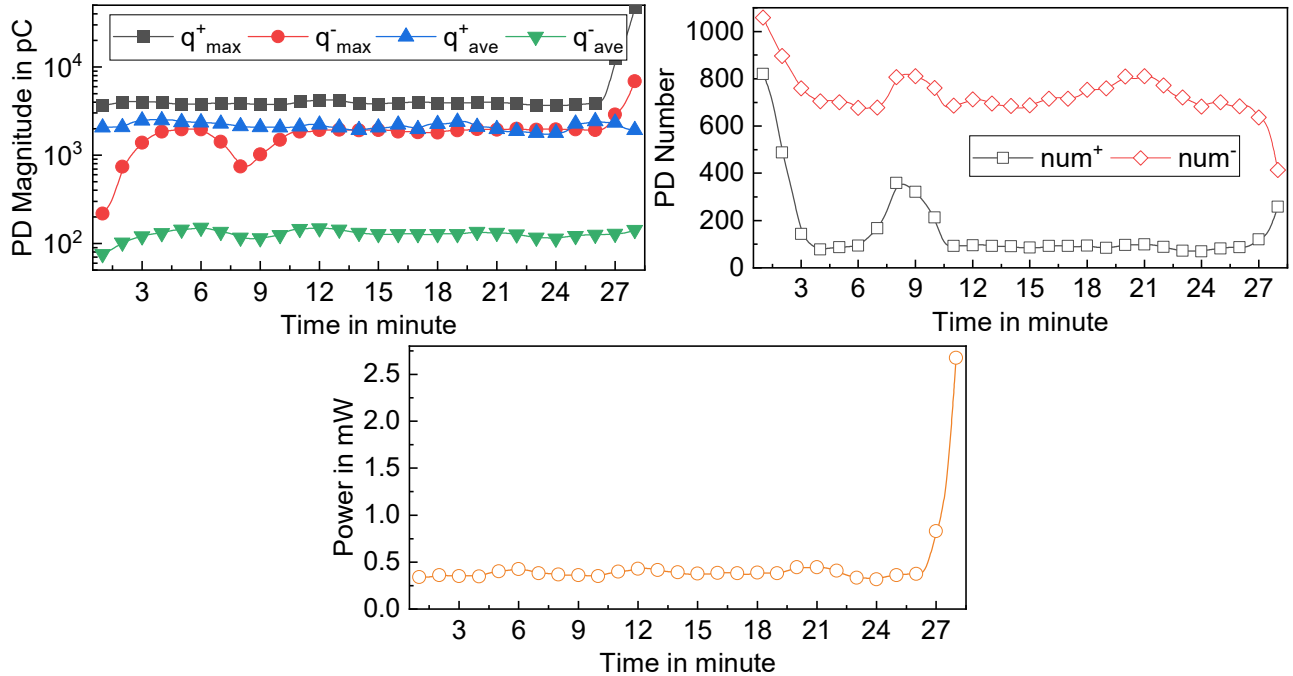


Figure 6.14 PD Quantities at 20 °C under constant stress

The PRPD discharge pattern and PD quantities of a full creeping discharge incident at 40 °C are given in Figure 6.15 and Figure 6.16, respectively. The whole test lasts for 18 minutes, and every sampling point lasts for 30 seconds.

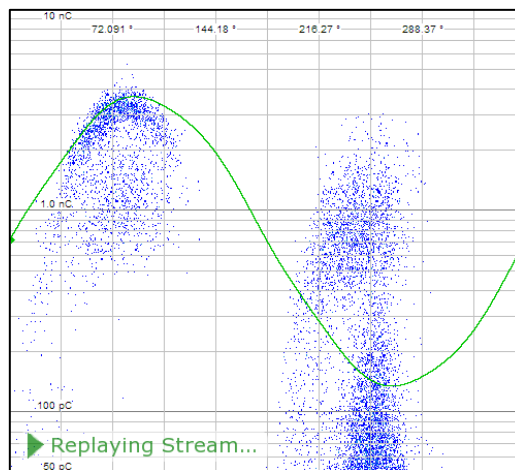


Figure 6.15 PRPD at 40 °C under constant stress

The PRPD at 40 °C is quite approximate to that at 20 °C, suggesting the discharge pattern is hardly altered by such a temperature rise. Besides, the scenario of PD magnitudes at 40 °C is also comparable to that at 20 °C. However, a major distinction in PD numbers can still be drawn between 20 °C and 40 °C. Owing to the reduction of negative PD number num^- , the PD number gap between positive and negative pulses at 40 °C is considerably narrowed: the numbers of negative pulses are merely 3

to 4 times those of positive ones. Therefore, it could be inferred with caution that the temperature rise might repress the activity of negative discharges. Nevertheless, the trends of PD numbers and PD power at 40 °C are still similar to those at 20 °.

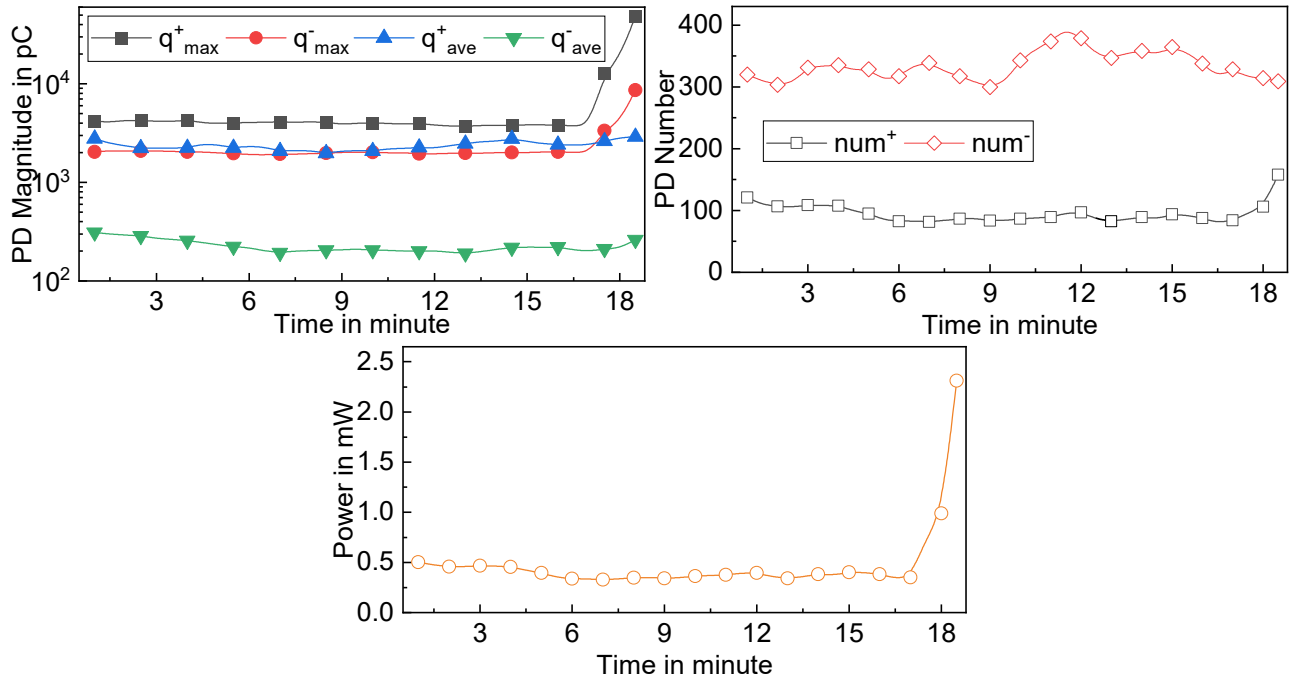


Figure 6.16 PD Quantities at 40 °C under constant stress

The PRPD pattern and PD quantities of a full creeping discharge incident at 60 °C are given in Figure 6.17 and Figure 6.18, respectively. The whole test lasts for 150 minutes, and every sampling point lasts for 30 seconds. In Figure 6.17, the PRPDs of different sampling periods starting from 1 minute, 60 minutes, and 120 minutes are compared, respectively.

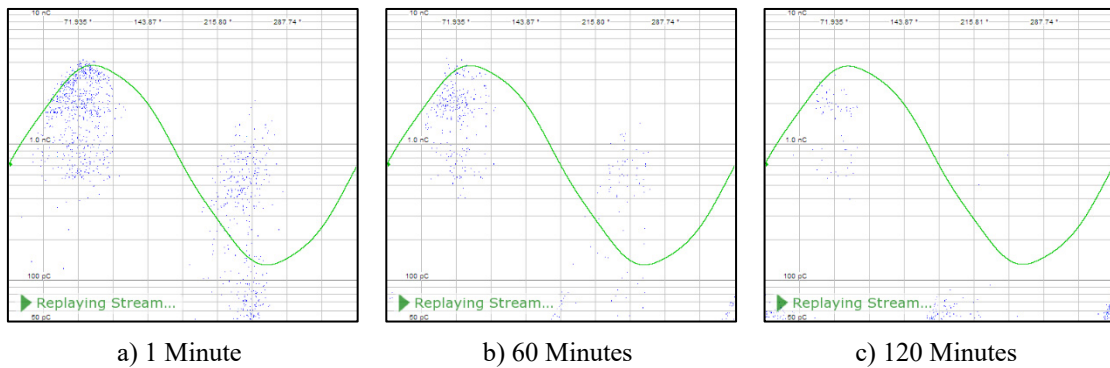


Figure 6.17 PRPD at 60 °C under constant stress.

As stated previously, the failure mechanism has been utterly changed when the test temperature increases to 60 °C. It is clearly shown in Figure 6.17 that creeping discharges at 60 °C exhibit ever-weaker PD activities with time. The descending trend of creeping discharges can be mainly ascribed to the formation of tracking on the pressboard surface.

The descending trend of creeping discharge is clearly reflected in the variations of PD quantities as well. As displayed in Figure 6.18, all magnitudes decline with test time. For instance, the maximum magnitude of the negative pulse q_{max}^- falls from 1000 pC at the beginning stages to merely 200 pC at the end stage. Moreover, in spite of several protrusions for unknown reasons, the PD numbers are maintained at low levels throughout the test. As a consequence, the PD power almost vanishes at the

end of the test. Furthermore, compared with the scenarios at 20 °C and 40 °C, the most appreciable changes are associated with negative PD pulses. In addition to the diminishing maximum magnitudes, its number is substantially decreased as well. Therefore, it is inferred that the descending trend of creeping discharge at 60 °C is caused by mitigation of negative partial discharges.

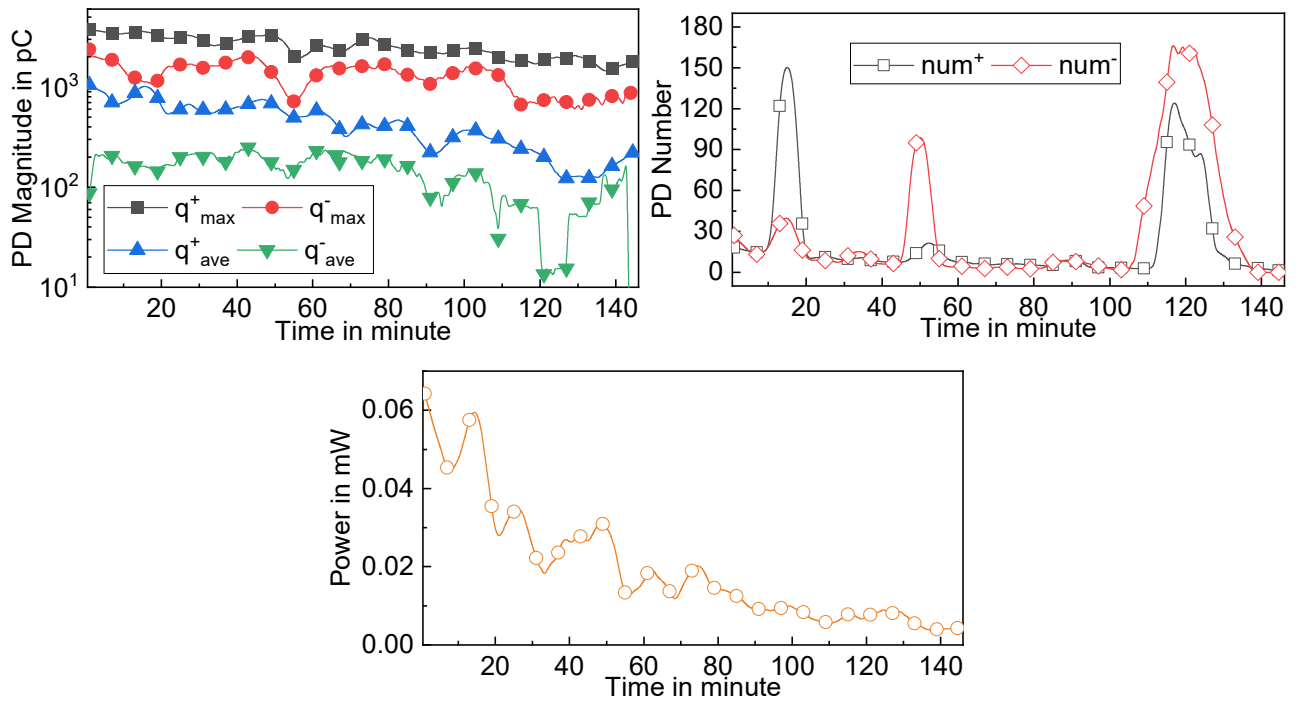


Figure 6.18 PD Quantities at 60 °C under constant stress

The PRPD discharge pattern and PD quantities of a full creeping discharge incident at 80 °C are given in Figure 6.19 and Figure 6.20, respectively. The whole test lasts for 35 minutes, and every sampling point lasts for 30 seconds.

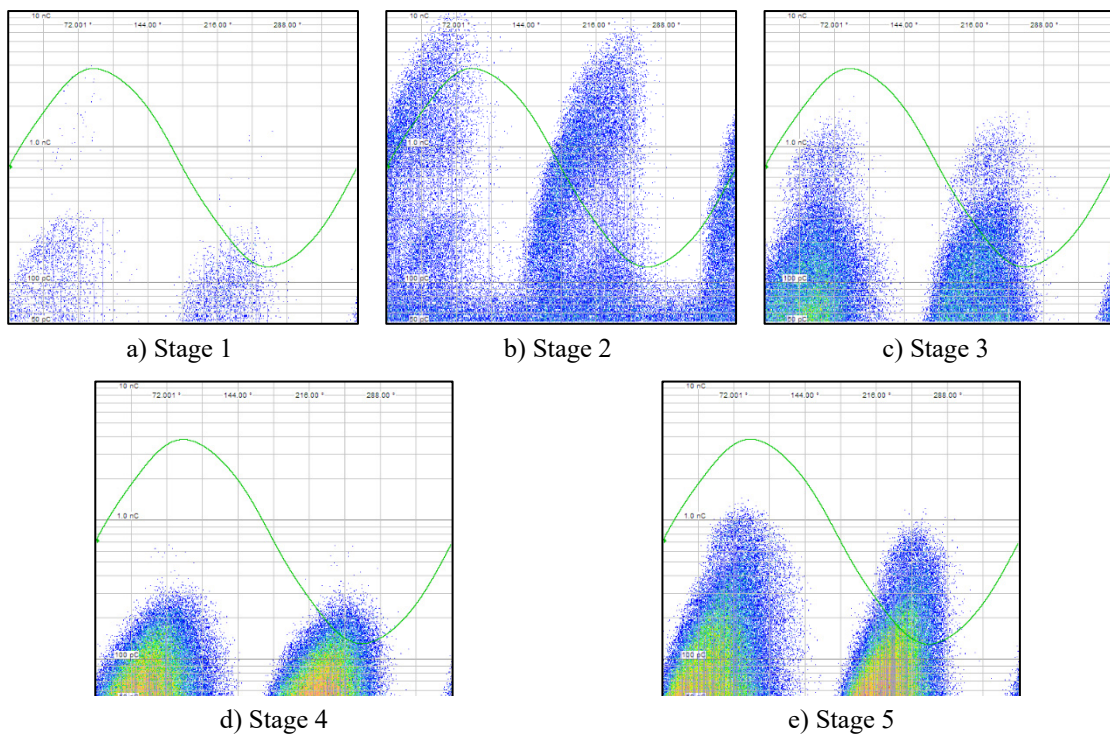


Figure 6.19 PRPD at 80 °C under constant stress

As shown in Figure 6.19, the temporal variations of the PRPD pattern at 80 °C are highly similar to

those of massively-aged pressboards with internal treeing. The fundamental cause of PRPD variations is that various discharge types dominate at different stages. A detailed investigation and an in-depth discussion of this phenomenon have already been given in Chapter 5.

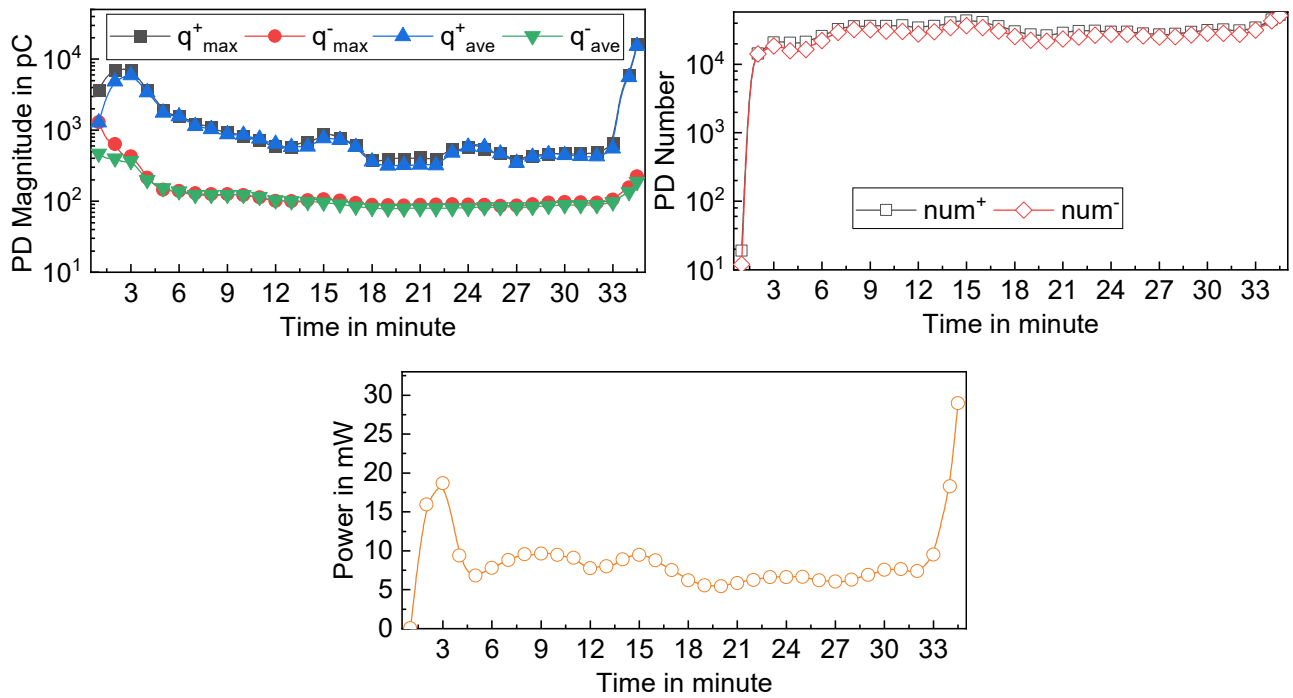


Figure 6.20 PD Quantities at 80 °C under constant stress

Moreover, as shown in Figure 6.20, the temporal variations of PD quantities at 80 °C resemble those of massively-aged pressboards with tracking as well. From the inception of discharges, PD magnitudes and numbers grow drastically and reach their respective local maxima. Afterwards, both quantities decline to varying extents. Subsequently, the PD magnitudes continue to decline, whereas the PD numbers begin to increase again steadily. Lastly, approaching the imminent flashover, both quantities rise exponentially till the end of the test.

Furthermore, it is noteworthy that the PD power at 80 °C is substantially higher than any of those at lower temperatures. Such a great amplitude of power is mainly due to the fact that the PD numbers at 80 °C are several orders of those at lower temperatures.

6.3.4 Long-term Creeping Discharge under Stepwise Stress

Prior to any tests under stepwise-stress tests, it is an imperative step to determine the appropriate waveform parameters. As a matter of fact, the task is somewhat a matter of subjectivity. Nevertheless, there are still basic rules to obey. Firstly, the voltage rise time (Δt) should be negligible compared with the voltage duration time (t) [189]. Secondly, the initial voltage level (U_0) should be lower than the short-time PD inception voltage. Thirdly, the voltage increment (ΔU) should be selected according to the short-time flashover voltage and initial voltage level [190].

Therefore, the initial voltage level (U_0) is determined through rounding off 80 % of the mean value of PDIVs; the voltage rise time (Δt) is set to be 10 seconds and the voltage duration time (t) is set to be 600 seconds; the voltage increment (ΔU) is set to be 2 kV and the voltage rising steepness (r) is set to be 1 kV/s. The detailed waveform parameters are enlisted in Table 6.4.

Table 6.4 Voltage parameters of step-wise stress tests

Temp. (°C)	U_0 (kV)	ΔU (kV)	Δt (s)	t (s)	r (kV/s)
20	20	2	10	600	1
40	25	2	10	600	1
60	25	2	10	600	1
80	30	2	10	600	1

Afterwards, five tests were implemented at each test temperature, and the failure statistics are presented in

Table 6.5.

Table 6.5 Creeping discharge failure statistics under stepwise stress

Temp. (°C)	Specimen No.	Breakdown Voltage (kV)	Breakdown Time (Minute)	Failure Mechanism
20	1	38	85	Flashover
	2	42	121	Flashover
	3	44	134	Flashover
	4	38	95	Flashover
	5	36	85	Flashover
40	1	37	65	Flashover
	2	37	67	Flashover
	3	37	64	Flashover
	4	37	62	Flashover
	5	35	54	Flashover
60	1	37	66	Flashover
	2	43	99	Flashover
	3	41	86	Flashover
	4	51	140	Surface tracking and Flashover
	5	>60	>180	Surface tracking
80	1	42	65	Flashover
	2	50	107	Flashover
	3	56	131	Surface tracking and Flashover
	4	>60	>180	Surface tracking
	5	>60	>160	Surface tracking

As can be seen, the influence of temperature on failure mechanism under stepwise stress is quite evident as well. At low temperatures (20 °C and 40 °C), all specimens fail due to tracking-free flashovers. At 60 °C, three specimens fail due to tracking-free flashover, one due to surface tracking (surface tracking), and one due to tracking and flashover. At 80 °C, two specimens fail due to

tracking-free flashover, two due to surface tracking, and one due to tracking and flashover. No incident of internal treeing (internal treeing) is found with all test specimens.

Comparing the results of constant-stress and stepwise-stress tests, it is found the failure mechanism is also subject to stress type. At high temperatures (60 °C and 80 °C), a noteworthy distinction between stress types is the tracking type and tracking severity of the pressboard. Under constant stress, all the test specimens are inflicted with internal treeing at 80 °C and the specimens failed due to an electrodes-bridging conductive carbonization channel. Under stepwise stress, on the contrary, no tracking of such a scale is found in any case of carbonized pressboards.

As shown in Figure 6.21, there are no significant differences in tracking severity between the specimens that failed due to tracking without flashover and those that failed due to tracking with flashover at 80 °C. As a matter of fact, the carbonization areas in both cases are almost identical and small. Therefore, it can be concluded that the voltage rise is the only reason for flashovers.

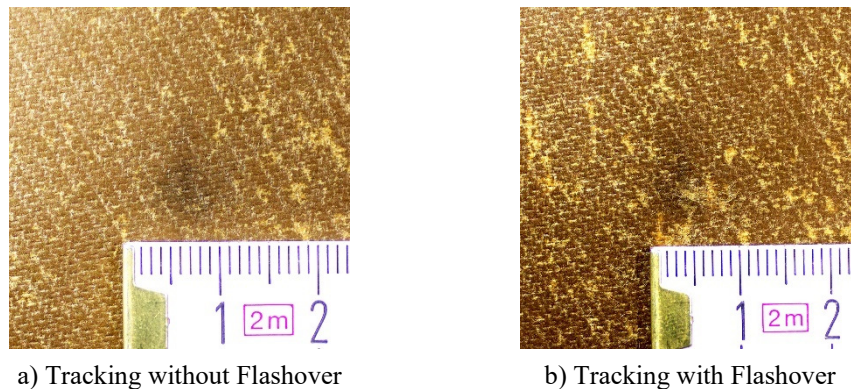


Figure 6.21 Failed pressboard specimen at 80 °C under step-wise stress

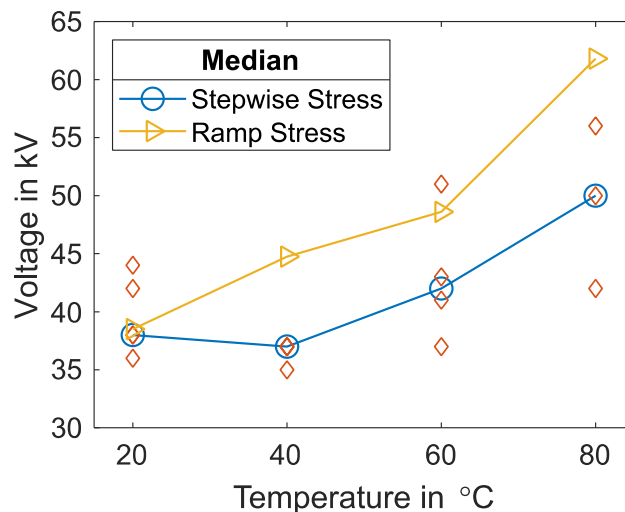


Figure 6.22 Stepwise-Stress interface flashover voltages versus temperatures

However, the effect of stress type is manifest only at high temperatures (60 °C and 80 °C). At 20 °C and 40 °C, however, the failure mechanism does not vary with stress types.

Moreover, the interface flashover voltages under stepwise stress are plotted versus test temperatures, as shown in Figure 6.22. The interface flashover voltages under ramp stress are added in the figure for comparison. Similar to the scenario of ramp-stress tests, the flashover voltage shows an ascending trend with test temperature in general terms. Moreover, expect at 20 °C, the flashover voltages under stepwise stress are clearly lower than their counterparts under ramp stress at the same temperature. The difference, as presumed earlier, could be a result of the cumulative effect of electric stressing.

The samples of stepwise-stress tests are grouped into two categories according to their failure mechanisms: one contains the specimens failed due to tracking-free flashovers, and the other contains those that failed due to flashover-free tracking. It is worth mentioning that little attention has been paid to the specimens having both tracking and flashover since their final failures, as discussed earlier, are identical to those failed due to tracking-free flashovers. The PD quantities of the first group are shown in Figure 6.23. Each sampling point stands for the average values taken from ten minutes-long recordings. Nevertheless, for the last step, the values are averaged from the valid test time.

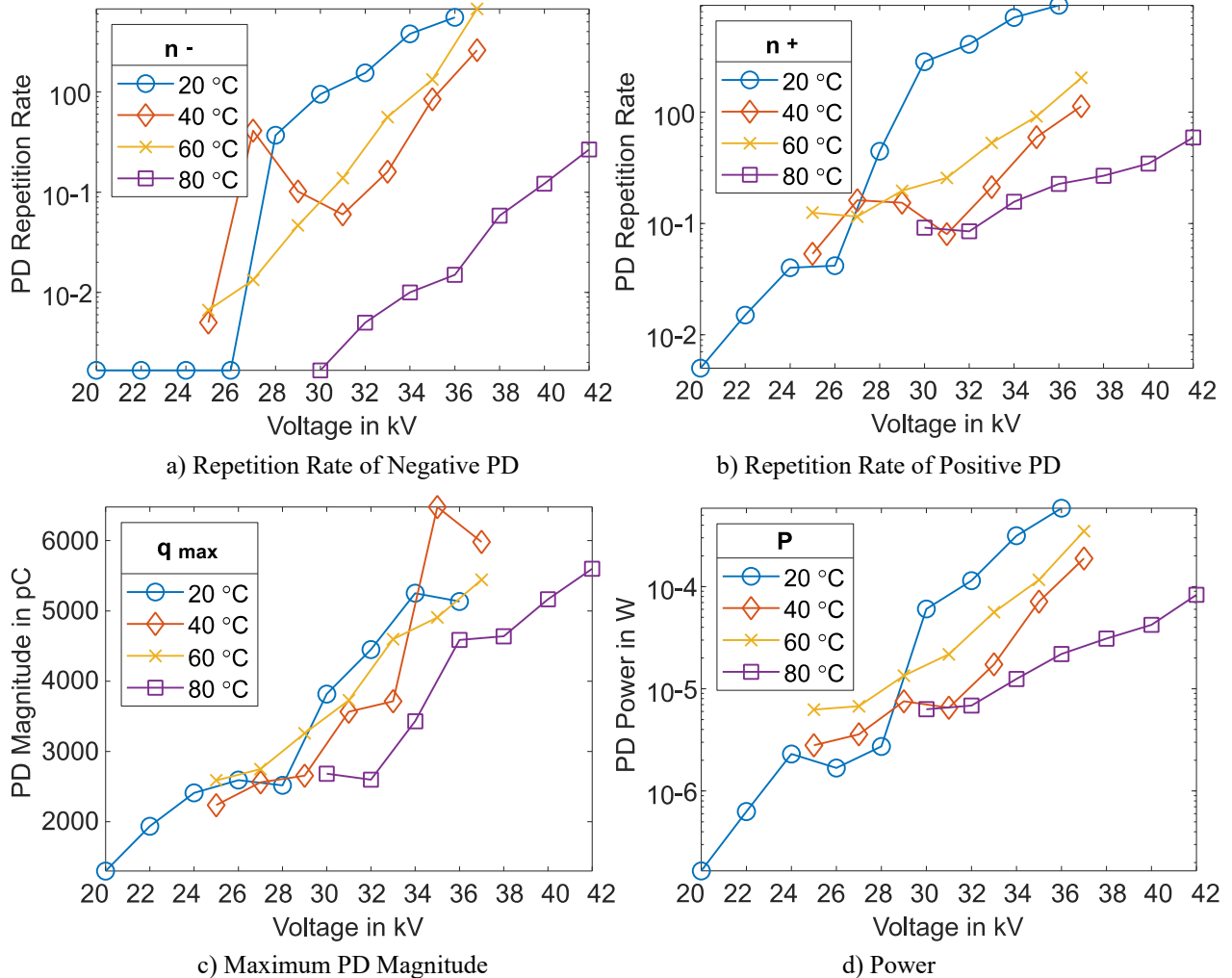


Figure 6.23 PD quantities of tracking-free samples versus step voltage levels

As displayed in Figure 6.23, the PD repetition rate exhibits clearly a positive correlation with voltage level, and there are no significant differences between negative pulses n_- and positive ones n_+ . Moreover, at the same voltage level, the PD repetition rates of either positive or negative pulses appear negatively correlated with test temperature. Similarly, the maximum PD magnitude q_{max} increases with voltage level at each test temperature. Besides, it is also found the PD magnitudes seem to be smaller at higher test temperatures under the same voltage level. In consequence, the PD power P increases with voltage level but is negatively correlated with test temperature.

It is quite straightforward that PD quantities are positively correlated with voltage levels. However, to expound on the relation between PD quantities and test temperature under stepwise stress, it probably has to take into account the interface electric strength. Since there are no obvious damages to the pressboard, the oil corona discharges are presumed to take a major part in this case. As reported, the electric strength of the oil-pressboard would be enhanced by rising oil temperature. As a result,

the PD activities would become weaker under higher temperatures at the same voltage level.

The PD quantities of the second group are shown in Figure 6.24. As voltage level steps up, in contrast to the scenarios of the first group, the PD amplitudes of tracking specimen experience drastic declines and thereafter stay at low levels till the end of the test. Although the PD repetition rates could be considered to increase with voltage level, the relations between them are not so monotonic as those of the first group. In fact, in spite of a general ascending trend, the PD repetition rates exhibit several rises and fall as the voltage level increases. Accordingly, the variation of PD power with voltage level displays a highly similar trajectory.

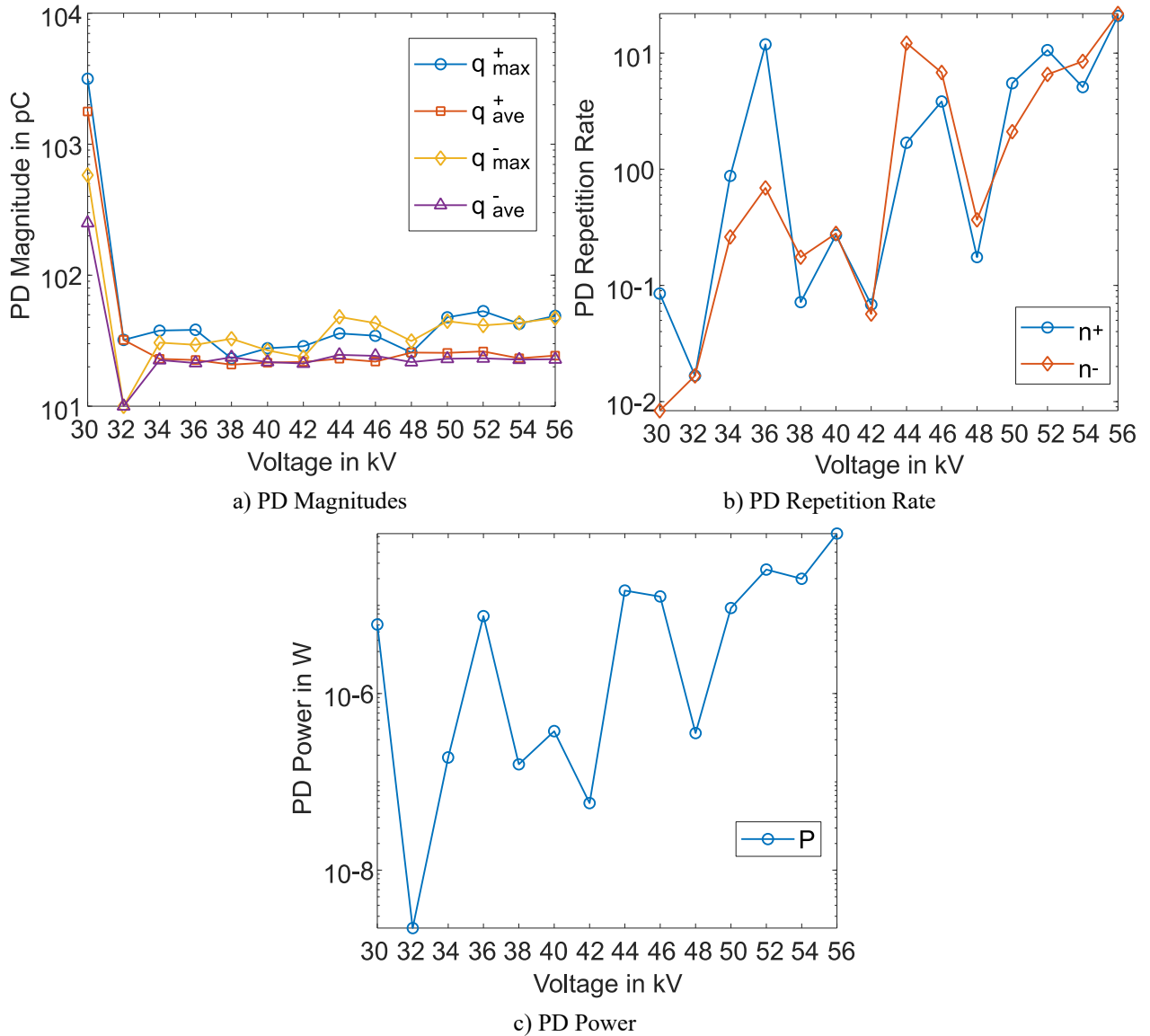


Figure 6.24 PD quantities of tracking specimen at 80 °C versus step voltage

The peculiar characteristics of PD quantities of tracking specimen are probably resulting from a joint effect of voltage rise and tracking process. More specifically, the carbonization of tracking could diminish the PD activities; whereas, the voltage rise can enhance PD activities. In this case, it seems the influence of voltage rise has outperformed that of tracking.

6.3.5 Detection of Tracking using Synchronous PD and Dielectric Measurements

Although the tracking of pressboard exhibits symbolic PD patterns, it is not easy to detect it because of the diminishing PD intensities during surface tracking and the small PD magnitudes in the intermediate stages of internal treeing. According to field experiences, the growth of tracking in pressboard barriers can readily elude the conventional PD detection techniques due to the interferences of external noises and the weak coupling effect of transformer windings. As a result, many faulty transformers having severe creeping discharges are regarded as “normal” until a catastrophic failure occurs. To meet the challenge, it is of great significance to develop a new detection method that can precisely reveal the growth of tracking in transformer major insulation systems. Therefore, efforts have been made in this Chapter to detect pressboard tracking via synchronous PD and dielectric measurements.

Aiming to generate severe tracking to pressboard, the synchronous measurements were carried out under constant stress of 35 kV at 80 °C. The dielectric characteristics, including capacitance, dielectric dissipation factor, and leakage current, were sampled every 0.5 seconds. The results of dielectric measurements are given in Figure 6.25 to Figure 6.27.

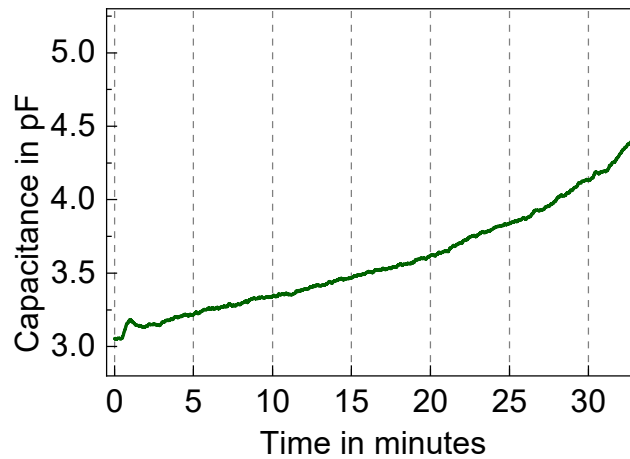


Figure 6.25 Capacitance of oil/pressboard interface during internal treeing

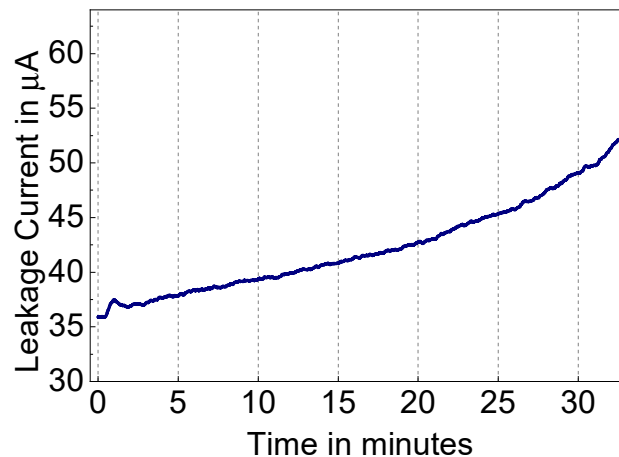


Figure 6.26 Leakage current of oil/pressboard interface during internal treeing

As shown, all dielectric parameters increase steadily even in the intermediate stages where PD magnitudes are quite trivial and have considerably steep rises in the final stage. Specifically, the dissipation factor ($\tan\delta$) increases from 2.5 % at the beginning to 25 % at the end, the leakage current from 36 μA to around 60 μA , and the capacitance from 3 pF to about 5 pF. The variations of the dielectric parameters indicate the properties of the oil/pressboard interface are greatly changed during

tracking expansion.

The ascending leakage current is probably a direct result of the increased conductivity of the pressboard. The ever-bigger dielectric dissipation factor could be indicative of the gradually deteriorated insulation condition of the pressboard and may suggest a temperature rise in somewhere of pressboard. The somewhat surprising rise of capacitance could be a consequence of an enlarged electrode area, which in this case means the carbonization trace.

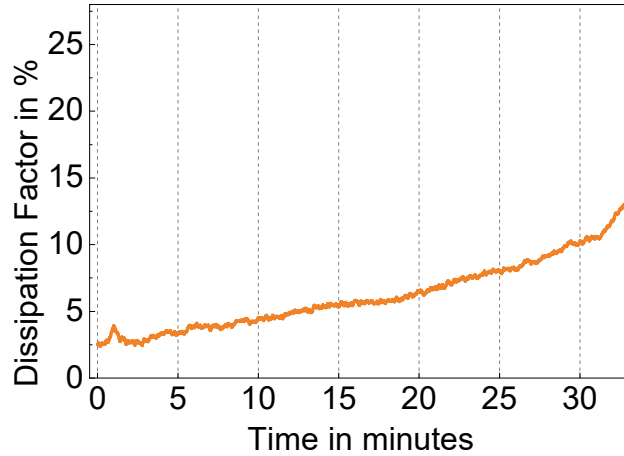


Figure 6.27 Dielectric dissipation factor of oil/pressboard interface during internal treeing

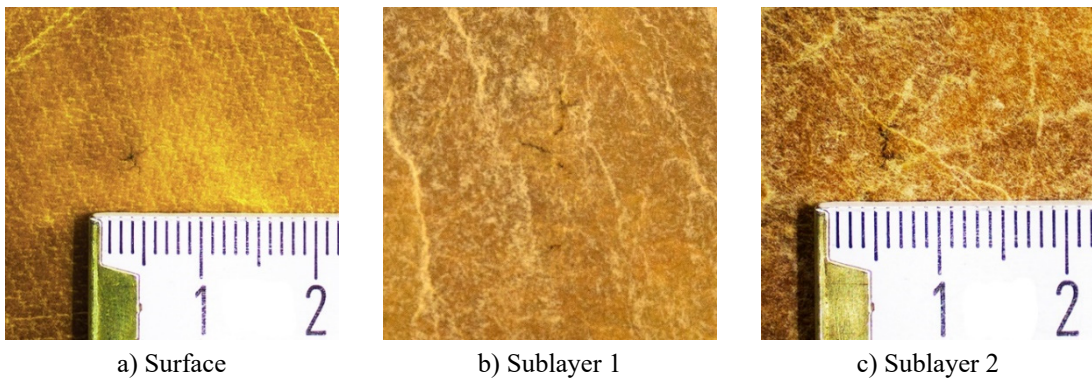


Figure 6.28 Post-mortem of pressboard sample with internal treeing at 80 °C

Subsequently, a post-mortem is carried out to examine the condition of the pressboard specimen, and the images are given in Figure 6.28. It is found that the pressboard specimen has experienced severe internal treeing. There is a small carbonization trace in the triple-junction area of the pressboard surface. More importantly, after dissecting the pressboard specimen, it is found the tracking has penetrated deep into the interior of the pressboard and extended to multiple layers. In fact, the pressboard interior seems much more damaged than the surface. The results indicate that the dielectric measurements have detected the development of tracking.

Moreover, the synchronously measured PD signals are analyzed as well, and the statistical results of PD quantities have already been shown in Figure 6.20. In addition, to study the potential inter-relations between PD activities and dielectric properties, the PD discharge current of the tracking process is also analyzed and shown in Figure 6.29, where the PD discharge current I_{PD} is expressed as [135]:

$$I_{PD} = \frac{1}{T_{ref}} (|q_1| + |q_2| + \dots + |q_i|) \quad (6.4)$$

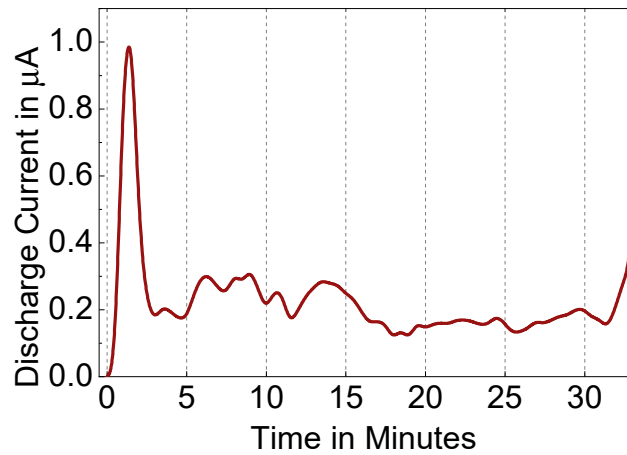


Figure 6.29 PD discharge current of the oil-pressboard interface during tracking

As can be seen in Figure 6.29, the first spike of PD discharges current at around 2 minutes denotes an alteration of PD discharge type. Accordingly, the same discharge type alteration brings about changes to the dielectric characteristics as well. Besides, another change of PD discharge type at about 34 minutes is clearly witnessed in both measurement results.

Having compared the results of PD and dielectric characteristics of the pressboard tracking process, it is reasonable to make the following statements. Firstly, the online dielectric measurement is highly indicative of the pressboard tracking process. Secondly, the online dielectric measurement holds a great advantage over conventional PD measurement in terms of detection sensitivity. Specifically, the conventional PD detection method suffers from a major drawback, i.e., the low-level PD magnitude in the intermediate stages of pressboard tracking, which may lead to an erroneous estimation of insulation conditions. In contrast, the online dielectric measurement is capable of precisely and timely detecting the deterioration process. Last but not least, the synchronous measurements indicate the dielectric characteristics can be correlated with PD quantities in some way. However, the online dielectric measurement is incapable of identifying the discharge type. Therefore, to obtain an in-time alert and a holistic picture of oil-pressboard interface creeping discharges in a running transformer, it is necessary to adopt a comprehensive detection methodology, which incorporates the advantages of different tools. As displayed in this chapter, the synchronous measurement of PD and dielectric characteristics proves a very promising candidate.

6.4 Discussion

6.4.1 Influence Mechanism of Temperature

As indicated by the results, elevated temperatures can enhance the interface electric strength, augment the interface field intensity, exacerbate the pressboard dielectric loss, and certainly lower the oil heat dissipation capability. Under the interplays of these processes, the temperature might eventually exert an intricate influence on the creeping discharge. In order to better understand the influence mechanism of temperature, Figure 6.30 discusses the possible responses of pressboard and oil to the temperature rises, where the test temperatures are divided into two categories, i.e., the low-temperature range (20 and 40 °C) and the high-temperature range (60 and 80 °C).

Within the low-temperature range, the temperature rise affects mainly the oil properties. As aforementioned, the temperature rise can lower the oil relative humidity, thereby enhancing the electric strengths of both bulk oil and interface. The pressboard properties, in contrast, would not be

seriously deteriorated. Resultantly, the pressboard eludes the permanent damages, and the creeping discharge is still a liquid-controlled process. Therefore, the temperature rise can even suppress the creeping discharges by alleviating the negative PDs.

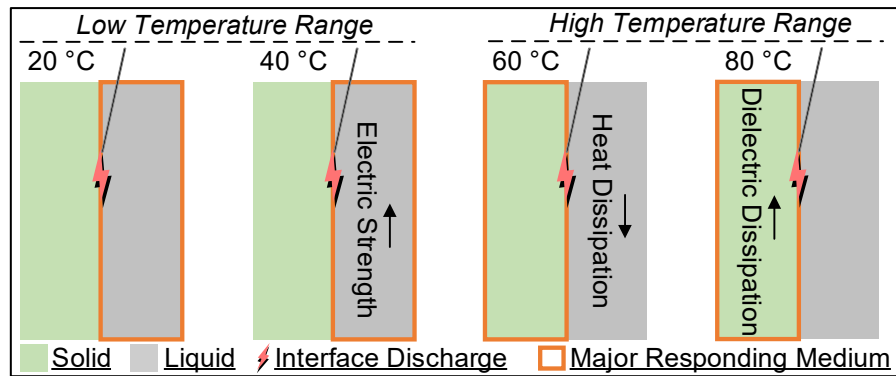


Figure 6.30 Illustration of temperature's influence on creeping discharges

On the contrary, the temperature's effect on the pressboard prevails over that on the oil within the high-temperature range. The creeping discharge is no longer a pure liquid-controlled phenomenon, and the pressboard gets involved in the fault development. At 60 °C, however, the influence of temperature is still insufficient to cause severe deteriorations to the bulk pressboard, and the damages are confined to the pressboard surface. Accordingly, the failure mode generated by the creeping discharge is surface tracking, which could mainly be attributed to the energies dissipated by the interface discharges and facilitated by the decline of oil heat dissipation. At 80 °C, the synergistic effect of high temperature and strong field comes into play eventually, resulting in the soaring of the pressboard dielectric loss. Consequently, the internal treeing takes place in the bulk pressboard and develops rapidly due to an auto-accelerated electrothermal process [3].

6.4.2 Influence Mechanism of Stress Type

The influence of stress type can be evaluated in two aspects, and both of them are closely linked to the temperature. The first refers to the cumulative effect of stressing and manifests itself mainly between the ramp and step stresses.

Figure 6.22 compares the average interface flashover voltages under the ramp and step stresses. At 20 °C, the flashover voltage appears independent of the stress type. At elevated temperatures (40, 60, and 80 °C), however, the stress type shows an appreciable effect on the interface strength: the average flashover voltages under the step stress are lower than those under the ramp stress. The result implies a non-negligible effect of the extended stressing time on the interface strength. Under the ramp stress, the flashover voltage is solely governed by the oil intrinsic strength. Under the step stress, however, other factors, e.g., the bubble formation, are possibly involved due to the extended stressing time. These factors can increase the probability of a breakdown and prejudice the interface strength. Nevertheless, high temperatures are required for such factors to take effect.

The second aspect is related to the voltage rising steepness and manifests itself between the constant and step stresses. The failure mode is internal treeing at 80 °C under constant stress, whereas no incident of internal treeing was found under the step stress, notwithstanding even higher voltages. The discrepancy suggests that the formation of internal treeing needs not only high temperatures and strong fields but also a steep voltage rise, which guarantees that the applied voltage can be raised to a threshold level within a short period of time. A possible explanation is that the onset of internal treeing necessitates a rapid heat accumulation and an instantaneous pressboard degradation, which

the step stress certainly cannot provide due to the comparatively long duration time at lower voltages. Therefore, the step stress cannot generate internal treeing to the pressboard, irrespective of the temperature and the voltage level.

6.5 Conclusions

This chapter sets out to unravel the effects of temperature and stress waveform on oil/pressboard interface creeping discharges. At first, the influences of temperature on pressboard dielectric properties were studied. Afterwards, the short-time electric strengths of the oil/pressboard interface were examined against temperatures under ramp stress. Subsequently, long-term progressive creeping discharge tests were carried out at different temperatures under constant and step-wise stresses, respectively. At last, a new method based on synchronous PD and online dielectric measurements was employed to detect pressboard internal treeing at 80 °C. Based on the obtained test results, the following conclusion can be drawn from the present study:

- The short-time electric strength of either interface or oil gap is positively correlated with temperature and follows the Gumble distribution. The increment in electric strength at elevated temperatures is probably due to a declined oil relative humidity. The capacitance and dielectric dissipation of the pressboard sample is positively correlated with temperature, and there is an obvious synergistic effect between temperature and strong field in exacerbating the dissipation factor of the pressboard.
- The temperature can determine the severity of creeping discharge and the related fault type. Under constant stress, all specimens fail due to tracking-free interface flashovers at 20 °C and 40 °C; all specimens exhibit surface tracking at 60 °C; all specimens fail due to internal treeing (internal treeing) and subsequent interface flashovers at 80 °C. The discrepancy is probably due to that oil and pressboard have distinct responses to temperature rise in different temperature ranges. Stress waveform has an obvious effect on the fault type only at high temperatures, and no incident of internal treeing is observed under step-wise stress. Moreover, owing to the cumulative effect of discharges, the interface flashover voltage at step-wise stress is lower than that at ramp stress.
- Under constant stress, the PD numbers of the tracking-free samples (20 °C and 40 °C) are negatively correlated with temperature. The PD activities of the surface tracking sample (60 °C) are gradually diminished due to weaker PD magnitudes as a result of ever-lesened field intensity. The PD characteristic of the fast-tracking sample (80 °C) is highly approximate to those of massively-aged pressboard samples at room temperature. Under step-wise stress, the PD quantities of the tracking-free samples are in general negatively correlated with temperature. For the slow-tracking samples, the PD magnitudes decline rapidly after the PD inception and thereafter do not vary greatly with voltage rise. However, the trends of their PD number and PD power with voltage level are jointly affected by surface carbonization and field enhancement.
- The proposed synchronous PD and dielectric measurement technique is highly indicative of the pressboard internal treeing process. The online dielectric measurement holds a great advantage in detection sensitivity, and the conventional PD detection method is capable of identifying discharge type. Moreover, the synchronous measurements indicate the dielectric characteristics can be correlated with PD quantities in some way.

7 INFLUENCES OF TEMPERATURE AND OIL FLOWING ON DC CREEPING DISCHARGES

7.1 Introduction

As a pivotal component of the HVDC transmission system, converter transformer usually adopts a ‘full-sized’ oil-barrier structure to build up its major insulation system, which in turn begets omnipresent oil/pressboard interfaces. It is known that oil/pressboard interface creeping discharge is one of the most dangerous failure modes of major insulation. Compared with the power transformer, the creeping discharge phenomenon in the converter transformer is complicated further by the complex stress conditions in its valve windings, which contain AC voltage, DC voltage, and current harmonics. It poses a severe challenge to the insulation integrity of the converter transformer. Plenty of researches have studied the short-time interface creeping discharges, i.e., flashovers, under DC or combined AC-DC voltages [120, 122–124]. Only a few pieces of research have reported the characteristics of long-term creeping discharges under combined AC-DC fields [126–128]. However, given the great discrepancies in field characteristics between AC and DC voltages, a lack of accurate knowledge of creeping discharges under pure DC fields might hinder the comprehension of creeping discharges under combined fields. In this respect, an in-depth study of progressive DC creeping discharges is expected to provide a meaningful benchmark for the following researches.

Therefore, using a needle-to-plate electrode configuration, this chapter carries out fundamental investigations on long-term DC creeping discharges. Temperature is a decisive factor in determining the DC field distribution in oil/pressboard composite insulation [191, 192]. Therefore, the influences of temperature on progressive DC creeping discharges are firstly studied. Moreover, the oil/pressboard interface in the converter transformer is also subject to incessant oil flows. The forced oil flows can distort the interface field distributions and space charge accumulation [130, 193] and impact the behaviors of creeping discharges [194]. Accordingly, DC creeping discharges with forced oil flows constitute another focus of the present study.

This chapter is subdivided into seven sections. Section 7.2 reviews the theoretical fundamentals of converter transformer stress conditions, DC field distributions, and DC partial discharge. Section 7.3 gives a brief introduction to sample preparation and test setup. Section 7.4 reports the effects of temperature on the basic properties of oil and pressboard as well as on the interface field distributions. Section 7.5 presents the test results of long-term creeping discharges with and without oil flows. The DC PD patterns and PD quantities are analyzed against temperature, voltage levels, and oil flowing speeds. Section 7.6 carries out detailed discussions on the possibly involved physical processes and space charges interactions. Section 7.7 gives the concluding remarks of this chapter.

7.2 Theoretical Background

7.2.1 Voltage Waveforms and Voltage Tests of Converter Transformer

Typically, the converter transformer is arranged as an earthed-wye winding in the primary side (AC line side) with floating-wye and delta windings in the secondary side (valve side), where a 30° phase shift exists between the secondary windings. Figure 7.1 displays the schematic diagram of a 12-pulse LCC converter bridge with a converter transformer, where U_d , U_D , U_{AH} , U_{AL} and U_{VO} denote the single-bridge nominal voltage, DC line voltage, valve wye winding phase-to-ground voltage, valve

delta winding phase-to-ground voltage, and valve wye winding phase-to-phase voltage, respectively.

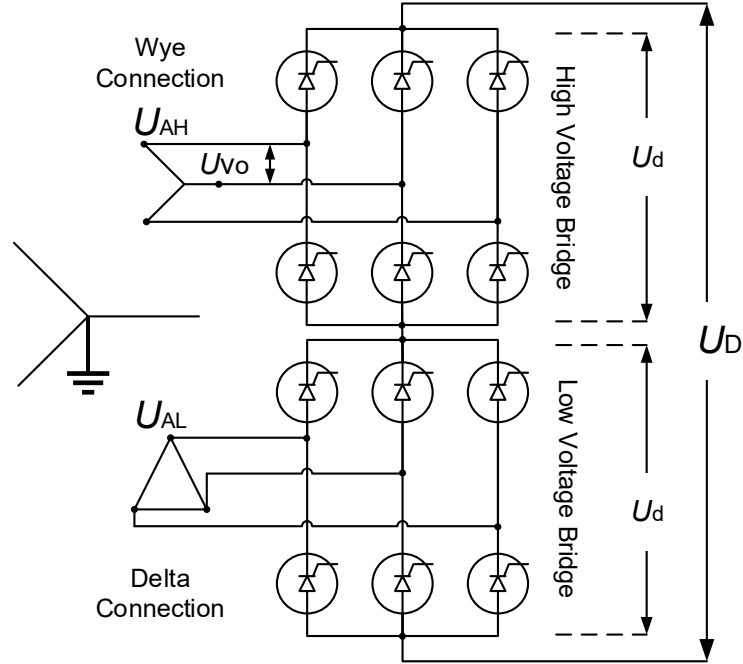


Figure 7.1 Schematic illustration of a conventional LCC 12-pulse converter bridge

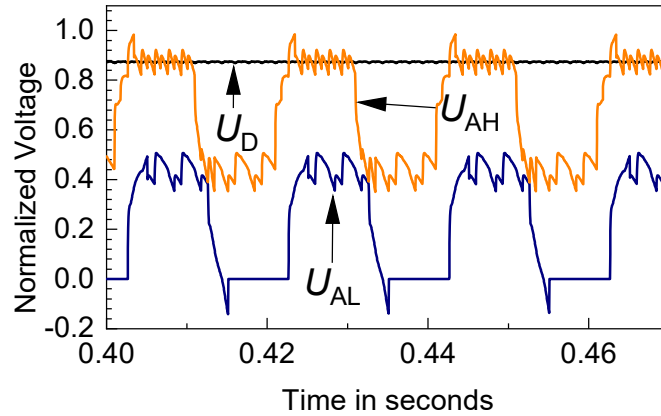


Figure 7.2 Voltages of DC line and converter transformer valve windings

For quantitatively evaluating the stress conditions of the valve windings, a modeling circuit was constructed based on the Cigré HVDC benchmark model [195], where the firing angle α is set to be 15° . The simulated valve winding voltage waveforms during normal operation are shown in Figure 7.2. Besides, the current and voltage frequency spectra of valve wye winding are demonstrated in Figure 7.3.

As displayed, the valve windings of the converter transformer withstand severely distorted voltage waveforms. In addition to a great DC bias, the valve winding voltage is also superimposed by a series of high-frequency components. Generally, the DC potential is equal to:

$$U_d * (n - 0.5) \quad (7.1)$$

where n denotes the 6-pulse bridge number starting from the ground. The high-frequency voltage components comprise harmonics of the order of $3n$ ($n = 1, 3, 5, 7, \text{etc.}$), harmonics of the order of $6k$ ($k = 1, 2, 3, \text{etc.}$) and harmonics of the order of $6k \pm 1$ ($k = 1, 2, 3, \text{etc.}$). Moreover, for a 12-pulse bridge, the current high-frequency components mainly comprise harmonics of the order of $12k \pm 1$

($k = 1, 2, 3$, etc.) [113]. Therefore, in addition to the conventional tests for power transformers, the valve windings of the converter transformer have to be subject to several special tests to check its insulation performance under different stresses.

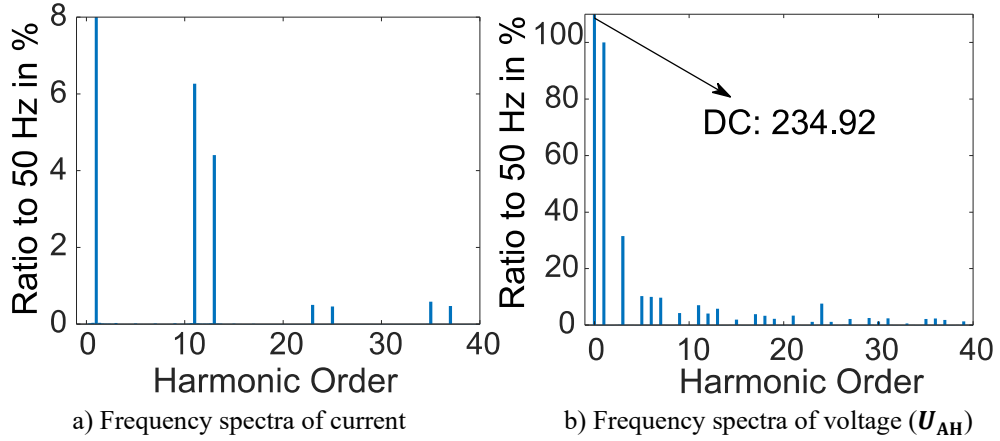


Figure 7.3 Current and voltage harmonics of valve windings

The additional tests include DC withstand voltage test, polarity reversal test, and AC applied voltage test, of which the respective test voltage levels U_{DC} , U_{PR} and U_{AC} are expressed as follows [196, 197]:

$$U_{DC} = 1.5 * [(n - 0.5) * U_d + 0.7 * U_{V0}] \quad (7.2)$$

$$|U_{PR}| = 1.25 * [(n - 0.5) * U_d + 0.35 * U_{V0}] \quad (7.3)$$

$$U_{AC} = \frac{1.5 * [(n - 0.5) * U_d + \sqrt{2} * (U_{V0}/\sqrt{3})]}{\sqrt{2}} \quad (7.4)$$

where U_d is the single-bridge nominal voltage, U_{V0} is the valve wye winding phase-to-phase voltage, and n is the 6-pulse bridge number starting from the ground. These tests are carried out at room temperature (20 ± 10 °C) and use separate DC and AC voltage sources. Moreover, considering the practical stress conditions, it is also recommended to implement a combined AC-DC test at elevated temperatures. The superimposed AC-DC voltage waveform could provide more accurate assessments of the valve winding insulation levels during initial operating conditions. However, limited by technical capacity, the application of this test can hardly be realized in most cases. The lack of standardized acceptable partial discharge levels impedes its application in practice as well [198].

7.2.2 Field Distribution under DC Voltage

It is known the DC field distribution in an insulating material is a function of material geometry and material resistivity. However, this statement is true only when the insulation system has reached a steady state. In fact, depending on material properties, it takes certain periods of time for the DC field distribution to shift from an initial transient state to the final steady state. Generally, the DC field distribution in an insulation system can be divided into four consecutive stages. An illustration of the stage division of DC field distribution is given in Figure 7.4 [199].

In Stage 1, a DC voltage U is raised from 0 to a stable level. In this stage, the field distribution is purely capacitive, i.e., solely governed by the relative permittivity of the material. In Stage 2, as a result of internal charges accumulation, the field distribution begins shifting from capacitive to resistive. In Stage 3, a purely resistive field, i.e., the steady-state, is eventually build up. In this stage, the field distribution is determined by the specific resistivity of the material. In Stage 4, the DC voltage U is switched off. However, the residual charges would not be dissipated very soon.

Therefore, a resistive field can still exist for a while [199].

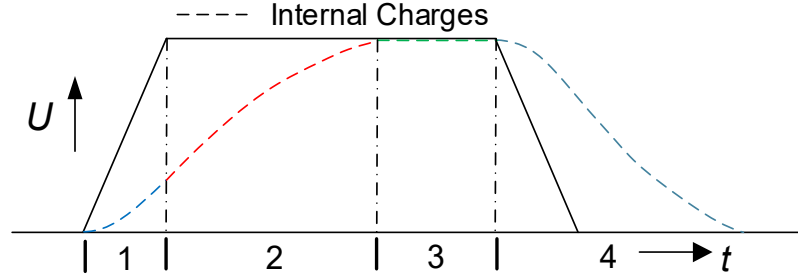
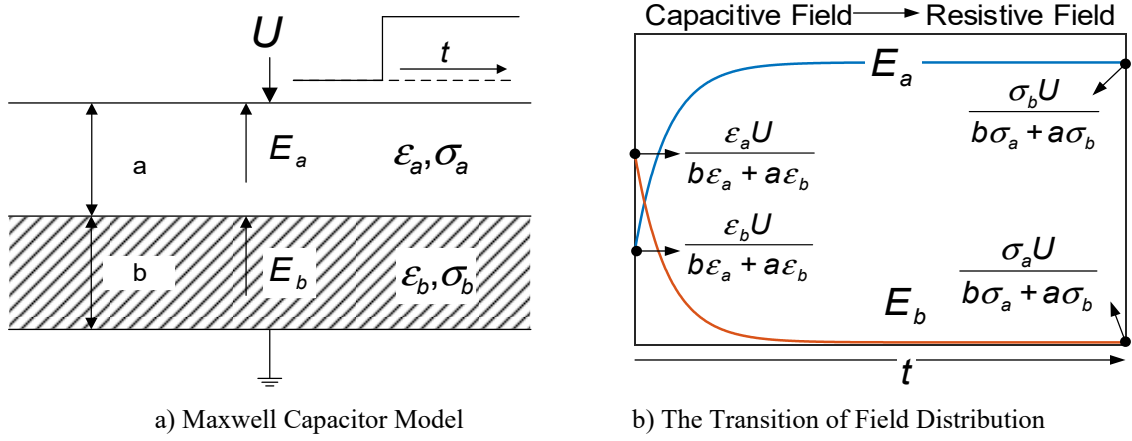


Figure 7.4 Stages of DC field distribution



a) Maxwell Capacitor Model

b) The Transition of Field Distribution

Figure 7.5 Maxwell capacitor model and field transition under DC voltage

With respect to a composite system, the DC field distribution among constituent materials can be analyzed using a so-called Maxwell capacitor model [199]. As shown in Figure 7.5 a), an ideal Maxwell capacitor model comprises two parallel electrodes and a double layer of insulating materials (A and B), where E_a , E_b and U denote the field intensities and a step DC voltage, respectively; a , ε_a and σ_a are the thickness, relative permittivity, and specific conductivity of A , respectively; and b , ε_b and σ_b are the thickness, relative permittivity, and specific conductivity of B , respectively. The DC field intensities of A and B can be calculated as follows [199]:

$$E_a = \frac{\sigma_b U}{b\sigma_a + a\sigma_b} * (1 - e^{-t/\tau}) + \frac{\varepsilon_b U}{b\varepsilon_a + a\varepsilon_b} * (e^{-t/\tau}) \quad (7.5)$$

$$E_b = \frac{U}{b} - \frac{a}{b} * E_a \quad (7.6)$$

where, t is time, and τ is a time constant, which is defined as:

$$\tau = \frac{b\varepsilon_a + a\varepsilon_b}{b\sigma_a + a\sigma_b} \quad (7.7)$$

Therefore, the transition process from a capacitive field at $t = 0$ to a resistive field at $t = \infty$ can be numerically investigated. An example of the calculation is given in Figure 7.5 b), where $a = b$, $\varepsilon_a > \varepsilon_b$, and $\sigma_a \ll \sigma_b$. As displayed, at the very first beginning, the capacitive field is inversely proportional to relative permittivity. Therefore, E_a is smaller than E_b . As a steady-state resistive field is established, the field intensity is inversely proportional to specific conductivity. Therefore, E_a is considerably greater than E_b at $t = \infty$.

The characteristics of DC field distribution are of vital importance to the insulation design of converter transformer, the major insulation structure of valve winding in particular. Accordingly,

compared with a conventional power transformer, converter transformer has to adopt a ‘full-sized’ major insulation structure, which means utilizing more pressboards to construct the oil-barrier system. The typical major insulation structure of the converter transformer valve winding is schematically illustrated in Figure 7.6.

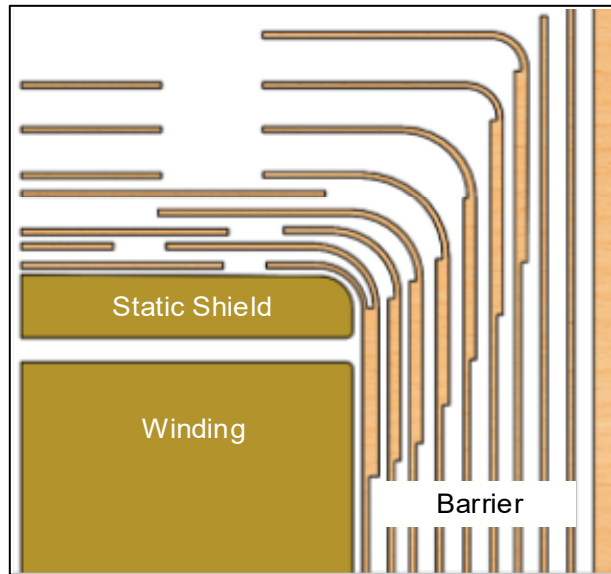


Figure 7.6 Major insulation structure of converter transformer

Moreover, by means of FEM simulations, an intuitive comparison has been made between the AC capacitive field and the DC resistive field of converter transformer oil-barrier structures. The results are shown in Figure 7.7, where the oil relative permittivity ϵ_{oil} , oil conductivity σ_{oil} , pressboard relative permittivity ϵ_{pr} , and pressboard specific conductivity σ_{pr} are set to be 2.2, $1 \cdot 10^{-13}$ S/m, 4.5, and $1 \cdot 10^{-15}$ S/m, respectively. Under AC voltage, it is the oil that withstands most of the electric stress. The field intensity in the oil gap is obviously higher than that in pressboard bulk. In contrast, it is the barrier that withstands most of the electric stress under DC voltage. The field intensity in the pressboard is much stronger than that of the oil gap. Therefore, the pressboard barriers in the converter transformer have to withstand a great portion of the DC field plus a strong AC field in service.

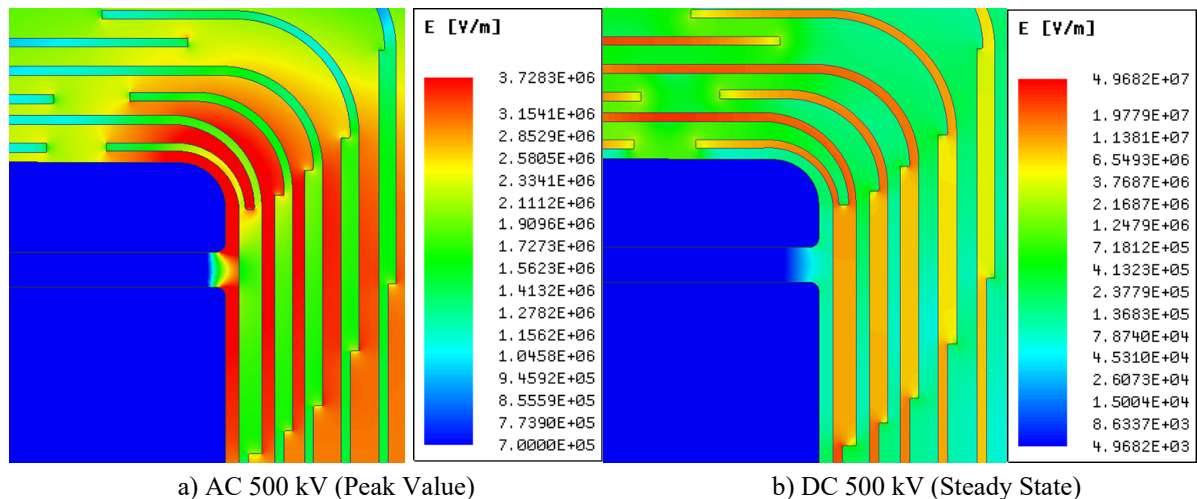


Figure 7.7 Field distributions of converter transformer major insulation structure

7.2.3 Partial Discharge under DC Voltage

The basic physical principle of DC partial discharge is almost identical to that of AC partial discharge. However, a major difference in PD quantities can still be drawn between AC and DC partial discharges. As illustrated in Figure 7.8, for a given single PD pulse (i^{th}) under AC voltage, the following quantities can be directly obtained: occurrence time $t(i)$, voltage level V_{peak} , occurrence phase angle $\varphi(i)$, and pulse magnitude $q(i)$. In contrast, there is no phase information for partial discharges under the DC field. For a given single PD pulse (i^{th}) under DC voltage, the directly obtained quantities include occurrence time $t(i)$, voltage level V_{DC} , and pulse magnitude $q(i)$.

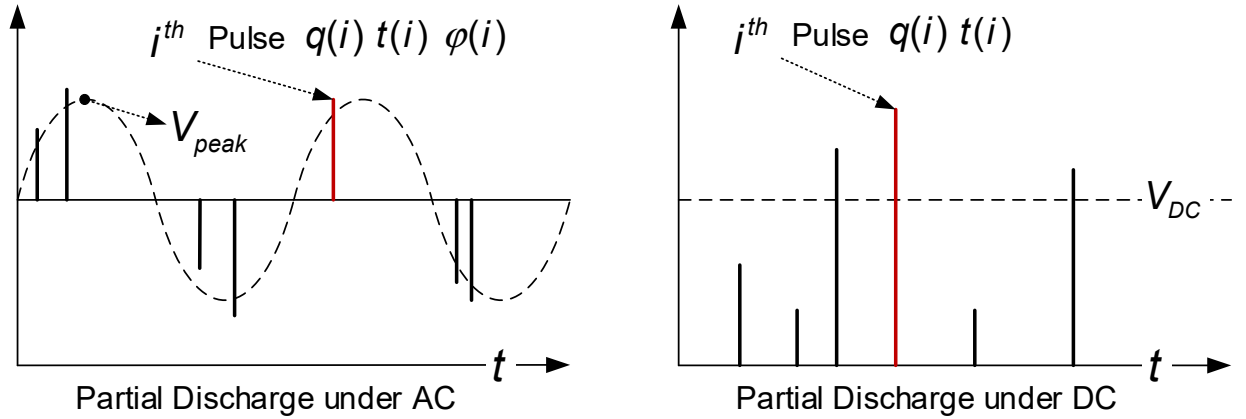
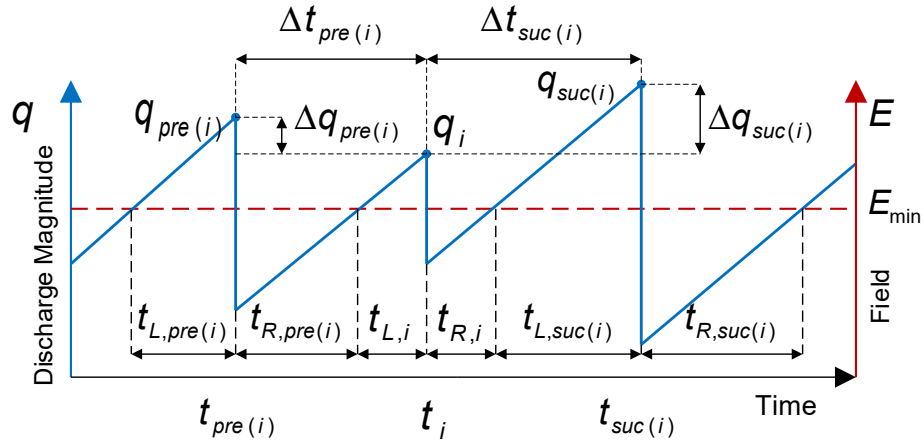


Figure 7.8 Fundamental quantities of AC and DC partial discharges

In consequence, the discharge patterns for evaluating AC partial discharge, e.g., PRPD, cannot be applied to DC discharges. Aiming to properly represent the patterns of DC partial discharge, it requires a systematic understanding of the DC PD mechanism. A time lag/recovery model was proposed by Fromm [200] to interpret the fundamental parameters pertinent to the PD occurrence and identification under the DC field, which is shown in Figure 7.9.



E Field Strength	$t_{pre(i)}$ Time of prev. pulse	$t_{L,i}$ Lag time of pulse i
q Discharge Magnitude	$t_{suc(i)}$ Time of succ. pulse	$t_{R,i}$ Recovery time of pulse i
q_i Mag. of pulse i	$\Delta q_{pre(i)}$ Mag. Diff. to prev.pulse	$t_{L,pre(i)}$ Lag time of prev. pulse
$q_{pre(i)}$ Mag. of prev. pulse	$\Delta q_{suc(i)}$ Mag. Diff.to succ. pulse	$t_{R,pre(i)}$ Recovery time of prev. pulse
$q_{suc(i)}$ Mag. of succ. pulse	$\Delta t_{pre(i)}$ Time to prev. pulse	$t_{L,suc(i)}$ Lag time of succ. pulse
t_i Time of pulse i	$\Delta t_{suc(i)}$ Time to succ. pulse	$t_{R,suc(i)}$ Recovery time of succ. pulse

Figure 7.9 Time lag/recovery model of DC partial discharge

As known, it has to satisfy two conditions to generate partial discharges: a sufficient field and an initial electron. As displayed in Figure 7.9, for a given DC partial discharge pulse i to occur, the local field E has to exceed the threshold value E_{\min} . However, the discharge would not take place immediately. Rather, it needs extra time to accumulate sufficient charges. This extra time is referred to as the lag time $t_{L,i}$. The local field would collapse as soon as a discharge pulse occurs. For the successive partial discharges to occur, it needs another period of time for the local field to reach the threshold value again. This period of time is referred to as the recovery time $t_{R,i}$.

With respect to a PD pulse train, the inter-relations of consecutive pulses can be interpreted using this model as well. For instance, the lag time of pulse i $t_{L,i}$ is dependent on the recovery time of its predecessor $t_{R,pre(i)}$. In turn, its recovery time $t_{R,i}$ also determines the lag time of its successor $t_{L,suc(i)}$. On the other hand, for an ideal dielectric, it is assumed that the internal charges come solely from the ionization process. Therefore, the magnitude of pulse i q_i is strongly dependent on its lag time, as the latter determines the number of accumulated charges. From this perspective, it can be argued that the discharge magnitudes of consecutive PD pulses are also mutually affected. Therefore, the DC PD pattern of a specific discharge type can be evaluated by analyzing the inter-relations of the consecutive pulses in a pulse train. The most used parameters include the time intervals between consecutive pulses ($\Delta t_{pre(i)}$, $\Delta t_{suc(i)}$) and the magnitude differences between consecutive pulses ($\Delta q_{pre(i)}$, $\Delta q_{suc(i)}$).

However, it is noteworthy that the above-discussed scenario is confined to the steady-state DC field. In the transient stages of DC field distribution, i.e., Stage 1 and Stage 2 in Figure 7.4, the partial discharge exhibits a capacitive nature due to the permittivity-governed field distribution [201]. In consequence, there are normally numerous discharges when the applied DC voltage is changed. This phenomenon is of particular importance to the investigation of DC partial discharges in a composite insulation system, such as the oil/pressboard structure.

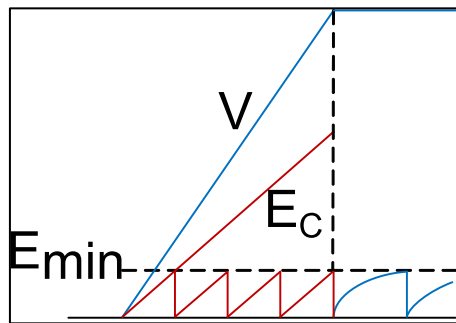


Figure 7.10 Generation of partial discharges with a rising DC voltage

The generation of partial discharges with a rising DC voltage is shown in Figure 7.10, which is adapted from [199]. Take the oil-pressboard structure for an example, as the applied DC voltage V rises, a capacitive field is generated and the oil part withstands most of the electric stress. The capacitive field in oil E_C may exceed the threshold value of oil discharge E_{\min} . As a result, a large number of discharge events in oil can be observed. As the field distribution reaches the steady state, it is now the pressboard that withstands most of the electric stress. In consequence, a certain number of discharge events in the pressboard are present. However, due to the physical nature of DC partial discharge and the comparatively high strength of pressboard, the PD repetition rate in a steady-state could be much lower than that in transient stages.

7.3 Sample Preparation and Test Setup

7.3.1 Sample Information

All pressboard specimens were processed following the procedures depicted in Section 3.3.3, and the oil samples were fairly dried. The average value of oil moisture throughout the entire test is about 13 ppm.

7.3.2 Test Setup

The tests can be divided into three groups. The first group of tests is referred to as preliminary tests. In preliminary tests, the oil conductivity and relative permittivity were measured using the Baur oil tester. The pressboard conductivity and relative permittivity were measured using the PDC method. FEM simulations were carried out using Ansys Maxwell[®].

The second group and the third group are referred to as static tests and dynamic tests, respectively. They use the same HV electrode geometry (see Section 3.1.2), the same grounding electrode (see Section 3.1.4), and the same test cell (see Section 3.2.2). PD signals were measured according to IEC 60270:2000, and the measurement circuit was constructed as shown in Section 3.4.5.

The heating devices, temperature monitoring devices, and the HV test circuit for static tests are illustrated in Section 3.5.3. The oil flowing circuit, temperature monitoring devices, streaming electrification model, streaming current measurement circuit, and HV test circuit for dynamic tests are illustrated in Section 3.5.4. All high-voltage tests were carried out in a well-shielded room. The actual arrangement of the needle-to-plate electrode for dynamic tests is shown in Figure 7.11.

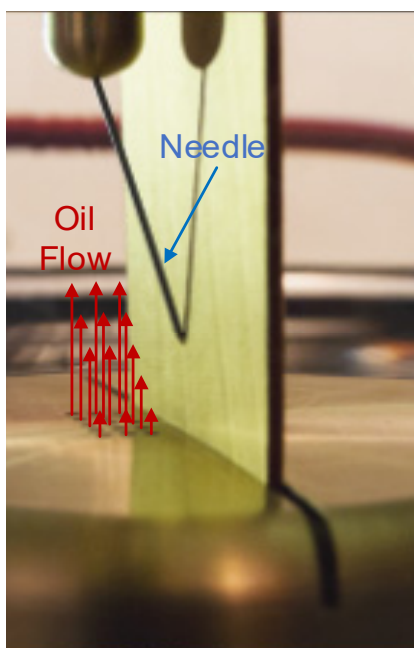


Figure 7.11 Actual image of needle-to-plate electrode for dynamic tests

7.4 Results of Preliminary Tests

7.4.1 Specific DC Conductivity of Oil and Pressboard

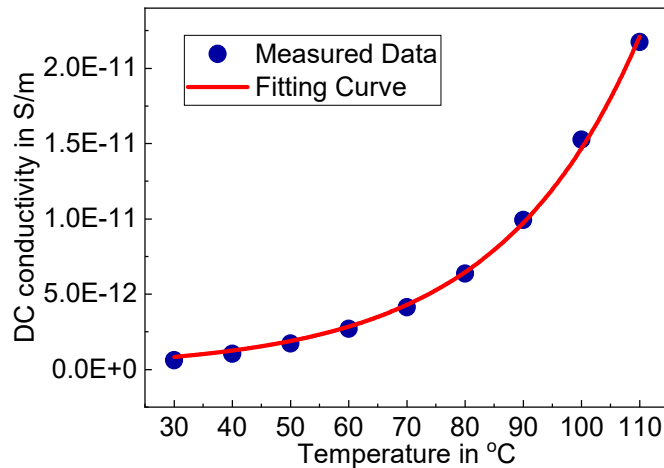


Figure 7.12 Oil specific conductivity versus temperature

The Baur oil tester was used to measure oil conductivity. The test temperatures ranged from 30 °C to 110 °C with an interval of 10 °C, and the applied electric field was 250 V/mm. The water content of the oil sample was 13 ppm. For eliminating probabilistic errors, four measurements were carried out at each temperature, and the average values were used for evaluation. The results are shown in Figure 7.12. As displayed, the DC specific conductivity of oil increases exponentially with temperature. The solid red line denotes an exponential function for fitting the growth of oil conductivity with temperatures.

PDC method was used to investigate the specific conductivity of the pressboard with temperature. The working principle of the PDC method and the relevant test devices are depicted in Section 3.4.2. Newly impregnated pressboard samples were used for investigations. The triple-electrode and pressboard specimens were contained in an oil-filled hermetic glass vessel and then heated in an air-circulated thermal oven. The test temperatures ranged from 30 °C to 110 °C with an interval of 20 °C, and the applied electric field was 100 V/mm. The measuring time was set to be 5000 s for either polarization or depolarization current, and the current data were recorded for every 1s. Three measurements were carried out at each temperature, and the average values were used for evaluation. An example of PDC measurement is given in Figure 7.13.

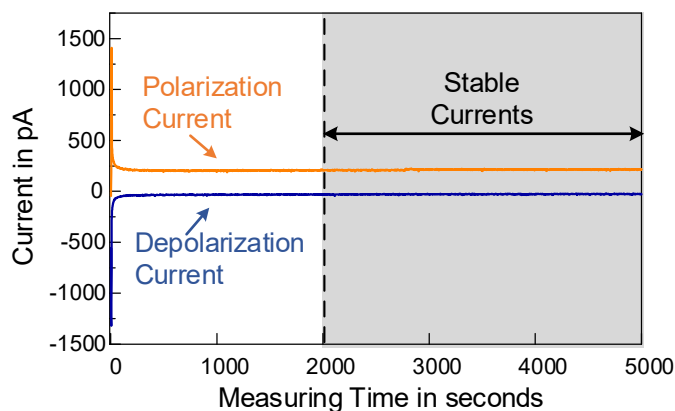


Figure 7.13 Polarization current and depolarization current of pressboard

As known, at the initial stages of DC field distribution, the measured currents contain a fraction of transient components, such as capacitive current and relaxation current. It takes a certain period of

time for either polarization or depolarization current to become stable. To properly calculate the specific conductivity of the pressboard, only the stable currents, i.e., the current data spanning from the 2000s to 5000s, are used to determine the intrinsic conduction current of the pressboard. The specific conductivity of the pressboard can be calculated using the following equations:

$$I_C = |I_P| - |I_D| \quad (7.8)$$

$$\sigma = \frac{I_C}{U_0} * \frac{d}{A} \quad (7.9)$$

where, I_C is the intrinsic conduction current a), $|I_P|$ and $|I_D|$ are the absolute values of the stable polarization and depolarization currents, respectively; σ denotes DC conductivity (S/m), d is the sample thickness (m), A is the electrode area (m²) and U_0 is the applied voltage (V). The intrinsic conduction currents and calculated specific conductivity of the pressboard are shown in Figure 7.14 and Figure 7.15, respectively.

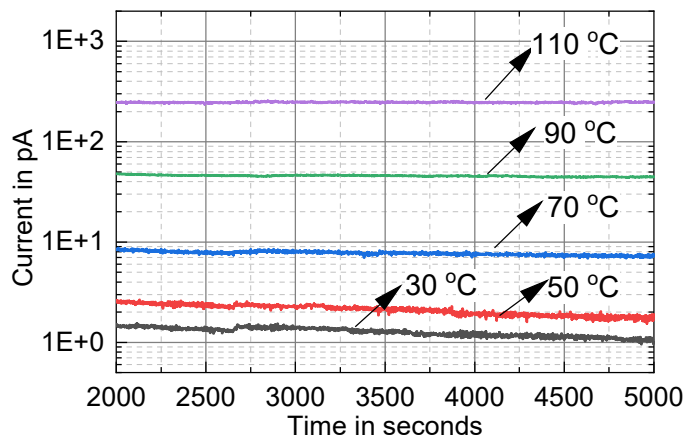


Figure 7.14 Intrinsic conduction currents of pressboard versus temperature

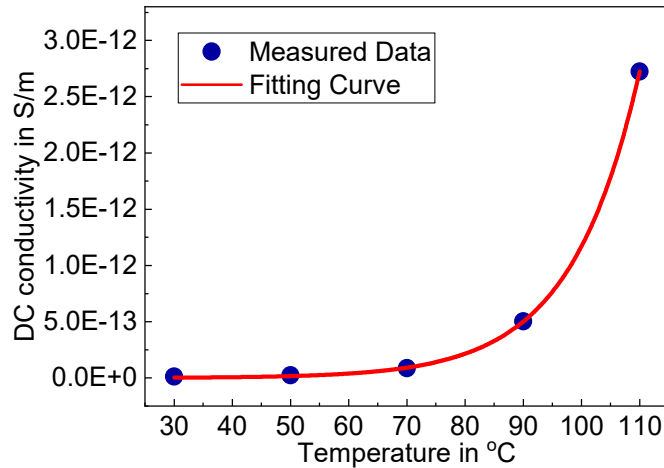


Figure 7.15 Pressboard specific conductivity versus temperature

As shown, both the intrinsic conduction currents and the specific conductivity of the pressboard increase exponentially with temperature. The solid red line in Figure 7.15 denotes an exponential function for fitting the growth of pressboard conductivity with temperatures. Moreover, the relations between specific conductivity and temperature are fitted using exponential equations. The fitting results are listed in Table 7.1, where T denotes temperature in °C.

Table 7.1 Exponential fitting of DC conductivities

Material	Fitting Equations	The goodness of Fit (R^2)
Pressboard	$1.335 * 1 * 10^{-15} * \exp(0.06898 * T)$	0.993
Oil	$1.73 * 1 * 10^{-13} * \exp(0.04431 * T)$	0.995

The difference in specific conductivity between oil and pressboard is clearly demonstrated: the exponential powers of oil and pressboard conductivity fitting equations are -13 and -15, respectively. Based on the equations in Table 7.1, furthermore, the DC conductivity of oil and pressboard is plotted versus temperatures, as shown in Figure 7.16.

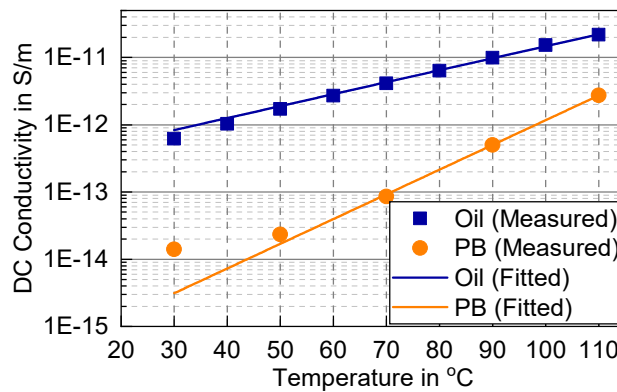


Figure 7.16 DC conductivity of oil and pressboard versus temperature

The difference in conductivity between oil and pressboard is greatly shrunk as the temperature rises. It is known that the DC field distribution is governed by the resistivity ratio for a given composite insulation geometry. Therefore, it infers that the DC field distribution in the oil/barrier structure must be influenced by varying temperatures. This basic fact is vital to any electric phenomenon related to oil/pressboard composite insulation under DC voltage.

7.4.2 Relative Permittivity and Relaxation Time Constant

In addition, the relative permittivity of oil and pressboard was measured against temperatures as well. The results are shown in Figure 7.17. The relative permittivity of the pressboard is almost twice that of oil at room temperature. Nevertheless, as temperature increases, the relative permittivity of pressboard steadily increases, whereas the relative permittivity of oil declines slightly. The relations between relative permittivity and temperature can be fitted using linear equations, as shown in Table 7.2, where T denotes temperature in °C.

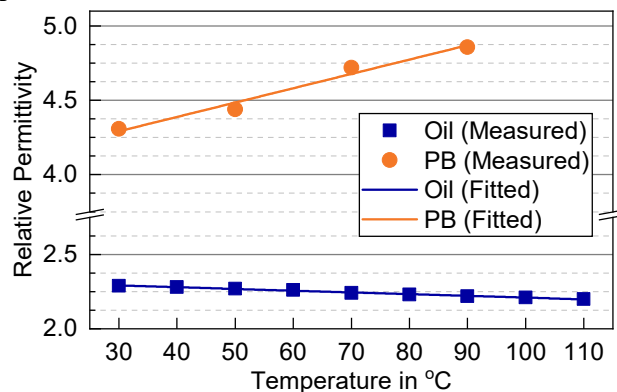


Figure 7.17 Relative permittivity of pressboard and oil versus temperature

Table 7.2 Linear fittings of relative permittivity

Material	Fitting Equations	The goodness of Fit (R ²)
Pressboard	$4.002 + 0.00965 * T$	0.978
Oil	$2.326 - 0.001167 * T$	0.993

Based on the fitting equations of conductivity and relative permittivity, the relaxation time constants of oil and pressboard can be estimated versus temperatures. For a given ideal dielectric, its relaxation time constant can be roughly calculated using the following equation [202]:

$$\tau = \frac{\epsilon_0 \epsilon_r}{\sigma} \tag{7.10}$$

The calculated relaxation time constants of oil and pressboard are shown in Figure 7.18.

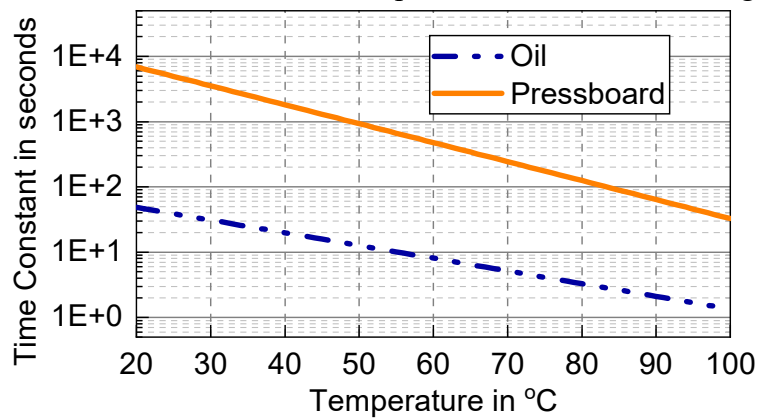


Figure 7.18 Relaxation time constants of oil and pressboard versus temperature

7.4.3 DC FEM Simulations of Different Temperatures

FEM simulations were carried out to investigate the influences of temperature on steady-state DC field distributions at the oil/pressboard interface. The basic principle and the simulation flowchart were explained in Section 3.4.12. Figure 7.19 shows the simulation geometry and the meshing network of the triple-junction area.

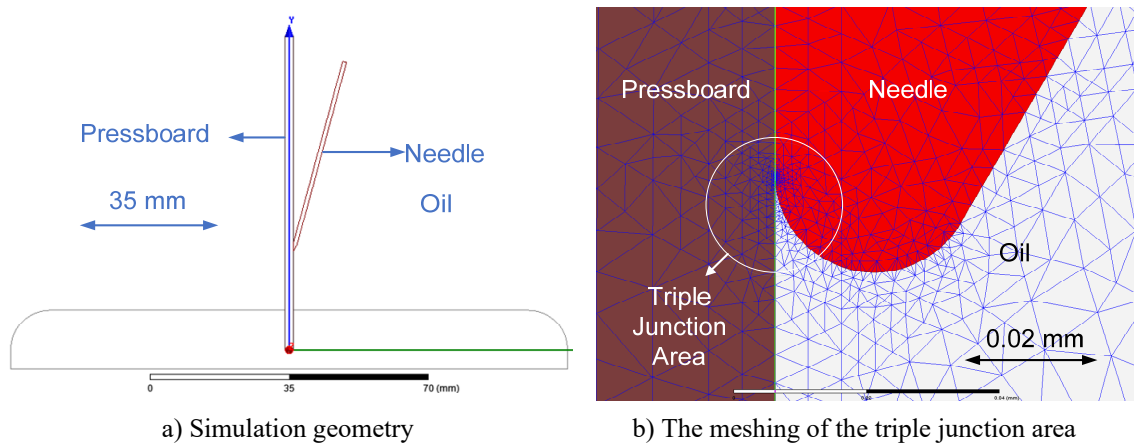


Figure 7.19 FEM design setting of the needle-to-plate electrode under DC voltage

The FEM simulations were carried out at 20 °C, 60 °C, and 80 °C, respectively. The applied DC voltage is 50 kV. Except material properties, the simulation settings at different temperatures are identical to each other. The material properties at different temperatures are listed in Table 7.3.

Table 7.3 Materials properties for FEM simulations under DC voltage

Material	Temperature (°C)	Relative Permittivity	Specific Conductivity (S/m)
Pressboard	20	4.19	5.3044e-15
	60	4.58	8.3741e-14
	80	4.77	3.3273e-13
Oil	20	2.30	4.1968e-13
	60	2.26	2.4698e-12
	80	2.23	5.9915e-12

The global potential distributions of the needle-to-plate geometry are shown in Figure 7.20. For a comparative analysis, the global potential distribution under an equivalent AC voltage is also added. As can be seen, the most appreciable difference between the AC and DC fields is the potential distribution in the oil part that lies behind the pressboard barrier. Under AC voltage, the potential distribution is somewhat ‘homogenous’ so that the oil part behind the pressboard is heavily stressed as well. In contrast, the pressboard acts like a ‘barrier’ under DC voltage so that the oil part behind the pressboard is much less stressed. Nevertheless, the stress in that oil part becomes ever-greater as temperature increases.

Moreover, the local field distributions at the triple-junction area at various temperatures are shown in Figure 7.21. It is known that the field intensity of the triple-junction area is considerably larger than those of other regions under AC voltage (see Section 4.3.5) because of the triple junction effect. Surprisingly, there is no field intensification in the triple junction area under DC voltage.

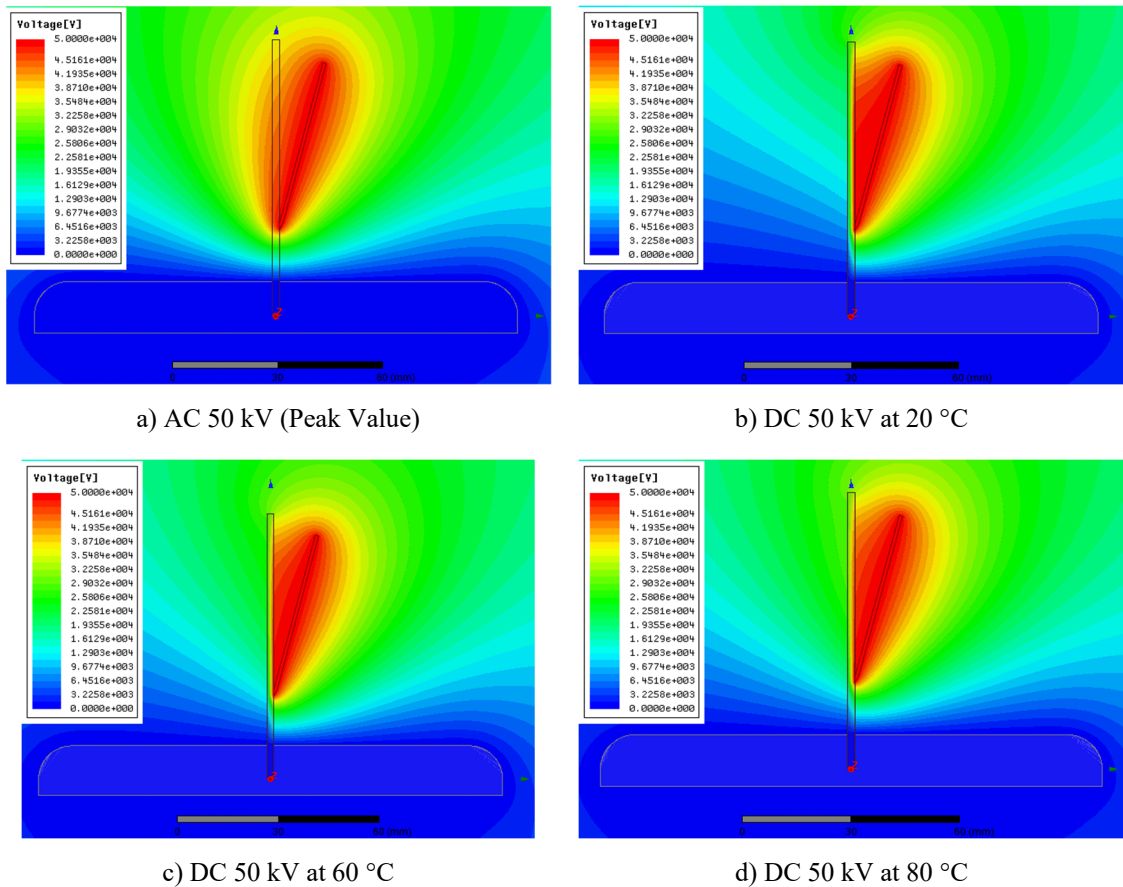


Figure 7.20 Global potential distribution of needle-plate electrode under DC voltage

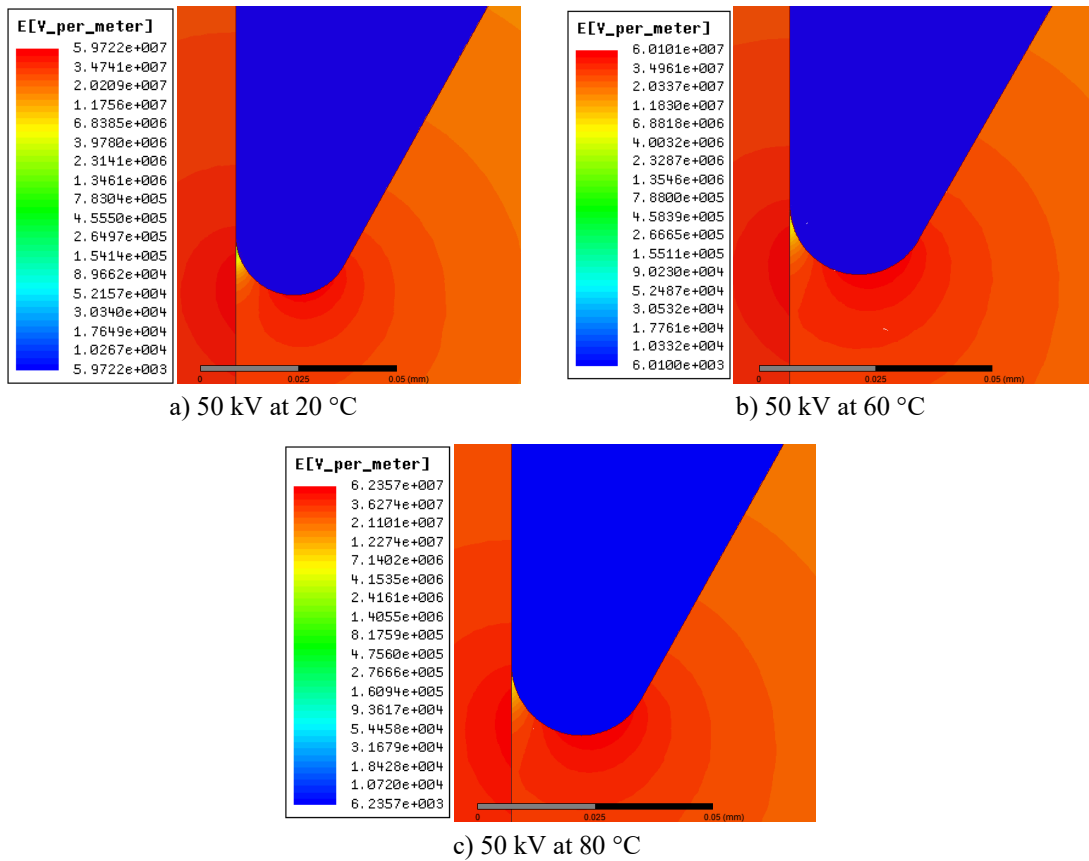


Figure 7.21 Local field distribution at the triple junction area under DC voltage

The DC field intensity in the triple junction area is obviously lower than that of pressboard and even lower than that of oil bulk. Therefore, it suggests that the triple junction contact may result in field reduction under the DC field. However, it is noteworthy that the effects of surface conduction are neglected in these simulations. More sophisticated experiments and simulations are needed for an in-depth investigation of this phenomenon.

In addition, it is also found that the maximum field intensity is slightly influenced by temperature. The maximum field intensities with temperatures are presented in Figure 7.22. Moreover, the temperature has a great impact on the current density. As shown in Figure 7.22, the maximum current density in oil increases exponentially as temperature increases.

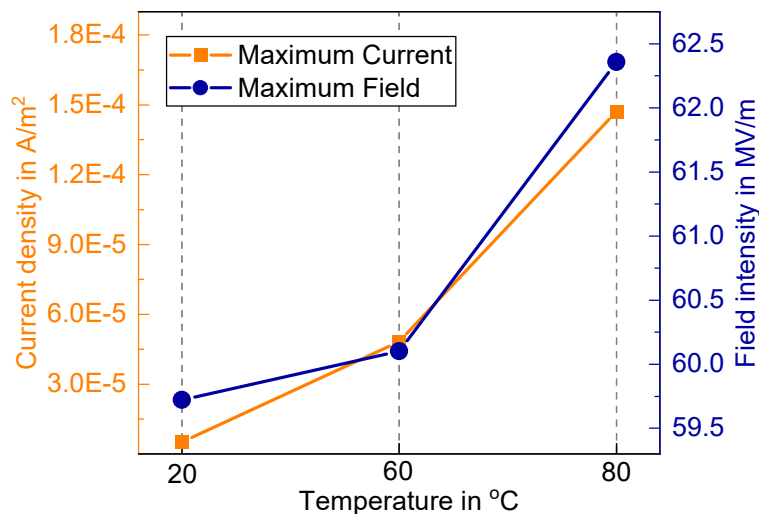


Figure 7.22 Maximum DC field intensity and current density versus temperature

Moreover, three reference lines were constructed in the simulation geometry to quantitatively evaluate the field distributions in different regions. The illustration of the reference lines is given in Figure 7.23. The first reference is placed in pressboard bulk and 0.01 mm away from the interface; the second line is exactly the interface, and the third line is placed in oil bulk and 0.01 mm away from the interface. The reference lines have lengths that are identical to pressboard height and are directed from top to the grounded electrode. The reference lines have lengths that are identical to pressboard height and are directed from top to the grounded electrode. For each reference line, the total electric field intensity E_{Total} are numerically evaluated against temperatures.

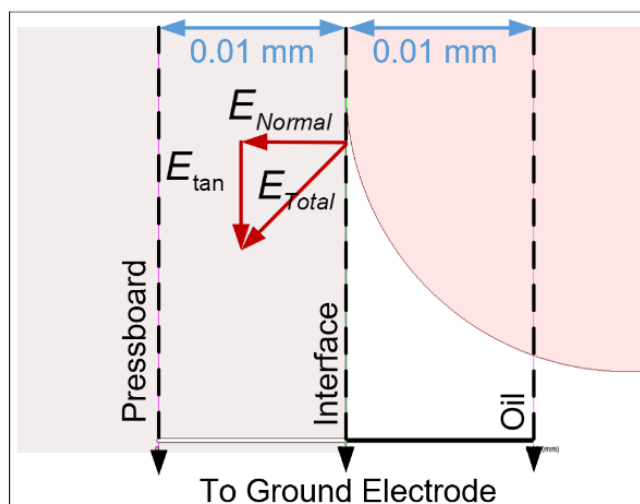


Figure 7.23 Reference lines for quantitative field analysis

The simulation results of the total electric fields versus temperatures are displayed in Figure 7.24, where the horizontal axis denotes the distance to the pressboard top. At 20 °C, as seen in Figure 7.24 a), the peak field intensities of all reference lines are located in the triple-junction area, and the peak field intensity of interface is considerably greater than those of pressboard and oil; in the regions above the triple junction area, however, the field intensity of pressboard is clearly the largest one and the field intensities of interface and oil are almost identical to one another; in the regions below the triple junction area, the field intensities of interface and pressboard are quite approximate to each other, and the field intensities of oil are the smallest one.

With respect to each individual region, the influence of temperature on field intensity is different. As shown in Figure 7.24 b), the field distribution of the interface is almost independent of temperature changes. Nevertheless, a closer look at the triple junction area still reveals that the peak field intensity of the interface is positively correlated with temperature. In contrast, a change in temperature has a pronounced effect on the field intensity of the pressboard. As shown in Figure 7.24 c), the field intensity of the pressboard is clearly negatively correlated with temperature. Nevertheless, the field intensity changes in the triple junction area are quite trivial compared with other regions. The field intensity in oil seems not much affected by temperature neither. However, similar to that of the interface, the peak field intensity of oil slightly increases with rising temperature.

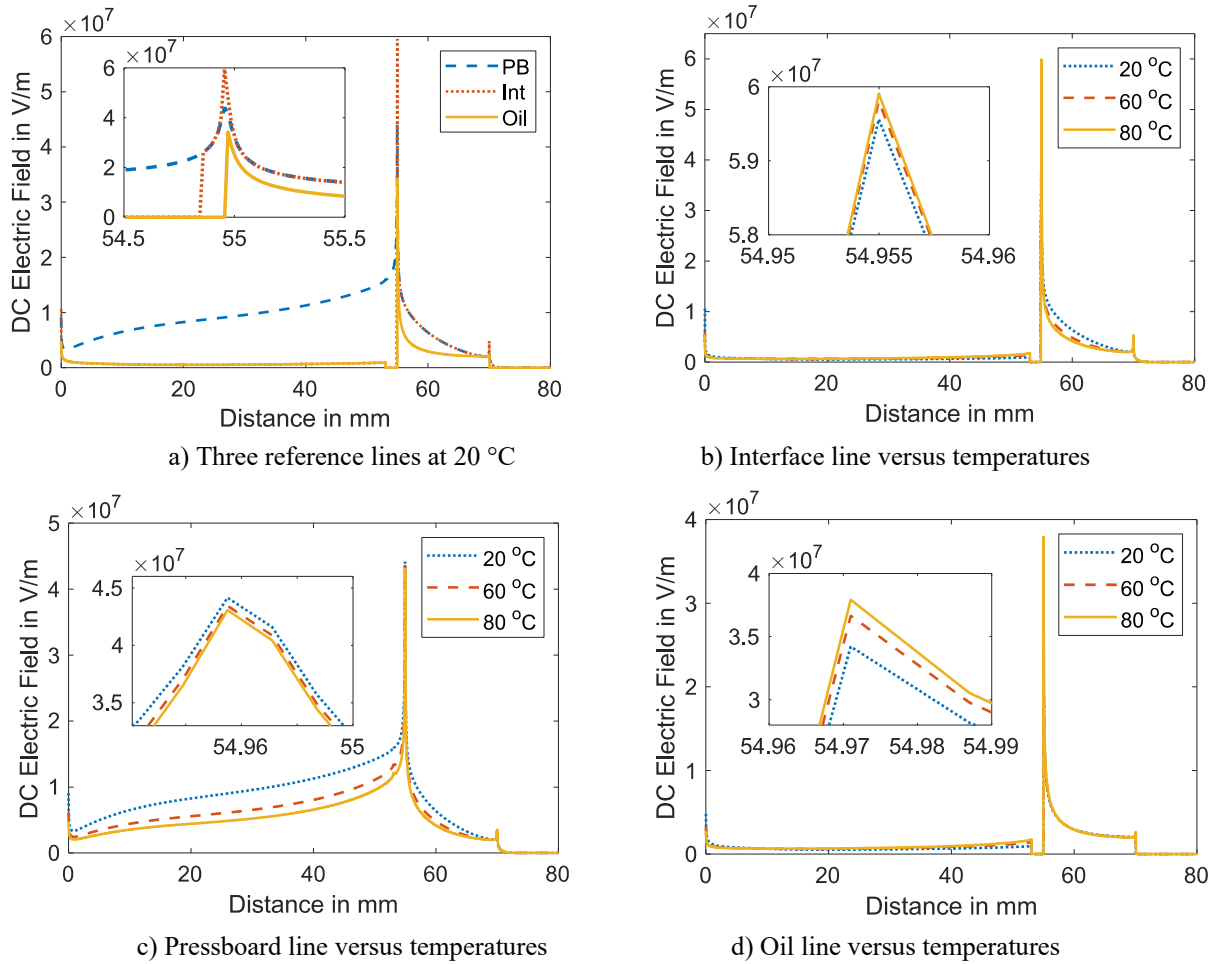


Figure 7.24 Total DC field intensity along three reference lines

Furthermore, a statistic of the maximum total field E_{total} and tangential field E_{tan} intensities of all regions is given in Figure 7.25.

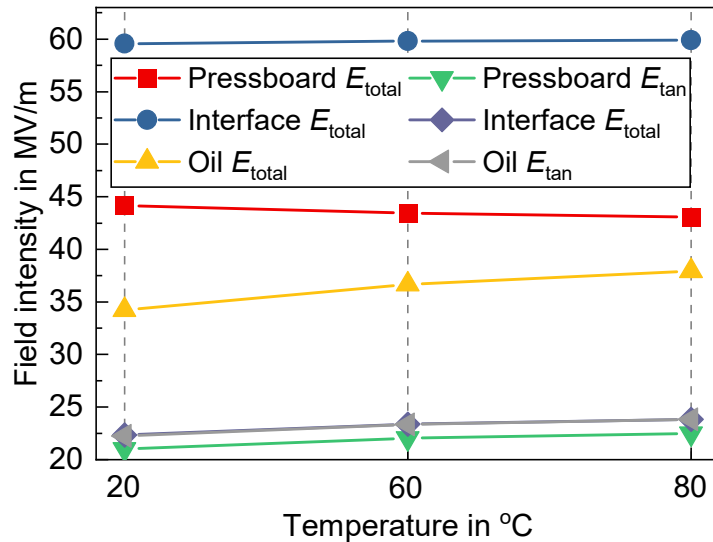


Figure 7.25 Maximum total and tangential field intensities versus temperatures

7.5 Results of DC Creeping Discharge Tests

7.5.1 Static Tests

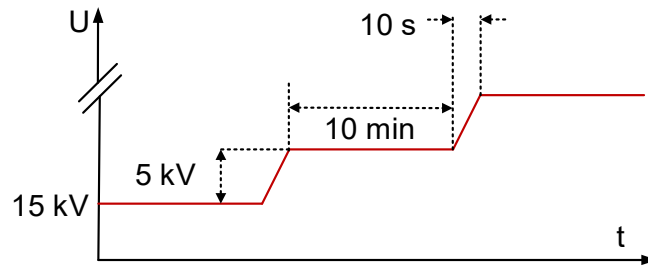


Figure 7.26 Step-voltage for static tests under DC stress

In static tests, there was no forced oil flow, and the test circumstance was therefore completely stationary. Step-wise voltage waveform was utilized for static tests. As shown in Figure 7.26, the applied DC voltage is increased from 15 kV to 55 kV with a step voltage rise of 5 kV. For each step, the test duration is 10 minutes, and the step voltage rising time is 10 s. The static tests were carried out at 20 °C, 60 °C, and 80 °C, respectively. Five repetitive tests were carried out at each temperature. The failure statistics are given in

Table 7.4, where NF denotes ‘No Flashover’. At each temperature, there are three specimens that survive the whole test, and all failures are due to interface flashover.

Table 7.4 DC Flashover voltages versus temperature in static oil

Specimen No.	Temperature (°C)		
	20	60	80
1	45 kV	50 kV	NF
2	NF	NF	45 kV
3	NF	NF	35 kV
4	40 kV	40 kV	NF
5	NF	NF	NF

In addition, PD measurements were implemented for all tests as well. The PD detection threshold is set to be 5 pC. At each temperature, no repetitive DC partial discharges were recorded until the voltage level was raised to 40 kV. More specifically, the scenarios of PD signals could be divided into three stages according to the voltage level. In stage 1, the voltage level ranges from 15 kV to 35 kV. In this stage, no repetitive DC discharges were recorded at any temperature.

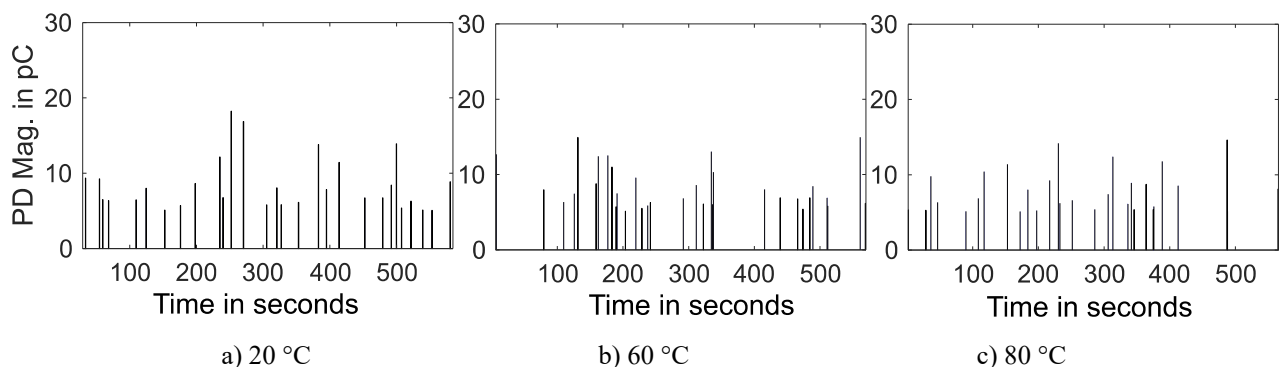


Figure 7.27 DC PD Q-T Pattern at 45 kV in static oil

In stage 2, the voltage level ranges from 40 kV to 45 kV. In this stage, repetitive discharges emerge, and ever-more PDs are recorded as voltage rises. However, the PD signals in stage 2 are characterized by low magnitudes and small time intervals. As shown in Figure 7.27 and Figure 7.28, the PD magnitudes at 45 kV are clearly below 30 pC, irrespective of the test temperature.

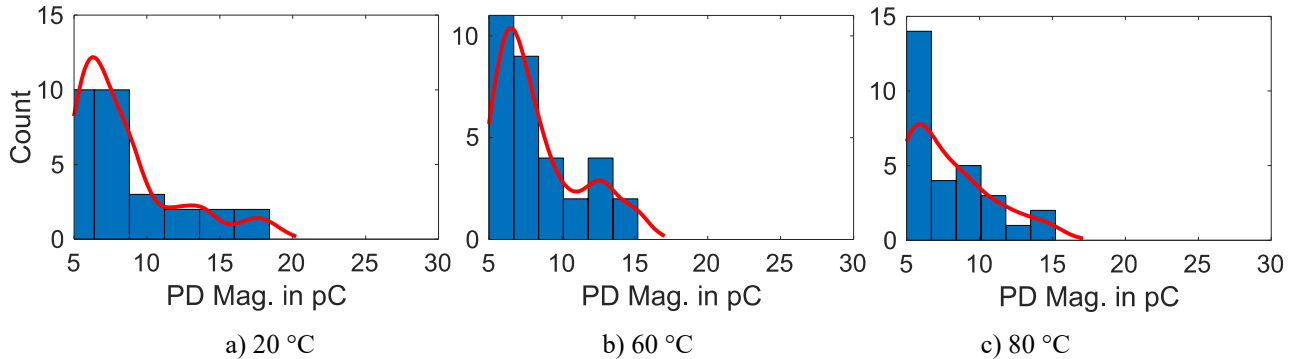


Figure 7.28 Histograms of DC PD magnitudes at 45 kV in static oil

In stage 3, the voltage level ranges from 50 kV to 55 kV. In this stage, a new kind of PD signal appears. As shown in Figure 7.29 and Figure 7.30, compared with the discharges that are already recorded in stage 2 (PD 1), the new kind of PD signals (PD 2) have distinctly greater magnitudes and wider time intervals. The appearance of PD 2 suggests another discharge type get probably involved in the DC interface creeping discharges.

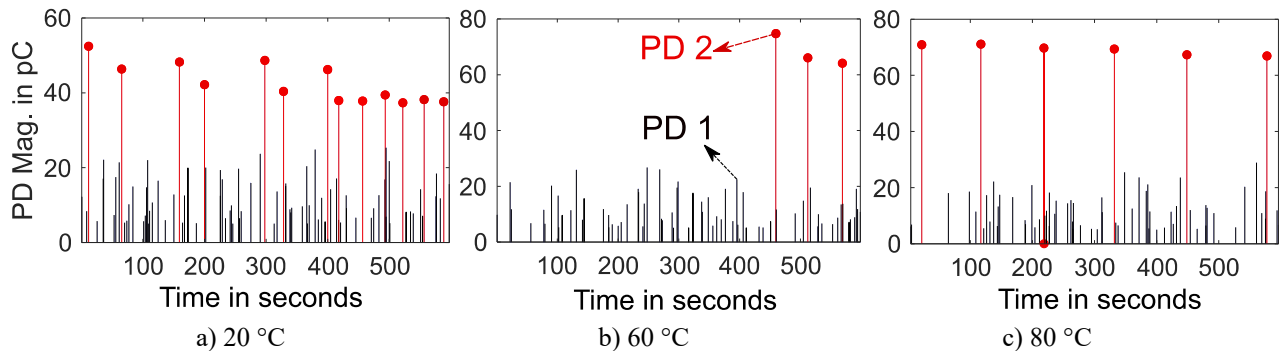


Figure 7.29 DC PD Q-T Pattern at 55 kV in static oil

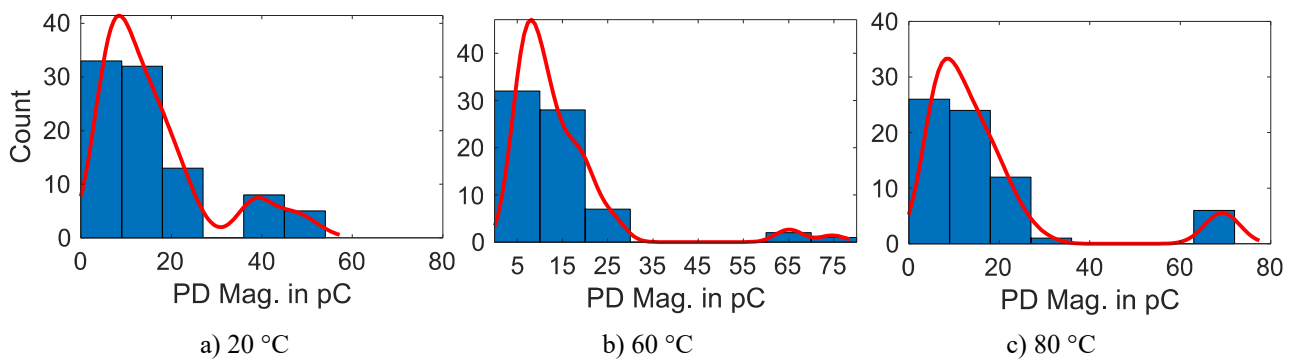


Figure 7.30 Histograms of DC PD Magnitudes at 55 kV in static oil

Afterwards, statistics of PD number and magnitude were made to PD 1, PD 2, and they combined (total PD), respectively. Their median values are evaluated as a function of voltage level. The results are shown in Figure 7.31.

As shown, the number of PD 1 is almost negligible in stage 1 and increases sharply with the voltage rise in stage 2 and stage 3. Besides, the number of PD1 at 20 °C is higher than those at 60 °C and

80 °C. Moreover, in stage 2 and stage 3, the median magnitude of PD 1 increases with voltage rise as well. However, no obvious variations in PD 1 magnitude are detected among different temperatures. With respect to PD 2, its number shows a positive correlation with voltage level as well, especially at 20 °C. Besides, similar to that of PD 1, the number of PD 2 at 20 °C is much greater than those at 60 °C and 80 °C. Moreover, the median amplitude of PD 2 increases with voltage. However, in contrast to that of PD 1, the median amplitude of PD 2 at 55 kV is closely related to temperature: it is around 80 pC at 80 °C, 70 pC at 60 °C, and merely 40 pC at 20 °C, respectively.

As a result, the numbers of Total PD increase sharply in stage 2 and stage 3, where the Total PD number at 20 °C is much larger than those at 60 °C and 80 °C. Moreover, due to the comparatively large number of PD 2, the magnitude of Total PD at 20 °C is still greater than those at other temperatures.

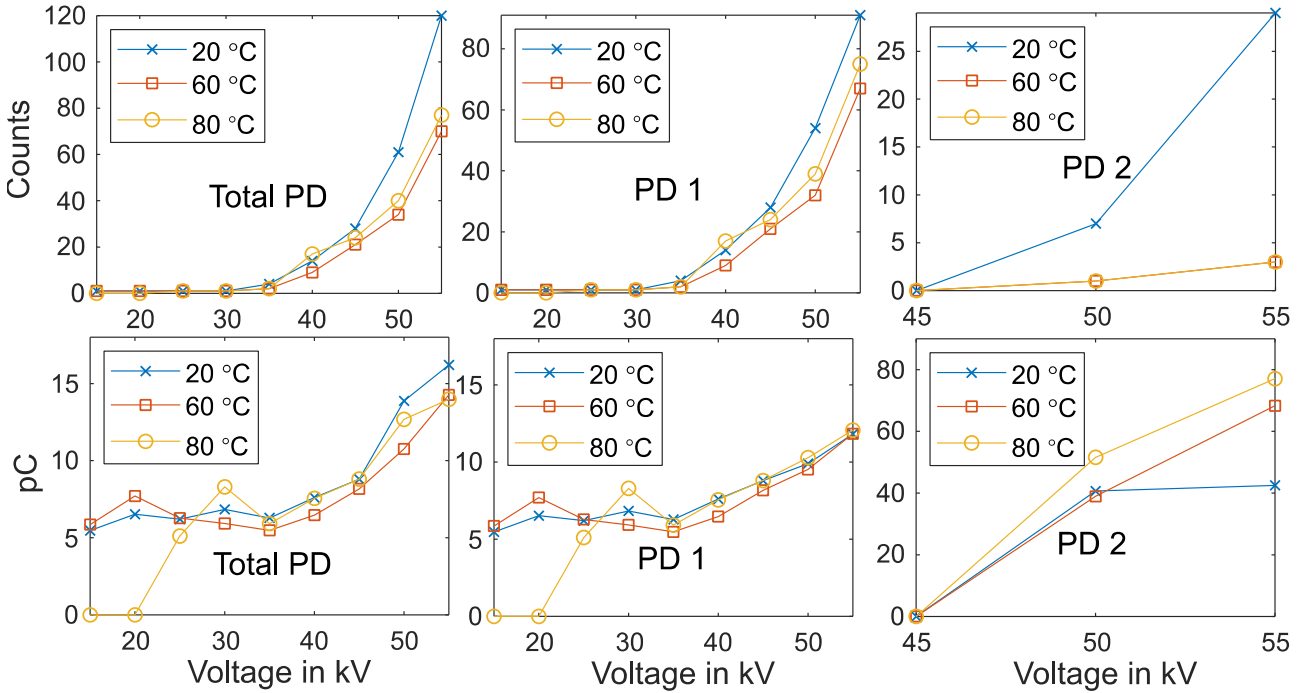


Figure 7.31 PD number and magnitude versus temperature and voltage in static oil

Subsequently, the chaotic analysis of PD (CAPD) was utilized to represent the PD pattern under DC voltage. The method used in this chapter was adapted from the methods proposed in [203, 204]. The method is based on two fundamental parameters of a DC discharge pulse, i.e., discharge amplitude q and occurrence time t (see Figure 7.8). The evaluation procedures of CAPD are given as follows:

- Obtaining Fundamental Quantities q and t
- Normalization of Fundamental Quantities

$$q^n = \frac{q - q_{\min}}{q_{\max} - q_{\min}} \quad (7.11)$$

where q^n and q denote the normalized magnitude and raw magnitude of a given PD pulse, respectively; q_{\max} and q_{\min} are the maximum and minimum PD pulses in the given PD dataset, respectively.

$$\Delta t_i^n = \frac{\Delta t_i}{\Delta t_{\max}} = \frac{t_i - t_{i-1}}{\Delta t_{\max}} \quad (7.12)$$

where Δt_i denotes the time interval between a given PD pulse (occurring at t_i) and its preceding PD

pulse (occurring at t_{i-1}); Δt_{\max} is the largest time interval between two consecutive pulses in the given PD dataset; Δt_i^n denotes the normalized value of Δt_i .

- Differentiation of Normalized Values

$$Q_i^N = q_i^n - q_{i-1}^n \quad (7.13)$$

where Q_i^N is the difference between the normalized magnitude of a given PD pulse and that of its preceding pulse and $-1 \leq Q_i^N \leq 1$.

$$\Delta T_i^N = \Delta t_i^n \quad (7.14)$$

where $0 < \Delta T_i^N \leq 1$.

- Comparison between Consecutive Discharges

$$Q_{i+1}^N = q_{i+1}^n - q_i^n \quad (7.15)$$

$$\Delta T_{i+1}^N = \Delta t_{i+1}^n \quad (7.16)$$

where Q_{i+1}^N denotes the difference in the normalized magnitude between a given PD pulse and its successive pulse and ΔT_{i+1}^N denotes the normalized value of time interval between a given PD pulse and its successive PD pulse.

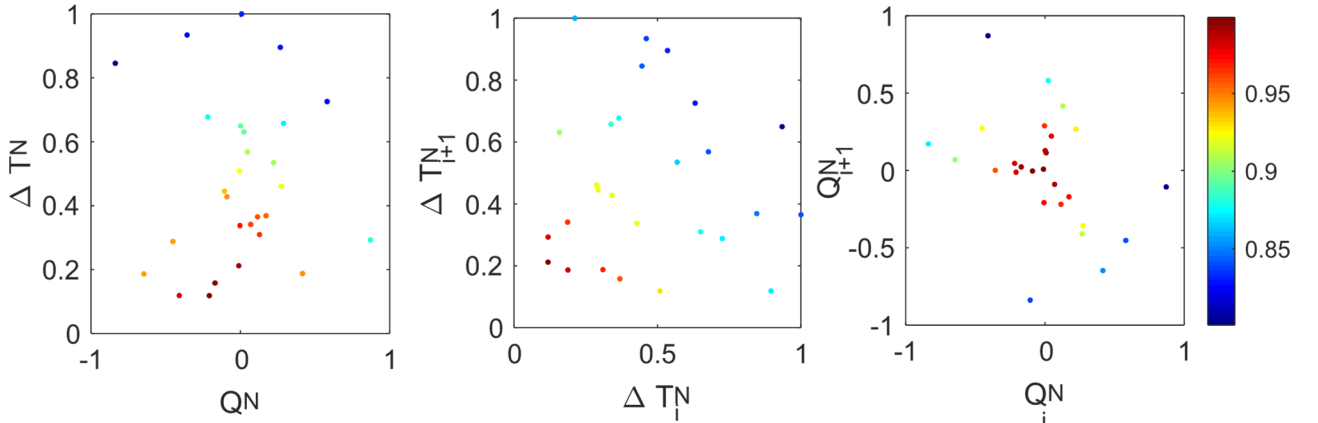


Figure 7.32 CAPD pattern of partial discharge under DC voltage (45 kV) in static oil

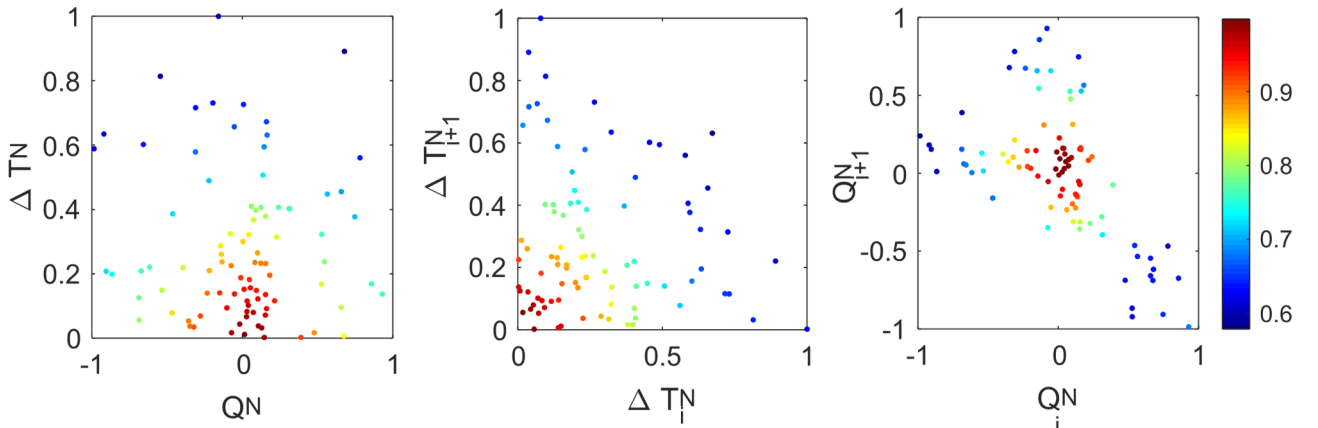


Figure 7.33 CAPD Pattern of partial discharge under DC voltage (55 kV) in static oil

Based on the above-listed parameters, three density scatter plots, i.e., $Q_i^N - \Delta T_i^N$, $\Delta T_i^N - \Delta T_{i+1}^N$, and $Q_i^N - Q_{i+1}^N$, could be made to represent the partial discharges under DC voltage. The representative CAPD patterns of partial discharge in static tests under 45 kV and 55 kV are shown in Figure 7.32 and Figure 7.33, respectively, where the color bar denotes the normalized density.

As shown, the presence of PD 2 could bring a conspicuous shift to the CAPD pattern. For instance,

the centroid of the cluster in the $Q_i^N - \Delta T_i^N$ plot is shifted downwards to (0,0) as voltage increases from 45 kV to 55 kV. Moreover, with respect to the $Q_i^N - Q_{i+1}^N$ plot, the points are scattered around the centroid of the cluster at 45 kV, whereas points of extremes are found at 55 kV, which are located around (-1,0), (0,1), and (1, -1), respectively.

7.5.2 Dynamic Tests

In dynamic tests, the oil was forced to flow at varying speeds by means of a liquid diaphragm pump. The diaphragm pump has eleven transfer speed levels. Three speed levels were chosen for circulating the heated oil. The oil flow velocities at chosen speed levels are shown in Figure 7.34. As shown, the oil flow velocities are affected by oil temperatures as well.

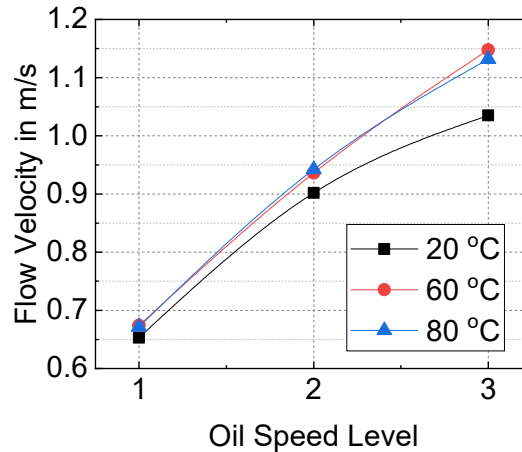


Figure 7.34 Oil flow velocity versus pump speed and temperature

Table 7.5 DC flashover voltages and time-to-flashovers versus temperature in flowing oil

Oil Speed Level	Specimen No.	Flashover Voltage (kV)			Time-to-Flashover		
		20 °C	60 °C	80 °C	20 °C	60 °C	80 °C
1	1	65	65	NB	129	121	NB
	2	60	70	60	115	132	111
	3	NB	NB	50	NB	NB	98
	4	70	70	65	134	131	122
	5	70	50	60	135	92	119
2	1	NB	60	50	NB	115	92
	2	55	NB	45	103	NB	81
	3	55	NB	50	102	NB	90
	4	60	NB	55	106	NB	104
	5	NB	70	50	NB	136	94
3	1	45	NB	50	82	NB	100
	2	55	65	70	102	121	133
	3	50	70	50	94	136	93
	4	55	NB	50	107	NB	96
	5	55	55	65	100	109	115

In dynamic tests, the waveform of the applied voltage is almost the same as that shown in Figure

7.26. The oil temperatures are 20 °C, 60 °C, and 80 °C, respectively. At each temperature, oil was forced to flow at three different levels, which makes in total nine test samples. For every single sample, five measurements were carried out to investigate the interface flashover voltages and times-to-flashovers. The maximum voltage level is 70 kV. The test specimens that did not break down were treated as singly censored data. No tracking phenomena were observed with all test samples.

Table 7.5 gives the failure statistics of dynamic tests, where ‘NB’ denotes no breakdown.

Figure 7.35 illustrates the DC flashover voltages as a function of temperature and oil flowing speed. At 20 °C, the flashover voltage steadily declines with oil flowing speed. However, no monotonic relation between oil speed and flashover voltage can be found at elevated temperatures. At 60 °C, the flashover voltage slightly increases as the oil speed rises but thereafter drops back. In contrast, at 80 °C, the flashover voltage firstly declines and subsequently ascends as oil speed increases.

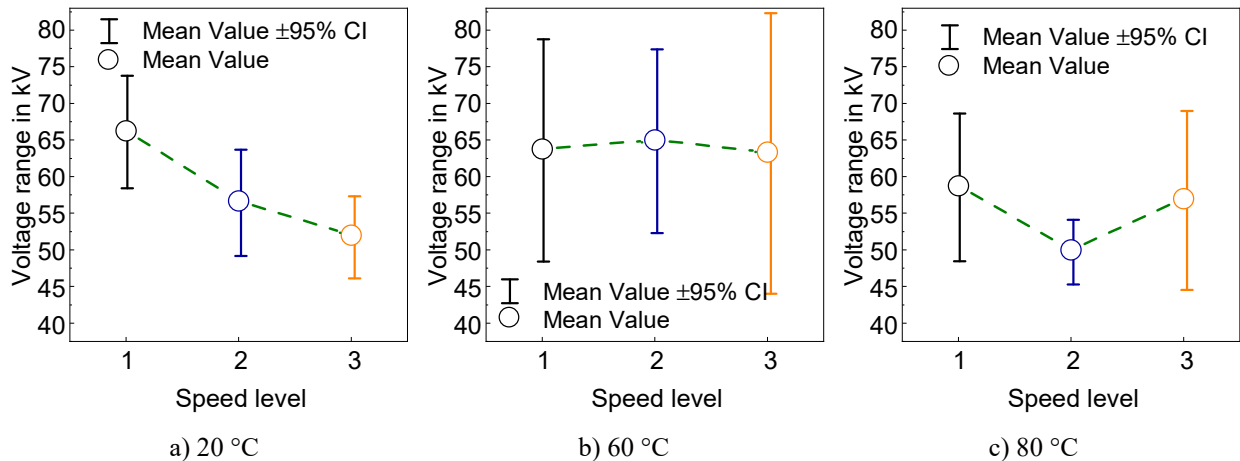


Figure 7.35 DC flashover voltages versus temperature and oil flowing speed

To study the effects of temperatures and oil flowing speeds on interface strength separately, the data were re-grouped according to temperature and oil flowing speed, respectively. For instance, the data obtained at the same temperature were categorized as one group irrespective of the oil flowing speeds and vice versa. Weibull distribution was utilized to fit the time-to-flashovers of the re-grouped data. The cumulative density function (CDF) of a two-parameter Weibull distribution is expressed as:

$$F(t; \alpha, \beta) = 1 - \exp \left\{ - \left(\frac{t}{\alpha} \right)^\beta \right\} \quad (7.17)$$

where, $F(t; \alpha, \beta)$ is the failure probability, t is the measured variable, α is the scale parameter, and β is the shape parameter. The scale parameter α is equivalent to the measured variable value for which the failure probability is 0.632. It is analogous to the mean of a Normal distribution. The shape parameter β reflects the range of the measured variable. The larger β is, the smaller is the range of measured values [205]. The Weibull probability plots of the time-to-flashovers versus oil flow speed and temperature are shown in Figure 7.36 a) and Figure 7.36 b), respectively. As shown, the re-grouped data fit Weibull distributions well.

Two methods were employed to estimate the Weibull scale and shape parameters of the singly censored time-to-flashovers. The first method is referred to as the IEEE empirical method, with which the distribution parameters can be calculated using a set of empirical equations and designated quantities provided in IEEE Std 930-2004 [205]. The second method is referred to as least squares regression, with which the distribution parameters are obtained through purely numerical computations.

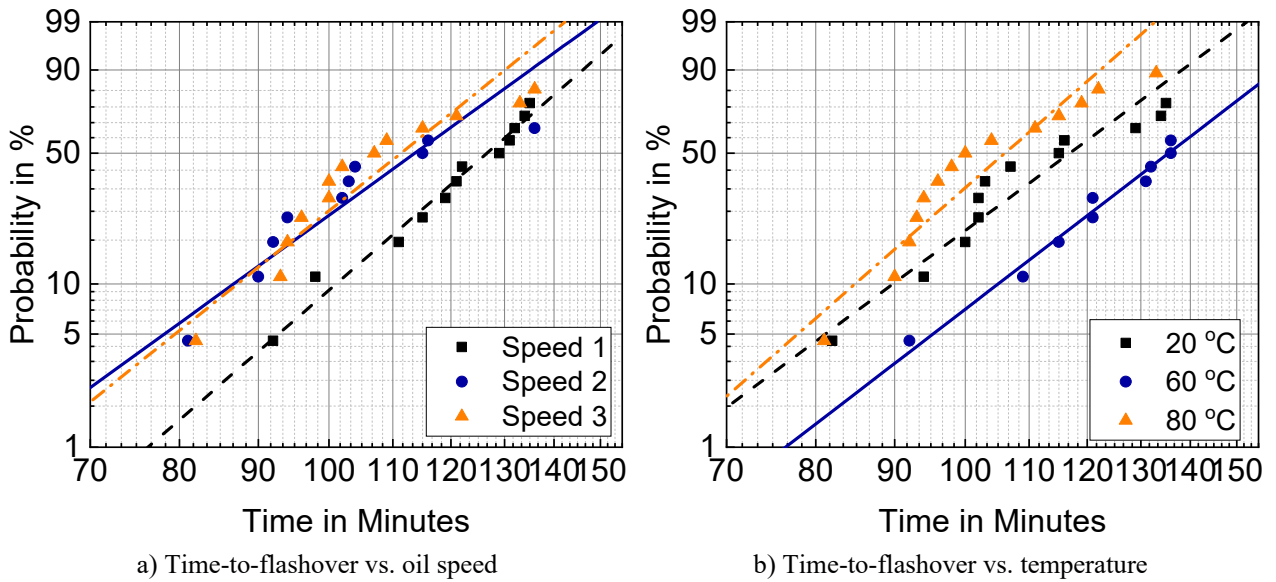


Figure 7.36 Weibull plot of time-to-flashover under DC stepwise voltage

The estimated parameters of DC time-to-flashover Weibull distributions are given in Table 7.6. As displayed, the scale parameters α are quite approximate to each other using different methods, whereas the shape parameters β exhibit comparatively great deviations. Accordingly, one can identify the respective influences of temperature and oil flowing speed on interface time-to-flashovers through evaluating the scale parameters. In general, increasing oil flowing speed could shorten the withstand time of interface to DC voltages. However, only a slight difference can be found between Speed 2 and Speed 3.

Table 7.6 Estimated parameters of Weibull distributions of DC time-to-flashover

Variables	IEEE Empirical Method		Least Square Regression	
	β	α	β	α
Temperature in °C				
20	6.03	124.9	7.14	123.0
60	8.24	141.1	7.40	142.4
80	6.67	111.6	8.41	110.8
Oil Speed Level	β	α	β	α
1	9.19	131.9	8.36	132.3
2	5.51	123.9	6.95	119.9
3	6.10	118.3	7.71	116.7

In contrast, the effects of temperature are not straightforward. As the temperature increases from 20 °C to 60 °C, the withstand time of the interface is greatly lengthened. However, as the temperature goes to 80 °C, the withstand time drops back and becomes even smaller than that at 20 °C. The phenomenon could be attributed to two antagonistic factors. The first is the declined relative humidity of oil, which could enhance the electric strength of oil; the second is the intensified electric field in oil bulk, as shown in Figure 7.24, which could enlarge the breakdown probability of oil. Besides, another possibly involved process is the bubble formation under high temperatures.

PD measurements were implemented for every test sample. However, limited by experimental

conditions, PD measurements were only carried out under 60 kV. The settings of PD measurements are the same as depicted in Section 7.5.1. The results of PD measurements of dynamic tests are reported in the following paragraphs.

The forced oil flow can alter the PD behaviors of DC creeping discharges drastically. The appearance of a special PD signal, i.e., the ‘Pulse Train,’ is of particular interest. The pulse train is composed of a great number of PD pulses, which have varying magnitudes and extremely small inter-pulse time intervals. As a result, the PD pulses appear to occur simultaneously in a relatively large time scale. Figure 7.37 gives the Q-T pattern of representative pulse trains recorded with forced oil flows.

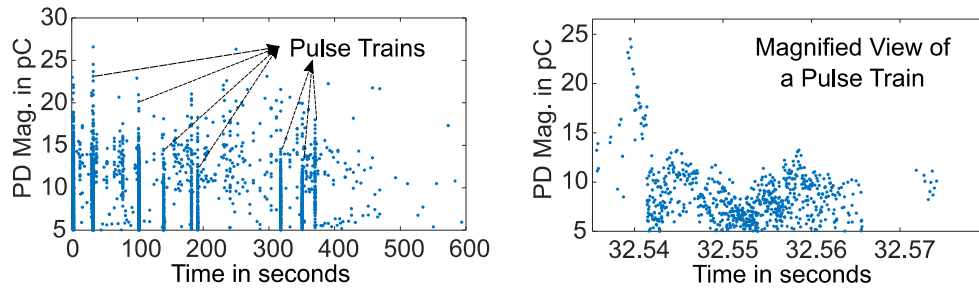


Figure 7.37 Typical DC PD pulse train with forced oil flow

As a result of the emergence of pulse trains, dramatic surges of PD numbers are observed with all test samples under high voltage levels. Unfortunately, due to the erratic nature of pulse trains, it is meaningless to give quantitative statistics of PD quantities with forced oil flows. Therefore, in the following paragraphs, the PD behaviors of creeping discharges would be qualitatively analyzed as a function of voltage level, oil flowing speed, and temperature. Therein, the emphasis is put on the characteristics of pulse trains, and the principal variable is temperature.

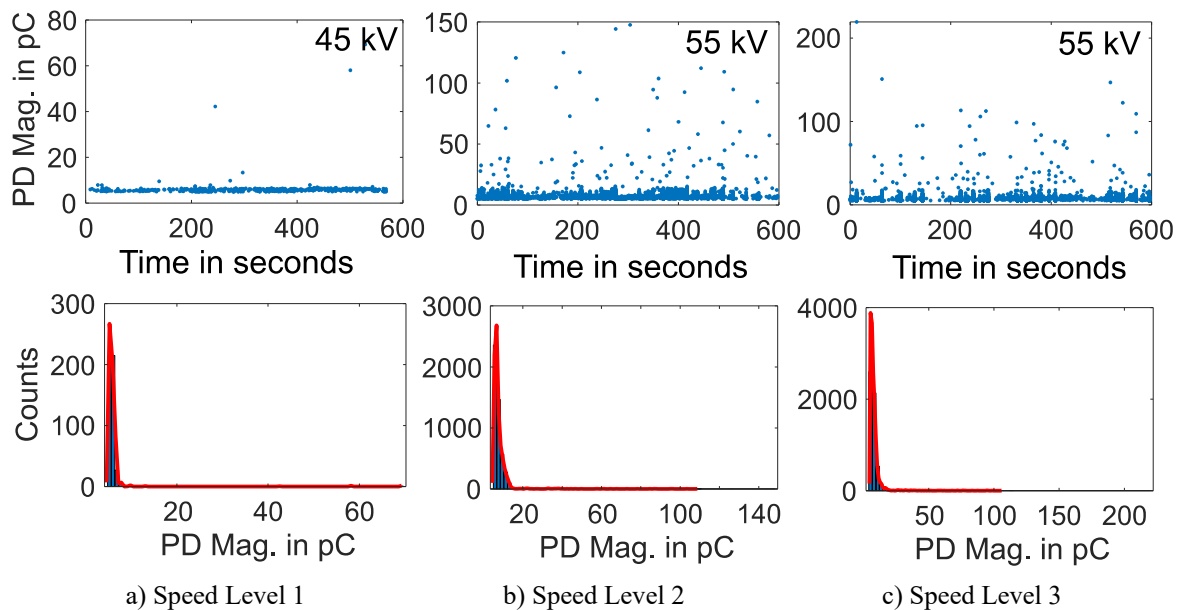


Figure 7.38 Q-T pattern and magnitudes histograms at 20 °C versus voltage and oil flowing speed

The Q-T trends of creeping discharges and the PD magnitude distributions at 20 °C are given in Figure 7.38. Similar to the situations under static oil, repetitive PD discharges begin to emerge when the voltage level reaches 45 kV under forced oil flow. Moreover, with respect to the influences of voltage and oil flowing speed, three major conclusions can be drawn as follows. Firstly, the PD numbers grow drastically as the voltage increases from 45 kV to 55 kV. The soaring trend in PD numbers can be mainly due to the ever-more pulse trains with rising voltage levels. Secondly, the

density of the pulse train is positively correlated with oil flowing speed as well. Thirdly, in addition to the pulse trains, a number of large-magnitude PDs are detected under 55 kV. The magnitude of these PDs can reach up to 200 pC. However, it is hard to establish its relation to oil flowing speed. The Q-T trends of creeping discharges and the PD magnitude distributions at 60 °C are given in Figure 7.39. The conclusions made on the situations at 20 °C apply to those at 60 °C as well. In fact, the positive correlation between the pulse train and oil flowing speed becomes clearer.

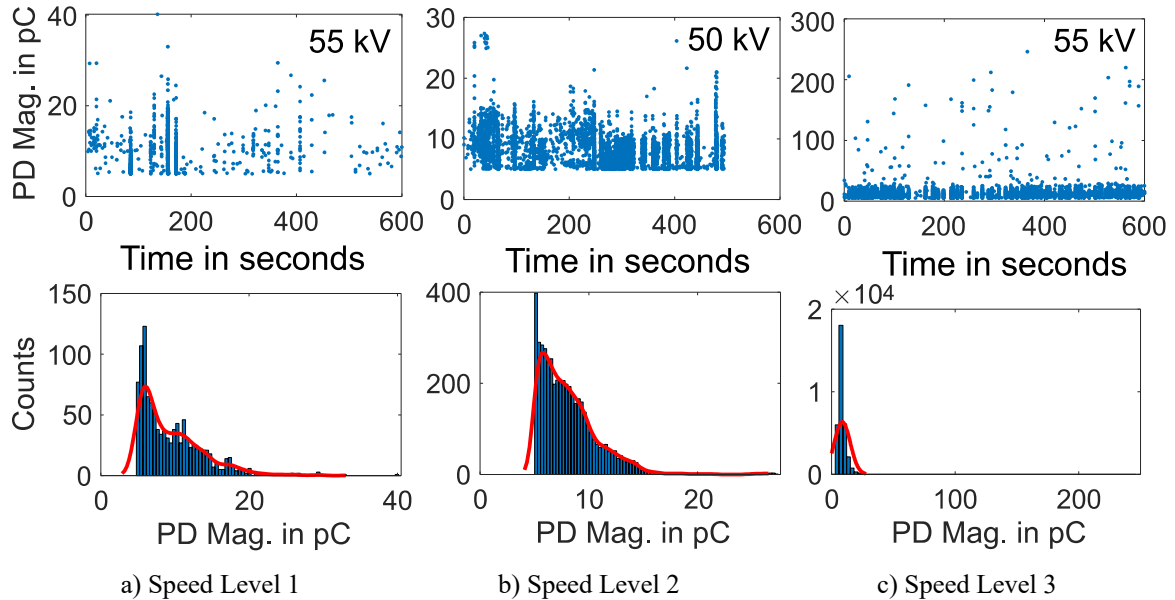


Figure 7.39 Q-T pattern and magnitudes histograms at 60 °C versus voltage and oil flowing speed

Moreover, a major difference between 20 °C and 60 °C lies in the density of the pulse train, which is clearly manifested when comparing Figure 7.38 c) and Figure 7.39 c). Under the same circumstances (55 kV and Speed level 3), the density of the pulse train at 60 °C is apparently higher than that at 20 °C, which results in several times more PD numbers at 60 °C. The results indicate the occurrence of the pulse train is also subject to temperature.

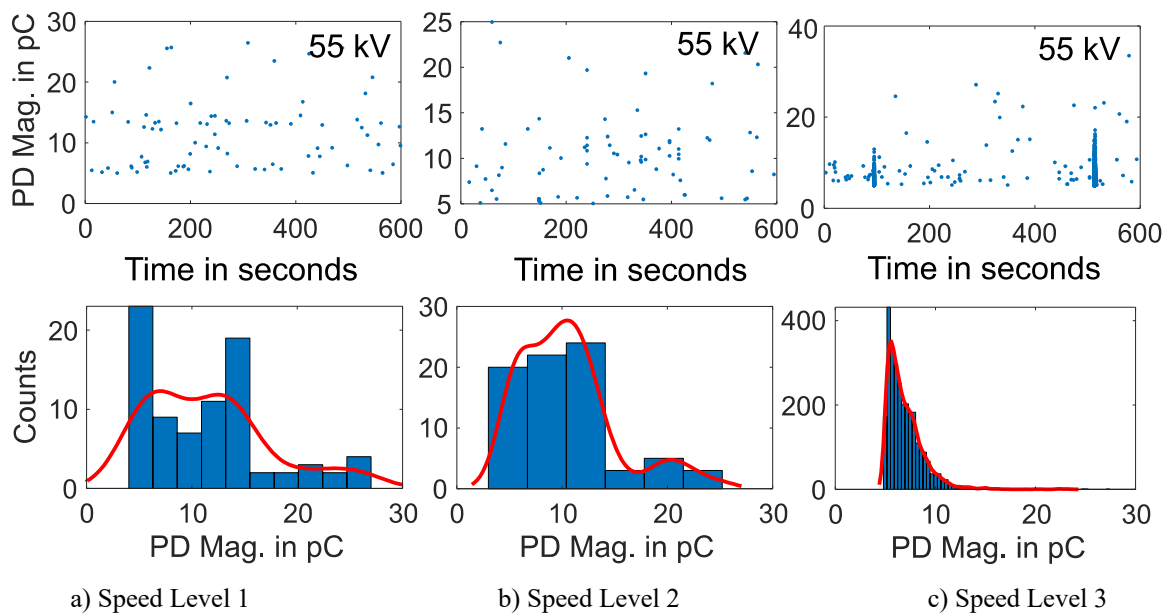


Figure 7.40 Q-T pattern and magnitudes histograms at 80 °C versus voltage and oil flowing speed

The Q-T trends of creeping discharges and the PD magnitude distributions at 80 °C are given in Figure 7.40. Surprisingly, the density of the pulse train declines drastically as the temperature

increases to 80 °C. In fact, the pulse train is detected only at 55 kV under oil speed level 3. This result highlights the role of temperature in determining the occurrence of the pulse train. Nevertheless, the effects of oil flowing speed and voltage are still the same as those at 20 °C and 60 °C. In addition to the mitigation of pulse trains, the large-magnitude pulses vanish at 80 °C as well. The coincidence suggests that there might be a correlation between the pulse trains and the large-magnitude pulses.

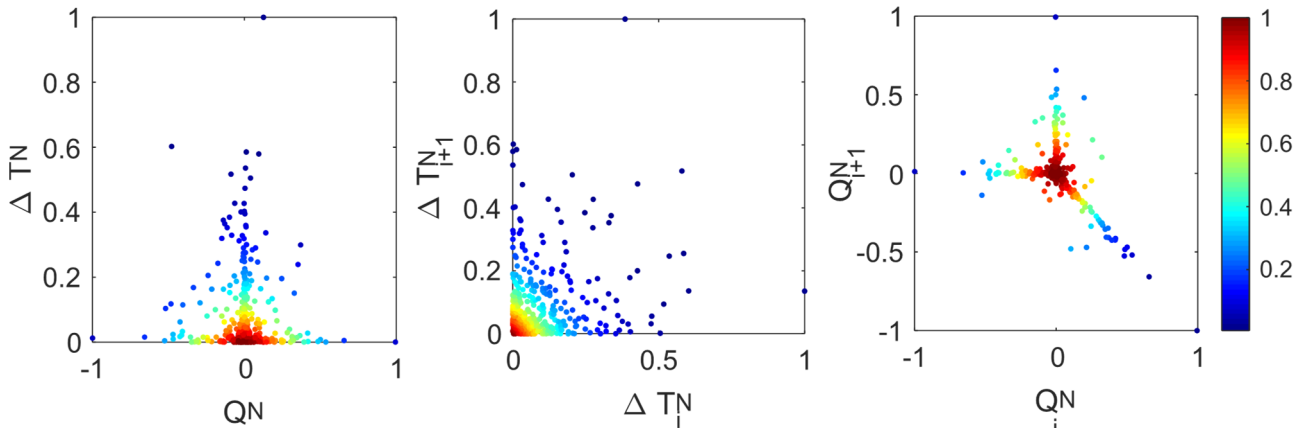


Figure 7.41 CPAD of DC creeping discharges with forced oil flow at 20 °C (55 kV, oil speed level 3)

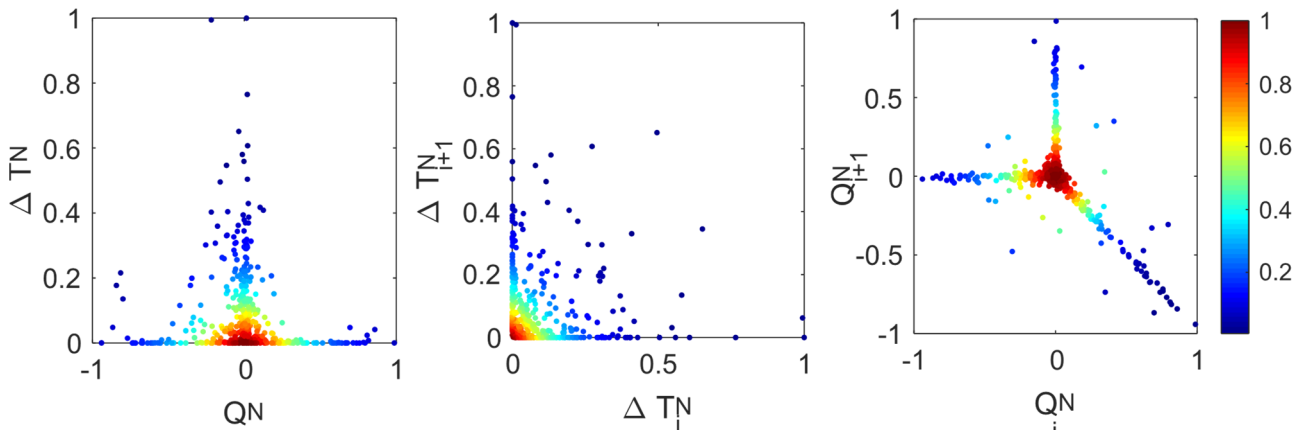


Figure 7.42 CPAD of DC creeping discharges with forced oil flow at 60 °C (55 kV, oil speed level 3)

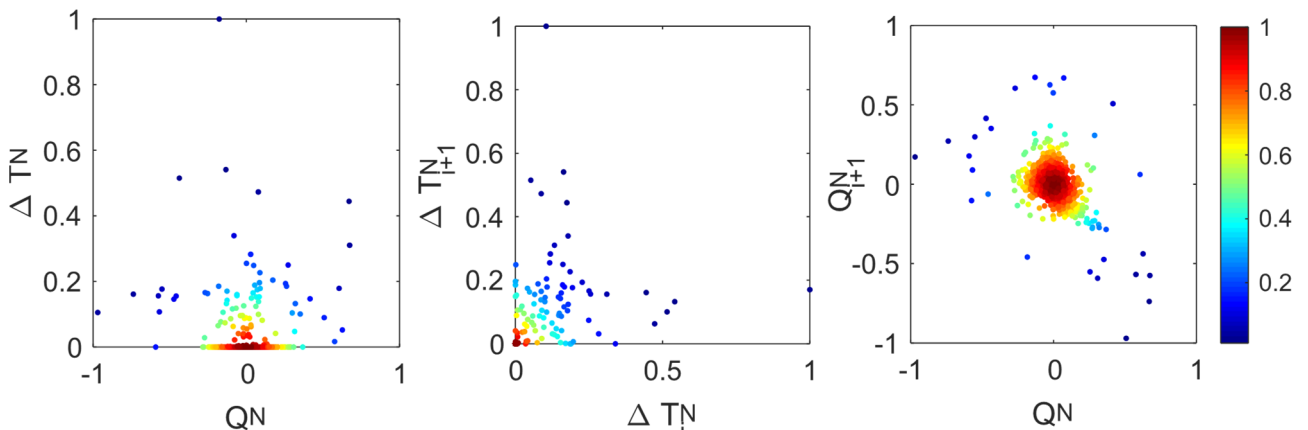


Figure 7.43 CPAD of DC creeping discharges with forced oil flow at 80 °C (55 kV, oil speed level 3)

Besides, the existence of pulse trains has a direct effect on the CAPD pattern. The representative CAPD patterns at different temperatures are shown in Figure 7.41 to Figure 7.43. As shown, due to the large numbers of pulse trains at 20 °C and 60 °C, there are extremely dense concentrations of scatter points around (0,0) in the $\Delta T_i^N - \Delta T_{i+1}^N$ plot. Moreover, due to the co-existence of pulse trains and large-magnitude pulses, the scatter points in the $Q_i^N - Q_{i+1}^N$ plots stretch from the cluster centroid

(0,0) to three extremes (-1, 0), (0,1), and (1, -1), at 60 °C in particular. In contrast, at 80 °C, the scatter points in the $Q_i^N - Q_{i+1}^N$ plots are distributed only in the vicinity of the cluster centroid.

Furthermore, the streaming currents were investigated as a function of voltage level, temperature, and oil flowing speed. Aiming to diminish probabilistic errors, five repetitive measurements were carried out to each test sample (different temperatures and different oil speeds). Afterwards, the streaming currents were evaluated against the step voltage level, and the measurement values of the same voltage step were averaged. Figure 7.44 shows the boxplots of five measurements of streaming currents versus temperatures and oil flowing speeds.

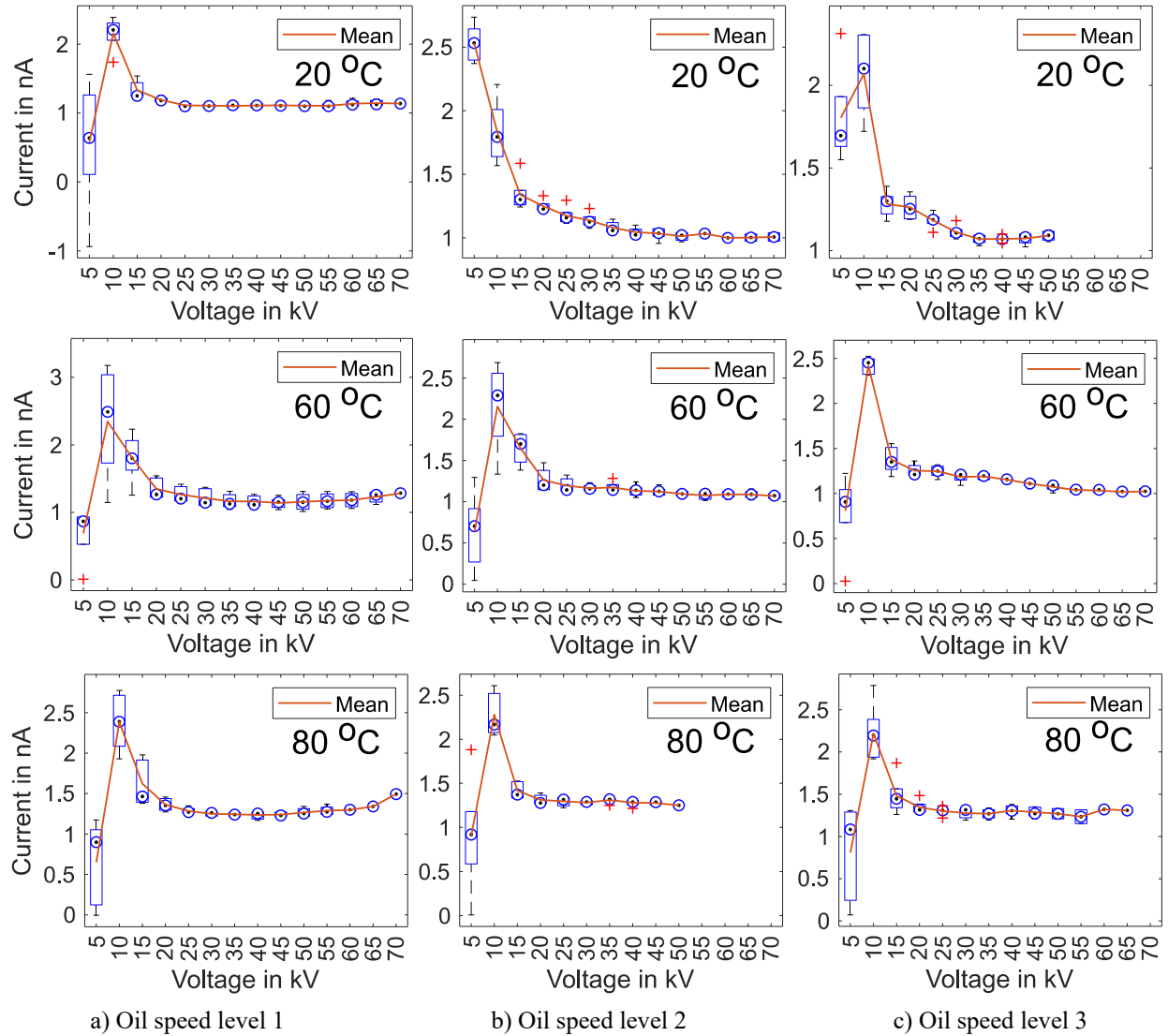


Figure 7.44 Boxplots of streaming currents under DC step voltage

The streaming currents exhibit a common trend with voltage for every test sample, irrespective of temperatures and oil flowing speeds. The streaming currents ascend as voltage increases from 5 kV to 10 kV. However, as the voltage level continues to step upwards, the streaming currents decline gradually and become stabilized eventually. In addition to the commonality in trend, no significant differences in current amplitudes were found among test samples either.

The results imply that no substantial extra DC fields were build up in the tests. Therefore, the influences of the pre-supposed extra DC fields due to flowing electrification can be excluded from the discussions on creeping discharges. Moreover, the information expressed in Figure 7.44 also suggests that the streaming currents in these tests are probably only a function of test time.

7.6 Discussion

Given the extremely inhomogeneous field distribution in the needle-to-plate geometry, it is reasonable to assume the observed partial discharge phenomenon takes place in a considerably confined region, i.e., the triple-junction area. Therefore, the following discussions focus mainly on the possible physical processes at the triple-junction area.

7.6.1 DC Creeping Discharges in Static Oil

To reveal the discharge mechanisms, one has to take into account a number of factors, such as surface charges accumulated on interface, excess space charges due to field ionization, and the competing effects of temperature. Due to the discontinuity of permittivity and conductivity, surface charges could accumulate at the interface between different materials under a DC field. The density of the accumulated surface charges ρ_{in} can be estimated using the Maxwell-Wagner equation [206]:

$$\rho_{in} = \frac{\varepsilon_{oil}\sigma_p - \varepsilon_p\sigma_{oil}}{d_{oil}\sigma_p + d_p\sigma_{oil}} U \left(1 - e^{-t/\tau_{WM}}\right) \quad (7.18)$$

where, ε_{oil} and ε_p denote the permittivity of oil and pressboard, respectively; σ_{oil} and σ_p denote the conductivity of oil and pressboard, respectively; d_{oil} and d_p denote the thickness of oil gap and pressboard, respectively; U is the applied voltage and t is time; τ_{WM} denotes the Maxwell-Wagner time constant and is expressed as:

$$\tau_{WM} = \frac{d_{oil}\varepsilon_p + d_p\varepsilon_{oil}}{d_{oil}\sigma_p + d_p\sigma_{oil}} \quad (7.19)$$

Given that $\sigma_{oil} > \sigma_p$ and $d_{oil} \ll d_p$ in the triple-junction area, Equation (7.19) can be rewritten as:

$$\tau_{WM} \approx \frac{\varepsilon_{oil}}{\sigma_{oil}} \quad (7.20)$$

Therefore, the transition time from a transient state to a steady state is solely determined by oil properties in this case. According to the calculation results in Figure 7.18, it is believed that the surface charge accumulations have reached a steady state in all tests. Therefore, the transient processes, e.g., discharges due to the capacitive field, can be excluded from the discussions.

Similar to AC creeping discharges, they comprise two kinds of PD signals, i.e., PD 1 and PD 2 (see Figure 7.29). Compared with PD 2, PD 1 has a lower inception voltage, lower magnitude, and much smaller time intervals between consecutive pulses. The distinct discrepancies between PD 1 and PD 2 indicate that two different discharge mechanisms are involved.

The comparatively weak ‘memory effect’ of PD 1 indicates that its charge recombination and relaxation processes occur at a fast pace. It is known that the mobility of charge carriers is determined by material conductivity. Therefore, it is believed PD 1 is from discharge in oil, as the conductivity of oil is significantly higher than that of pressboard. In contrast, the strong ‘memory effect’ of PD 2 indicates a slow charge transfer process in a highly resistive material. Therefore, PD 2 is thought to be correlated with discharge in the pressboard.

To give an explanation of the proposed assumptions, two schematic illustrations were made to expound and compare the discharges processes under low and high voltages, respectively. They are displayed in Figure 7.45 and Figure 7.46.

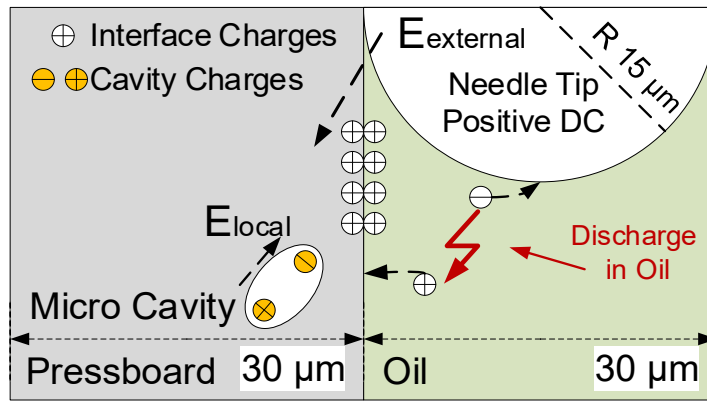


Figure 7.45 Discharge processes at triple-junction area under low voltage

As shown in Figure 7.45, positive charges accumulate at the oil/pressboard interface as a result of Maxwell-Wagner polarization. Once a partial discharge is triggered in oil, the generated negative ions would be soon absorbed by the positive electrode, whereas the positive ions drift slowly to the interface. With the elapse of time and increase of voltage, the interface charge density would gradually increase, and some charges can even penetrate into pressboard bulk [207, 208]. However, the external field is still not potent enough to induce discharges in the pressboard.

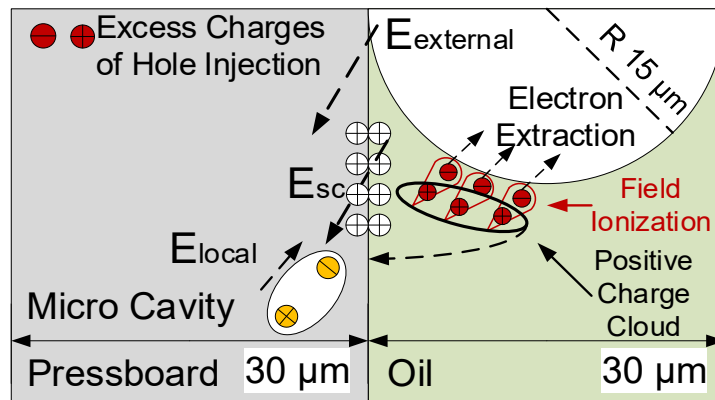


Figure 7.46 Discharge processes at triple-junction area under low voltage

As voltage continues to rise, the liquid molecules, unsaturated aromatics, in particular, can be ionized by field and thereby generating excess free electrons and a cloud of positive charges in the vicinity of needle electrode, as shown in Figure 7.46. This process is often referred to as field ionization or hole injection [10]. Similar to the oil discharge process, the generated excess electrons are absorbed by the electrode, whereas the positive ions are deposited on the interface. Eventually, the surface charges can build up an extra field E_{sc} . In consequence, the micro-cavity in the pressboard is subject to not only a raised external field but also a strong extra field of space charges. The superimposed field ($E_{external} + E_{sc}$) could conquer the cavity local field E_{local} and thus initiating discharges in pressboard.

However, it is not an easy task to clarify the influences of temperature. It is known the external field in oil is positively correlated with temperature (see Figure 7.24 d)). Surprisingly, the number of PD 1 at 20 °C is greater than those at 60 °C and 80 °C. A possible explanation for that is moisture migration. At elevated temperatures, moisture would migrate from the interface region into distant oil bulk and thereby impeding the initiation of discharges in the triple-junction area. This effect could outperform the rise of field intensity when the temperature rises from 20 °C to 60 °C. Nevertheless,

when the temperature rises from 60 °C to 80 °C, the rise of the external field dwarfs the effect of moisture migration. Therefore, the number of PD 1 at 60 °C is smaller than that at 80 °C.

On the contrary, the external field in pressboard bulk decreases with rising temperature (see Figure 7.24 c)). Therefore, the number of PD 2 at 20 °C is greater than those at 60 °C and 80 °C. Moreover, according to the time/lag recovery model for DC internal discharges [200], the average magnitude of PD 2 at 20 °C is thus relatively small.

7.6.2 DC Creeping Discharges in Forced Oil Flow

In fact, PD signals in the form of pulse trains have been observed in many defect types under DC stress, such as corona discharge [209, 210], surface discharge [211, 212], and floating discharge in GIS [212]. However, only Beyer attempted to provide an explanation [209]. According to his presumption, the pulse train results from successive discharges in incessantly disintegrating bubbles. The mother bubble is disintegrated into smaller descendent bubbles due to partial discharges, where the magnitude of discharge is determined by bubble size. Therefore, the first bubble has the largest magnitude and thereafter progressively decreasing. However, this theory could not explain the elimination of pulse trains at 80 °C and is thus not validated for oil flowing conditions.

Attempting to clarify the underlying mechanisms, the following discussions are divided into two parts with the same spotlight on the role of space charges. The first part deals with streaming electrification with an emphasis on the influences of temperature and oil flowing velocity. The second part discusses the possible interactions between spaces charges from different sources, i.e., streaming electrification and charge injection.

As mentioned in Section 2.3.6, streaming electrification is a dynamic process comprising four consecutive stages. The extra DC potential caused by streaming electrification is mainly determined by two stages, i.e., charge generation and charge leakage. With respect to the charge leakage stage, due to the existence of the bare electrode and its relative position to the oil entrance, it is hard to generate a significant streaming current in the test setup.

With respect to the charge generation stage, the separation of charges is strongly influenced by temperature and oil flowing velocity. The influences of oil flowing velocity and temperature on charge density in oil are shown in Figure 7.47 and Figure 7.48, respectively.

The influence of flow velocity is quite straightforward. Increased flow velocity means stronger shear stress at the interface and a greater oil volume for charge separation. Therefore, the charge density increases evidently with oil flowing speed. In fact, oil flow velocity impacts charge transportation as well. Within the low-velocity region, the oil flow is laminar, and the charge density increase almost linearly with flow velocity; whereas, within the high-velocity region, the oil flow is turbulent, and the charge density increases drastically with oil flow velocity [65].

In contrast, the temperature has competing effects on streaming electrification. On the one hand, evermore charged particles become available as temperature rises and thus promoting electrification. On the other hand, oil conductivity is enhanced by temperature, which could decrease the relaxation time of charge particles and thus alleviating streaming electrification via charge neutralization. In consequence, the maximum static charging in insulating oils normally occurs within the intermediate temperature ranges, e.g., from 30 °C to 60 °C [61] or from 30 °C to 50 °C [62].

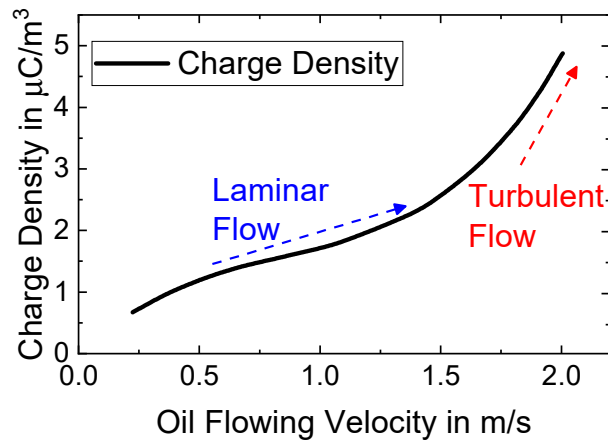


Figure 7.47 Influence of oil flowing velocity on charge density [213]

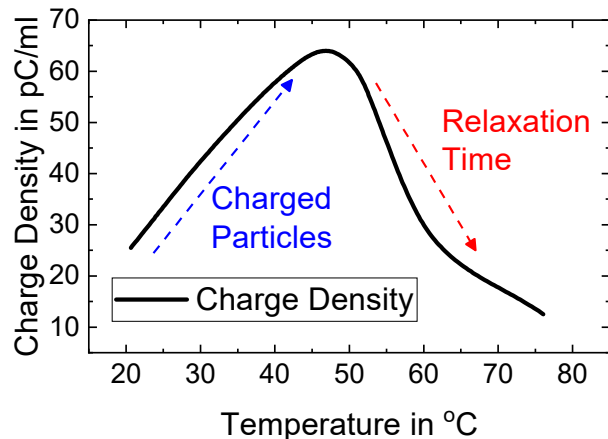


Figure 7.48 Influence of temperature on charge density [62]

It is found the varying trends of the pulse train versus influential factors (temperature and oil velocity) are coincidental with those of space charges due to streaming electrification. Therefore, it is speculated that the pulse train is a result of massive charge neutralization at the triple-junction area. The possible electrical and physical processes at the triple-junction area under forced oil flows are schematically illustrated in Figure 7.49.

Under oil flowing conditions, the discharge processes presented in Section 7.6.1 still hold. Additionally, there is a significant amount of space charges in oil due to streaming electrification (henceforth called flowing charges). A portion of the separated charges is transported from the oil entrance to the triple junction area by the forced oil flow. As a result of the interactions between streaming electrification, discharges in oil, and charge injections from the needle at the area, a so-called charge neutralization effect could take place [213, 214].

As displayed in Figure 7.49, the flowing charges could be neutralized with surface charges and injected charges via recombination processes. Besides, the negative charges could be absorbed by the positive needle electrode as well. These processes give birth to the so-called pulse train in PD measurement devices. Moreover, considering the polarity of surface charges and the electron absorption of the electrode, the neutralization process leaves a number of net positive charges. A fraction of the net positive charges is expelled by the positive field. More importantly, the others are drifted to interface and thus enhancing the field intensity in pressboard bulk. As a result, it might eventually result in the large-magnitude pulses observed at 20 °C to 60 °C.

From 20 °C to 60 °C, the above-mentioned processes are strengthened by temperature rise, voltage increment, and oil velocity increase. However, when the temperature rises to 80 °C, the quantity of

flowing charges is considerably limited. Accordingly, the formation of pulse trains and large-magnitude pulse is greatly mitigated.

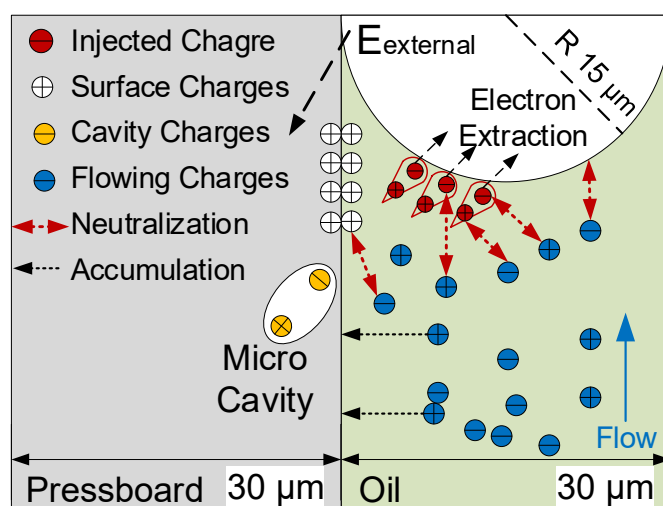


Figure 7.49 Electrical and physical processes at triple-junction area with oil flows

7.7 Conclusions

This chapter sets out to understand oil/pressboard interface creeping discharges under highly divergent positive DC fields as well as to examine the influences of temperatures and forced oil flows on their characteristics. Based on the obtained test results and discussions, the following conclusion can be drawn from the present study:

- The DC conductivity of both oil and pressboard increases exponentially with temperature. The resistivity ratio of pressboard to oil declines drastically as temperature rises. Moreover, elevated temperature also shortens the oil/pressboard interface relaxation time. FEM simulations reveal that the maximum DC field is located exactly at the oil/pressboard interface rather than in the oil wedge of the triple-junction area. As temperature rises, the field intensity of pressboard bulk decreases, whereas those of interface and oil bulk increase. In the triple-junction area, the field intensity of oil is more susceptible to temperature variations than those of pressboard bulk and interface.
- Under static oil, it is found that the DC creeping discharge comprises two types of partial discharges (PD1 and PD2). However, they do not necessarily occur concurrently. Compared with PD 2, PD 1 has a lower inception voltage, smaller pulse magnitudes, and shorter inter-pulse time intervals. It is assumed that PD 1 and PD 2 are associated with discharges in oil and pressboard, respectively. Accumulated surface charges and excess charges due to oil field ionization could probably facilitate the occurrence of PD2.
- Under static oil, the numbers of both PD 1 and PD 2 increase with the voltage level. The temperature has an intricate impact on the number of PD 1. PD 1 number is the greatest at 20 °C, followed by 80 °C and 60 °C. This phenomenon is probably due to the competing effects between field intensification and interface moisture migration. By contrast, the temperature has a straightforward impact on PD 2. The elevated temperatures decrease the number of PD 2 whereas increasing its average magnitude. This phenomenon can be readily explained by the time lag/recovery model of DC void discharge.
- Forced oil flows have different influences on the short-time DC interface flashover voltages

at different temperatures. Moreover, the interface withstand time is in general negatively correlated with the oil flow velocity and shows intricated relations to the temperature. The interface withstand time is the greatest at 60 °C, followed by 20 °C and 80 °C. This phenomenon is probably due to a joint effect of field intensification and relative oil humidity reduction.

- Forced oil flows can alter PD behaviors of DC creeping discharges drastically and generate a peculiar PD type (Pulse Train). A pulse train is composed of a great number of PD pulses that have varying magnitudes and extremely small inter-pulse time intervals. The occurrence of the pulse train is subject to applied voltage level, temperature, and oil flowing velocity. The density of pulse train is found consistent with the variations of charge density of streaming electrification, and it is, therefore, speculated that the pulse train is the result of interactions between space charges from different sources, i.e., space charges due to oil discharges, accumulated interface charges, excess charges of hole injection, and separated charges due to streaming electrification.

8 CONCLUSIONS

Progressive creeping discharge is one of the most dangerous failure modes of transformers under normal operating conditions. However, the discharge phenomena as well as the mechanisms of their related failures have thus far not been fully understood, which impedes the development of effective detection and identification methods of relevant faults and thus posing a great challenge to the safe operation of transformers. To address the pressing problems, therefore, the present thesis sets out to gain sound knowledge and a deeper insight into the specific discharge phenomenon and to contribute to the advancement of an effective monitoring and diagnostic methodology.

Using a long-gap needle-plate electrode configuration, this study has explored the nature and long-term characteristics of oil/pressboard creeping discharges under AC and DC voltages, respectively. Using various experimental tools, the influences of critical factors, viz., ageing, voltage level, temperature, stress waveform, and oil flowing, on creeping discharges have been systematically evaluated, and the relevant underlying mechanisms have been discussed in detail. In-depth analyses have been made to the different insulation fault types. Their characteristics have been comparatively investigated and their fundamental causes theoretically examined. Moreover, a technical framework has been proposed to detect the severe creeping discharge-induced faults in transformers. Based on the test results and discussions, the major findings of this thesis are summarized as follows.

- (1) The characteristics of damage-free progressive creeping discharge and the influences of pressboard ageing and field intensity
 - AC progressive creeping discharge is a compound discharge phenomenon that exhibits peculiar discharge patterns and various discharge signals. Oil corona discharge and surface discharge are believed to be the major discharge sources. Pressboard ageing affects the inception voltage of creeping discharges but has no influence on the interface breakdown strength. The damage-free progressive creeping discharge exhibits a constant PRPD pattern but a diminishing PD intensity with time, which could be caused by the interface moisture migration.
 - Nevertheless, the pressboard ageing degree and voltage level can jointly determine whether the damage-free progressive creeping discharge is vanished or sustained at a certain level at a large time scale. The intensified negative discharges are the major cause of a sustained creeping discharge. The damage-free progressive creeping discharge generates hydrogen principally and is located between D1/ D2 fault zones in the classical Duval's Triangle.
- (2) The fundamental insulation failures due to dangerous creeping discharge and the corresponding monitoring and diagnostic methodology
 - Under AC voltage, the progressive creeping discharges could generate two distinct faults to the pressboard, i.e., internal treeing (internal treeing) and surface tracking (surface tracking). The fault type is dependent on pressboard ageing, voltage level, and pressboard density. The growth of the internal treeing is characterized by several noticeable phenomena and varying PD characteristics, whereas the growth of the surface tracking is much more straightforward.
 - The development of internal treeing can be illustrated using a generalized four-stage model. The filament-like carbonization tracks in the pressboard interior are the fundamental driving force for internal treeing and its related phenomena. The onset and growth of the internal

carbonization track are revealed using a two-staged model, which considers the important factors such as charge emission and percolation theory.

- The internal treeing process is characterized by a steep temperature rise on the pressboard surface and a great concentration of hydrogen in the free gases due to the bubbling effect. Accordingly, this thesis proposes a tentative detection methodology of internal treeing, which is mainly based on continuous PD measurements, online temperature monitoring, and gas analysis. However, due to the PD disappearance, it is still hard to detect a severe surface tracking fault using the conventional PD detection method.
- (3) Influences of temperature and voltage waveforms on progressive creeping discharges and a new detection method
- The short-time electric strength of either interface or oil gap is positively correlated with temperature, which is probably due to a declined oil relative humidity. High temperature and strong field could generate a synergistic in exacerbating the dissipation factor of pressboard. The temperature can determine the fault types and discharge severity of progressive creeping discharge under either constant or step-wise stress, whereas the stress waveform has an obvious effect on the fault type only at high temperatures.
 - Under constant stress, all specimens fail due to tracking-free interface flashovers at 20 °C and 40 °C, and the PD numbers of the tracking-free samples are negatively correlated with temperature. At 60 °C, all specimens exhibit surface tracking and exhibit ever-weaker discharge amplitudes. At 80 °C, all specimens fail due to internal treeing (internal treeing) and subsequent interface flashovers. Under step-wise stress, no incident of internal treeing is observed. The PD quantities of the tracking-free samples are in general negatively correlated with temperature, and the PD magnitudes of the slow-tracking samples decline rapidly after the PD inception.
 - The proposed synchronous PD and dielectric measurement technique is highly indicative of the pressboard internal treeing process. The online dielectric measurement and the conventional online PD detection method can complete each other to achieve high detection sensitivity as well as discharge identification capability, and their results can be inter-correlated.
- (4) The fundamentals of progressive creeping discharges under DC voltage and the influences of temperature as well as forced oil flows
- Temperature affects the DC conductivity of both oil and pressboard, the resistivity ratio of pressboard to oil, and the oil/pressboard interface charge relaxation time. Accordingly, FEM simulations reveal that the field intensity of pressboard bulk decreases as temperature rises, whereas those of interface and oil bulk increase. Both oil flow speed and temperatures affect the short-time DC interface electric strength. However, the role of temperature in this respect is more intricate than that of oil flow due to its competing effects on the DC interface field distribution and the oil properties.
 - The DC creeping discharge under static oil comprises two types of partial discharges (PD1 and PD2). The two types of discharges have different inception voltages, pulse magnitudes, and inter-pulse time intervals. PD 1 and PD 2 are presumably associated with discharges in oil and pressboard, respectively. The PD numbers of both PD 1 and PD 2 increase with the

voltage level. The temperature has an intricate impact on PD 1 due to its competing effects on the DC interface field distribution and the oil properties. By contrast, the influence of temperature on PD 2 is straightforward and can be readily expounded using the time lag/recovery model of DC void discharge.

- Forced oil flows can alter PD behaviors of DC creeping discharges drastically and generate a peculiar PD type (Pulse Train). A pulse train is composed of a great of PD pulses that have varying magnitudes and extremely small inter-pulse time intervals. The occurrence of the pulse train is subject to applied voltage level, temperature, and oil flowing velocity. It is believed that the pulse train is the result of interactions between space charges from different sources, i.e., space charges due to oil discharges, accumulated interface charges, excess charges of hole injection, and separated charges due to streaming electrification.

The present thesis extends the fundamental knowledge of the oil/pressboard progressive creeping discharges under AC and DC fields, systematically revisits the multi-faceted influences of critical factors, provides a clear demonstration and reasonable elucidation of relevant faults and failures, and offers a framework for monitoring and diagnosing the dangerous creeping discharge in power transformer. The research is expected to serve as a base for future scientific studies and a piece of valuable information for practical applications pertinent to progressive creeping discharges.

REFERENCES

- [1] E. Gockenbach and H. Borsi, "Condition Monitoring and Diagnosis of Power Transformers," in *Int. Symp. Electr. Insul. Mater. (ISEIM)*, Mie, Japan, 2008, pp. 16–19.
- [2] V. I. Kogan *et al.*, "Failure analysis of EHV transformers," *IEEE Trans. Power Delivery*, vol. 3, no. 2, pp. 672–683, 1988.
- [3] S. Chakravorti, D. Dey, and B. Chatterjee, *Recent Trends in the Condition Monitoring of Transformers*, London, Springer London, 2013.
- [4] V. Sokolov, S. Tsurpal, and A. Drobyshevski, "Reliability problems with large power transformers and shunt reactors: Typical failure modes and failure causes," in *Cigré SC A2 Colloquium*, Moscow Russia, 2005.
- [5] J. Lapworth and T. McGrail, "Transformer failure modes and planned replacement," in *IEE Colloquium Transformer Life Management*, London, UK, 1998.
- [6] Cigré WG A2.18, *Life management techniques for power transformers*. Technical Brochure 227, Paris, CIGRÉ, 2003.
- [7] Cigré WG A2.37, *Transformer Reliability Survey*. Technical Brochure 642, Paris, CIGRÉ, 2015.
- [8] Cigré AG B4.04, *HVDC LCC Converter Transformers, Converter Transformer Failure, survey results from 2003 to 2012*. Technical Brochure 617, Paris, CIGRÉ, 2015.
- [9] Cigré WG 15.02, "Review on Insulating Liquids," *Cigré Electra*, vol. 171, 1997.
- [10] R. Bartnikas, Ed., *Engineering Dielectrics: Volume III Electrical Insulating Liquids*, Philadelphia PA, ASTM, 1994.
- [11] T. O. Rouse, "Mineral insulating oil in transformers," *IEEE Electr. Insul. Mag.*, vol. 14, no. 3, pp. 6–16, 1998.
- [12] R. Arora and W. Mosch, *High voltage and electrical insulation engineering*, Piscataway, NJ, IEEE Press, 2011.
- [13] Cigré TF D1.01.10, *Ageing of cellulose in mineral-oil insulated transformers*. Technical Brochure 323, Paris, CIGRÉ, 2007.
- [14] A. M. Emsley and G. C. Stevens, "Kinetics and mechanisms of the low-temperature degradation of cellulose," *Cellulose*, vol. 1, no. 1, pp. 26–56, 1994.
- [15] H. V. Lee, S. B. A. Hamid, and S. K. Zain, "Conversion of lignocellulosic biomass to nanocellulose: Structure and chemical process," *Sci. World J.*, vol. 2014, pp. 1–20, 2014.
- [16] G. C. Stevens and A. M. Emsley, "Review of chemical indicators of degradation of cellulosic electrical paper insulation in oil-filled transformers," *IEE Proc.: Sci., Meas. Technol.*, vol. 141, no. 5, pp. 324–334, 1994.
- [17] J. S. N'cho *et al.*, "Aged oils reclamation: Facts and arguments based on laboratory studies," *IEEE Trans. Dielect. Electr. Insul.*, vol. 19, no. 5, pp. 1583–1592, 2012.
- [18] D. H. Shroff and A. W. Stannett, "A review of paper aging in power transformers," *IEE Proc. C Gener. Transm. Distrib. UK*, vol. 132, no. 6, p. 312, 1985.
- [19] L. E. Lundgaard *et al.*, "Aging of Oil-Impregnated Paper in Power Transformers," *IEEE Trans. Power Delivery*, vol. 19, no. 1, pp. 230–239, 2004.
- [20] T. V. Oommen and T. A. Prevost, "Cellulose insulation in oil-filled power transformers: Part II maintaining insulation integrity and life," *IEEE Electr. Insul. Mag.*, vol. 22, no. 2, pp. 5–14, 2006.
- [21] K. Giese, "Electrical strength of pressboard components for transformer insulations," *IEEE Electr. Insul. Mag.*, vol. 12, no. 1, pp. 29–33, 1996.
- [22] C. Krause, "Power transformer insulation – history, technology and design," *IEEE Trans. Dielect. Electr. Insul.*, vol. 19, no. 6, pp. 1941–1947, 2012.
- [23] V. Dahinden, K. Schultz, and A. Kuchler, "Function of solid insulation in transformers," in *Transformer 98*, pp. 20–21.
- [24] Y. Kening, *The Design Principles of Transformer*, Beijing, China, China Electric Power Press, 2003.

- [25] Fitton, S. J., "Surface discharges within oil insulated apparatus," in *IEE Colloquium on An Engineering Review of Liquid Insulation*, 1997.
- [26] T. Takuma and B. Techaumnat, *Electric fields in composite dielectrics and their applications*, Dordrecht, London, Springer, 2010.
- [27] M. Beyer *et al.*, *Hochspannungstechnik: Theoretische und praktische Grundlagen*, Berlin, Heidelberg, Springer, 1986.
- [28] R. J. Taylor, "Effect of permittivity matching on the flashover of solid/liquid interfaces," *Proc. Inst. Electr. Eng.*, vol. 124, no. 10, pp. 899–904, 1977.
- [29] M. U. Anker, "Effect of test geometry, permittivity matching and metal particles on the flashover voltage of oil/solid interfaces," *IEEE Trans. Power Appar. Syst.*, PAS-102, no. 12, pp. 3796–3802, 1983.
- [30] T. Takuma, "Field behaviour at a triple junction in composite dielectric arrangements," *IEEE Trans. Electr. Insul.*, vol. 26, no. 3, pp. 500–509, 1991.
- [31] T. Takuma and T. Kawamoto, "Field enhancement at a triple junction in arrangements consisting of three media," *IEEE Trans. Dielect. Electr. Insul.*, vol. 14, no. 3, pp. 566–571, 2007.
- [32] P. Atten, "Electrohydrodynamic instability and motion induced by injected space charge in insulating liquids," *IEEE Trans. Dielect. Electr. Insul.*, vol. 3, no. 1, pp. 1–17, 1996.
- [33] P. Atten and J. Seyed-Yagoobi, "Electrohydrodynamically induced dielectric liquid flow through pure conduction in point/plane geometry," *IEEE Trans. Dielect. Electr. Insul.*, vol. 10, no. 1, pp. 27–36, 2003.
- [34] J. D. Cross, "Breakdown across a dielectric spacer in insulating oil and the role of electrohydrodynamics in liquid breakdown," *IEEE Trans. Electr. Insul.*, vol. 17, no. 6, pp. 493–498, 1982.
- [35] J. K. Nelson, "Dielectric fluids in motion," *IEEE Electr. Insul. Mag.*, vol. 10, no. 3, pp. 16–28, 1994.
- [36] E. A. Cherney and J. D. Cross, "Electrical breakdown at solid-liquid interfaces," *IEEE Trans. Electr. Insul.*, vol. 12, no. 3, pp. 214–218, 1977.
- [37] V. V. Sokolov and B. V. Vanin, "Experience with in-field assessment of water contamination of large power transformers," in *Proc. EPRI Substation Equipment Diagnostics Conference VII*, New Orleans, 1999, pp. 1–9.
- [38] V. Aralkellian and I. Fofana, "Water in oil-filled high-voltage equipment: Part I: states, solubility, and equilibrium in insulating materials," *IEEE Electr. Insul. Mag.*, vol. 23, no. 4, pp. 15–27, 2007.
- [39] D. F. Garcia, B. Garcia, and J. C. Burgos, "A review of moisture diffusion coefficients in transformer solid insulation: Part 1: Coefficients for paper and pressboard," *IEEE Electr. Insul. Mag.*, vol. 29, no. 1, pp. 46–54, 2013.
- [40] P. Griffin, V. Sokolov, and B. Vanin, "Moisture equilibrium and moisture migration within transformer insulation system," in *Cigre SC12 Transformer Colloquium*, pp. 1–23.
- [41] M. Koch and S. Tenbohlen, "Evolution of bubbles in oil-paper insulation influenced by material quality and ageing," *IET Electr. Power App.*, vol. 5, no. 1, pp. 168–174, 2011.
- [42] Cigré WG A2.30, *Moisture equilibrium and moisture migration within transformer insulation systems*. Technical Brochure 349, Paris, CIGRÉ, 2008.
- [43] B. Sparling, "Assessing Water Content in Solid Transformer Insulation from Dynamic Measurement of Moisture in Oil," in *IEEE PES Seminar*, Vancouver, Canada, 2008.
- [44] H. Gasser, C. Krause, and T. Prevost, "Water Absorption of Cellulosic Insulating Materials used in Power Transformers," in *Proc. IEEE Int. Conf. Solid Dielectr. (ICSD)*, Winchester, UK, 2007, pp. 289–293.
- [45] P. Przybyłek, "The influence of temperature and aging of cellulose on water distribution in oil-paper insulation," *IEEE Trans. Dielect. Electr. Insul.*, vol. 20, no. 2, pp. 552–556, 2013.
- [46] Y. Tu *et al.*, "Moisture migration in oil-impregnated film insulation under thermal ageing," *IEEE Trans. Dielect. Electr. Insul.*, vol. 23, no. 2, pp. 1135–1141, 2016.
- [47] J. Fabre and A. Pichon, "Deteriorating processes and products of paper in oil. Application to transformers," in *Cigre 1960*.
- [48] T. Oommen, "Moisture equilibrium charts for transformer insulation drying practice," *IEEE Trans. Power Appar. Syst.*, PAS-103, no. 10, pp. 3062–3067, 1984.

- [49] Y. Du *et al.*, "Moisture equilibrium in transformer paper-oil systems," *IEEE Electr. Insul. Mag.*, vol. 15, no. 1, pp. 11–20, 1999.
- [50] V. Vasovic *et al.*, "Equilibrium charts for moisture in paper and pressboard insulations in mineral and natural ester transformer oils," *IEEE Electr. Insul. Mag.*, vol. 30, no. 2, pp. 10–16, 2014.
- [51] M. Koch, S. Tenbohlen, and T. Stirl, "Diagnostic Application of Moisture Equilibrium for Power Transformers," *IEEE Trans. Power Delivery*, vol. 25, no. 4, pp. 2574–2581, 2010.
- [52] T. V. Oommen and S. R. Lindgren, "Bubble evolution from transformer overload," in *IEEE PES Trans. Distribution Conf. Expo.*, Atlanta, USA, 2001, pp. 137–142.
- [53] P. Przybylek, "The influence of cellulose insulation aging degree on its water sorption properties and bubble evolution," *IEEE Trans. Dielect. Electr. Insul.*, vol. 17, no. 3, pp. 906–912, 2010.
- [54] C. Y. Perkasa *et al.*, "A comparison of the formation of bubbles and water droplets in vegetable and mineral oil impregnated transformer paper," *IEEE Trans. Dielect. Electr. Insul.*, vol. 21, no. 5, pp. 2111–2118, 2014.
- [55] F. W. Heinrichs, "Bubble formation in power transformer windings at overload temperatures," *IEEE Trans. Power Appar. Syst.*, PAS-98, no. 5, pp. 1576–1582, 1979.
- [56] G. H. Kaufmann and C. J. McMillen, "Gas bubble studies and impulse tests on distribution transformers during loading above nameplate rating," *IEEE Trans. Power Appar. Syst.*, PAS-102, no. 8, pp. 2531–2542, 1983.
- [57] W. J. McNutt, T. O. Rouse, and G. H. Kaufmann, "Mathematical modelling of bubble evolution in transformers," *IEEE Trans. Power Appar. Syst.*, PAS-104, no. 2, pp. 477–487, 1985.
- [58] P. Przybylek, Z. Nadolny, and H. Moscicka-Grzesiak, "Bubble effect as a consequence of dielectric losses in cellulose insulation," *IEEE Trans. Dielect. Electr. Insul.*, vol. 17, no. 3, pp. 913–919, 2010.
- [59] G. H. Kaufmann, "Gas bubbles in distribution transformers," *IEEE Trans. Power Appar. Syst.*, vol. 96, no. 5, pp. 1596–1601, 1977.
- [60] M. Gao *et al.*, "Investigation on bubbling phenomenon in oil-paper insulation," *IEEE Trans. Dielect. Electr. Insul.*, vol. 24, no. 4, pp. 2362–2370, 2017.
- [61] S. Shimizu, H. Murata, and M. Honda, "Electrostatics in Power Transformers," *IEEE Trans. Power Appar. Syst.*, PAS-98, no. 4, pp. 1244–1250, 1979.
- [62] T. Watanabe *et al.*, "Static Electrification by Forced Oil Flow in Large Power Transformer," *IEEE Trans. Power Appar. Syst.*, PAS-99, no. 1, pp. 335–343, 1980.
- [63] D. W. Crofts, "The electrification phenomena in power transformers," *IEEE Trans. Elect. Insul.*, vol. 23, no. 1, pp. 137–146, 1988.
- [64] J. K. Nelson, M. A. Brubaker, and J. A. Palmer, "The formulation of models for the description of streaming electrification in transformer structures," *IEEE Trans. Dielect. Electr. Insul.*, vol. 10, no. 6, pp. 920–932, 2003.
- [65] A. Washabaugh and M. Zahn, "Static Electrification," in *Wiley Encyclopedia of Electrical and Electronics Engineering*, J. Webster, Ed. John Wiley & Sons, Inc, 1990, pp. 423–435.
- [66] A. P. Washabaugh, D. E. Schliker, and M. Zahn, "Flow electrification measurements of transformer insulation," in *Symposium Proceedings: Transformer reliability: Management of static electrification in power transformers*, EPRI, Ed. Palo Alto, CA, 2009, pp. 142–169.
- [67] J. F. Roach and J. B. Templeton, "An Engineering Model for Streaming Electrification in Power Transformers," in *Electrical insulating oils*, H. G. Erdman, Ed. Philadelphia: ASTM, 1988, 119–135.
- [68] T. V. Oommen, "Static electrification properties of transformer oil," *IEEE Trans. Elect. Insul.*, vol. 23, no. 1, pp. 123–128, 1988.
- [69] Cigré JWG 12/15.13, *Static Electrification in Power Transformers*. Technical Brochure 170, Paris, CIGRÉ, 2000.
- [70] E. Kelley and R. Hebner, "Measurement of the Electric Field in the Vicinity of an Oil-Pressboard Interface Parallel to the FIELD," *IEEE Trans. Electr. Insul.*, EI-19, no. 6, pp. 519–523, 1984.

- [71] E. F. Kelley *et al.*, "The effect of an oil-paper interface parallel to an electric field on the breakdown voltage at elevated temperatures," *IEEE Trans. Electr. Insul.*, vol. 23, no. 2, pp. 249–259, 1988.
- [72] M. Krins, H. Borsi, and E. Gockenbach, "Parameters governing the AC and LI flashover strength of interfaces between epoxy resin tubes and transformer oil," in *Conf. Rec. IEEE Int. Symp. Electr. Insul. (ISEI)*, Anaheim, CA, USA, 2000, pp. 431–434.
- [73] M. Krins, H. Borsi, and E. Gockenbach, "Impact of different water contents on the electrical strength of oil gaps and solid/liquid interfaces in the presence of carbon particles," in *Proc. IE EE Int. Conf. Dielectr. Liq. (ICDL)*, Nara, Japan, 1999, pp. 281–285.
- [74] M. Krins, H. Borsi, and E. Gockenbach, "Impact of carbon particles on the impulse flashover behavior of different solid/liquid interfaces in a non-uniform field," in *Int. Symp. Electr. Insul. Mater. (ISEIM)*, Toyohashi, Japan, 1998, pp. 363–368.
- [75] M. Krins *et al.*, "Breakdown and flashover phenomena related to the presence of high absolute water contents in clean and carbonized transformer oil," in *Annu. Rep. - Conf. Electr. Insul. Dielectr. Phenom. (CEIDP)*, Cancun, Mexico, 2002, pp. 252–255.
- [76] H. Okubo *et al.*, "Creepage Flashover Characteristics of Oil/Pressboard Interfaces and Their Scale Effects," *IEEE Trans. Power Delivery*, vol. 2, no. 1, pp. 126–132, 1987.
- [77] M. P. Wilson *et al.*, "Surface flashover of oil-immersed dielectric materials in uniform and non-uniform fields," *IEEE Trans. Dielect. Electr. Insul.*, vol. 16, no. 4, pp. 1028–1036, 2009.
- [78] M. P. Wilson *et al.*, "Effect of applied field and rate of voltage rise on surface breakdown of oil-immersed polymers," *IEEE Trans. Electr. Insul.*, vol. 18, no. 4, pp. 1003–1010, 2011.
- [79] Anderson, J. G. and Liao, T. W., "The propagation mechanism of impulse creepage discharges over oil-immersed surfaces," *Trans. Am. Inst. Electr. Eng.*, Part 1, vol. 74, no. 2, pp. 218–226, 1955.
- [80] J. C. Devins and S. J. Rzed, "Streamer Propagation in Liquids and over Liquid-Solid Interfaces," *IEEE Trans. Electr. Insul.*, EI-17, no. 6, pp. 512–516, 1982.
- [81] P. Atten and A. Saker, "Streamer propagation over a liquid/solid interface," *IEEE Trans. Electr. Insul.*, vol. 28, no. 2, pp. 230–242, 1993.
- [82] A. Saker and P. Atten, "Potential distribution along single negative creeping streamer in transformer oil," *IEE Proc.-A: Sci., Meas. Technol.*, vol. 140, no. 5, pp. 375–381, 1993.
- [83] L. Lundgaard *et al.*, "Propagation of positive and negative streamers in oil with and without pressboard interfaces," *IEEE Trans. Dielect. Electr. Insul.*, vol. 5, no. 3, pp. 388–395, 1998.
- [84] Xiao Yi, "Characteristics of Creepage Discharges along Ester-Pressboard Interfaces under AC Stress," PhD Dissertation, School of Electrical and Electronic Engineering, University of Manchester, Manchester, UK, 2012.
- [85] Y. Nakao *et al.*, "Studies of the creepage discharge on the surface of liquids," *IEEE Trans. Electr. Insul.*, vol. 23, no. 4, pp. 677–687, 1988.
- [86] Y. Nakao *et al.*, "Influence of insulating barrier on the creepage discharge in transformer oil," *IEEE Trans. Dielect. Electr. Insul.*, vol. 4, no. 6, pp. 775–779, 1997.
- [87] Y. Nakao *et al.*, "Studies of impulse creepage discharge in transformer oil," *IEEE Trans. Electr. Insul.*, vol. 26, no. 4, pp. 732–738, 1991.
- [88] A. Beroual *et al.*, "Investigation on creeping discharges propagating over pressboard immersed in mineral and vegetable oils under AC, DC and lightning impulse voltages," *IEEE Trans. Dielect. Electr. Insul.*, vol. 20, no. 5, pp. 1635–1640, 2013.
- [89] F. Sadaoui and A. Beroual, "AC creeping discharges propagating over solid/gas interfaces," *IEE Proc.: Sci., Meas. Technol.*, vol. 8, no. 6, pp. 595–600, 2014.
- [90] A. Beroual *et al.*, "Analysis of creeping discharges activity at solid/liquid interfaces subjected to ac voltage," *IET Gener. Transm. Distrib.*, vol. 5, no. 9, p. 973, 2011.
- [91] A. K. Lokhanin *et al.*, "Internal insulation failure mechanisms of HV equipment under service conditions," in *Cigré Session 2002*.

- [92] V. V. Sokolov and B. Vanin, "Evaluation of power transformer insulation through measurement of dielectric characteristics," in *Proc. 63rd Annual Intern. Conf. Doble Clients*, 1996, pp. 18–37.
- [93] Cigré WG D1.11, *Service Aged Insulation Guidelins on Managing the Ageing Process*. Technical Brochure 228, Paris, CIGRÉ, 2003.
- [94] J. A. Lapworth and A. Wilson, "Transformer Internal Over-Voltages Caused by Remote Energisation," in *IEEE PES Conf. Expo. in Africa*, Johannesburg, South Africa, 2007, pp. 1–6.
- [95] V. V. Sokolov, "Understanding Failure Modes of Transformers," in *Proc. Euro TechCon*, 2005, pp. 43–65.
- [96] V. Sokolov, Z. Berler, and V. Rashkes, "Effective methods of assessment of insulation system conditions in power transformers: A view based on practical experience," in *Proc. Electr. Insul. Conf. Electr. Manuf. Coil Winding Conf.*, Cincinnati, USA, 1999, pp. 659–667.
- [97] J. Dai, Z. Wang, and P. Jarman, "Creepage Discharge on Insulation Barriers in Aged Power Transformers," *IEEE Trans. Dielect. Electr. Insul.*, vol. 17, no. 4, pp. 1327–1335, 2010.
- [98] P. M. Mitchinson *et al.*, "A new approach to the study of surface discharge on the oil-pressboard interface," in *Proc. IEEE Int. Conf. Dielectr. Liq. (ICDL)*, Futuroscope-Chasseneuil, 2008, pp. 382–385.
- [99] P. M. Mitchinson, "Surface Tracking in the Inter-Phase Region of Large Transformers," PhD Dissertation, School of Electronics and Computer Science, University of Southampton, Southampton, UK, 2008.
- [100] Mitchinson, P. M. *et al.*, "Tracking and Surface Discharge at the Oil-Pressboard Interface," *IEEE Electr. Insul. Mag.*, vol. 26, no. 2, pp. 35–41, 2010.
- [101] Y. Cheng *et al.*, "Experimental research on creepage discharge between oil-impregnated pressboard layers," in *Annu. Rep. - Conf. Electr. Insul. Dielectr. Phenom. (CEIDP)*, Toronto, ON, Canada, 2016, pp. 999–1002.
- [102] H. Zainuddin, P. L. Lewin, and P. M. Mitchinson, "Partial discharge characteristics of surface tracking on oil-impregnated pressboard under AC voltages," in *Proc. IEEE Int. Conf. Solid Dielectr. (ICSD)*, Bologna, Italy, 2013, pp. 1016–1019.
- [103] H. Zainuddin, "Study of Surface Discharge Behaviour at the Oil-Pressboard Interface," PhD Dissertation, School of Electronics and Computer Science, University of Southampton, Southampton, UK, 2013.
- [104] X. Yi and Z. Wang, "Surface tracking on pressboard in natural and synthetic transformer liquids under AC stress," *IEEE Trans. Dielect. Electr. Insul.*, vol. 20, no. 5, pp. 1625–1634, 2013.
- [105] F. Murdiya *et al.*, "Creeping discharge developing on vegetable-based oil / pressboard interface under AC voltage," *IEEE Trans. Dielect. Electr. Insul.*, vol. 21, no. 5, pp. 2102–2110, 2014.
- [106] G. C. Azcarraga, A. Cavallini, and G. C. Montanari, "The influence of oil speed and temperature on PD phenomena in transformer insulation," in *Conf. Rec. IEEE Int. Symp. Electr. Insul (ISEI)*, San Juan, Puerto Rico, 2012, pp. 494–497.
- [107] V. V. Sokolov *et al.*, On-site partial discharge measurements on power transformers, Available: <http://www.ztz-service.com.ua/Sokolov/Articles/>.
- [108] R. James *et al.*, "Challenges for Advanced Diagnostic Techniques Faults Undetectable by Existing Electrical Methods," in *Cigré Session 2000*.
- [109] ABB Technology Ltd., "ABB Review Special Report: 60 years of HVDC," Zurich, Switzerland, 2014, Available: www.abb.com/abbreview.
- [110] Siemens AG, "High Voltage Direct Current Transmission: Proven Technology for Power Exchange," Erlangen, Germany, 2011, Available: www.siemens.com/energy/hvdc.
- [111] C. R. Bayliss and B. J. Hardy, *Transmission and distribution electrical engineering*, 3rd ed., Amsterdam, Newnes, 2007.
- [112] Alstom Grid, "HVDC for Beginners and Beyond," Available: www.grid.alstom.com.
- [113] Cigré WG B4.51, *Study of Converter Transients Imposed on the HVDC Converter Transformers*. Technical Brochure 609, Paris, CIGRÉ, 2015.

- [114] Cigré JTF B4.04/A2-1, *Analysis of HVDC Thyristor Converter Transformer Performance*. Technical Brochure 240, Paris, CIGRÉ, 2004.
- [115] A. C. F. J. and A. B., “Thermal problems caused by harmonic frequency leakage fluxes in three-phase, three-winding converter transformers,” *IEEE Trans. Power Delivery*, vol. 19, no. 1, pp. 208–213, 2004.
- [116] W. McDermid, A. Glodjo, and J. C. Bromley, “Analysis of Winding Failures in HVDC Converter Transformers,” in *Proc. Electr. Insul. Conf. Electr. Manuf. Coil Winding Conf.*, Cincinnati, USA, 1999, pp. 653–657.
- [117] W. McDermid *et al.*, “Analysis of converter transformer failures and application of periodic on-line partial discharge measurements,” in *Conf. Rec. IEEE Int. Symp. Electr. Insul. (ISEI)*, Cincinnati, USA, 2001, pp. 577–582.
- [118] D. H. Grant and W. McDermid, “Assessment of thermal aging of HVDC converter transformer insulation,” in *Conf. Rec. IEEE Int. Symp. Electr. Insul. (ISEI)*, Indianapolis, USA, 2004, pp. 230–232.
- [119] I. Ohshima *et al.*, “HVDC Breakdown of Transformer Oil and the Effect of Space Charge on it,” *IEEE Trans. Power Appar. Syst.*, PAS-102, no. 7, pp. 2208–2215, 1983.
- [120] A. Kurita *et al.*, “DC Flashover Voltage Characteristics and Their Calculation Method for Oil-Immersed Insulation Systems in HVDC Transformers,” *IEEE Trans. Power Delivery*, vol. 1, no. 3, pp. 184–190, 1986.
- [121] C. Krause and R. Woschitz, “The temperature dependence of the dielectric strength of transformer oil and pressboard insulation at HVDC polarity reversal stress,” in *Proc. IEEE Int. Conf. Dielectr. Liq. (ICDL)*, 2002, pp. 182–185.
- [122] Y. Ebisawa *et al.*, “DC creepage breakdown characteristics of oil-immersed insulation,” *IEEE Trans. Dielect. Electr. Insul.*, vol. 16, no. 6, pp. 1686–1692, 2009.
- [123] M. R. Raghuveer *et al.*, “Surface electric strength of processed pressboard under composite AC and DC and conventional stresses,” *IEEE Trans. Electr. Insul.*, vol. 25, no. 2, pp. 341–350, 1990.
- [124] S. S. Tulasi Ram, M. Kamaraju, and B. P. Singh, “Flashover behaviour of converter transformer insulation subjected to superimposed ac and dc voltages,” in *Annu. Rep. - Conf. Electr. Insul. Dielectr. Phenom. (CEIDP)*, Arlington, USA, 1994, pp. 810–815.
- [125] M. R. Raghuveer, G. Zhang, and F. David, “Effect of DC bias on surface strength of processed pressboard under lightning and switching impulses,” *IEEE Trans. Electr. Insul.*, vol. 26, no. 4, pp. 806–810, 1991.
- [126] B. Qi, Z. Wei, and C. Li, “Creepage discharge of oil-pressboard Insulation in AC-DC composite field: phenomenon and characteristics,” *IEEE Trans. Dielect. Electr. Insul.*, vol. 23, no. 1, pp. 237–245, 2016.
- [127] Y. X. Zhou *et al.*, “Effects of thermal aging on creepage discharge in oil-impregnated pressboard under combined AC-DC voltage,” *IEEE Trans. Dielect. Electr. Insul.*, vol. 22, no. 5, pp. 2737–2746, 2015.
- [128] X. Li *et al.*, “Analysis of creeping discharges on oil-impregnated pressboard under combined AC and DC voltages,” *IEEE Trans. Dielect. Electr. Insul.*, vol. 25, no. 6, pp. 2380–2388, 2018.
- [129] U. Gafvert *et al.*, “Electrical field distribution in transformer oil,” *IEEE Trans. Electr. Insul.*, vol. 27, no. 3, pp. 647–660, 1992.
- [130] H. Okubo *et al.*, “Charge behavior in flowing oil in oil / pressboard insulation system by electro-optic field measurement,” *IEEE Trans. Dielect. Electr. Insul.*, vol. 10, no. 6, pp. 956–962, 2003.
- [131] *Electrical Strength of Insulating Materials - Test Methods Part 1: Tests at Power Frequencies*, IEC 60243-1: 2013, 2013.
- [132] *Insulating liquids — Measurement of relative permittivity, dielectric dissipation factor ($\tan \delta$) and d.c. resistivity*, IEC 60247: 2004, 2004.
- [133] T. K. Saha and P. Purkait, “Investigation of polarization and depolarization current measurements for the assessment of oil-paper insulation of aged transformers,” *IEEE Trans. Dielect. Electr. Insul.*, vol. 11, no. 1, pp. 144–154, 2004.

- [134] G. Lala *et al.*, "Influence of the geometric orientation of cellulosic fibers on the electrical behavior of pressboard under DC stresses," in *IEEE Electr. Insul. Conf. (EIC)*, Montreal, Canada, 2016, pp. 472–475.
- [135] *High-voltage test techniques - Partial discharge measurements: Partial discharge measurements*, IEC 60270: 2000, 2000.
- [136] *Insulating liquids - Oil-impregnated paper and pressboard - Determination of water by automatic coulometric Karl Fischer titration*, IEC 60814: 1997, 1997.
- [137] Metrohm AG, "Instructions for Use of 756/831 KF Coulometer," Herisau, Switzerland, 2003.
- [138] Metrohm AG, "Instructions for Use 832 KF Thermoprep," Herisau, Switzerland, 2004.
- [139] O. Kleboth-Lugova, B. Buerschaper, and T. Leibfried, "Feuchtebestimmung in Isoliermedien - ein Erfahrungsbericht," in *ETG Fachtagung Diagnostik*, Cologne, 2004.
- [140] M. Koch *et al.*, "Reliability and Improvements of Water Titration by the Karl Fischer Technique," in *15th Int. Symp. High-Voltage Engineering (ISH 2007)*, Ljubljana, Slovenia, 2007, pp. 1–6.
- [141] *Test Methods for Sampling and Testing Untreated Paper Used for Electrical Insulation*, ASTM D202-08, 2008.
- [142] ENERGY Support GmbH, "Operating instructions for the TOGA GC," Neuss, Germany, 2006.
- [143] N. Bakar, A. Abu-Siada, and S. Islam, "A review of dissolved gas analysis measurement and interpretation techniques," *IEEE Electr. Insul. Mag.*, vol. 30, no. 3, pp. 39–49, 2014.
- [144] Neoptix Canada LP., "Product Brochure of Neoptix T1 Probe," Québec, Canada, 2013.
- [145] Wikipedia, Scanning Electron Microscope, Available: <https://en.wikipedia.org/w/index.php?oldid=809622242>.
- [146] Keyence Corporation, "Color 3D Laser Microscope Reference Manual," Osaka, Japan, 2008.
- [147] I. ANSYS SAS IP, "Maxwell Online Help," Canonsburg, Pennsylvania, U.S.A., 2012.
- [148] *IEEE Guide for Loading Mineral-Oil-Immersed Transformers and Step-Voltage Regulators*, IEEE Std C57.91- 2011, 2012.
- [149] *Pressboard and Presspaper for Electrical Purposes - Part 2: Methods of Tests*, IEC 60641-2, 2004.
- [150] Wikipedia, Jurin's law, Available: https://en.wikipedia.org/wiki/Jurin%27s_law.
- [151] R.-j. Liao *et al.*, "Thermal aging micro-scale analysis of power transformer pressboard," *IEEE Trans. Dielect. Electr. Insul.*, vol. 15, no. 5, pp. 1281–1287, 2008.
- [152] N. C. Sahoo, Salama, M. M. A., and R. Bartnikas, "Trends in partial discharge pattern classification: a survey," *IEEE Trans. Dielect. Electr. Insul.*, vol. 12, no. 2, pp. 248–264, 2005.
- [153] Andreas Küchler, *Hochspannungstechnik: Grundlagen - Technologie - Anwendungen*, 3rd ed., Berlin, Heidelberg, Springer, 2009.
- [154] M. Hoof and R. Patsch, "Pulse-sequence analysis: A new method for investigating the physics of PD-induced ageing," *IEE Proc.: Sci., Meas. Technol.*, vol. 142, no. 1, pp. 95–101, 1995.
- [155] Cigre Task Force 15.01.04, "Partial discharges in transformer insulation," in *Cigré Session 2000*, pp. 1–12.
- [156] E. Gulski and F. H. Kreuger, "Computer-aided recognition of discharge sources," *IEEE Trans. Electr. Insul.*, vol. 27, no. 1, pp. 82–92, 1992.
- [157] E. Gulski, "Discharge pattern recognition in high voltage equipment," *IEE Proc.: Sci., Meas. Technol.*, vol. 142, no. 1, pp. 51–61, 1995.
- [158] Doble Lemke GmbH, "User Manual of Digital Partial Discharge Measuring System LDS-6," Kesselsdorf, Germany, 2015.
- [159] S. Chandrasekar and G. Montanari, "Analysis of partial discharge characteristics of natural esters as dielectric fluid for electric power apparatus applications," *IEEE Trans. Dielect. Electr. Insul.*, vol. 21, no. 3, pp. 1251–1259, 2014.
- [160] X. Ma, C. Zhou, and I. J. Kemp, "Interpretation of wavelet analysis and its application in partial discharge detection," *IEEE Trans. Dielect. Electr. Insul.*, vol. 9, no. 3, pp. 446–457, 2002.

- [161] L. Satish and B. Nazneen, "Wavelet-based denoising of partial discharge signals buried in excessive noise and interference," *IEEE Trans. Dielect. Electr. Insul.*, vol. 10, no. 2, pp. 354–367, 2003.
- [162] X. Ma, C. Zhou, and I. J. Kemp, "Automated wavelet selection and thresholding for PD detection," *IEEE Electr. Insul. Mag.*, vol. 18, no. 2, pp. 37–45, 2002.
- [163] X. Zhou, C. Zhou, and I. J. Kemp, "An improved methodology for application of wavelet transform to partial discharge measurement denoising," *IEEE Trans. Dielect. Electr. Insul.*, vol. 12, no. 3, pp. 586–594, 2005.
- [164] S. Singh and M. N. Bandyopadh, "Duval Triangle: A Noble Technique for DGA in Power Transformers," *Int. J. Elec. Power Eng.*, vol. 4, no. 3, pp. 193–197, 2010.
- [165] *IEEE Guide for the Interpretation of Gases Generated in Oil-Immersed Transformers*, IEEE Std C57.104-2008, 2008.
- [166] J. Faiz and M. Soleimani, "Dissolved gas analysis evaluation in electric power transformers using conventional methods a review," *IEEE Trans. Dielect. Electr. Insul.*, vol. 24, no. 2, pp. 1239–1248, 2017.
- [167] P. Mirowski and Y. LeCun, "Statistical Machine Learning and Dissolved Gas Analysis: A Review," *IEEE Trans. Power Delivery*, vol. 27, no. 4, pp. 1791–1799, 2012.
- [168] *Mineral oil-impregnated electrical equipment in service – Guide to the interpretation of dissolved and free gases analysis*, IEC/CEI 60599:1999+A1:2007, 2007.
- [169] M. Duval, "A review of faults detectable by gas-in-oil analysis in transformers," *IEEE Electr. Insul. Mag.*, vol. 18, no. 3, pp. 8–17, 2002.
- [170] H. Illias, G. Chen, and P. L. Lewin, "Modeling of partial discharge activity in spherical cavities within a dielectric material," *IEEE Electr. Insul. Mag.*, vol. 27, no. 1, pp. 38–45, 2011.
- [171] L. A. Dissado, "Understanding electrical trees in solids: From experiment to theory," *IEEE Trans. Dielect. Electr. Insul.*, vol. 9, no. 4, pp. 483–497, 2002.
- [172] K.-C. Kao, *Dielectric phenomena in solids: With emphasis on physical concepts of electronic processes*, San Diego, Elsevier Academic Press, 2004.
- [173] T. Baumann *et al.*, "Field-enhancing defects in polymeric insulators causing dielectric aging," *IEEE Trans. Elect. Insul.*, vol. 24, no. 6, pp. 1071–1076, 1989.
- [174] M.M. Tang and R. Bacon, "Carbonization of cellulose fibers—I. Low temperature pyrolysis," *Carbon*, vol. 2, no. 3, pp. 211–220, 1964.
- [175] Y.-C. Lin *et al.*, "Kinetics and Mechanism of Cellulose Pyrolysis," *J. Phys. Chem. C*, vol. 113, no. 46, pp. 20097–20107, 2009.
- [176] Y.-R. Rhim *et al.*, "Changes in electrical and microstructural properties of microcrystalline cellulose as function of carbonization temperature," *Carbon*, vol. 48, no. 4, pp. 1012–1024, 2010.
- [177] H. Chen, *Handbook of Power Equipment Abnormal Operation & Accidents Handling*, 1st ed., Beijing, China Water&Power Press, 2009.
- [178] T. Tanaka, "Internal Partial Discharge and Material Degradation," *IEEE Electr. Insul. Mag.*, EI-21, no. 6, pp. 899–905, 1986.
- [179] T. Ishida, M. Nagao, and M. Kosaki, "Relation between swarming pulsive microdischarges and surface roughness of dielectric materials in terms of surface potential distribution," in *11th Int. Symp. High-Voltage Engineering (ISH 99)*, London, UK, 1999, 309-312.
- [180] *Power transformers – Part 2: Temperature rise for liquid-immersed transformers*, IEC 60076-2, 2011.
- [181] H. Borsi and U. Schröder, "Initiation and formation of partial discharges in mineral-based insulating oil," *IEEE Trans. Dielect. Electr. Insul.*, vol. 1, no. 3, pp. 419–425, 1994.
- [182] H. Borsi, "The relation between thermal and electrical stress and the PD behavior of epoxy-resin transformers," *IEEE Trans. Elect. Insul.*, vol. 28, no. 6, pp. 1007–1015, 1993.
- [183] *IEEE Standard Test Procedure for Thermal Evaluation of Insulation Systems for Liquid-Immersed Distribution and Power Transformers*, IEEE Std C57.100-2011, 2011.

- [184] G. C. Montanari and M. Cacciari, "On the electrical endurance characterization of insulating materials by constant and progressive stress test," *IEEE Trans. Elect. Insul.*, vol. 27, no. 5, pp. 1000–1008, 1992.
- [185] *Electrical Insulating Materials-A.C. Voltage Endurance Evaluation-Introduction*, IEC/TS 61251: 2008, 2008.
- [186] A. Nosseir *et al.*, "Effect of Temperature on the Breakdown Probability of Liquid Dielectrics," *IEEE Trans. Electr. Insul.*, EI-15, no. 6, pp. 502–505, 1980.
- [187] R. m. Radwan, T. d. Eish, and S. Ramadan, "Factors Affecting Breakdown Phenomenon in Transformer oil with Uniform and Non-uniform Fields," in *IEEE Int. Conf. Conduct. Breakdown Dielectr. Liq. (ICDL)*, Salford, UK, 1987, pp. 455–459.
- [188] *IEEE Guide for the Statistical Analysis of Electrical Insulation Breakdown Data*, IEEE Std 930-2004, 2004.
- [189] W. Hauschild and W. Mosch, *Statistical techniques for high-voltage engineering*, London, IEE, 1992.
- [190] *Electrical Strength of Insulating Materials - Test Methods Part 1: Tests at Power Frequencies*, IEC 60243-1:2013, 2013.
- [191] P. Morshuis *et al.*, "Stress conditions in HVDC equipment and routes to in service failure," *IEEE Trans. Dielect. Electr. Insul.*, vol. 22, no. 1, pp. 81–91, 2015.
- [192] S. J. Cho *et al.*, "DC field distribution in HVDC transformer considering the effects of space charge and temperature due to presence of oil immersed pressboard," *IEEE Trans. Dielect. Electr. Insul.*, vol. 21, no. 2, pp. 866–872, 2014.
- [193] N. Inoue *et al.*, "Mechanism of charge accumulation at flowing oil/pressboard interface based on optical measurement of electric field," in *IEEE Conf. Electr. Insul. Dielectr. Phenom (CEIDP)*, Ontario, Canada, 2001, pp. 536–539.
- [194] Yang Jia-xiang *et al.*, "Creeping discharge performance of oil-paper insulation with streaming electrification," *IEEE Trans. Dielect. Electr. Insul.*, vol. 4, no. 6, pp. 780–784, 1997.
- [195] M. Szechtman, T. Wess, and C. V. Thio, "A Benchmark Model for HVDC System Studies," in *Proc. Int. Conf. AC/DC Power Transmission*, 1991, pp. 374–378.
- [196] *Converter Transformers - Part 2: Transformer for HVDC Applications*, CEI/IEC 61378-2:2001, 2001.
- [197] *Standard for General Requirements and Test Code for Oil-Immersed HVDC Converter Transformers*, IEEE Std C57.129-2007, 2008.
- [198] A. Lindroth, "The Relationship between Test and Service Stresses as a Function of Resistivity Ratio for HVDC Converter Transformers and Smoothing Reactors," *Cigre Electra*, vol. 157, pp. 32–58, 1994.
- [199] F. H. Kreuger, *Industrial High DC Voltage: Fields, Breakdown and Tests*, Delft, Delft University Press, 1995.
- [200] U. Fromm, "Interpretation of Partial Discharges at DC Voltages," *IEEE Trans. Dielect. Electr. Insul.*, vol. 2, no. 5, pp. 761–770, 1995.
- [201] P. Morshuis, M. Jeroense, and J. Beyer, "Partial discharge. Part XXIV: The Analysis of PD in HVDC equipment," *IEEE Electr. Insul. Mag.*, vol. 13, no. 2, pp. 6–16, 1997.
- [202] J. Fabian *et al.*, "Current challenges and issues of designing HVDC converter transformers," in *Annu. Rep. - Conf. Electr. Insul. Dielectr. Phenom. (CEIDP)*, Cancun, Mexico, 16-19, Oct. 2011.
- [203] I. J. Seo *et al.*, "Identification of insulation defects by modified chaotic analysis partial discharge under DC stress," in *Cigre Session*, Paris, 2012, pp. 1–8.
- [204] I.-J. Seo *et al.*, "Identification of Insulation Defects Based on Chaotic Analysis of Partial Discharge in HVDC Superconducting Cable," *IEEE Trans. Appl. Supercond.*, vol. 25, no. 3, pp. 1–5, 2015.
- [205] *Guide for the Statistical Analysis of Electrical Insulation Breakdown Data*, IEEE Std 930-2004, 2004.
- [206] M. Hao *et al.*, "Space charge behavior in oil gap and impregnated pressboard combined system under HVDC stresses," *IEEE Trans. Dielect. Electr. Insul.*, vol. 23, no. 2, pp. 848–858, 2016.
- [207] K. Wu *et al.*, "Space charge behavior in the sample with two layers of oil-immersed-paper and oil," *IEEE Trans. Dielect. Electr. Insul.*, vol. 21, no. 4, pp. 1857–1865, 2014.

-
- [208] C. Yi-long *et al.*, “Characteristics of surface charge on oil impregnated pressboard under non-uniform DC stress,” in *IEEE Conf. Electr. Insul. Dielectr. Phenom. (CEIDP)*, Shenzhen, China, 2013, pp. 303–306.
- [209] J. Beyer, “Space Charge and Partial Discharge Phenomena in High Voltage DC Devices,” PhD Dissertation, Technical University of Delft, Delft, the Netherlands, 2002.
- [210] A. Pirker and U. Schichler, “Partial discharge measurement at DC voltage — Evaluation and characterization by NoDi* pattern,” *IEEE Trans. Dielect. Electr. Insul.*, vol. 25, no. 3, pp. 883–891, 2018.
- [211] M. R. Rahimi, R. Javadinezhad, and M. Vakilian, “DC partial discharge characteristics for corona, surface and void discharges,” in *Proc. 11th Int. Conf. Prop. Appl. Dielectr. Mater. (ICPADM)*, Sydney, Australia, 2015, pp. 260–263.
- [212] S. Blufpand, “Partial Discharge Recognition of Defects in Gas Insulated Systems under DC Voltage,” MSc Thesis, Technical University of Delft, Delft, the Netherlands, 2014.
- [213] J. Yang *et al.*, “Study of the influence of injected charge on streaming electrification,” *IEEE Trans. Dielect. Electr. Insul.*, vol. 5, no. 4, pp. 513–517, 1998.
- [214] Y. Jiaxiang *et al.*, “Study of influence of corona discharge on streaming electrification of transformer oil,” in *Proc. 3rd Int. Conf. Prop. Appl. Dielectr. Mater. (ICPADM)*, Tokyo, Japan, 1991, pp. 863–866.